

---

# Investigating the Influence of the Probe Tip in Scanning Near-field Optical Microscopy

---

*Author:*

**Panji ACHMARI**

Sarjana Sains/ Bachelor of Science (S.Si)

Master of Philosophy (MPhil)

*A thesis submitted in total fulfillment of the requirements  
for the degree of Doctor of Philosophy (PhD)*

*in the*

Department of Chemistry and Physics

School of Molecular Sciences

College of Science, Health, and Engineering

**LA TROBE UNIVERSITY**

Victoria, Australia

December 2021





## Declaration of Authorship

I, Panji ACHMARI, declare that this thesis titled, “Investigating the Influence of the Probe Tip in Scanning Near-field Optical Microscopy” and the work presented in it are my own. I confirm that:

- This work was done wholly while in candidature for a research degree at La Trobe University.
- This thesis has not been submitted for a degree or any other qualification at this University or any other tertiary institution.
- Where I have consulted the published work of others, this is always clearly attributed.
- Where I have quoted from the work of others, the source is always given. With the exception of such quotations, this thesis is entirely my own work.
- I have acknowledged all main sources of help.

Signed: Panji Achmari

Date: 14 December 2021



# *Abstract*

Over the past few decades, scanning near-field optical microscopy (SNOM) has developed into an established method for obtaining images of the near-surface region of samples. Using an optical probe scanned at a specified subwavelength probe-sample distance, SNOM maps the optical properties of surfaces and interfaces with sub-diffraction limited spatial resolution. Fundamental to SNOM imaging is the probe tip. Although the probe is widely acknowledged to play a significant role in image formation there have, thus far, only been a limited number of studies into its influence on near-field imaging. Within this thesis, we present a custom-developed simulation model based on the finite-difference time-domain (FDTD) method. When combined with experimental data generated from SNOM scans, the relative influence of the probe tip on SNOM image formation was systematically investigated. A model sample, consisting of slit apertures of varying dimensions in a metal film, was imaged using SNOM and characterised via a simulation model which incorporated the near-field influence of the probe. The probe tip was found to have a rather profound effect on the shape of the measured intensity profiles and its inclusion in the calculation resulted in a dramatic improvement in the quality of fit between simulated and experimental image intensity profiles. A key finding from this study is that the probe tip is a crucial component in understanding SNOM imaging experiments and its inclusion is essential in the model in order to be able to replicate the key features of SNOM imaging. We applied the simulation model developed and refined here to further investigate the image degradation arising from the convolution between the probe tip and the sample. The resulting point spread function (PSF) of the SNOM imaging system was modelled based on these simulations. It is envisaged that this approach could be applied to the deconvolution of the PSF and the SNOM image, potentially improving the image spatial resolution and quality.



## *Acknowledgements*

- This work was supported by James T. Riady Research Scholarship.
- Dr Shanshan Kou. I would like to thank her efforts and support during my candidature as my principal supervisor. She had a substantial influence in all aspects of this study and provided an invaluable guide for me during the candidature.
- Prof Brian Abbey. He has been very involved during this study as my co-supervisor. I thank him for the support and encouragement to keep doing better as a research student.
- Dr Arif Siddiquee, for the great help, particularly on the discussions on the experimental parts of this study.
- Dr Jiao Lin, for all helpful discussions, particularly on the nanophotonics and simulation parts of this study.
- Dr Guangyuan Si, for the help of sample fabrication at Melbourne Centre for Nanofabrication.
- Prof Paul Pigram and Dr Narelle Brack, as part of my research progress panel.
- La Trobe University staffs. Special thanks to Optics group and CoE Imaging group.
- Fellow students at La Trobe University and Indonesian Students Association (PPIA).
- To my wife, Leni Yani, and my son, Senandika Achmari, thank you for the great journey we have had together. We stayed strong and we keep going.
- My families in Indonesia.
- My friends in the online community, especially in Hotwheels Discord server. It has been fun, especially during the pandemic situation when we could not spend much time outside.
- Everyone else that has been involved but I cannot mention one by one. Thank you all.



# Contents

<b>Declaration of Authorship</b>	<b>iii</b>
<b>Abstract</b>	<b>v</b>
<b>Acknowledgements</b>	<b>vii</b>
<b>Contents</b>	<b>ix</b>
<b>List of Figures</b>	<b>xiii</b>
<b>List of Tables</b>	<b>xxix</b>
<b>List of Abbreviations</b>	<b>xxxi</b>
<b>1 Introduction</b>	<b>1</b>
1.1 Imaging with Scanning Near-field Optical Microscopy (SNOM)	1
1.1.1 SNOM Overview . . . . .	1
1.1.2 The Diffraction Limit . . . . .	4
1.1.3 Near-field and Far-field Optics . . . . .	5
1.2 Motivation . . . . .	8
1.3 Objectives . . . . .	10
1.4 Organisation of the Thesis . . . . .	12
1.5 Publication . . . . .	13
<b>2 Background and Literature Review</b>	<b>15</b>
2.1 Introduction . . . . .	15
2.2 Near-field Optics for Nanoscale Imaging . . . . .	16
2.3 Scanning Near-field Optical Microscopy (SNOM) . . . . .	19
2.3.1 SNOM and Its Impact in High-Resolution Imaging	19

2.3.2	The Configurations of SNOM . . . . .	25
2.3.3	Probe Tip in the SNOM Imaging and Author's Contributions . . . . .	30
2.4	Spatial Resolution and Image Restoration . . . . .	36
2.4.1	Spatial Resolution in Microscopy Imaging . . . . .	36
2.4.2	Deconvolution Algorithm for Image Restoration . . . . .	38
2.5	Chapter Summary . . . . .	43
<b>3</b>	<b>Methods</b>	<b>47</b>
3.1	Introduction . . . . .	47
3.2	SNOM Data Acquisition . . . . .	48
3.2.1	SNOM Setup . . . . .	48
3.2.2	Intensity Profiles from One-Dimensional Samples . . . . .	50
3.2.3	Fitting Functions . . . . .	50
3.3	Simulations using the Finite-Difference Time-Domain (FDTD) Method . . . . .	52
3.3.1	Introduction to the FDTD Method . . . . .	52
3.3.2	Components of the FDTD Simulation . . . . .	57
3.4	Image Deconvolution using the Richardson-Lucy Algorithm . . . . .	60
3.5	Chapter Summary . . . . .	62
<b>4</b>	<b>Simulation Model of the SNOM Imaging System</b>	<b>65</b>
4.1	Introduction . . . . .	65
4.2	Simulation Model of Subwavelength Structures and SNOM Imaging . . . . .	67
4.2.1	Simulation Model with Two-Dimensional Plane Detectors . . . . .	68
4.2.2	Simulation Model with the Probe Tip Included . . . . .	69
4.3	Simulation without the Probe Tip . . . . .	71
4.3.1	Transmission Spectra of Periodic Structures . . . . .	71
4.3.2	Near-field Images of Apertures . . . . .	76
4.4	Simulation including the Probe Tip . . . . .	79
4.4.1	Snapshots of Intensity Profiles . . . . .	79
4.4.2	Absorption by the Nanostructure . . . . .	80
4.4.3	Intensity Profiles of a Single Object . . . . .	82
4.4.4	Intensity Profiles of Adjacent Objects . . . . .	90



4.5	Chapter Summary . . . . .	95
<b>5</b>	<b>The Probe Tip Influence in the SNOM Imaging</b>	<b>97</b>
5.1	Introduction . . . . .	97
5.2	Slit Apertures as Characterisation Sample . . . . .	99
5.2.1	Single-Slit and Double-Slit Apertures . . . . .	99
5.2.2	SNOM Images of Characterisation Sample . . . . .	101
5.2.3	Estimating the SNOM Spatial Resolution . . . . .	105
5.3	Influence of the Probe Tip Parameters on the Intensity Profiles using FDTD Simulations . . . . .	105
5.4	Comparison between Experimental and Simulated Results	110
5.4.1	Single-Slit Apertures . . . . .	110
5.4.2	Double-Slit Apertures . . . . .	114
5.5	Predicting the Actual Slit Size from SNOM Images using Iterations . . . . .	117
5.6	Effect of Wavelength Variation . . . . .	119
5.7	Chapter Summary . . . . .	121
<b>6</b>	<b>Restoring SNOM Images using Deconvolution</b>	<b>125</b>
6.1	Introduction . . . . .	125
6.2	Point Spread Function (PSF) of the SNOM System . . . . .	127
6.2.1	Determining PSF using the Simulation Model . . . . .	128
6.2.2	Determining PSF from the Experimental Data . . . . .	131
6.3	Denoising SNOM Images . . . . .	134
6.4	Convergence Test with Gaussian and Pseudo-Voigt PSF . . . . .	137
6.5	Deconvolution of Slit Apertures Images . . . . .	141
6.5.1	Deconvolution with Gaussian and Pseudo-Voigt PSF	141
6.5.2	Deconvolution with a Simulated PSF . . . . .	149
6.5.3	Deconvolution with Experimental PSF . . . . .	157
6.6	SNOM Images of Fresnel Zone Plate . . . . .	162
6.7	Chapter Summary . . . . .	165
<b>7</b>	<b>Conclusions and Future Work</b>	<b>167</b>
7.1	Conclusions . . . . .	167
7.1.1	Simulation model of the SNOM Imaging System . . . . .	168

7.1.2	Probe Tip Influence in the SNOM Imaging (using Experimental Data) . . . . .	170
7.1.3	Restoring SNOM Images using Deconvolution . . .	172
7.2	Future Work . . . . .	173
7.2.1	Modelling a deficient probe tip and its imperfections	174
7.2.2	Modifications of the SNOM probe tip or the sample surface . . . . .	174
7.2.3	Improving deconvolution method for SNOM im- age post-processing . . . . .	176
<b>Bibliography</b>		<b>179</b>

# List of Figures

1.1	Evolution of diffraction patterns moving from near-field observation (Fresnel diffraction) to far-field observation (Fraunhofer diffraction) [12]. The object is a slit indicated by the red line on the horizontal axis. . . . .	6
1.2	Schematics of far-field and near-field imaging. (a) Far-field imaging using lens to collect light at a long-range distance (much larger than the wavelength), (b-c) Near-field imaging using aperture probe placed at a short-range distance (within subwavelength) (b) in collection mode and (c) in illumination mode. . . . .	7
2.1	Simplified schematic of far-field and near-field imaging (adapted from [1]). (a) In the far-field, light is focussed onto the sample and the transmitted light is collected by another lens, focusing it onto the detector. (b) Near-field imaging enables propagation of the high spatial frequency components by focusing the light through a subwavelength aperture. . . . .	17
2.2	Schematic of localised illumination at short-range distance to couple near-field optical signals from the sample, using (a) aperture-type probe and (b) scattering-type probe [47].	18

2.3	SNOM scan of metal island film [8]. (a) Schematic of hexagonal arrangement of the metal patches around the spheres. (b) SNOM images at the same location of the sample with polarisations indicated by the arrow. (c) Intensity profile along the horizontal white line shown in Fig.(b), confirming 50 nm resolution. (d) High-pass filtered image of the SNOM scan, revealing clearer features. . . . .	21
2.4	Images obtained simultaneously from (a) near-field fluorescence and (b) shear force topography of two rectangular single molecule of proteins. (c), (d) The intensity profiles along the lines 1 and 2 respectively (lines shown in Fig.(a) and (b)) with the arrows on the graphs indicate the respective $y$ -axis for each plot. [8] . . . . .	22
2.5	Interference of modes on an array of V-antennas made of gold [17]. (a) SEM image of V antennas with different opening angles and orientations. The antennas were illuminated with the incident polarisation ( $E_{inc}$ ) perpendicular to the detected polarisation, as indicated by the arrows. The near-field intensity of the V-antennas obtained from the (b) SNOM experiment (exp), (c) simulation (sim), and (d) isolated simulation (iso) for each antenna. The phase profile on the antennas are also shown for (e) experimental, (f) simulated, and (g) isolated simulated results. . . . .	23
2.6	Near-field images of a spiral antenna under left-handed and right-handed circularly polarised (LCP and RCP) illumination [66]. (a) An SEM image of the 5-turn spiral antenna with (b) illustration of directional wave at the active zone of the antenna (dashed green circle). (c,d) Experimental electric field amplitudes near the sample surface for (c) LCP and (d) RCP. . . . .	24
2.7	The standard setup for aperture-type SNOM in illumination mode, consisting of (a) the illumination unit, (b) the collection and redistribution unit (in an inverted microscope), and (c) the detection module (adapted from Ref. [8]). . . . .	29

2.8	Corrugated SNOM probe for achieving high energy throughput, with (a) circular grooves and (b) oval grooves [29]. . .	30
2.9	Simulation setup for investigating the scattering effect of the probe tip in image formation of a circular disc [41]. . .	31
2.10	Simulated near-field intensity above a circular disc (a-b) without and (c-d) with the probe included in the calculation (blue lines) [41]. The first column (a,c) is in a constant gap mode and the second column (b,d) is in a constant height mode. The top-hat profile at the bottom of each figure (orange line) shows the disc location. . . . .	32
2.11	Study of the SNOM resolution investigated with a sample consisting of a boundary between metal and dielectric materials. (a) The schematic of the probe scattering while scanning the sample and (b) the intensity profiles observed across the boundary. . . . .	33
2.12	Interference pattern produced by a square arrangement of four slit apertures, producing two different patterns of (a) diamond-like symmetry and (b) square-like symmetry from different interferences between in-plane and out-of-plane components arising from the surface plasmon effects of the slit apertures [4]. . . . .	34
2.13	(a) Schematic of the simulation model of the SNOM scan on the double-slit aperture in a gold film, and (b) the SEM and (c) SNOM scan images of a double slit apertures [34]. .	35
2.14	Schematic for investigating spatial resolution using two closely spaced objects [1]. . . . .	36
2.15	Deconvolution of an OCT image of a human fingertip skin sample. (a) PSF of the imaging system, (b) image before deconvolution, and (c) image after deconvolution. [85] . .	41
2.16	Schematic showing the convolution process during the SNOM scan. A top-down view of the sample is shown with the aperture scanning above it. The circles indicate the locations of the probe tip aperture between the scan steps, with the dashed circle representing before and the solid circle after probe movement. . . . .	42

2.17	Simulation model of SNOM images based on an AFM image. (a) AFM image, (b) simulated SNOM image derived from (a), (c) simulated SNOM image with added noise, and (d) simulated SNOM image after denoising. (e,f,g) Deconvolution results for the images shown in Figs. (b,c,d) respectively. [87] . . . . .	43
3.1	The layout of aperture-type SNOM in the collection mode used in this study. . . . .	49
3.2	A schematic showing the lines drawn for calculating the average intensity profile perpendicular to the slit. The vertical dashed blue line represents the line of brightest intensity which is in the middle of the slit. The intensity profiles were measured along the green horizontal lines and were averaged to obtain the final intensity profile. . . . .	51
3.3	Updating scheme of the electric and magnetic fields as a function of time based on Yee algorithm. . . . .	54
3.4	Arrangement of the electric and magnetic field nodes on the FDTD unit cell, based on Yee algorithm. . . . .	55
3.5	Closer look at the field nodes on the top face of Yee cell shown in Fig. 3.4. . . . .	56
3.6	Overview of the Lumerical FDTD software interface. . . .	57
3.7	A demonstration of Richardson-Lucy algorithm to restore blurred image. (a) The original image, (b) the degraded image, (c) the restored image using the Richardson-Lucy algorithm, and (d) the Gaussian PSF used in this demonstration. Figure adapted from Ref. [96]. . . . .	61
4.1	Schematic of simulation model with a 2D plane detector, without the probe. The detector is placed at a near-field distance $h$ . . . . .	68
4.2	Schematic of simulation model with the probe tip included. The set up scans the sample at a near-field distance $h$ , with a tip aperture diameter $D$ . Inset: lateral section of probe tip, showing the probe materials. . . . .	70

4.3	Schematic of simulations for calculating the transmittance through an array of (a) circular apertures and (b) slit apertures using a 2D plane detector. . . . .	72
4.4	The transmittance through an array of circular apertures with a periodicity of $p = 400$ nm and a 250 nm-thick metal film made from (a) gold and (b) silver. The aperture diameter was $d = p/1.75$ . The reference (Ref) data was taken from [110], with simulated data generated using the simulation (sim), with coarse (10 nm) and fine (2 nm) meshes. .	73
4.5	The transmittance through an array of circular apertures with the same configuration as in Fig. 4.4, but the metal film was made from (a) copper and (b) aluminium [110], showing the reference (Ref) data from the literature and simulated data using the FDTD (sim). . . . .	74
4.6	The transmittance through an array of slit apertures in a metal film with various thickness $t$ using the RCWA method (solid lines) [111]. Data was reproduced using the FDTD simulations (dashed lines) with (a) coarse mesh of 10 nm, (b) medium mesh of 5 nm, and (c) fine mesh of 2 nm. . . .	75
4.7	Schematic of the simulation for calculating the near-field intensity profile of adjacent objects in the form of a pair of circular apertures. The profile was detected using a 2D plane detector, placed at a height $h$ from the sample, without including the probe tip. . . . .	76
4.8	Intensity profiles of a pair of circular apertures with $d = 200$ nm and $s = 50$ nm at a distance of (a) 10 nm, (b) 50 nm, and (c) 100 nm, using simulations incorporating a 2D detector. The locations of the apertures are annotated with blue circles. . . . .	77
4.9	Intensity profiles of a pair of circular apertures with $d = 200$ nm and $s = 100$ nm at a distance of (a) 10 nm, (b) 50 nm, and (c) 100 nm, obtained from the simulations with 2D plane detector. The locations of the apertures are indicated by blue circles. . . . .	78

4.10	Intensity profiles of a pair of circular apertures with $d = 100$ nm and $s = 200$ nm at a distance of (a) 10 nm, (b) 50 nm, and (c) 100 nm, obtained from simulations using a 2D plane detector. The locations of the apertures are indicated by blue circles. . . . .	79
4.11	(a) Intensity profile at $h = 50$ nm from the sample, generated from the simulation without the probe. (b) Intensity profile at the tip of the probe, at a distance $h = 50$ nm from the sample, generated from the simulation with the probe.	80
4.12	Schematic illustrating calculations of the absorption using a detector enclosing the object for (a) a circular aperture in a gold film and (b) a disc on a glass substrate. . . . .	80
4.13	The absorbed power by a circular aperture with $d = 200$ nm and film thickness 200 nm using a probe tip with $D = 100$ nm at various tip distances $h$ from the aperture. (a) The absorption spectra in the wavelength range $\lambda = 400$ nm to $\lambda = 900$ nm and (b) zoomed-in version in the range $\lambda = 620$ nm to $\lambda = 660$ nm. . . . .	82
4.14	The absorbed power by the disc with $d = 200$ nm and thickness 200 nm using a probe tip of size of $D = 100$ nm located at a distance $h$ from the top surface of the disc. (a) The absorption spectra in the wavelength range of $\lambda = 400$ nm to $\lambda = 900$ nm and (b) zoomed-in version in the range of $\lambda = 600$ nm to $\lambda = 700$ nm. . . . .	83
4.15	Schematic of the simulation for calculating the intensity profile of a single structure measured using SNOM, with the probe tip included. The samples are (a) a single circular aperture and (b) a single-slit aperture in a metal film. .	84
4.16	Intensity profiles measured using SNOM along the line through the centre of a circular aperture with (a) $d = 100$ nm and (b) $d = 200$ nm. . . . .	85



4.17	Simulated intensity profile detected by the probe tip for a single circular aperture with $d = 200$ nm, using probe parameters $h = 10$ nm and (a) $D = 150$ nm and (b) $D = 300$ nm. (c) Simulated intensity profile using a 2D plane detector at $h = 10$ nm. . . . .	86
4.18	(a) Simulated intensity profile detected by the probe tip for a single circular aperture with $d = 200$ nm, using probe parameters $h = 50$ nm and $D = 150$ nm. (b) Simulated intensity profile using a 2D plane detector at $h = 50$ nm. . . . .	87
4.19	Simulated intensity profiles across a single-slit aperture with a width of (a) $w = 200$ nm and (b) $w = 400$ nm, measured using an optical probe with various $h$ and $D$ . . . . .	88
4.20	Simulated intensity profiles calculated with inhomogeneous and homogeneous spacing between the probe measurements for a single-slit aperture with (a) $w = 200$ nm and (b) $w = 400$ nm. The data points are indicated by dots (inhomogeneous step) and crosses (homogeneous step). Profiles are shifted upward for clarity. . . . .	89
4.21	Schematic of the simulation for calculating the intensity profile of two adjacent structures measured using SNOM, with the probe tip included. The samples are (a) a pair of circular apertures and (b) a double-slit aperture in a metal film. . . . .	90
4.22	Intensity profiles measured using SNOM along the line through the centre of a pair of circular apertures with (a) $d = 200$ nm, $s = 100$ nm and (b) $d = 200$ nm, $s = 200$ nm. . . . .	91
4.23	(a) Simulated intensity profile detected by the SNOM probe tip with $h = 10$ nm and $D = 150$ nm for a pair of circular apertures with $d = 200$ nm and $s = 200$ nm, and (b) simulated intensity profile detected by a 2D plane detector at $h = 10$ nm. . . . .	92
4.24	Simulated intensity profile detected by the SNOM probe tip with $h = 10$ nm and $D = 300$ nm for a pair of circular apertures with $d = 200$ nm and $s = 200$ nm. . . . .	93

4.25	Simulated intensity profile measured using a probe tip with $h = 50$ nm, and probe tip size parameters of (a) $D = 150$ nm and (b) $D = 300$ nm, across a double-slit aperture with $w = 200$ nm and various separation gap $s$ . . . . .	94
5.1	Schematics of the characterisation samples, (a) single-slit aperture and (b) double-slit aperture. . . . .	100
5.2	SNOM scan result of a single-slit aperture with $w = 180$ nm. (a) The raw SNOM image, and (b) the same image showing the lines used for the slit profile analysis. (c) The average intensity profile across the slit, resulting from averaging 100 lines between two green lines shown in (b). . . . .	101
5.3	SNOM scan result of a double-slit aperture with $w = 470$ nm and $s = 140$ nm. (a) The raw SNOM image, and (b) showing the lines used for the slit profile analysis. (c) The average intensity profile across the slit, measured from 100 lines between two green lines shown in (b). . . . .	102
5.4	SNOM scan results of single-slit apertures with (a) $w = 150$ nm and (b) $w = 410$ nm and intensity profiles across the slits. . . . .	103
5.5	SNOM scan results of double-slit apertures with (a) $w = 480$ nm, $s = 230$ nm, and (b) $w = 410$ nm, $s = 80$ nm, and intensity profiles across the slits. . . . .	104
5.6	Estimating the spatial resolution of the SNOM using the derivative of the intensity profiles to determine the FWHM associated with the sharp edges of the slits. The intensity profiles are taken from single-slit apertures of width of $w = 150$ nm and $w = 180$ nm. . . . .	106
5.7	Intensity profiles across (a) single-slit with $w = 180$ nm and (b) double-slit with $w = 470$ nm and $s = 140$ nm from simulations without the probe, using a near-field 2D detector at height $h = 10$ nm to 100 nm from the sample. The intensity profiles were normalised to the same amplitudes and displaced vertically for clarity. . . . .	107

5.8	Intensity profiles across a single-slit aperture with $w = 180$ nm from simulations with the probe at (a) constant $D = 300$ nm, different $h$ , and (b) constant $h = 10$ nm, different $D$ . The intensity profiles were normalised to the same amplitudes and displaced vertically for clarity. . . . .	108
5.9	Intensity profiles across a single-slit aperture with $w = 180$ nm from simulations with the probe at (a) constant $D = 300$ nm, different $h$ , and (b) constant $h = 10$ nm, different $D$ . The intensity profiles were normalised to the same amplitudes and displaced vertically for clarity. . . . .	109
5.10	Example comparison between the experimental (exp) and simulated (sim) intensity profiles for a single-slit with $w = 180$ nm. The simulated results are shown for both simulations with and without the probe tip. Inset: SEM and SNOM images of the single-slit. . . . .	111
5.11	Comparison between the experimental (exp) and simulated (sim) intensity profiles for single-slits with (a) $w = 150$ nm and (b) $w = 410$ nm. The simulated results are shown for both simulations with and without the probe tip. Inset: SEM images of the single-slit. . . . .	112
5.12	Example comparison between the experimental (exp) and simulated (sim) intensity profiles for a double-slit with $w = 470$ nm and $s = 140$ nm. The simulated results are shown for both simulations with and without the probe tip. Inset: SEM and SNOM images. . . . .	115
5.13	Comparison between the experimental (exp) and simulated (sim) intensity profiles for double-slits with (a) $w = 480$ nm and $s = 230$ nm and (b) $w = 410$ nm and $s = 80$ nm. The simulated results are shown for both simulations with and without the probe tip. Inset: SEM images. . . . .	116

- 5.14 Estimating the physical dimension of single-slit apertures by finding the best match with the smallest absolute error  $e_{abs}$  between the experimental (exp) and simulated (sim) intensity profiles. The probe parameters used were  $D = 300$  nm and  $h = 10$  nm. The iterations were performed for (a)  $w_{SEM} = 150$  nm and (b) 180 nm as confirmed from SEM images. Minimum error values are highlighted in red-shaded boxes, initially using coarse step of 50 nm (left column), then with finer steps of 10 nm (right column). The profiles are displaced vertically for clarity. . . . . 118
- 5.15 Simulated intensity profiles across a single-slit aperture with  $w = 180$  nm and double-slit apertures with  $w = 470$  nm and  $s = 140$  nm. The results from five incident wavelengths between 500 nm and 640 nm are shown with the probe-tip included (solid lines) and without the probe-tip included (dashed lines). The yellow shaded areas indicate the physical extent of the slit(s). The profiles were normalised such that the integral over the distance ( $x$ ) (i.e. area under the profile) was the same in each case. . . . . 120
- 6.1 Simulated intensity profiles of the transmitted light through the circular aperture with diameter (a)  $d=80$  nm, (b)  $d=100$  nm, and (c)  $d=150$  nm, illuminated with  $x$ -polarised beam, detected using a probe tip with  $h = 10$  nm and  $D = 300$  nm. . 129
- 6.2 Simulated intensity profiles of the transmitted light through the circular aperture with diameter (a)  $d = 80$  nm, (b)  $d = 100$  nm, and (c)  $d = 150$  nm, illuminated with unpolarised beam, detected using a probe tip with  $h = 10$  nm and  $D = 300$  nm. 130
- 6.3 Simulated intensity profiles of the transmitted light through a circular aperture with diameter  $d = 100$  nm, illuminated with an  $x$ -polarised beam, detected using the probe tip with the size of (a)  $D = 150$  nm and (b)  $D = 500$  nm. . . . . 130

6.4	Simulated intensity profiles of the transmitted light through the circular aperture with diameter $d = 100$ nm, illuminated with an unpolarised beam, detected using a probe tip with the size of (a) $D = 150$ nm and (b) $D = 500$ nm. . .	131
6.5	SEM images of the circular apertures in a metal film with a diameter of (a) $d = 80$ nm, (b) $d = 100$ nm, and (c) $d = 150$ nm. . . . .	132
6.6	Experimental data obtained from the SNOM scans of circular apertures in a metal film with a diameter of (a) $d = 80$ nm, (b) $d = 100$ nm, and (c) $d = 150$ nm (the colour range is not to scale). . . . .	133
6.7	Comparison between (a) simulated and (b) experimental PSF, using a SNOM scan of a circular aperture with $d = 100$ nm. . . . .	133
6.8	The (a) $x$ - and (b) $y$ -sections of the intensity profiles of simulated (sim) and experimental (exp) PSF shown in Fig. 6.7, along the lines through the centre of the image. . . . .	134
6.9	The images of a single-slit aperture with $w = 180$ nm, (a) before and (b) after the noise was reduced. . . . .	135
6.10	The images of a single-slit aperture with $w = 410$ nm, (a) before and (b) after the noise was reduced. . . . .	136
6.11	The images of a single-slit aperture with excessive denoising leads to inaccurate image. Images are shown for single-slit with $w = 180$ nm, (a) before and (b) after denoising. . .	136
6.12	(a) Approximated PSF using pseudo-Voigt function with FWHM=300 nm and (b) its line profile across the centre. . .	137
6.13	Deconvolution process of a single-slit aperture with $w = 180$ nm using a Gaussian PSF with FWHM=300 nm, showing (a) original image before deconvolution, and (b-f) the resulting deconvolved images after 20, 50, 100, 150, and 200 iterations. . . . .	138

6.14	Deconvolution process of a single-slit aperture with $w = 180$ nm using a pseudo-Voigt PSF with FWHM=300 nm, showing (a) original image before deconvolution, and (b-f) the resulting deconvolved images after 20, 50, 100, 150, and 200 iterations . . . . .	139
6.15	Deconvolution process for a single-slit aperture with $w = 410$ nm using a pseudo-Voigt PSF with FWHM=300 nm, showing (a) original image before deconvolution, and (b-f) the resulting deconvolved images after 20, 50, 100, 150, and 200 iterations . . . . .	140
6.16	Deconvolution of the SNOM image of a single-slit aperture with $w = 180$ nm using Gaussian PSF with FWHM=300 nm, showing (a) original image before deconvolution and (b) deconvolved image. . . . .	142
6.17	Intensity profile across the slit from the original and deconvolved images of single-slit aperture with $w = 180$ nm, using a Gaussian PSF with FWHM=300 nm. . . . .	142
6.18	Deconvolution of the SNOM image of the single-slit aperture with $w = 180$ nm using the pseudo-Voigt PSF with FWHM=300 nm, showing (a) original image before deconvolution and (b) deconvolved image. . . . .	143
6.19	Intensity profile taken across the slit for the original and deconvolved images of the single-slit aperture with $w = 180$ nm, using the pseudo-Voigt PSF with FWHM=300 nm. . . . .	144
6.20	Intensity profile across the slit for the original and deconvolved images of the single-slit aperture with $w = 180$ nm, using the pseudo-Voigt PSF with (a) FWHM=150 nm and (b) FWHM=500 nm. . . . .	145
6.21	Deconvolution of the SNOM image of a single-slit aperture with $w = 150$ nm using the pseudo-Voigt PSF with FWHM=300 nm, showing (a) original image and (b) deconvolved image. . . . .	146
6.22	Intensity profile across the slit using the original and deconvolved images of a single-slit aperture with $w = 150$ nm, using the pseudo-Voigt PSF with FWHM=300 nm. . . . .	147

6.23	Deconvolution of the SNOM image of a single-slit aperture with $w = 410$ nm using the pseudo-Voigt PSF with FWHM=300 nm, showing (a) original image before deconvolution and (b) deconvolved image. . . . .	148
6.24	Intensity profile across the slit for the original and deconvolved images of single-slit aperture with $w = 410$ nm, using the pseudo-Voigt PSF with FWHM=300 nm. . . . .	148
6.25	Deconvolution of the SNOM image for a single-slit aperture with $w = 180$ nm using a simulated PSF obtained from a circular aperture with $d = 100$ nm and probe parameters $h = 10$ nm and $D = 300$ nm, showing (a) original image before deconvolution and (b) deconvolved image. . . . .	149
6.26	Intensity profile across the slit for the original and deconvolved images of a single-slit aperture with $w = 180$ nm, using a simulated PSF obtained from a circular aperture with $d = 100$ nm and probe parameters $h = 10$ nm and $D = 300$ nm. . . . .	150
6.27	Deconvolution of the SNOM image for a single-slit aperture with (a-b) $w = 150$ nm and (c-d) $w = 410$ nm using a simulated PSF obtained from a circular aperture with $d = 100$ nm and probe parameters $h = 10$ nm and $D = 300$ nm, showing (a,c) original images before deconvolution and (b,d) deconvolved images. . . . .	151
6.28	Intensity profile across the slit for the original and deconvolved images of single-slit apertures with (a) $w = 150$ nm and (b) $w = 410$ nm, using a simulated PSF obtained from a circular aperture with $d = 100$ nm and probe parameters $h = 10$ nm and $D = 300$ nm. . . . .	152
6.29	Deconvolved images of single-slit aperture with $w = 180$ nm using simulated PSF obtained using a circular aperture with (a) $d = 80$ nm and (b) $d = 150$ nm and probe parameters $h = 10$ nm and $D = 300$ nm. . . . .	153

- 6.30 Intensity profile across the slit for the original and deconvolved images of single-slit aperture with  $w = 180$  nm, using a simulated PSF obtained from a circular aperture with (a)  $d = 80$  nm and (b)  $d = 150$  nm, and probe parameters  $h = 10$  nm and  $D = 300$  nm. . . . . 153
- 6.31 Deconvolved images of single-slit aperture with  $w = 410$  nm using a simulated PSF obtained from a circular aperture with  $d = 100$  nm, with probe parameters  $h = 10$  nm, and (a)  $D = 150$  nm and (b)  $D = 500$  nm. (c,d) The intensity line profiles across the slit, from the images above, for  $D = 150$  nm and  $D = 500$  nm respectively. . . . . 154
- 6.32 Deconvolution of a SNOM image of the double slit aperture with  $w = 470$  nm and  $s = 140$  nm, using a PSF obtained with parameters  $d = 100$  nm,  $h = 10$  nm, and  $D = 300$  nm. (a) Original and (b) deconvolved images are shown, the intensity profiles perpendicular to the double-slit shown in (c). . . . . 155
- 6.33 Deconvolution result for a SNOM image of the double slit aperture with  $w = 410$  nm and  $s = 80$  nm, using a PSF obtained with parameters  $d = 100$  nm,  $h = 10$  nm, and  $D = 300$  nm. (a) Original and (b) deconvolved images are shown, with the intensity profiles perpendicular to the double-slit shown in Fig. (c). . . . . 156
- 6.34 Deconvolution of the SNOM image of a single-slit aperture with  $w = 150$  nm using the experimental PSF obtained from a circular aperture with  $d = 100$  nm, showing (a) original image before deconvolution and (b) deconvolved image. . . . . 157
- 6.35 Intensity profile across the slit for the original and deconvolved images of single-slit aperture with  $w = 150$  nm, using an experimental PSF obtained from a circular aperture with  $d = 100$  nm. . . . . 158



6.36	Deconvolution of the SNOM image of the single-slit aperture with $w = 150$ nm using the experimental PSF obtained from a circular aperture with $d = 100$ nm, showing (a) original image before deconvolution and (b) deconvolved image. . . . .	159
6.37	Intensity profile across the slit for the original and deconvolved images of single-slit aperture with $w = 150$ nm, using experimental PSF obtained from a circular aperture with $d = 100$ nm. . . . .	159
6.38	Deconvolution of the SNOM image for a single-slit aperture with $w = 410$ nm using an experimental PSF obtained from a circular aperture with $d = 100$ nm, showing (a) original image before deconvolution and (b) deconvolved image. . . . .	160
6.39	Deconvolution of the SNOM image of the double-slit aperture with $w = 470$ nm and $s = 140$ nm using the experimental PSF obtained from a circular aperture with $d = 100$ nm, showing (a) original image before deconvolution and (b) deconvolved image. . . . .	161
6.40	Intensity profile across the slit using the original and deconvolved images of (a) single-slit aperture with $w = 410$ nm and (b) double-slit apertures with $s = 140$ nm shown in Figs. 6.38 and 6.39 respectively, using the experimental PSF obtained from a circular aperture with $d = 100$ nm. . .	161
6.41	Deconvolution of the SNOM image of a Fresnel zone plate using experimental simulated PSF obtained from a circular aperture with $d = 100$ nm and probe parameters $h = 10$ nm and $D = 300$ nm, showing (a) original image before deconvolution and (b) deconvolved image. . . . .	162
6.42	Intensity line profiles taken across the $x$ - and $y$ - sections of the images in Fig. 6.41, for both the original and deconvolved images. . . . .	163

- 6.43 Deconvolution of the SNOM image of a Fresnel zone plate using a simulated PSF obtained from a circular aperture with  $d = 100$  nm and probe parameters  $h = 10$  nm and  $D = 300$  nm, showing (a) original image before deconvolution and (b) deconvolved image. . . . . 164
- 6.44 Intensity line profiles taken across the  $x$ - and  $y$ - sections of the images in Fig. 6.43, for both the original and deconvolved images. . . . . 164

# List of Tables

2.1	Configurations for near-field microscopy, categorised by their illumination and detection methods. The table is adapted from Ref. [1]. . . . .	26
5.1	The slit apertures dimensions (width $w$ and separation $s$ ), confirmed using scanning electron microscopy (SEM). . . .	100
5.2	Summary of FWHM of the intensity profiles from the experimental (exp) and simulated (sim) results of single-slit apertures. . . . .	113
5.3	Summary of the differences between experimental and FDTD simulation results for double slit apertures, comparing FWHM, and peak-to-peak distance. Center-to-center distances between the slits obtained from SEM images are included. Note that data for $s = 80$ nm is omitted as the peaks could not be resolved (see Fig. 5.13(b)). . . . .	117
5.4	Summary of simulated intensity profiles for the single-slit aperture with $w = 180$ nm for 5 different incident wavelengths. The relative intensity amplitudes were normalised such that the integral over the distance ( $x$ ) (i.e. area under the profile) are the same for all profiles. FWHM is calculated from the pseudo-Voigt fitting. . . . .	121

- 5.5 Summary of simulated intensity profiles for the double-slit apertures with  $w = 470$  nm and  $s = 140$  nm, for 5 different incident wavelengths. The relative intensity amplitudes were normalised such that the integral over the distance ( $x$ ) (i.e. area under the profile) are the same for all profiles. FWHM and peak-to-peak distance are calculated from pseudo-Voigt fitting. . . . . 121

# List of Abbreviations

<b>1D</b>	one-dimensional
<b>2D</b>	two-dimensional
<b>3D</b>	three-dimensional
<b>Al</b>	aluminium
<b>AFM</b>	atomic force microscopy
<b>BC</b>	boundary condition
<b>Co</b>	cobalt
<b>Cr</b>	chromium
<b>CCD</b>	charged-coupled device
<b>CPU</b>	central processing unit
<b>DDA</b>	discrete dipole approximation
<b>EM</b>	electromagnetic
<b>Eq.</b>	equation
<b>ERF</b>	edge response function
<b>FEM</b>	finite element method
<b>FDTD</b>	finite-difference time-domain (method)
<b>FIB</b>	focussed ion beam
<b>FZP</b>	Fresnel zone plate
<b>Fig.</b>	figure
<b>FWHM</b>	full-width at half-maximum
<b>LCP</b>	left-handed circular polarisation
<b>LSF</b>	line spread function
<b>LSP</b>	localised surface plasmon
<b>MCN</b>	Melbourne Centre for Nanofabrication
<b>NA</b>	numerical aperture
<b>Ni</b>	Nickel

<b>NSOM</b>	near-field scanning optical microscopy
<b>PEI</b>	polyethylenimine
<b>PML</b>	perfectly matched layer
<b>PMT</b>	photo multiplier tube
<b>PSF</b>	point spread function
<b>Pt</b>	platinum
<b>RAM</b>	random access memory
<b>RCWA</b>	rigorous coupled-wave analysis
<b>RCP</b>	right-handed circular polarisation
<b>Ref.</b>	reference
<b>RL</b>	Richardson-Lucy (deconvolution algorithm)
<b>OCT</b>	optical coherent tomography
<b>PSTM</b>	photon scanning tunneling microscopy
<b>SAM</b>	self-assembled monolayer
<b>SEM</b>	scanning electron microscopy
<b>SNR</b>	signal-to-noise ratio
<b>SPM</b>	scanning probe microscopy
<b>STED</b>	stimulated emission depletion (microscopy)
<b>STM</b>	scanning tunneling microscopy
<b>STOM</b>	scanning tunneling optical microscopy
<b>SNOM</b>	scanning near-field optical microscopy
<b>SPP</b>	surface plasmon polariton
<b>TEM</b>	transmission electron microscopy
<b>TFSF</b>	total-field/ scattered-field (boundary)

# Chapter 1

## Introduction

### 1.1 Imaging with Scanning Near-field Optical Microscopy (SNOM)

#### 1.1.1 SNOM Overview

Microscopy is a technique for viewing and observing small objects, which are otherwise invisible to the naked eye. Microscopy generally exploits the refraction or reflection properties of the light (or waves in general) in order to form a magnified image of an object. Optical microscopy is limited by diffraction such that the maximum possible resolution is half of the smallest wavelength in the visible spectrum, which is about 200 nm [1]. To overcome this limitation, electron microscopy has been developed which offers a higher resolution using electron waves which inherently have a much shorter wavelength than photons. Due to the fact that electron wavelengths are typically about the size of the atom, the electron microscope can achieve a sub-1 nm resolution.

However, a problem arises when imaging biological samples using electron microscopy as the electrons carry a high amount of energy that could damage or even destroy the samples. Electron microscopy also requires a vacuum environment for the electrons to not be scattered by the air molecules. This poses another problem as most biological samples contain a significant amount of water that will vaporise in the vacuum. In

addition, the sample preparation required for electron microscopy imaging could distort of the samples' actual structure and composition, limiting the accuracy of the observation.

Scanning probe microscopy (SPM) techniques, such as atomic force microscopy (AFM), provide another alternative method for high-resolution imaging. In AFM, a probe is placed at a close distance from the sample surface. The probe 'senses' the force between the sample and the probe tip while scanning the designated area of the sample, maintaining either a constant separation or a constant force with respect to the sample surface. The system uses this information to generate a sample morphology, but no optical information is observed.

High resolution optical images can also be obtained with fluorescence microscopy, including, confocal microscopy. The sample being imaged is treated with fluorescent particles or fluorophores, and is then illuminated with a suitable wavelength for exciting the fluorophores. The emitted light from the fluorophores has a longer wavelength than the incident wavelength, which is then filtered and detected, allowing the observation of only the fluorescent parts of the sample. In confocal microscopy, a set of two pinholes with a specific confocal configuration is used to focus the illumination over a very small area of the sample. The sample is then scanned and an image of the sample is generated. This technique offers excellent spatial resolution, although it is still diffraction limited due to the nature of far-field illumination, which has the effect of limiting the focussed beam spot size. A variant of confocal microscopy, stimulated emission depletion (STED) microscopy, can achieve super-resolution beyond diffraction limit by using selective deactivation of the fluorophores.

The diffraction limit in optical microscopy can be overcome when the optical signals are measured at short-range distance within the subwavelength regime. At this distance, the light is undiffracted, and as a result, reconstruction of a super resolution image is possible in principle. At a subwavelength distance, Fourier components responsible for the fine details of the object can be measured, as opposed to when the object is viewed in the far-field. These components include high spatial-frequency components and non-propagating components, which exist as



evanescent waves. Evanescent waves decay exponentially in the direction of propagation and are not observable over a distance much larger than the wavelength. The region where these short-range optical interactions occur is called the near-field zone, while long-range interactions occur within the far-field zone. SNOM exploits the near-field optical signal by using an optical probe placed at a short-range distance from the sample surface. The probe has a very sharp tip for illumination or detection over a localised area of the sample surface. Similar to AFM, the sample-probe distance is adjusted depending on the relative force between them. A very high resolution image with subwavelength resolution can be produced using SNOM and morphological information from the sample surface generated from the force feedback. In comparison to electron microscopy, SNOM is less destructive and the condition of the sample, especially in the case of biological specimens, can be preserved. As no labelling is required, such as the case with fluorescence microscopy, no specific sample preparation is required.

Although it is now well established, there are still a number of challenges that remain in SNOM imaging. In particular, image artifacts can arise due to defects in the probe tip [2]. A blunt probe tip due to damage incurred during the scanning process, for example, can cause image degradation. The  $z$ -direction movement, perpendicular to the sample plane, of the probe tip due to the force feedback mechanism can produce false optical contrast [3].

As the probe tip can have an influence on image formation in SNOM, it is imperative to optimise the probe to be able to generate a very high resolution image. A modified probe with increased sensitivity to certain types of material can be useful for enhancing the resulting images. Understanding probe effects is crucial for determining the optimum design for the optical probe. Generally, a sharper probe tip can generate higher resolution images due to a high localisation of the near-field signal, but this also means the signal can be very weak due to its small effective size.

Although the probe tip plays an important role in the SNOM imaging, the optical near-field response of a sample is usually calculated or modelled without considering the probe tip. The near-field properties of the sample are calculated as a function of the distance from the sample

in modelling the image detected by SNOM. This fast approach is good for approximating the near-field behaviour of the sample, but lacks in accuracy. Some optical near-field phenomena can only be accurately described when the probe tip is included in the numerical calculation [4, 5].

The influence of the probe can also be modelled via a point spread function (PSF). Every optical system has a specific optical response to a point source or object, which effectively blurs the signal from a point source/ object over a larger area in the resulting image. If the PSF of the imaging system can be accurately determined, it is possible to reverse the blurring effect to extract the 'original' image with better sharpness and clarity via deconvolution.

The measured image is a result of the convolution between the original image and the PSF of the imaging system with some additional background noise. We note that the presence of noise can impact the effectiveness of the deconvolution algorithm since it can be significantly amplified by this process, preventing the original image being restored. Richardson-Lucy algorithm is an iterative deconvolution method for restoring an image that works effectively in the presence of noise [6, 7]. Applying this method to the image produced by a SNOM scan can further increase the image quality by effectively eliminating the effect due to the presence of the probe tip.

### **1.1.2 The Diffraction Limit**

Conventional optical microscopy is fundamentally limited in the size of objects that it can resolve. When visible light is used, the spatial resolution is limited to about 200 to 300 nm, which is approximately half of the incident wavelength. This means that features in the order of ten nanometers to around one hundred of nanometres cannot be observed with conventional optical microscopy.

To produce images with very high (subwavelength) resolution, other microscopy techniques, such as electron scanning electron microscopy (SEM), scanning tunnelling microscopy (STM), and atomic force microscopy

(AFM) are used. Despite providing resolution beyond the optical diffraction limit, these techniques have a limited capability for mapping the spectral and dynamic properties of the sample [8]. They also lack other advantages associated with optical microscopy such as the ability to control the polarisation state of the illumination [9]. The requirement for extensive sample preparation can also impact the flexibility of performing experiments that requires specific environments [9].

Abbe's diffraction limit states that the maximum possible resolution that can be achieved is limited by the wavelength of the light source and the Numerical Aperture (NA) of the lens [8, 10]. The fine features of the object correspond to the nonpropagating high spatial frequencies. At lateral spatial frequencies greater than  $k_0 = 2\pi/\lambda$ , the wave propagation vector becomes imaginary and the wave decays exponentially away from the surface [11]. These are known as evanescent waves, which cannot be measured in the far-field. In practice, the spatial resolution is also limited by the NA of the lens, which in general makes it less than the theoretical limit of  $k_0$ . To recover the information associated with these high spatial frequencies, a detection scheme which operates within the subwavelength regime can be used to detect evanescent waves near the sample surface. The probe also needs to be very sharp, typically with a subwavelength feature size, and placed at a distance from the sample surface not greater than the probe tip size. By collecting this near-field information, the images obtained using SNOM can be pushed to a spatial resolution beyond the diffraction limit. This type of measurement scheme is called the collection mode. The beam path may also be reversed by using the probe to locally illuminate the sample and recording the far-field response of the sample. This reversed configuration is called the illumination mode.

### 1.1.3 Near-field and Far-field Optics

Far-field and near-field optics differ in terms of the length scales associated with the illumination or detection of the signal from the sample being measured. The difference between the near-field and far-field can

be visualised using the diffraction pattern from a single slit aperture. Depending on the observation distance, the diffraction patterns can be categorised as Fresnel diffraction (near-field) or Fraunhofer diffraction (far-field). A schematic illustrating this is shown in Fig. 1.1.

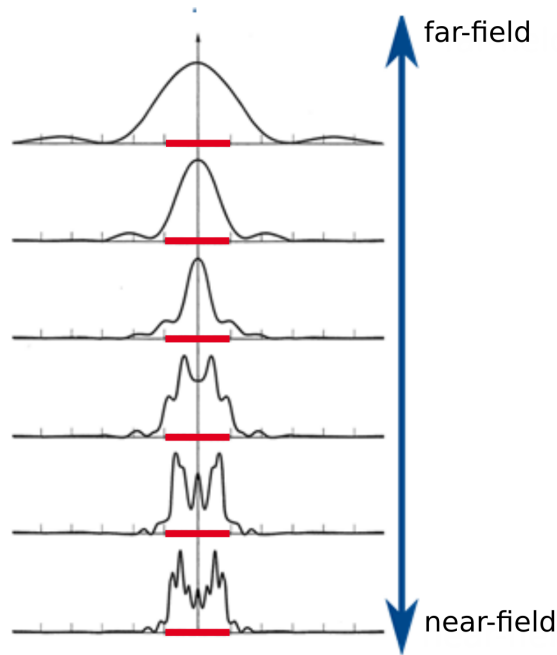


**Figure 1.1:** Evolution of diffraction patterns moving from near-field observation (Fresnel diffraction) to far-field observation (Fraunhofer diffraction) [12]. The object is a slit indicated by the red line on the horizontal axis.

In the far-field, the observed pattern shows a different shape between the observed intensity pattern and the slit, with the central peak larger than the actual slit. As the observation distance decreases, the pattern has a smaller central peak, with a width closer to the actual width of the slit. The peak is not smooth and rounded anymore, and is eventually closer to a top-hat function. In the near-field, the light is undiffracted, and includes all Fourier components producing an image closer to its true shape and size.

The schematic for the comparison between far-field and near-field imaging is shown in Fig. 1.2 for the transmitted light through the sample. In conventional (far-field) microscopy (Fig. 1.2(a)), the light transmitted through the sample is collected using a lens placed at a distance

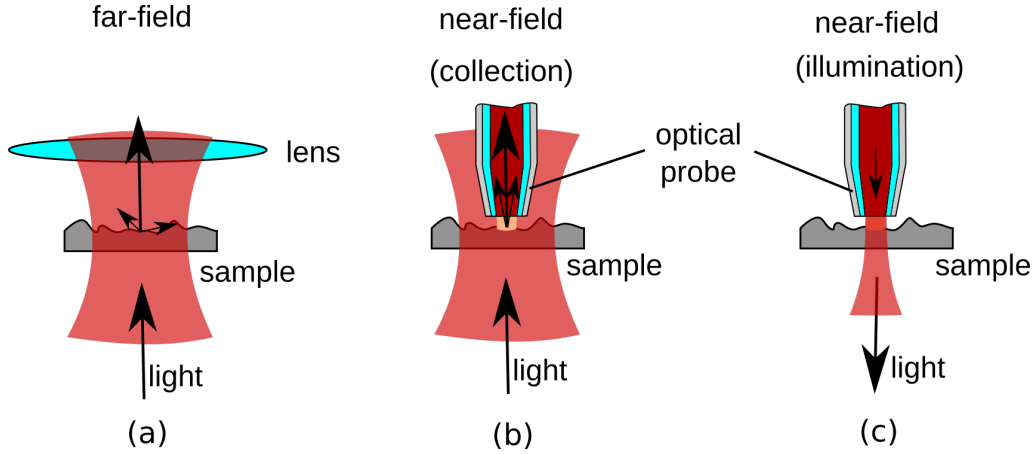


**Figure 1.2:** Schematics of far-field and near-field imaging. (a) Far-field imaging using lens to collect light at a long-range distance (much larger than the wavelength), (b-c) Near-field imaging using aperture probe placed at a short-range distance (within subwavelength) (b) in collection mode and (c) in illumination mode.

much larger than the wavelength, to focus it on the detector. Some of the high spatial-frequency components, denoted by the small arrows, are not collected, preventing reconstruction of the image with the resolution beyond the diffraction limit. On the other hand, by using a SNOM system, an optical probe is placed within a subwavelength distance from the sample, allowing all components to be collected by the optical probe (Fig. 1.2(b): collection mode). Hence, an image with very high spatial resolution (beyond the diffraction limit) can be achieved. Equivalently, the light can be coupled into the optical probe, with the transmitted light emerging through a small aperture at the tip, illuminating the sample over a very small localised area. Near-field interactions with the sample are then measured in the transmitted light collected at the end of the probe (Fig. 1.2(c): illumination mode).

In practice, near-field optical interactions are not easy to determine due to the complexity of the mathematical calculation involved. This is particularly difficult when the optical probe is included in the calculation. Some simplifications are performed by analysing only the light transmitted through the probe [13, 14], or only the near-field optics of

the sample without involving the probe in the calculation [15, 16]. Numerical calculation methods are usually used in analysing near-field optics. In this study, simulations based on the finite-difference time-domain (FDTD) method are utilised for the accurate modelling of the near-field optics.

## 1.2 Motivation

Due to its ability to deliver subwavelength optical resolution, SNOM has been used for a range of applications including for investigating the near-field profiles of nanophotonics devices [17, 18], single molecules [19–21], biological cells [22–25], and near-field Raman spectroscopy [26, 27]. The probe tip is a particularly important part of SNOM and the investigation of its influence on image formation remains largely unexplored. It is acknowledged that the probe tip plays a critical role in determining the image quality and resolution obtained from a SNOM scan. Extensive literature investigated the electromagnetic behaviour inside and outside of the probe tip and yielded potential new designs for the probe tip [28–31]. These studies, however, did not calculate the intensity profile detected by the probe tip during the SNOM scans.

Simplified near-field image calculation is typically performed by placing a 2D plane, which records the electromagnetic fields for a very short distance from the sample [16, 32]. The calculation just involving the sample is usually already very complex such that the probe tip is excluded from the model. There is a gap to be explored here, which is calculating the probe effects involving both the sample and the probe tip. Some literature indicates that the measured image is affected by the probe tip [4, 5], but the number of studies which have investigated this effect are still very limited.

The main theme of the study reported in this thesis is the influence of the probe tip in SNOM image formation. The effect of the probe tip in SNOM imaging was investigated, by building a simulation model of the probe tip scanning the sample. The simulation model was based on the finite-difference time-domain (FDTD) method for electromagnetism [33]. In order to characterise the model, objects with subwavelength features

were used as the sample and were examined both using simulations and experiments. The characterisation samples were single-slit and double-slit apertures in a metal film. Due to their one-dimensional symmetry, these were simpler to calculate and to analyse. For the simulation model, circular apertures in a metal film were also investigated.

The influence of the probe tip on the resulting SNOM images was carefully investigated to confirm whether it has a major influence on the quality of the SNOM scans [34]. The intensity profiles obtained from the simulation and experiment were compared and discussed. The simulation model not including the probe tip was also considered as a control for the model of the SNOM probe tip.

Understanding the probe tip influence in SNOM image formation is crucial for accurate analysis of the near-field behaviour of the sample. The influence of the probe tip can also be further explored by investigating the effects of modifying of the probe tip and/ or the sample. By understanding the probe tip behaviour, the PSF of the SNOM system can be determined accurately. An image post-processing can then be performed to improve the image quality from the SNOM scans using a deconvolution algorithm.

Knowledge of the SNOM probe tip influence is also valuable for other studies involving modifications of the SNOM probe tip. With accurate modelling, a SNOM probe tip may be modified to alter its optical response or to alter its shearforce feedback within a specific domain in the sample. This could improve the sensitivity of the SNOM imaging to the physical and/ or optical properties of the samples, producing images with better contrast and spatial resolution. Probe modifications are actively being investigated in other microscopy techniques, such as atomic force microscopy (AFM) and scanning tunnelling microscopy (STM) [35–38], and could possibly be extended and applied to SNOM [29, 39].

Following on from previous SNOM studies, the optical probe is a critical component which enables high-resolution, sub-diffraction limited, imaging [40]. However, the presence of the probe tip in the near-surface region of the sample during scanning has been largely ignored in calculations of SNOM image formation. This is, in part, due to the mathematical complexity introduced by the presence of the near-field optical probe. Of

the few studies that have explored the influence of the probe tip, the majority have been based on simulations only [13, 29, 41] and do not extend to SNOM image formation from actual samples.

The novelty of the present work lies in the combination calculations of the probe tip influence performed using FDTD simulations with experimental SNOM data used to validate our model [34]. The influence of the probe tip in SNOM imaging was systematically characterised using the simulations. Furthermore, the model representation of the probe tip takes into account a set of parameters which mirror the actual experimental conditions. Since the optical probe tip is critical in the image formation using SNOM, this experimental verification of the model is important for a robust representation of the optical probe tip in any SNOM experiments.

The characterisation model of the SNOM probe tip can be further applied in resolution enhancement of images using deconvolution. While this approach is widespread in other microscopy techniques [42], thus far, this types of deconvolution has only been applied in a very small number of cases using SNOM. The research presented in this study is significant in bringing the resolution improvements which could extend applications of SNOM in resolution demanding situations, such as in material science or biophysics [43–45].

### 1.3 Objectives

This study presented here includes the investigation and characterisation of the probe tip in the context of image formation using SNOM. As previously described, the SNOM probe tip plays an important role during the SNOM scanning process and has a significant effect on the resulting images. To achieve this, first, a simulation model must be built that includes the probe tip in the calculation. Comparison between the simulations with and without the probe tip is to be performed. The simulation model is then validated with experimental data from SNOM scans of the model samples. Based on this model, an accurate PSF of the SNOM system, particularly the probe tip, can be determined. This information is useful for restoring blurred or degraded images using the deconvolution



process. This further improves the quality and clarity of SNOM imaging, producing sharper images with even better resolution.

In summary, the objectives of the study are:

1. **To develop a simulation model for the SNOM image formation**

A simulation model based on the finite-difference time-domain (FDTD) method is constructed for investigating the influence of the SNOM probe tip. The FDTD method involves rigorous electromagnetic wave calculation investigating the wave propagation and its interaction with the surrounding media and objects. An optical probe is included in the simulation and an algorithm for calculating the image detected by probe is applied.

2. **To analyse the results of the simulation model with and without the probe tip incorporated**

Near-field images are usually investigated using a two-dimensional plane to record electromagnetic fields in the near-field, essentially ignoring the structure of the probe tip in the calculation. The two different approaches, simulations with and without the probe tip are compared and the influence of the probe tip is investigated.

3. **To validate the simulation model using experimental data from model samples**

The simulation model including the probe tip is analysed by comparing it to the experimental data from model samples. The samples are single-slit and double-slit apertures since the shapes were one-dimensional and easy to analyse. All slit apertures are of sub-wavelength size in order to validate the accuracy of the simulation model.

4. **To analyse the intensity profiles obtained from the SNOM scans**

Intensity profiles across the slit apertures from the experiment are reproduced using simulations. The shapes and widths of the intensity peaks are analysed and discussed.

5. **To determine the PSF of the SNOM system**

Once the probe parameters are known, the PSF of the SNOM system, which is predominantly affected by the probe tip, can be determined. This measures how effective imaging using SNOM with a particular set-up can be and also shows the extent of the influence of the probe tip in the imaging. An accurate PSF is useful for restoring degraded images from the scans due to the limitation of the probe tip.

**6. To use image deconvolution to improve the clarity of the images obtained from SNOM scans**

The PSF of the SNOM is used in a deconvolution process using the Richardson-Lucy algorithm. Various configurations of the deconvolution are discussed to obtain improved images by effectively removing the effect of the probe tip.

## 1.4 Organisation of the Thesis

This thesis is organised into 7 chapters, with 3 introductory chapters, 3 results chapters, and 1 conclusion chapter. Chapters 1 to 3 provide background and introduction, as well as methods. Chapters 4 to 6 discuss the results of the study, and Chapter 7 provides the conclusions.

*Chapter 1* consists of background, motivation, and a brief introduction to the topic of the thesis. *Chapter 2* is background and literature review which includes past studies and a more in-depth introduction to the study. In *chapter 3*, methods are discussed, including the experimental data processing, simulation using the FDTD method, and the Richardson-Lucy deconvolution algorithm.

*Chapter 4* introduces the simulation model, comparing the results of simulations without and with the probe. Parameters in the simulations are discussed. *Chapter 5* validates the simulation model with a characterisation sample. The intensity profiles produced from both simulation and experiment are discussed in detail. *Chapter 6* utilises the model and knowledge of the probe tip to determine the PSF of the SNOM system. The PSF is then used in the deconvolution algorithm to improve the SNOM scan results.

The final chapter, *Chapter 7*, discuss the conclusions of the study and provides suggestions for future work.

## 1.5 Publication

An article based on the results presented in Chapters 4 and 5 was published in an open-access journal, *OSA Continuum*, with the title of "Investigating the probe-tip influence on imaging using scanning near-field optical microscopy" [34]. The article investigated the influence of a probe tip using a simulation model that was validated using experimental data obtained using SNOM.



## Chapter 2

# Background and Literature Review

### 2.1 Introduction

This chapter presents a background summary and literature review for the field of scanning near-field optical microscopy (SNOM). This includes a more specific discussion of the influence of the probe tip on image formation using SNOM. Image post-processing using deconvolution algorithms is also discussed as one of the topics in this study.

Near-field optics is fundamental to SNOM imaging, achieving sub-wavelength spatial resolution. This chapter starts with an introduction to near-field optics and the diffraction limit. Near-field optics exploits the fact that a small object or a small feature within an object contains high spatial-frequency components in the Fourier domain. These components are non-propagating and exist at the sample plane with their intensity decaying exponentially perpendicular to the sample plane.

A section describing the fundamental principles of SNOM follows the theory of near-field optics. This covers the history of the SNOM development and its impact and applications within the field of nanoimaging. Several different types of SNOM configurations are reviewed, followed by a discussion of the influence of the probe tip in SNOM imaging. The influence of the probe tip on image formation using SNOM is a key topic for this thesis, which forms one of the main contributions of this research.

The final section covers the basic principles of image restoration. This includes a discussion of the spatial resolution in imaging and how this can be quantified in the analysis. This is followed by an introduction to the deconvolution algorithm for image restoration and some examples of this being applied for microscopy imaging.

## 2.2 Near-field Optics for Nanoscale Imaging

Near-field describes the electromagnetic interactions over a short-range distance. These interactions occur on a subwavelength scale, which for visible light, extends up to several hundreds of nanometres ( $\sim 300$  nm to  $350$  nm). Within this scale range, paraxial approximations are no longer valid [1, 46].

Consider an object on the  $xy$ -plane, illuminated by a light source incident from the  $z$ -direction originating at a distance much longer than the wavelength (i.e. in the far field). The transmitted light from the object propagates along the  $z$ -axis and is measured by a detector placed at some distance in the  $+z$ -direction (also in the far-field). The schematic of this situation is shown in Fig. 2.1(a). The light is focussed onto the sample by an objective lens and the transmitted light is collected by another lens, the light is then directed onto the detector. In the Fourier domain, the object can be described in terms of  $k_x$  and  $k_y$ , which are the spatial frequency components in the  $x$  and  $y$ -directions respectively. The propagating component of light emitted from the sample along the optical axis is given by

$$k_z = \sqrt{k^2 - k_x^2 - k_y^2}, \quad (2.1)$$

where  $k = n\omega/c$  is the wavenumber of the light in a medium with refractive index  $n$ . The term  $\omega$  is the frequency of the incident light and  $c$  is the speed of light. The problem arises when the parallel component is larger than the wavenumber, i.e.  $k_{\parallel} = \sqrt{k_x^2 + k_y^2} > k$ , producing an imaginary  $k_z$ . The components with imaginary  $k_z$  are nonpropagating and exist as evanescent waves on the object plane ( $xy$ -plane), which decay exponentially in the  $z$ -direction. Objects that are small in size possess higher spatial-frequency components and these are the components that

contain information on the fine features of the object that are typically not detected in the far-field. Qualitatively, this characterises the diffraction limit. Abbe's diffraction limit is approximately half of the wavelength being used. In practice, the spatial-frequency component bandwidth is also limited by the numerical aperture (NA) of the lenses being used.

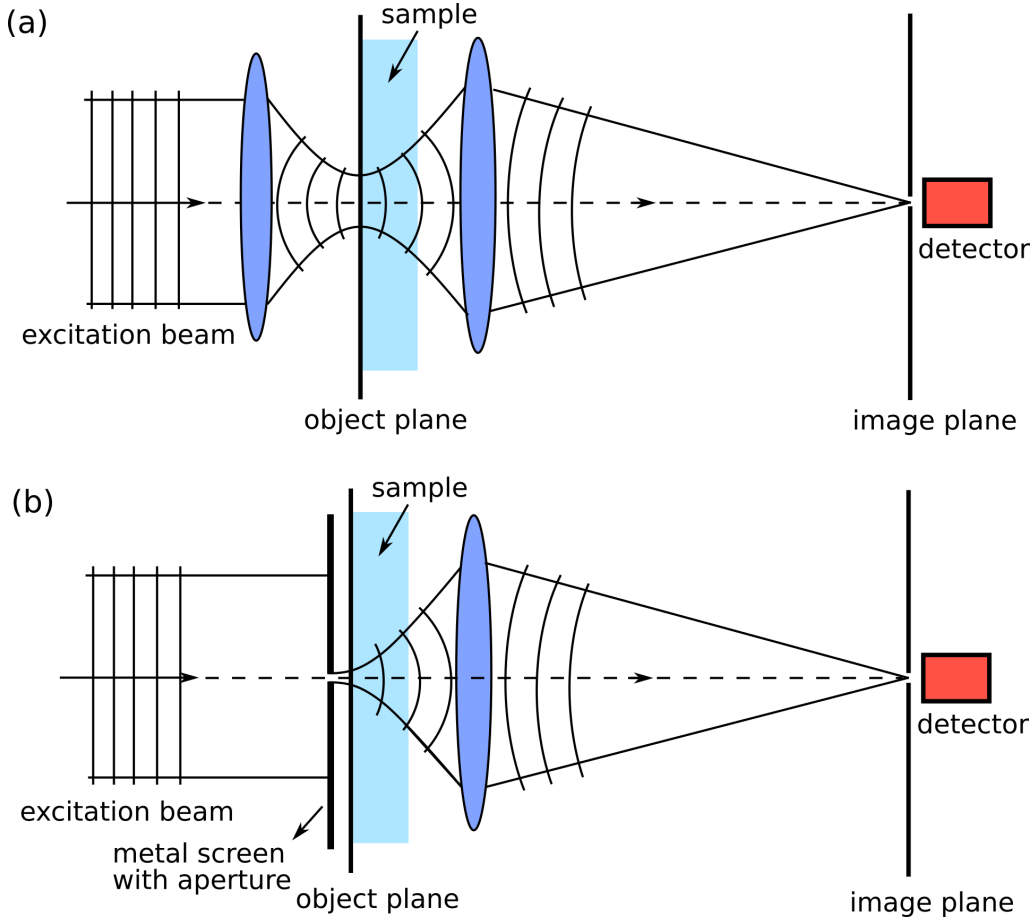


**Figure 2.1:** Simplified schematic of far-field and near-field imaging (adapted from [1]). (a) In the far-field, light is focussed onto the sample and the transmitted light is collected by another lens, focusing it onto the detector. (b) Near-field imaging enables propagation of the high spatial frequency components by focusing the light through a subwavelength aperture.

Near-field optical microscopy overcomes the issues of nonpropagating components by providing point source illumination at a subwavelength distance with a localised illumination. A simplified schematic in Fig. 1.2(b), shows that instead of far-field illumination on the sample,

the light from the source passes through a small subwavelength aperture, placed at a very close distance from the sample surface. With this configuration, the source effectively has a broader spectrum of lateral frequency components  $k_{\parallel}$ , expanding the spatial-frequency component bandwidth. This effectively enables the nonpropagating components to be included in the light scattered by the object and subsequently coupled to the transmitted light. The transmitted light is then collected by the lens and detected in the far-field. The detected signals now include more information on higher spatial-frequency components to reconstruct high-resolution images.

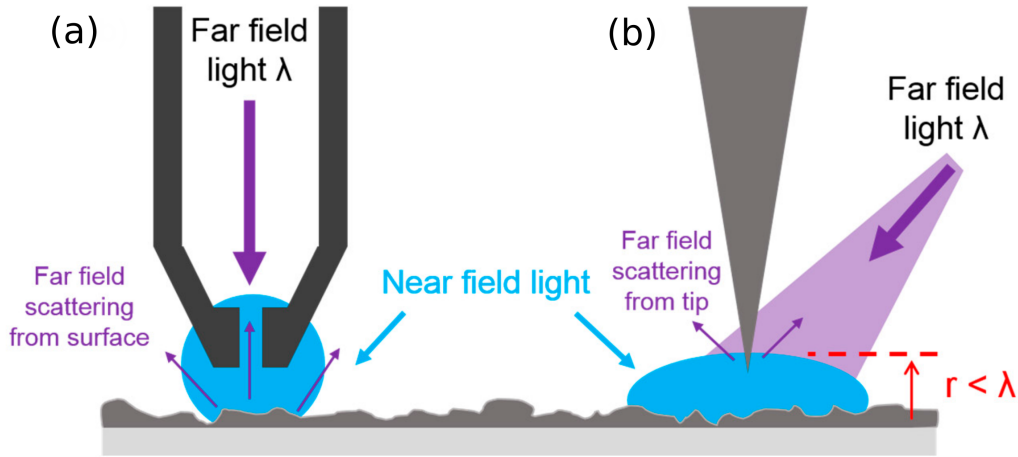


**Figure 2.2:** Schematic of localised illumination at short-range distance to couple near-field optical signals from the sample, using (a) aperture-type probe and (b) scattering-type probe [47].

In practice, the source does not consist of a small hole within an opaque screen, but is instead provided by an optical probe ending in a very sharp tip. The probe tip illuminates the sample at a sub-wavelength distance from the sample surface. There are several different types of near-field probes. The first is the aperture probe. This probe is made from a tapered optical fibre, coated with metal layers, but with a very small aperture at the tip [8]. Another type of probe, a metallic tip, scatters the far-field illumination and effectively creates a near-field illumination source at the tip [48]. A schematic of these probes is shown in Fig. 2.2.



## 2.3 Scanning Near-field Optical Microscopy (SNOM)

### 2.3.1 SNOM and Its Impact in High-Resolution Imaging

The spatial resolution of optical microscopy is fundamentally limited by the wavelength of the light being used. Within the visible spectrum, this limit occurs at about  $0.2\ \mu\text{m}$  to  $0.3\ \mu\text{m}$  for the maximum possible resolution. This limit can be overcome by using electrons as the illumination source instead of visible light. However, electron microscopy comes with its own set of limitations, such as the requirement for a vacuum environment and for the sample surface to be conductive. Near-field imaging uses a different approach in order to overcome the optical diffraction limit, by exploiting the optical signal at a very short range, within a subwavelength distance. At this distance, the signals are ideally undiffracted, such that high-resolution imaging beyond the diffraction limit is possible.

The idea of near-field imaging was first proposed by Synge in 1928 [49], in which a very intense light source illuminates a subwavelength hole (in the order of  $100\ \text{nm}$ ) within a thin and opaque metal film. Synge's calculation showed that the transmitted radiation through such a very small hole is about 10 orders of magnitude weaker than the total incident power, which made the idea seem impossible at that time. Due to the practical hurdles, the basic concept behind SNOM was not experimentally realised until the 1980's. At this time, nanofabrication technology was developing, making it possible for the subwavelength holes to be fabricated.

Pohl at the IBM laboratory in Switzerland [50–52], and Lewis at Cornell university [53], independently developed a device similar to the one Synge had proposed, utilising a point source produced by a subwavelength hole. An optical probe with a sharp tip was used as a device for localised illumination in the near-field zone. The device was able to image the sample with a very high resolution, down to the subwavelength scale. At the time, this near-field imaging device was called an 'optical stethoscope' [50, 54], which later gained wider attention for its high-resolution

imaging capabilities. This imaging technique is now widely known as scanning near-field optical microscopy, abbreviated as SNOM<sup>1</sup>.

Another important component in the development of SNOM is the implementation of a feedback loop for to maintain the constant distance between the probe tip and the sample. The sensor works by vibrating the tip in the lateral direction and detecting the force between the probe tip and the sample, while maintaining a steady feedback to maintain a constant distance.

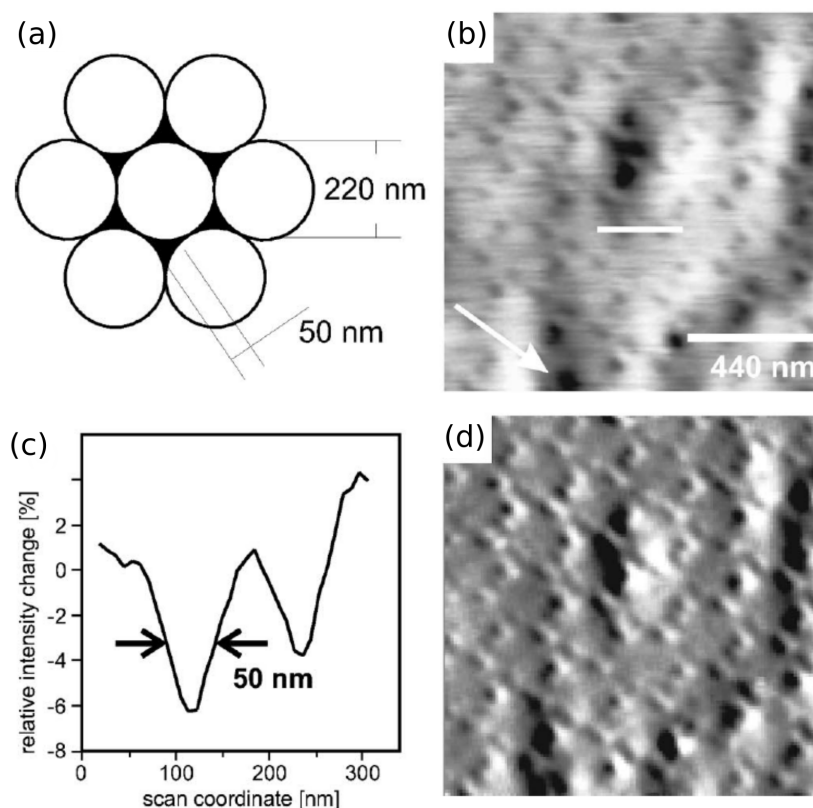
Due to its high-resolution imaging capabilities, SNOM has been used for a wide range of applications, including investigating nanophotonics devices, single molecules, and biological specimens [8, 9, 22]. In a review of SNOM with aperture probe, several test samples were examined highlighting the subwavelength imaging capabilities of SNOM [8]. These samples include metal patches formed in between a hexagonal arrangement of spheres and a single protein molecule, which are discussed below.

Figure 2.3 shows an example of amplitude contrast imaging using SNOM scan [8]. An aluminium island of 15 nm thickness was fabricated using the latex sphere shadow mask technique, in the gaps between the spheres, as shown in Figure 2.3(a). The metal patches are formed by evaporation and subsequent dissolution of the spheres. The film was scanned using constant height mode with the result shown in Fig. 2.3(b). The intensity profile between two neighbouring patches is shown in Figure 2.3(c), along the line shown in Fig. 2.3(b). The width analysis of the profile shows that the spatial resolution can be as high as 50 nm. A better visualisation of Figure 2.3(d) was produced using high-pass filtering by removing far-field modulation, shown in Fig. 2.3(d).

SNOM was also shown to be able to image a single molecule, as shown in Figure 2.4. Patches of protein molecules (immunoglobulin) from chicken were labelled using four dye molecules for each protein molecule. The excitation was performed at 514 nm and detected at 570 nm using an oil immersion objective and a single photon counting avalanche photodiode [8]. Figures 2.4(a-b) show the near-field fluorescence image of two

---

<sup>1</sup>Another terminology, near-field scanning optical microscopy (NSOM) is also commonly used.



**Figure 2.3:** SNOM scan of metal island film [8]. (a) Schematic of hexagonal arrangement of the metal patches around the spheres. (b) SNOM images at the same location of the sample with polarisations indicated by the arrow. (c) Intensity profile along the horizontal white line shown in Fig.(b), confirming 50 nm resolution. (d) High-pass filtered image of the SNOM scan, revealing clearer features.

patches of protein and its shearforce topography, collected simultaneously. The intensity profiles along lines 1 and 2 in Figs. 2.4(a) and 2.4(b) are shown in Figs. 2.4(c) and 2.4(d) respectively, with a spatial resolution of 80 nm. There was a slight shift when comparing the optical and shearforce images, which is a known effect in SNOM imaging.

Other applications in chemical studies, including single molecule imaging, thin film analysis, and biological sciences are reviewed in Ref. [9]. The images obtained with SNOM have the advantage of higher spatial resolution compared to the far-field techniques, with the added benefit that chromophore orientation information can also be acquired [55, 56]. Measurements of single fluorescence lifetime have also been demonstrated with a count rate that is sufficient to reveal both spectroscopic and

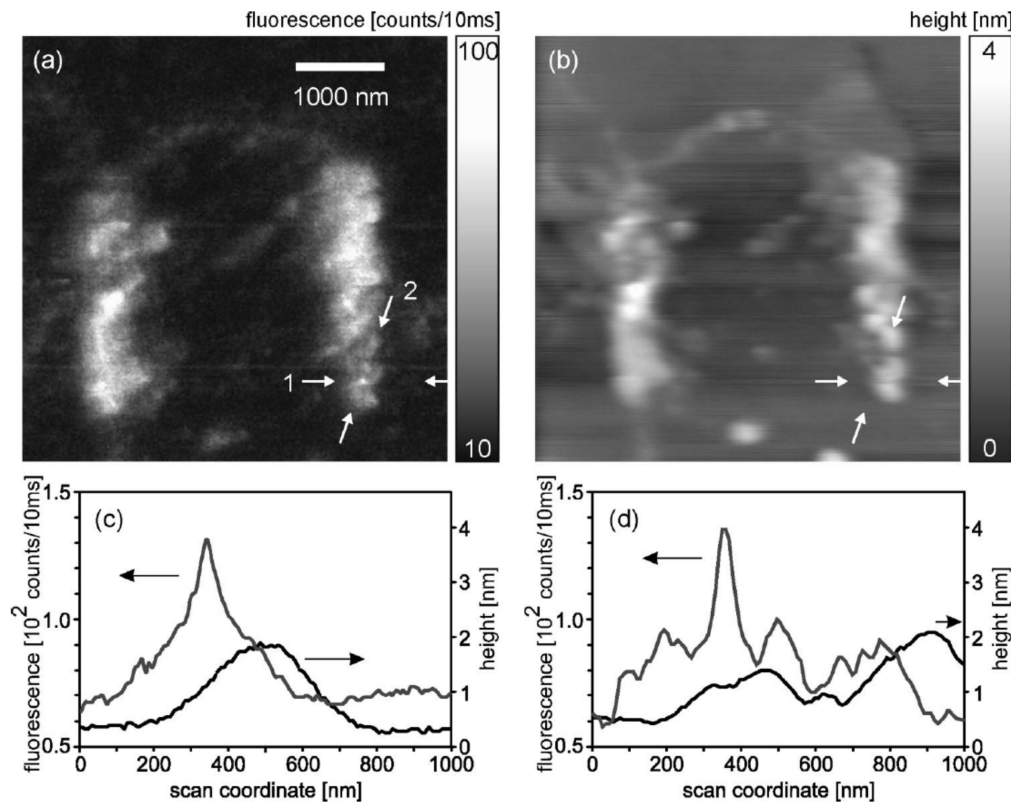


**Figure 2.4:** Images obtained simultaneously from (a) near-field fluorescence and (b) shear force topography of two rectangular single molecule of proteins. (c), (d) The intensity profiles along the lines 1 and 2 respectively (lines shown in Fig.(a) and (b)) with the arrows on the graphs indicate the respective y-axis for each plot. [8]

time-resolved information [9, 57, 58]. For example, SNOM fluorescence images of single molecules at different time snapshots were recorded during lateral diffusion [59]. Furthermore, the orientation of the diffused molecules can be traced by detecting two perpendicular components associated with polarised fluorescence [60]. The SNOM technique was also shown to expand the chemical information for various aggregates and small molecule studies, including light-emitting polymers [61, 62] and liquid crystals [63, 64].

In the field of nanophotonics, devices are typically built based on nanostructures, designed to manipulate local interactions with the incident light [17, 18, 65, 66]. These interactions can be studied closely by looking at the near-field influence of the nanostructures. SNOM has

also been used for analysing the near-field properties of optical nanodevices. Field enhancement, localisation, and manipulation of light within the near-field regions using these devices are interesting topics to be explored. Examples of the near-field characterisation of nanodevices using SNOM were demonstrated using phased array metasurfaces consisting of V-antennas with different opening angles [17] and on spiral antennas [66]. The results are shown in Figures 2.5 and 2.6.

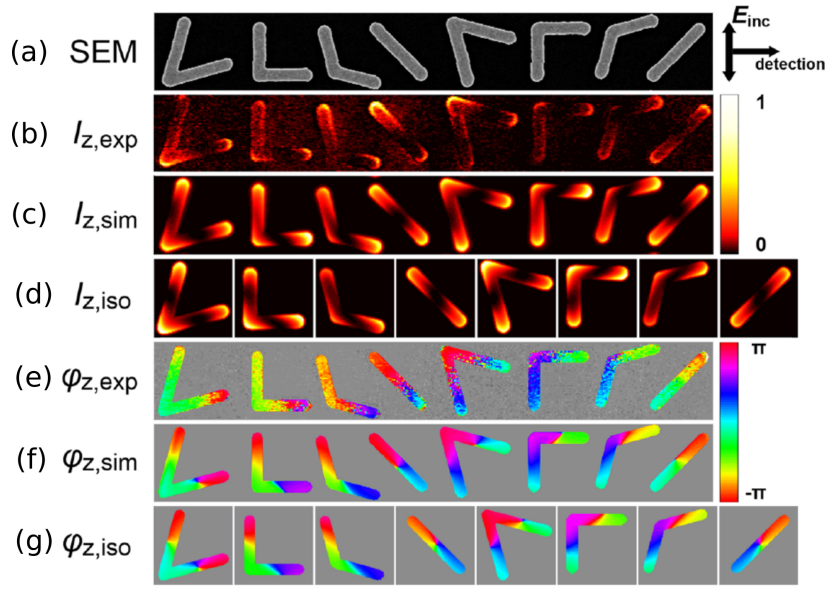


**Figure 2.5:** Interference of modes on an array of V-antennas made of gold [17]. (a) SEM image of V antennas with different opening angles and orientations. The antennas were illuminated with the incident polarisation ( $E_{inc}$ ) perpendicular to the detected polarisation, as indicated by the arrows. The near-field intensity of the V-antennas obtained from the (b) SNOM experiment (exp), (c) simulation (sim), and (d) isolated simulation (iso) for each antenna. The phase profile on the antennas are also shown for (e) experimental, (f) simulated, and (g) isolated simulated results.

In Fig. 2.5, the resonance modes of V-antennas were investigated using SNOM. The opening angles of the antennas are  $45^\circ$ ,  $90^\circ$ ,  $135^\circ$ , and  $180^\circ$ , another four antennas have the same angles but rotated by  $90^\circ$ . SEM images of the antennas are shown in Fig. 2.5(a). The experimental results (Fig. 2.5(b)) show that the intensity profiles are asymmetric, suggesting that both symmetric and antisymmetric modes on the V-antenna were excited. The results also show good agreement with the simulations

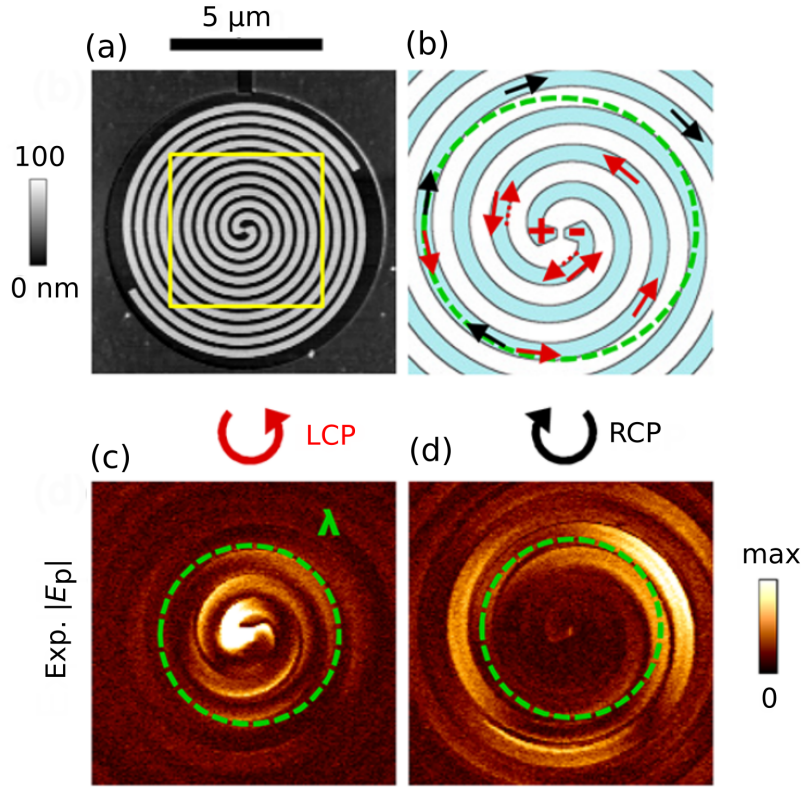


**Figure 2.6:** Near-field images of a spiral antenna under left-handed and right-handed circularly polarised (LCP and RCP) illumination [66]. (a) An SEM image of the 5-turn spiral antenna with (b) illustration of directional wave at the active zone of the antenna (dashed green circle). (c,d) Experimental electric field amplitudes near the sample surface for (c) LCP and (d) RCP.

in Figs. 2.5(c) and 2.5(d). Furthermore, the phase profiles for the antennas were also obtained and compared with the simulations on an array and on a single isolated antenna in Figs. 2.5(e), 2.5(f), and 2.5(g).

A similar study was performed on spiral antennas, as shown in Fig. 2.6. Due to the symmetrical nature of the structures, the antennas were investigated using left-handed and right-handed circularly polarised (LCP and RCP) light. The different modes were excited on the antennas when using the two different polarisations, as shown by the intensity profiles in Figures 2.6(c) and 2.6(d) for the experimental results using LCP and RCP respectively. The structures are shown to have a nanofocusing effect on the incident light and the intensity distributions can be altered by using different incident polarisations.

In the biological sciences, the SNOM technique has been demonstrated to provide a shearforce feedback mechanism that is noninvasive with respect to the sample being probed. In addition, the spatial resolution of SNOM can still be maintained using a relatively thick sample [67]. On the samples with complex surface topology or that have a high contamination, high spatial resolution remains achievable. SNOM was also found to significantly reduce fluorescence photobleaching compared to equivalent studies using confocal microscopy. SNOM can also simultaneously map fluorescence and force topography, and this is often used to complement other techniques such as confocal microscopy and atomic force microscopy. After the initial report of successful biological sample imaging, further reports of SNOM imaging using biological samples have been demonstrated, such as the photosynthetic system, genetic material, membrane organisation in cells, and green fluorescence protein [9].

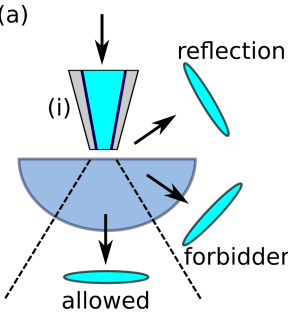
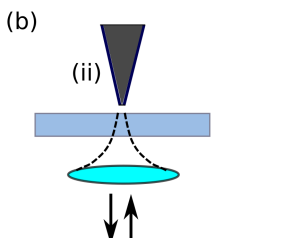
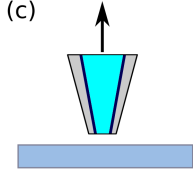
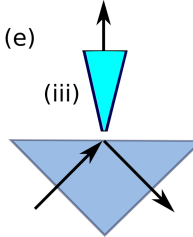
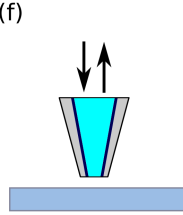
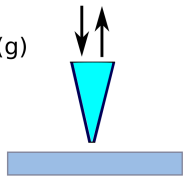
SNOM imaging has been demonstrated to help analyse the intensity and spectral distribution of lasers and optical fibres. The intensity distribution of propagating modes of the diode laser inside a waveguide was analysed using SNOM [68] and the profile of the higher modes could be identified to high spatial resolution. The near-field spectra of embedded nanocrystals in a double-clad optical fibre were observed at various locations within the inner cladding and the intensity map of the propagating wave was also obtained [69]. This device has a potential to be used for ultra-high-resolution optical coherence tomography (OCT). The light confinement within a nanostructured optical fibre was also successfully imaged with SNOM, illustrating its modes of propagation as well as the intensity profile, which could be compared to the calculated model [70].

### 2.3.2 The Configurations of SNOM

SNOM set-ups come in various configurations and in general can be grouped in three different categories based on their method of illumination and detection. These categories are summarised in Table 2.1. Two examples of the SNOM set-up are provided in each category, along with the different types of probes being used. In all cases, the optical probe

is placed within the near-field regime, at a subwavelength distance from the sample surface.

**Table 2.1:** Configurations for near-field microscopy, categorised by their illumination and detection methods. The table is adapted from Ref. [1].

Illumination Detection	Near-field Far-field	Far-field Near-field	Near-field Near-field
Set-ups	<p>(a) </p> <p>(b) </p>	<p>(c) </p> <p>(e) </p>	<p>(f) </p> <p>(g) </p>

The probe tip can be categorised as aperture-type tip (i), scattering-type tip (ii), or an uncoated tip (iii), as illustrated in Table 2.1. For the aperture-type probe, the probe tip is made from a tapered optical fibre, coated with a metal cladding, leaving an aperture at the tip. Scattering-type tips use a sharp metallic tip, in which the scattered light from the tip generates near-field illumination on the sample. The uncoated tip is made from a dielectric material, but without any metal cladding. These different probe tip types are discussed below along with the SNOM set-up in which they are used.

In the first category (Table 2.1), the sample is illuminated within the near-field region. Using the aperture-type probe (Fig. (a)), this can be achieved by coupling light into the optical fibre, with the localised illumination emitted from the tip aperture [8]. Near-field optical signals from the sample are coupled to the scattered light, which propagates to



the far-field and is detected either in the reflected or transmitted light. A critical angle exists for the transmitted light, separating the allowed and forbidden zones. When the transmitted light is detected at these two different locations, both absorption and scattering contrast can be obtained [71].

The second example uses a scattering-type probe, in which the illumination is focussed on to a metal tip (Fig. (b)). The metal tip scatters the light, with its sharp tip producing localised illumination on the sample [48, 72, 73]. In the same manner as the set-up for the aperture probe, the near-field optical signals are coupled to the scattered light from the sample and propagate to the far-field, which is detected by the same lens. A variation of this set-up (not shown) uses reflected light originating from the surface of a reflective sample. The illumination is performed at an oblique angle, focussed onto the metallic tip, and the reflected light containing the near-field signal is detected.

In the second category, the illumination and detection methods are reversed, with the illumination originating from the far-field, and the signals detected within the near-field [52]. In the first set-up (Fig. (c)), the sample illumination is focussed using a lens. The aperture probe, with the tip located in the near-field zone, detects the near-field intensity at the sample surface. The signals are collected using the tip aperture and propagate into the glass core of the tip and through the optical fibre and detected at the end of the fibre. This is the set-up that was used for the work presented in this thesis.

Another variation of this set-up uses a prism illuminated above the critical angle, enabling total internal reflection on one side of the prism (Fig. (d)). The sample is placed on this side of the prism, with the evanescent waves generated at the sample plane. The optical near-field is then detected using an uncoated probe, in which the light propagates through the optical fibre in the same manner as the set-up with the aperture probe. This set-up is referred to as scanning tunneling optical microscope (STOM) or photon scanning tunneling microscope (PSTM) [74, 75].

The last category contains the set-ups where both illumination and detection are performed in the near-field. These can be performed either

with an aperture probe (Fig. (e)) or an uncoated probe (Fig. (f)) [76, 77]. Light is coupled into the optical fibre and propagates to the aperture at the probe tip. The light illuminates the sample locally from the near-field, but the generated near-field optical signals are collected by the same probe tip. The scattered light is coupled back to the probe tip and through the optical fibre where it is detected. This application is however limited when the aperture probe is used because the signal from the transmitted light through the tip aperture is already very weak, and even weaker signals are detected after passing back through the tip.

Figure 2.7 shows an example of a standard set-up for SNOM with an aperture probe [8]. This shows a SNOM system in illumination mode (near-field illumination and far-field detection). There are three main blocks of components: (a) illumination unit, (b) collection and redistribution unit, and (c) detection module.

The illumination unit consists of the light source and other components redirecting the light onto the sample. In this example, a laser is used as the light source, and light passes through a polarisation control with the beam coupled into the optical fibre with a SNOM probe tip at the end of the fibre. The light from the probe tip illuminates the sample at a near-field distance. In order to regulate the distance between the probe tip and sample, a feedback control unit is attached to a tuning fork as the shearforce detection block. The probe tip is attached to the tuning fork which vibrates laterally with respect to the sample surface, typically in the range of 1 to 5 nm. At distances which are typically less than 20 nm, the shearforce between the sample and the probe tip dampens the oscillation, leading to changes in the amplitude and oscillation phase. These changes in the detected shearforce are used to regulate the probe tip distance to the sample surface.

The second block is the collection and redistribution unit, which consists of a sample stage attached to a sample scanner. The sample can be moved in three-dimensions, with the  $z$ -position regulated by the feedback control unit to achieve a specified distance between the probe tip and the sample. The stage is also moved in the  $x$ - and  $y$ -directions for raster scanning over the area of the sample. An objective lens is placed with its focal plane at the sample surface to collect the transmitted light

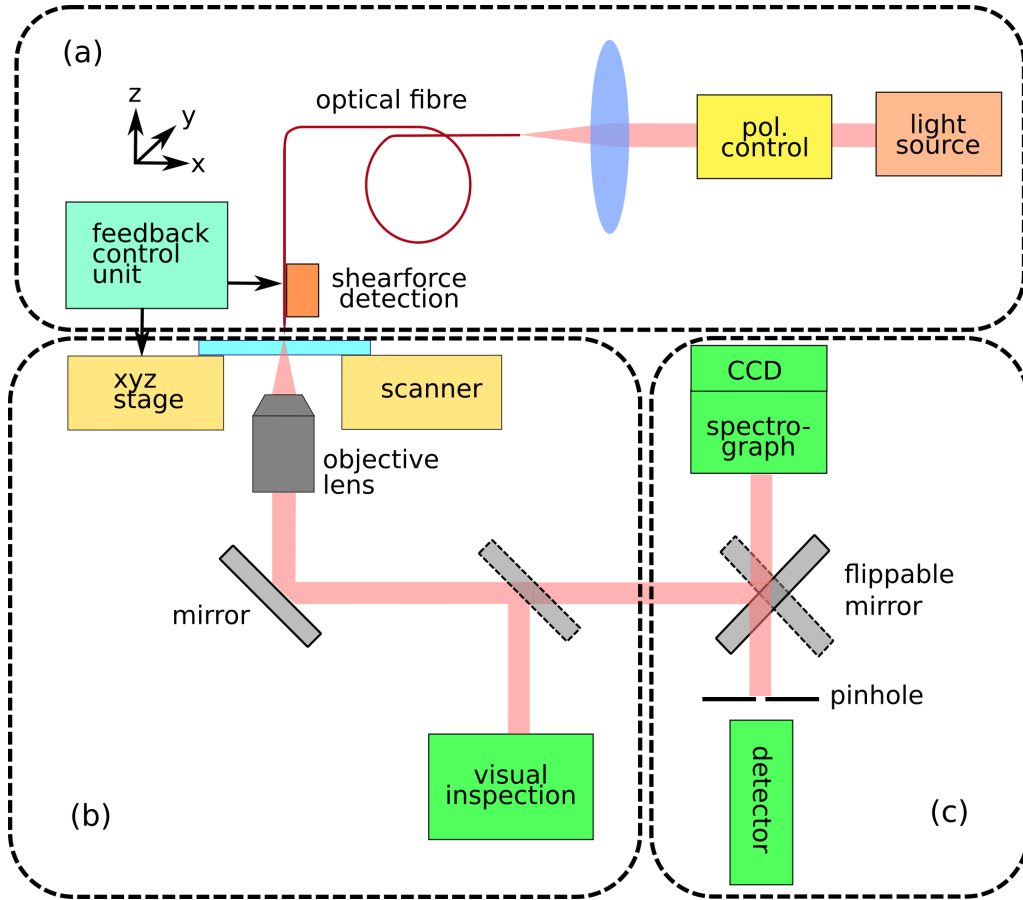


**Figure 2.7:** The standard setup for aperture-type SNOM in illumination mode, consisting of (a) the illumination unit, (b) the collection and redistribution unit (in an inverted microscope), and (c) the detection module (adapted from Ref. [8]).

from the sample with illumination from the probe tip. The collected light is then redirected by a mirror to the detector block. A beam splitter or a mirror may be added into the light path for visual inspection, and to align the beam path between the probe tip, the sample, and the objective lens.

As the name implies, the detection module consists of devices for detecting the transmitted light which is then collected by the objective lens from the sample as a result of near-field illumination by the probe. A suitable set of detectors and CCD cameras may be used for detecting the optical signals, including any filter or a pinhole.

### 2.3.3 Probe Tip in the SNOM Imaging and Author's Contributions

The optical probe is an important component of the SNOM system. The quality of the probe determines the image quality produced by SNOM. The probe tip needs to be maintained at a sufficiently short-range distance from the sample surface. This is to ensure that the undiffracted near-field signal can be detected at subwavelength distances from the sample surface. The resolution of SNOM will depend on the size of the probe tip that interacts with the sample [40].

In order to retrieve optical information from the sample, the efficiency of radiation energy transfer between the probe and the sample is crucial. To obtain high spatial resolution, the optical energy between the probe and the sample needs to be kept in a small laterally confined zone while maximising the energy flux between them. A strong localisation of the EM field is observed at the tip of the probe and the efficiency is strongly correlated to the type of the probe and its geometry [40]. In an aperture probe, the energy transfer is limited to the size of the aperture at the tip. While a small tip size is preferred for localisation, and hence high resolution, it has a low associated transmittance.

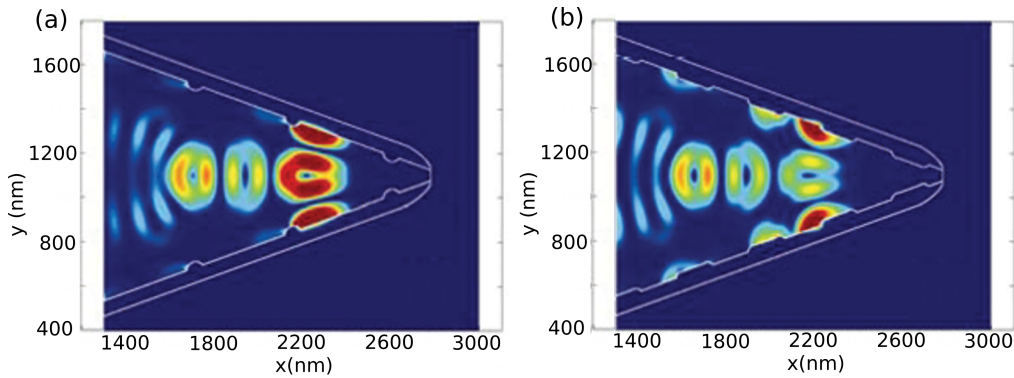


**Figure 2.8:** Corrugated SNOM probe for achieving high energy throughput, with (a) circular grooves and (b) oval grooves [29].

There have been attempts to increase the efficiency of the energy transfer at the probe tip. For example, a probe tip with a corrugated cladding was proposed to be fabricated at the boundary between the glass core

and the cladding [29]. Sections of the proposed probe tip with two different groove shapes are shown in Fig. 2.8. The grooves are expected to facilitate surface plasmon excitation to increase the energy transfer efficiency. The study reported that the energy transfer can be increased by one order of magnitude by fine-tuning the groove parameters, it should thus be possible to reduce the probe tip size while maintaining this level of energy transfer. The smaller sized probe is expected to produce at least twice the spatial resolution.

A modified probe tip with a gold nanoparticle attached to the probe tip for apertureless SNOM was studied using simulation [13]. This study investigated different shapes for the nanoparticle including cone and pyramid with the sharp tip facing the sample surface. The geometry of the nanoparticles is tailored for large field enhancement, allowing for higher resolution up to 10 nm.

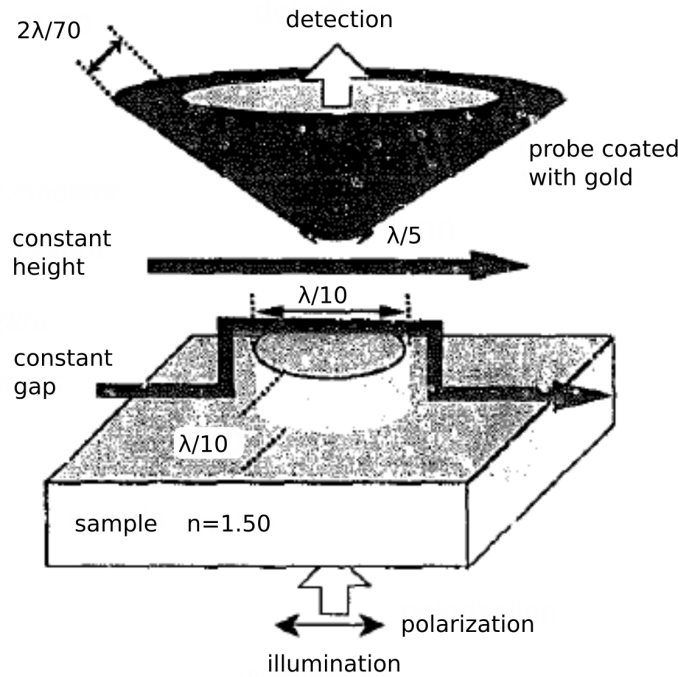


**Figure 2.9:** Simulation setup for investigating the scattering effect of the probe tip in image formation of a circular disc [41].

One of the first studies of investigating the influence of the probe tip in SNOM imaging was performed by simulating light scattering from a disc [41]. The probe tip was incorporated into the simulation and the intensity

profile was measured by scanning the probe above the disc with constant distance/ gap and constant height modes. The schematic is shown in Fig. 2.9. In constant gap mode, the probe is moved up or down while it is scanning the substrate area, so that it is always at the same distance from the sample surface. In constant height mode, the probe is held at a fixed height with respect to the substrate during scanning, so that the relative gap between the probe and sample surface changes while it is scanning the sample.

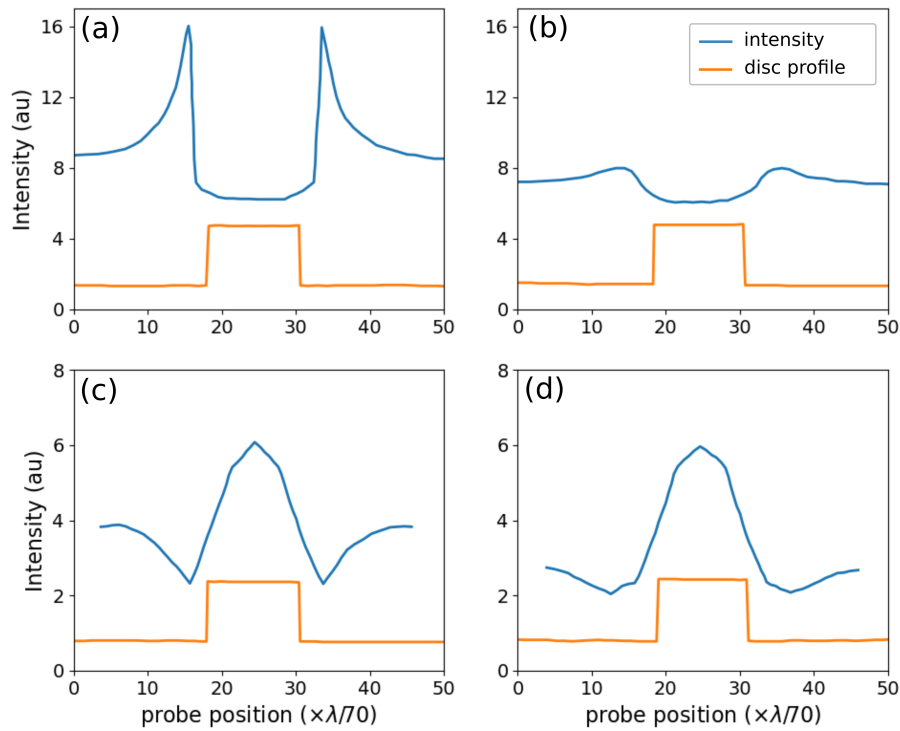


**Figure 2.10:** Simulated near-field intensity above a circular disc (a-b) without and (c-d) with the probe included in the calculation (blue lines) [41]. The first column (a,c) is in a constant gap mode and the second column (b,d) is in a constant height mode. The top-hat profile at the bottom of each figure (orange line) shows the disc location.

The probe tip has been found to have a significant effect in image formation. The simulation results are shown in Fig. 2.10 for the intensity profile calculated without and with the probe included. Without the probe tip, the intensity reaches its maximum peak at the edges of the disc

(Fig. 2.10(a-b)). The intensity profile shows high localisation in this region with sharp peaks observed. The intensity peaks are weaker when detected using a constant height mode.

Significant differences in the intensity profiles are observed when the probe tip is incorporated in the calculation (Fig. 2.10(c-d)). The sharp peaks at the edges of the disc are no longer observed in both modes. Instead, the maximum of the intensity peak was found at the centre of the disc, with a relatively smooth peak. The intensity reaches a minimum near the edges of the disc. It is clear that the probe tip presence alters the electromagnetic fields of the sample, leading to a difference in the image formation.

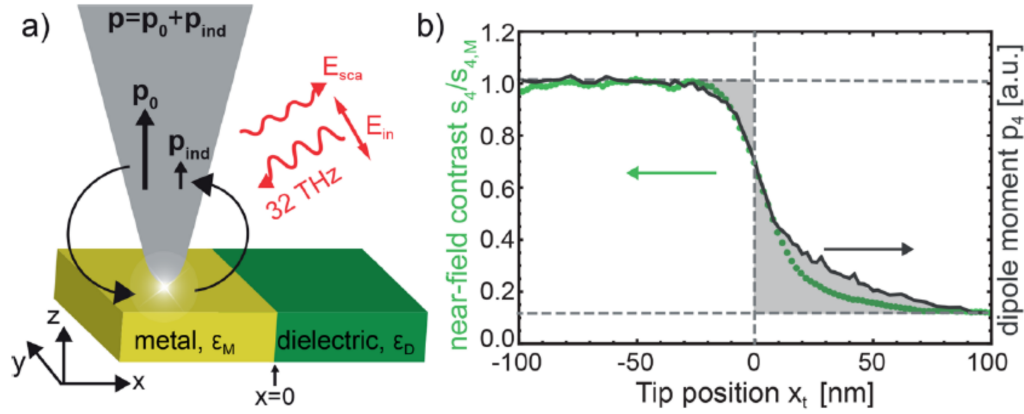


**Figure 2.11:** Study of the SNOM resolution investigated with a sample consisting of a boundary between metal and dielectric materials. (a) The schematic of the probe scattering while scanning the sample and (b) the intensity profiles observed across the boundary.

A more recent study involving the probe tip was the investigation of the resolution of apertureless SNOM [5]. A schematic and an example of the results are shown in Fig. 2.11. The probe tip is made of metal which scatters reflected light from the sample. To reduce topography effects, the sample was taken from a hard disk drive which provides a sharp boundary between the metal and dielectric, and it also has a very flat surface. It was found that the intensity profile is asymmetric when the probe scans above the metal and dielectric regions. This asymmetry could not be reproduced without involving the probe tip in the calculation. The probe-sample interaction is modified when it is scanning different materials in

the sample.

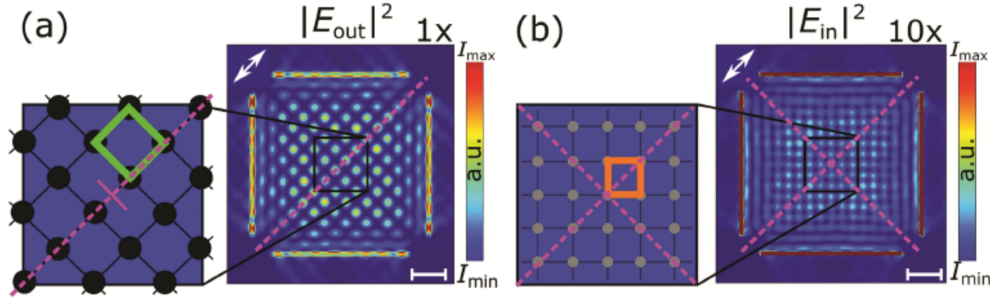


**Figure 2.12:** Interference pattern produced by a square arrangement of four slit apertures, producing two different patterns of (a) diamond-like symmetry and (b) square-like symmetry from different interferences between in-plane and out-of-plane components arising from the surface plasmon effects of the slit apertures [4].

A more in-depth analysis of the SNOM probe tip was performed by investigating a near-field interference patterns from a square arrangement of four slit apertures [4]. The out-of-plane component of the electromagnetic fields generated from the slit apertures produced a diamond-like interference pattern. On the other hand, the in-plane components produce a square-like interference pattern. These different patterns are generated depending on the excitation light and the wavelength used. In theoretical calculations, only the pattern from the in-plane components can be detected by the optical probe, but it was observed that both patterns can be imaged with SNOM, provided appropriate excitation light is used for each condition. A simulation involving the probe tip was performed to confirm the detection of interference by the SNOM system. The probe tip was crucial in analysing the imaging process for this sample.

This study investigated the influence of the probe tip on the image formation using SNOM. In order to understand this influence, a simulation model of SNOM imaging was constructed based on the FDTD method. The FDTD method rigorously calculates the electromagnetic fields on the sample while also incorporating the presence of the probe tip near the sample.

By carefully selecting the appropriate parameters for the probe tip, the model was tested using experimental data of SNOM scans. The scans were performed on characterisation samples of slit apertures in a gold



film using SNOM equipment. By analysing the intensity profiles obtained from the experiments, and comparing these with the results from the modelling, the influence of the probe tip was analysed.

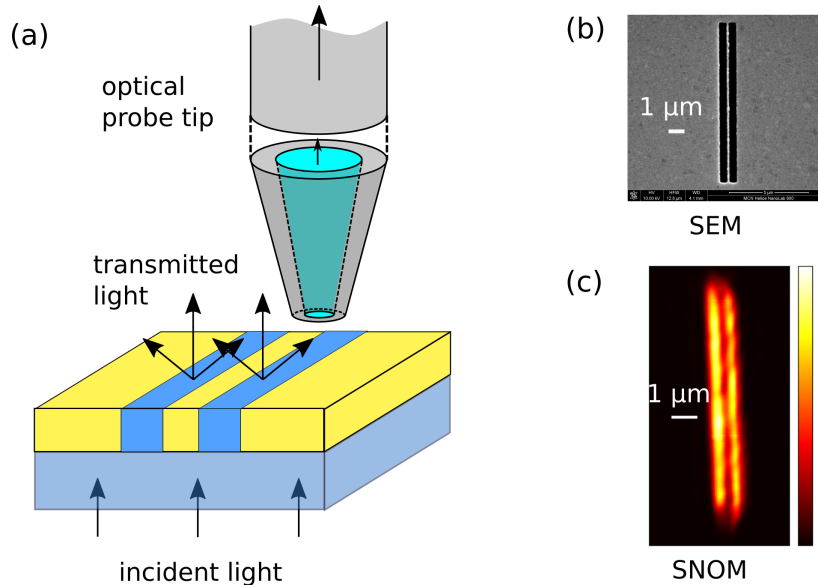


**Figure 2.13:** (a) Schematic of the simulation model of the SNOM scan on the double-slit aperture in a gold film, and (b) the SEM and (c) SNOM scan images of a double slit apertures [34].

An article based on this study was published in *OSA Continuum*, investigating the probe tip influence on SNOM image formation [34]. Characterisation samples comprising slit apertures (double-slit in Fig. 2.13), were imaged experimentally using SNOM, and the results were analysed using the simulation model, with the probe tip included. The image was constructed in the simulation by moving the probe across the sample, in order to mimic how the measurements are made in the experiments.

Furthermore, knowledge of the probe tip influence and a realistic simulation model are crucial for improving image quality via post-processing. In this study, the calibrated simulation model was used for calculating the PSF of the SNOM system, which is strongly affected by the probe tip. After the PSF is determined, the images from SNOM scan results can be further improved via implementation of a deconvolution algorithm, which ameliorates the deleterious effect of the SNOM probe on the images. The challenges for this approach lie in accurately determining the PSF of the SNOM system while accounting for the noise in the images.

## 2.4 Spatial Resolution and Image Restoration

### 2.4.1 Spatial Resolution in Microscopy Imaging

Spatial resolution is one of the key metrics which characterise the performance of any imaging device. The spatial resolution determines the smallest feature size that can be resolved. The definition of spatial resolution can mathematically be described in an unambiguous way, but in practice, the measurement of spatial resolution is not straightforward. Ref. [78] proposes a standardization of resolution claims when reporting the spatial resolution characteristics of a given microscopy method.

One of the key characteristics of imaging device is the point spread function (PSF). As the name implies, it measures how much a point source or a point object will spread out in terms of the width when imaged using that particular device. Ideally, this point source/object has an infinitely small size, and hence can be modelled using the Dirac delta function with infinite spatial-frequency components. Using the dipole analysis, the distribution of the electromagnetic fields of a point source or object can be determined, albeit with some paraxial approximations. The PSF of the imaging system depends on the orientation of the dipole moment of the point source. Despite using paraxial approximations, the calculation shows good agreement for the dipole moment of the source perpendicular to the optical axis for high NA illumination [1].

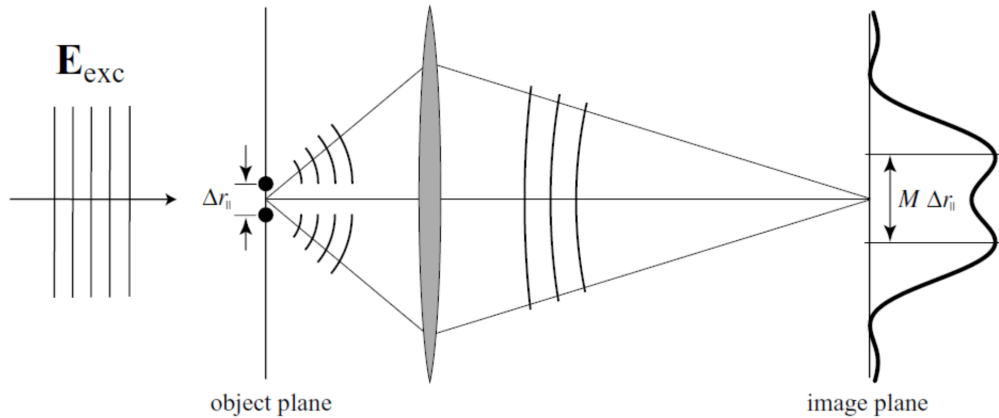


**Figure 2.14:** Schematic for investigating spatial resolution using two closely spaced objects [1].

A common method of investigating the resolution is by observing two closely spaced objects. One intensity peak is detected for each object corresponding to its location, with the peak width indicative of the PSF. The two peaks from the two objects tend to merge when the objects are very close to each other, separated by a distance which is smaller than the resolution limit of the imaging system. The smallest possible separation that can be resolved defines the resolution limit of the imaging device.

Fig. 2.14 presents a schematic illustrating a typical means for determining the resolution limit for an imaging system using two closely spaced features. The objects are separated by a distance  $\Delta r_{\parallel}$ , parallel to the sample plane and perpendicular to the optical axis. The peaks from the two objects are detected at the image plane a distance  $M\Delta r_{\parallel}$  apart from each other, where  $M$  is the magnification.

In far-field imaging, the information content of the optical signals is limited by the bandwidth of spatial frequencies detected. Using a lens with numerical aperture NA, the minimum separation is

$$\text{Min}[\Delta r_{\parallel}] = \frac{\lambda}{2\pi\text{NA}}. \quad (2.2)$$

Abbe's formulation considers the dipole orientation of the scattered light by the objects. Using this formulation, the diffraction limit is less optimistic, with the minimum resolvable separation increasing by a factor of 3.8, which is given by [79]

$$\text{Min}[\Delta r_{\parallel}] = 0.6098 \frac{\lambda}{\text{NA}}. \quad (2.3)$$

In incoherent microscopy, the intensity detected in the image plane is linear with respect to the emitted intensity from the objects, i.e.  $I \propto |E_1|^2 + |E_2|^2$ . This is not the case when the illumination is from a coherent source, such as a laser, coherent x-rays, and electron sources. The images obtained using coherent microscopy can suffer from degradation due to interference between the scattered waves from the sample. The detected intensity depends on the interference between the individual waves, i.e.  $I \propto |E_1 + E_2|^2$ , which also depends on the polarisation and phase difference between them. This means that *a priori* information from the optical

system is required to correctly measure the spatial resolution that it can achieve.

Another approach for determining the spatial resolution in microscopy imaging is by using the sharp edge or boundary between two materials [80, 81]. This line profile across this boundary is called the edge response function (ERF). Using this approach, the intensity gradient or change between two different materials at a sharp boundary is affected by the spatial resolution of the device. The characteristic width of the intensity profile, determined via its derivative, is known as the line spread function (LSF). This characteristic width determines the spatial resolution according to a specific criterion, such as Rayleigh or Sparrow criteria [5, 46].

## 2.4.2 Deconvolution Algorithm for Image Restoration

In Fourier optics, any lens or imaging device is a transfer function that translates the original object to the resulting image. These devices can be viewed as a set of rules of the change in optical path of the propagating EM fields, e.g. due to refraction from the incoming to the outgoing light through the device. The type of the device (e.g. lens) and its specific parameters (e.g. focal length) determines the transfer function.

An object can be viewed as a collection of point sources in which the incident light is either transmitted, reflected, or scattered by the object. The device, in effect, distorts the incident light from the object and forms an image of the object. In the case of a point object, this distortion typically results in broadening of the point in the resulting image. Assuming the optical path is perfect, the function relating the point source to the resulting image is called the PSF. With knowledge of PSF, it is possible to trace back the original object from the distorted image to produce a better quality image, for example with sharper edges.

In the space domain, multiplication between the original object and the transfer function is achieved via convolution. Image formation by an optical system is the convolution between the original intensity distribution and the transfer function of the system. Due to various processes in the imaging system, the resulting images can suffer from a degradation in

quality. Restoring the degraded image to its original better quality image using knowledge of PSF can be achieved with deconvolution.

In mathematics, the image formation and deconvolution can be described as follows. Given a perfect 2D object,  $X$ , measured using an optical system with a PSF of  $c$  and a signal-independent noise  $\delta$ , the resulting 2D image is

$$Y = c * X + \delta, \quad (2.4)$$

where  $*$  denotes the convolution operation. Equivalently, in the frequency domain, this can be written as a multiplication,

$$Y = \mathcal{F}^{-1}\{\mathcal{F}(c)\mathcal{F}(X)\}, \quad (2.5)$$

where  $\mathcal{F}$  denotes the Fourier transform. The goal of deconvolution is to arrive at an estimate of the original object,  $\tilde{X}$ , from the blurry and noisy measured image  $Y$ , as described by Eqs. 2.4 and 2.5 [82].

Using inverse filtering, the solution  $\tilde{X}$  can be found by dividing the image with the PSF (in the Fourier domain).

$$\tilde{X} = \mathcal{F}^{-1}\left\{\frac{\mathcal{F}(Y)}{\mathcal{F}(c)}\right\} \quad (2.6)$$

Unfortunately, this solution causes problems when the PSF contains small values (or has many zeroes), which is usually the case for most optical devices. Because of the division by zero (or by a number close to zero), the measurement noises are amplified, preventing the original image being restored.

Wiener deconvolution solves this problem by introducing a damping factor in the above equation, reducing the effect of noise in the calculation. The equation is now given by

$$\tilde{X} = \mathcal{F}^{-1}\left\{\left[\frac{|\mathcal{F}(c)|^2}{|\mathcal{F}(c)|^2 + \frac{1}{\text{SNR}}}\right] \frac{\mathcal{F}(Y)}{\mathcal{F}(c)}\right\}, \quad (2.7)$$

where SNR is the signal-to-noise ratio. At zero noise, the SNR is infinite and Eq. 2.7 reduces to Eq. 2.6.

Another technique called Richardson-Lucy deconvolution was derived

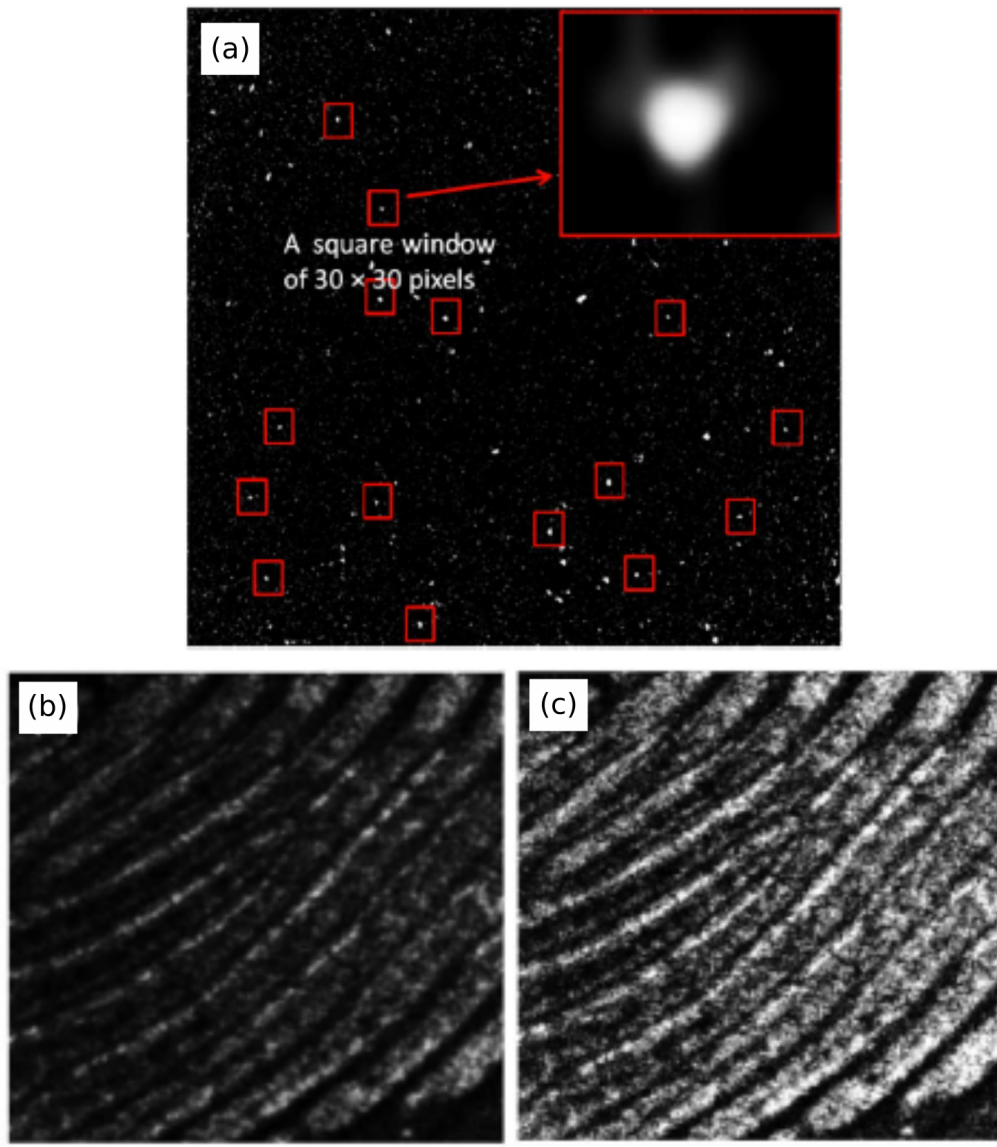
using a different approach. The algorithm is based on Bayes's theorem of conditional probability. Assuming the image suffers from Poisson's noise, the algorithm solves the deconvolution problem via an iterative method. The resulting restored image is the most-likely image obtained after several iterative steps assuming a known PSF. The algorithm is very robust in the presence of noise. A more detailed discussion of Richardson-Lucy deconvolution is provided in Chapter 3.

Deconvolution is a common technique used in astronomy [83] for improving the quality of noisy and blurry images, and is also widely used in several imaging applications [42] and microscopy techniques, such as confocal microscopy [84], OCT [85], and fluorescence microscopy [86].

Figure 2.15 shows an example of deconvolution applied to images obtained using OCT. The PSF was determined using a solid phantom consisting of dispersed monosized gold particles in a resin, which is shown in Fig. 2.15(a). A few reliable spots (within the red squares) are chosen to calculate the average PSF. One example of deconvolution was performed on an image of the human fingertip skin sample shown in Figs. 2.15(b-c). Deconvolution was able to improve the image clarity by improving the homogeneity of the brightness and the overall sharpness of the image.

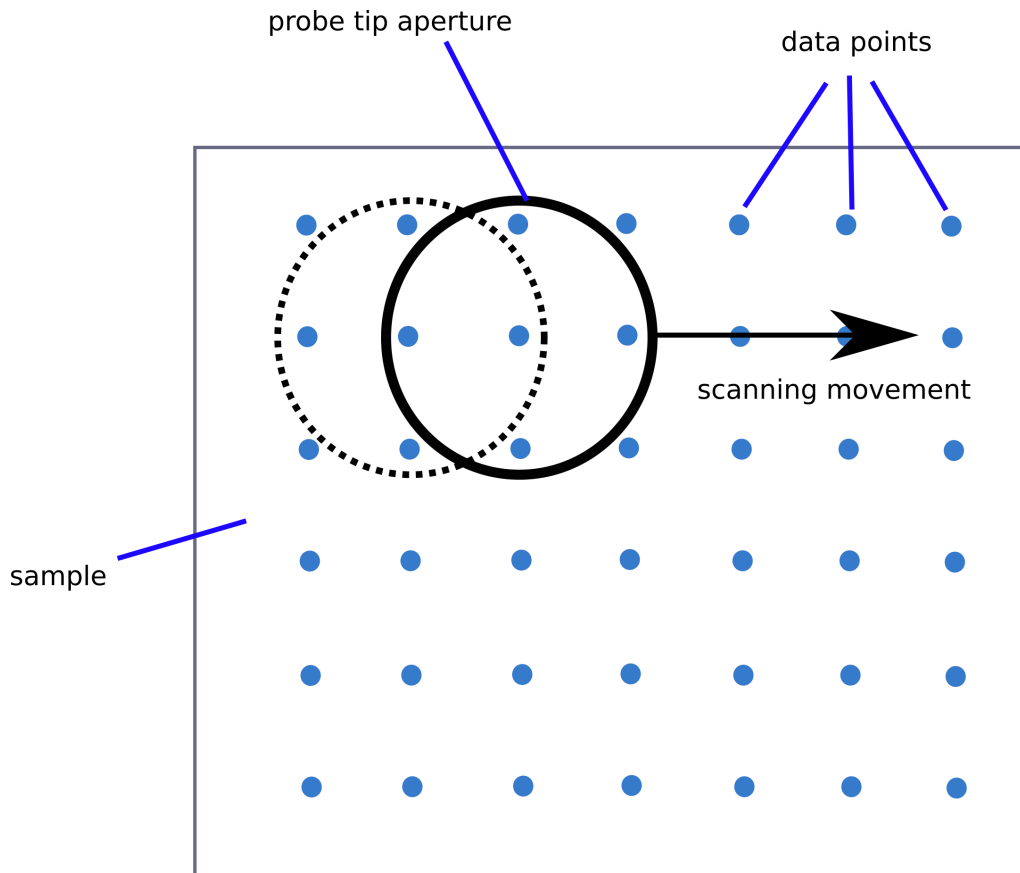
The convolution that occurs during SNOM imaging can be visualised as the probe tip with a finite size, scanning the sample with overlap between data points. The corresponding schematic is shown in Fig. 2.16. The scan step is usually set smaller than the probe tip size. Data points between the scan steps overlap when the probe detects the intensity at a particular position. As the probe scans the sample, the imaging can be viewed as a 2D convolution between the sample surface and the probe tip over the sample while it is scanning, within a designated area. Deconvolution is performed to reverse this effect by ameliorating the effect of the finite size of the probe, ideally reducing the probe tip to a delta function. This can potentially improve the sharpness and quality of the scanned images.

Figure 2.17 shows the calculated model for SNOM imaging derived from an AFM image of Co/Pt pillars embedded in a Pt matrix and the deconvolution results. The SNOM image in Fig. 2.17 (b) was simulated using the convolution of the AFM image in Fig. 2.17(a) with an aperture



**Figure 2.15:** Deconvolution of an OCT image of a human fingertip skin sample. (a) PSF of the imaging system, (b) image before deconvolution, and (c) image after deconvolution. [85]

of diameter 200 nm. A more realistic SNOM image was modelled with added noise in Fig. 2.17(c), and the image was then denoised, giving the image in Fig. 2.17(d). Deconvolution was performed on the images in Figs. 2.17(b,c,d), with the respective result shown below each image in Figs. 2.17(e,f,g). The simulated SNOM image is blurry due to convolution between the sample and the probe tip, which is further degraded



**Figure 2.16:** Schematic showing the convolution process during the SNOM scan. A top-down view of the sample is shown with the aperture scanning above it. The circles indicate the locations of the probe tip aperture between the scan steps, with the dashed circle representing before and the solid circle after probe movement.

by the noise. Deconvolution result in a simulated SNOM image without noise (Fig. 2.17(e)) shows that the image quality can be restored. With noise, however, the result is not as clear as the contrast between the objects and the medium is low. This can be overcome by performing a denoising process before the deconvolution algorithm is applied. The result in Fig. 2.17(g) shows an improvement compared to the result in Fig. 2.17(f) when the signal-to-noise ratio is low.

The results demonstrated in Fig. 2.17 show the potential of deconvolution when applied to the results of SNOM scans, even though this was only a simulation. This also can potentially be applied to other probe microscopy techniques, such as AFM.



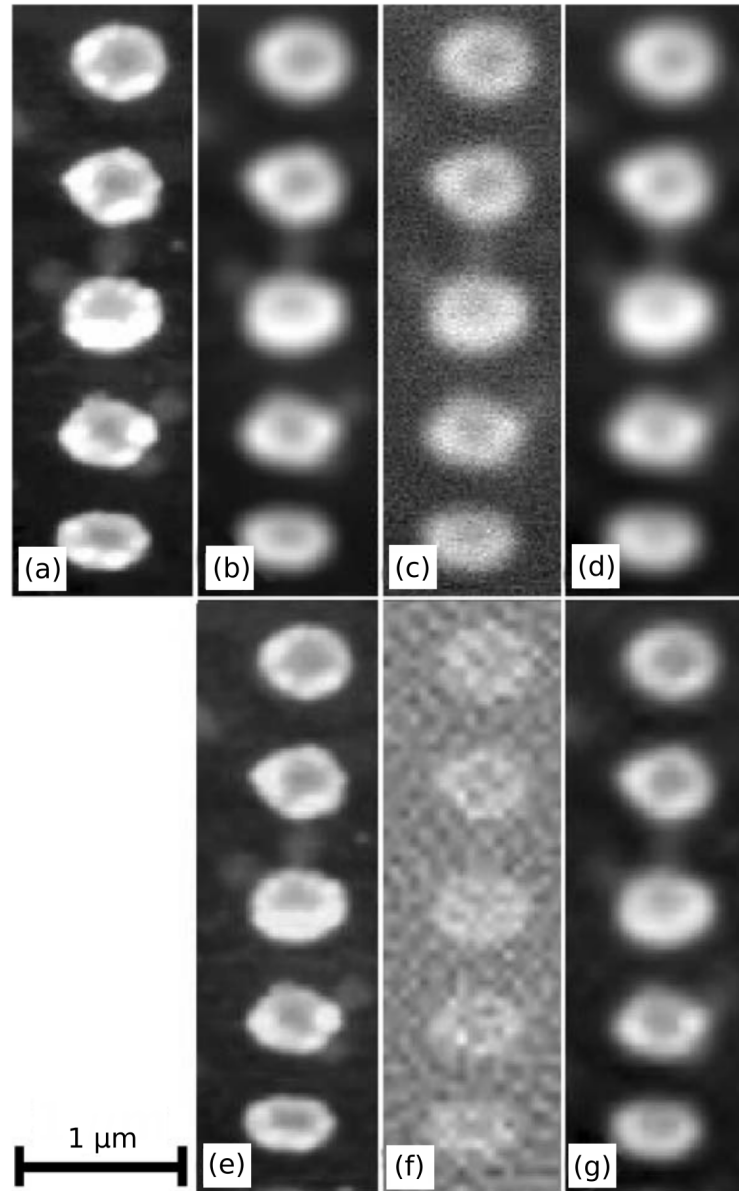


**Figure 2.17:** Simulation model of SNOM images based on an AFM image. (a) AFM image, (b) simulated SNOM image derived from (a), (c) simulated SNOM image with added noise, and (d) simulated SNOM image after denoising. (e,f,g) Deconvolution results for the images shown in Figs. (b,c,d) respectively. [87]

## 2.5 Chapter Summary

In microscopy imaging, the bandwidth of spatial frequencies that can be detected in the far-field (at distance much larger than the wavelength) is

limited by the wavenumber of the light ( $k = n\omega/c$ ), and practically, by the numerical aperture (NA) of the lens or imaging system. In the Fourier domain, higher spatial frequency components are not propagating, and hence cannot be detected in the far-field. This effectively limits the spatial resolution according to the diffraction limit, and it restricts the feature sizes that can be resolved to about half of the incident wavelength.

SNOM exploits the near-field optical signals which exist as nonpropagating evanescent waves at the sample surface. These waves have an intensity which decays exponentially along the optical axis (perpendicular to the sample plane). With SNOM, an optical probe is placed at a short-range distance from the sample, inducing these components to be scattered and coupled to the far-field and thus detected. This allows for high-resolution imaging beyond the diffraction limit.

SNOM has been used in a wide range of applications especially because of its high-resolution capabilities. Compared to electron microscopy techniques like SEM and TEM, this technique requires less sample preparation and is nondestructive. In the field of nanophotonic devices, SNOM has been used for investigating the local electromagnetic interactions between the nanostructures and incident light as well as the internal interaction between the nanostructures itself. In the field of biochemistry and microbiology, SNOM has been used for single molecule, tissue, and cell imaging. These biological specimens are usually too fragile to image under vacuum using electron microscopy.

The probe tip is an important component of SNOM equipment because it is the part that interacts with the near-field signal originating from the sample. Its presence in the near-field region leads to complex electromagnetic interactions in the vicinity of the sample. Ignoring the probe tip in SNOM simulations leads to inaccuracies in the results and hence an unrealistic model of SNOM imaging. Several studies have been performed that investigate the electromagnetic field distribution inside and surrounding the probe tip to achieve better resolution and sensitivity with respect to the optical properties of the sample.

Image post-processing may be further applied to the results of SNOM imaging. When the probe scans the sample, the resulting image is affected by the convolution between the probe tip (which has a finite

size) and the sample. Using a deconvolution algorithm, the influence of the finite probe size may be reduced and the image quality can be improved. Deconvolution is a common technique used in astronomy and has been applied in several other microscopy imaging techniques, such as OCT and fluorescence microscopy.



# Chapter 3

## Methods

### 3.1 Introduction

This chapter provides a summary of the experimental and simulation methods used in this thesis. The set-up of the SNOM equipment and methods used for analysing the experimental data are discussed. The SNOM system was used in collection mode, in which the optical probe detected the light intensity within a near-field distance, with the sample illuminated from the far-field. Aperture-type SNOM was used in this study, with an optical probe made from a tapered optical fibre, coated with metal layers, and a small aperture at the tip [8]. The samples used in the experiment were slit apertures in a metal film. To generate the 1D line profiles, the intensity from multiple line scans taken from different points along the slit was averaged in order to improve the signal-to-noise ratio. [5]. The intensity profiles were fitted using the pseudo-Voigt function, which is the linear combination of Gaussian and Lorentzian functions.

The section follows with a summary of the FDTD method for solving electromagnetic problems [33, 88, 89]. The simulation model was constructed based on the FDTD method to simulate the propagation of the incident light and its interactions with the sample. This model also accounted for interactions with the SNOM probe tip. The components of the simulation are discussed, which include the FDTD cells, objects/samples, boundary conditions, electromagnetic source, and detectors.

In the final section, a deconvolution method using the Richardson-Lucy algorithm [6, 90] is discussed. The algorithm is based on Bayes's theorem and employs an iterative method to restore degraded images. The method was used for deconvolving SNOM images to reduce the probe tip influence to obtain images with better quality and resolution. The point spread function of the SNOM system is required as an input for this approach.

## 3.2 SNOM Data Acquisition

### 3.2.1 SNOM Setup

The principle experimental technique used for this research was SNOM. Data was recorded in collection mode, where the sample illumination was placed in the far-field with respect to the measurement plane. The probe tip scans an area of the sample with a distance very close to the sample surface while collecting the near-field optical signals from the sample. The SNOM system used in this study was the NTEGRA Solaris SNOM supplied by NT-MDT. This is an aperture-type SNOM with an optical probe made from a tapered optical fibre coated with a metal cladding. A small, subwavelength, aperture at the tip collects the light from the sample.

Figure 3.1 shows the layout of the SNOM system in collection mode. The light source was a monochromatic red laser (OBIS FP 640LX) with a wavelength of 640 nm. The spatially filtered light was directed to a beam splitter that reflected a part of the beam into an objective lens. The focused beam from the objective lens illuminates the sample. The objective lens position was adjusted such that the sample was illuminated just outside of the focal plane of the objective. The focal plane was located at about 5 mm to 10 mm from the sample surface. This configuration generated a broad incident illumination with a near-homogeneous intensity distribution over the scanned area. The beam diameter on the sample surface was between 300  $\mu\text{m}$  to 600  $\mu\text{m}$ . A camera was used to measure the reflected light from the sample in order to align the beam, sample, and probe tip.

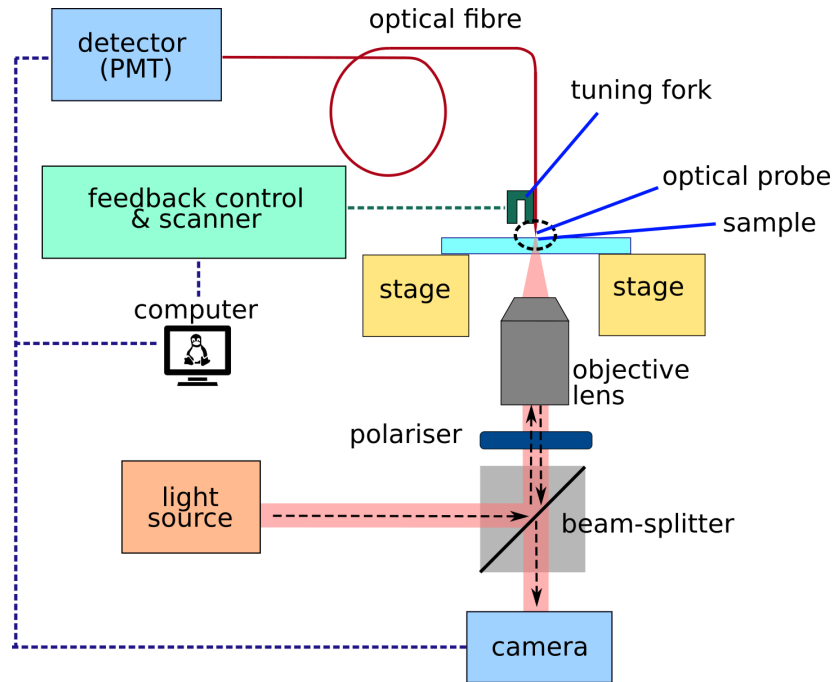


**Figure 3.1:** The layout of aperture-type SNOM in the collection mode used in this study.

The probe was purchased from Tips Nano (product code MF113\_NTF) and was designed to accommodate wavelengths ranging between 600 nm and 770 nm with a corresponding transmittance of between  $10^{-4}$  to  $10^{-5}$ . The probe was attached to a tuning fork that vibrates at 170 kHz to 190 kHz in the direction parallel to the sample surface. It was connected to a feedback control and a sensor which detected the change in the amplitude due to variations in the Van der Waals force interaction as the probe tip scanned over the sample surface. The feedback control system adjusts the sample-tip distance during the scan based on the change in the measured amplitude as the probe moves in and out of the near-field of the sample surface. The feedback mechanism relies on changes in the shear forces measured by the probe. The feedback system and scanner were also used to control the size of the area to be scanned and the scan speed via the software supplied with the system.

The signal detected by the probe propagated through the optical fibre, with its end being attached to a photo-multiplier tube (PMT). The PMT detected the transmitted light and converted it to an electrical signal that was sent to the computer. The signal was then processed by the

software, which is integrated into the software provided as part of the SNOM system.

### 3.2.2 Intensity Profiles from One-Dimensional Samples

Some of the test samples used in this study were one-dimensional structures in the form of slit apertures in a gold film. These structures had length of 10  $\mu\text{m}$ , much greater than their width, which was less than 0.5  $\mu\text{m}$ . The intensity profile across the subwavelength width of the slit aperture (perpendicular to the slits long axis) is the focus of this study for assessing the SNOM image formation.

Since the slits were uniform (on the nanoscale) parallel to their long axis, several line scans were averaged in order to improve the signal to noise ratio. The schematic of the sample is shown in Figure 3.2, with the red area being the intensity peak of the transmittance through the slit. A blue line was drawn at the middle of the slit, parallel to the long axis of the slit. This line acts as a reference line for calculating the intensity perpendicular to the slit, to be measured along the green lines, which are perpendicular to the long axis of the slit. The intensity profile across the slit was calculated as the average values of these intensity profiles measured along the green lines. In the calculation, the average value was taken from 100 lines rather than just the 5 shown in the schematic.

### 3.2.3 Fitting Functions

The intensity profiles have peaks with a shape close to a Gaussian or a Lorentzian function. For quantitative analysis, the intensity profiles were fitted to the function, so that the important characteristics of the profile, such as its width, can be determined. The Gaussian function  $f_G$  and Lorentzian function  $f_L$  are given by

$$f_G = A \exp \left( -\frac{(x - x_0)^2}{2\sigma^2} \right) \quad (3.1)$$

$$f_L = \frac{A}{1 + \left( \frac{x - x_0}{\gamma} \right)^2} \quad (3.2)$$



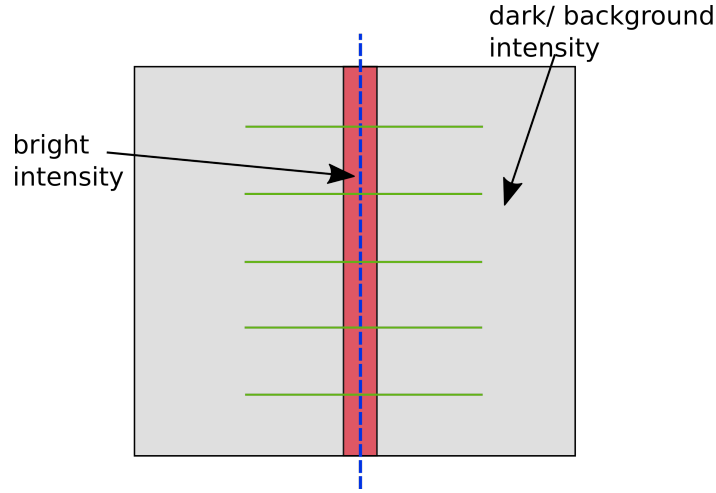


**Figure 3.2:** A schematic showing the lines drawn for calculating the average intensity profile perpendicular to the slit. The vertical dashed blue line represents the line of brightest intensity which is in the middle of the slit. The intensity profiles were measured along the green horizontal lines and were averaged to obtain the final intensity profile.

where  $A$  is the peak amplitude,  $x_0$  is the position of the peak maximum, and  $\sigma$  and  $\gamma$  are peak-width parameters (see Eqs. 3.1 and 3.2). The full-width at half-maximum (FWHM) of the peak can be calculated as follow.

$$\text{FWHM} = (2\sqrt{2\ln 2})\sigma \text{ (Gaussian)} \quad (3.3)$$

$$\text{FWHM} = 2\gamma \text{ (Lorentzian)} \quad (3.4)$$

After a few trials, a combination of these two functions gave the most accurate fitting. The composite fitting function is called the pseudo-Voigt function, which is a linear combination of Gaussian and Lorentzian functions. The pseudo-Voigt function  $f_V$  can be written as

$$\begin{aligned} f_V &= \eta f_L + (1 - \eta) f_G \\ &= \eta \frac{A}{1 + \left(\frac{x-x_0}{\gamma}\right)^2} + (1 - \eta) A \exp\left(-\frac{(x-x_0)^2}{2\sigma^2}\right) \end{aligned} \quad (3.5)$$

where  $\eta$  is the linear combination factor with the value of  $0 \leq \eta \leq 1$ . The optimum values for  $\eta$ ,  $A$ ,  $x_0$ , and FWHM were calculated using non-linear least-squares fitting.

### 3.3 Simulations using the Finite-Difference Time-Domain (FDTD) Method

#### 3.3.1 Introduction to the FDTD Method

To model the electromagnetic interactions between the probe tip and the sample, simulations based on the FDTD method were employed. The method is based on four Maxwell's equations in differential form. With this method, the simulated region is divided into three-dimensional rectangular grids with finite size. In each cell, the materials are defined by their electric and magnetic properties via permittivity  $\epsilon$  and permeability  $\mu$ . The electromagnetic source is generated in the simulated region and its propagation and interaction with the media or materials are calculated as a function of time.

One of the advantages of the FDTD method is the algorithm calculates both the electric and magnetic fields of the system being investigated. This is unlike, for example, the discrete dipole approximation (DDA) method, in which only the electric fields are calculated, assuming the magnetic fields follow the same behaviour. This increases the accuracy of the model and offers flexibility in terms of the materials to be introduced into the simulation.

Due to its rigorous calculation, the FDTD method has the disadvantage that it requires significant computational resources and time. There is always a trade-off between the accuracy of the simulation achieved using finer mesh and the computational resources required for solving for the electromagnetic field distribution. This limitation means that in order to achieve a highly accurate simulation, the mesh size has to be as small as possible. Another disadvantage is that the shape of the mesh is always rectangular, so it can struggle to model a curved shape like a sphere or a cylinder. Subpixel algorithms for material boundaries may be applied to overcome the 'staircasing' effect which can be observed when modelling curved surfaces [91, 92].

In the FDTD method, two of Maxwell's equations that involve taking the curl of magnetic and electric fields components (i.e.  $\nabla \times \vec{H}$  and  $\nabla \times \vec{E}$ ) are used as the basis for updating the relevant field equations.

The other two equations which involve taking the divergence of the field components, i.e. Gauss's law for magnetic and electric fields, are implemented implicitly by the choice of the grid used in the simulation, ensuring divergence-free conditions when no charge is present. For linear media, the relevant macroscopic Maxwell's equations are given by

$$\nabla \times \vec{H} = \vec{J}_e + \epsilon \frac{\partial \vec{E}}{\partial t}, \quad (3.6)$$

and

$$\nabla \times \vec{E} = \vec{J}_m - \mu \frac{\partial \vec{H}}{\partial t}. \quad (3.7)$$

The curl of the fields (e.g.  $\nabla \times \vec{E}$ ) can be expanded in terms of their partial-derivative components (e.g.  $\partial E_x / \partial y$  and  $\partial E_y / \partial z$ ). The partial derivatives are then replaced by finite-difference terms, for example,  $\partial E_x / \partial x = \Delta E_x / \Delta x$ . Rewriting Maxwell's equations in terms of coordinate vectors  $\hat{x}$ ,  $\hat{y}$ , and  $\hat{z}$ , these become

$$\frac{\Delta E_x}{\Delta t} = \frac{1}{\epsilon} \left( \frac{\Delta H_z}{\Delta y} - \frac{\Delta H_y}{\Delta z} - J_x \right) \quad (3.8a)$$

$$\frac{\Delta E_y}{\Delta t} = \frac{1}{\epsilon} \left( \frac{\Delta H_x}{\Delta z} - \frac{\Delta H_z}{\Delta x} - J_y \right) \quad (3.8b)$$

$$\frac{\Delta E_z}{\Delta t} = \frac{1}{\epsilon} \left( \frac{\Delta H_y}{\Delta x} - \frac{\Delta H_x}{\Delta y} - J_z \right) \quad (3.8c)$$

$$\frac{\Delta H_x}{\Delta t} = \frac{1}{\mu} \left( \frac{\Delta E_z}{\Delta y} - \frac{\Delta E_y}{\Delta z} \right) \quad (3.9a)$$

$$\frac{\Delta H_y}{\Delta t} = \frac{1}{\mu} \left( \frac{\Delta E_x}{\Delta z} - \frac{\Delta E_z}{\Delta x} \right) \quad (3.9b)$$

$$\frac{\Delta H_z}{\Delta t} = \frac{1}{\mu} \left( \frac{\Delta E_y}{\Delta x} - \frac{\Delta E_x}{\Delta y} \right) \quad (3.9c)$$

Equations 3.8(a-c) and 3.9(a-c) are the update equations for the FDTD method, which calculate each component of  $\vec{E}$  and  $\vec{H}$  as a function of time, with a time-step  $\Delta t$ , provided that the initial values of the  $\vec{E}$  and  $\vec{H}$  are known. In this form, the change of  $\vec{E}$  depends on the distribution of  $\vec{H}$ , and vice versa. The updates are performed in a leap-frog pattern,

where  $\vec{E}$  and  $\vec{H}$  are not updated at the same discrete time, but rather separated by a half time-step. A schematic of this process is shown in Figure 3.3. The field  $\vec{E}(t)$  is calculated to advance one time-step  $\Delta t$ , to obtain  $\vec{E}(t + \Delta t)$  from the distribution of magnetic fields  $\vec{H}(t + 0.5\Delta t)$ . Similarly, the next step is to obtain  $\vec{H}(t + 1.5\Delta t)$  from the distribution of  $\vec{E}(t + \Delta t)$  found previously. The algorithm repeats until the simulation is terminated. The equations above are used for the three-dimensional (3D) simulation of the electromagnetic wave and its interaction with the sample. A simplified two-dimensional version can also be derived from the equations, by describing the fields in terms of their in-plane and out-of-plane components [33].

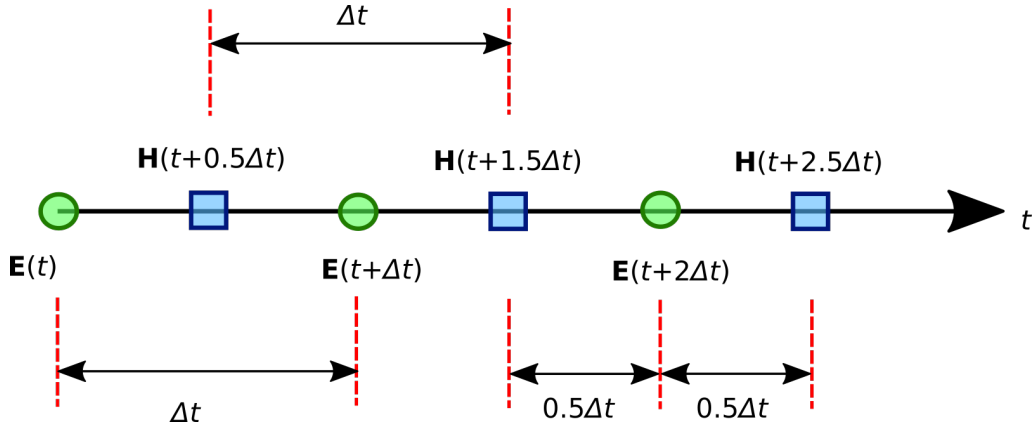


**Figure 3.3:** Updating scheme of the electric and magnetic fields as a function of time based on Yee algorithm.

To calculate the finite difference terms from the field distributions  $\vec{E}(\vec{r})$  and  $\vec{H}(\vec{r})$ , the field nodes are arranged in a particular way in each cell of the rectangular grids. This is referred to as Yee cell, which calculates the finite-difference via second-order central-difference. Figure 3.4 shows the arrangement of the field nodes in a Yee cell within a rectangular cuboid shape. The electric and magnetic field components are not placed at the same location, but instead are spread out in a staggered arrangement. The electric field components are placed at the edges of the cuboid, parallel to the edges, and the magnetic components at the faces of the cuboid perpendicular to the faces.

In applying the Yee algorithm, one example is given in Figure 3.5 for updating  $H_z(t)$ , which is the top face of the Yee cell in Fig. 3.4. From

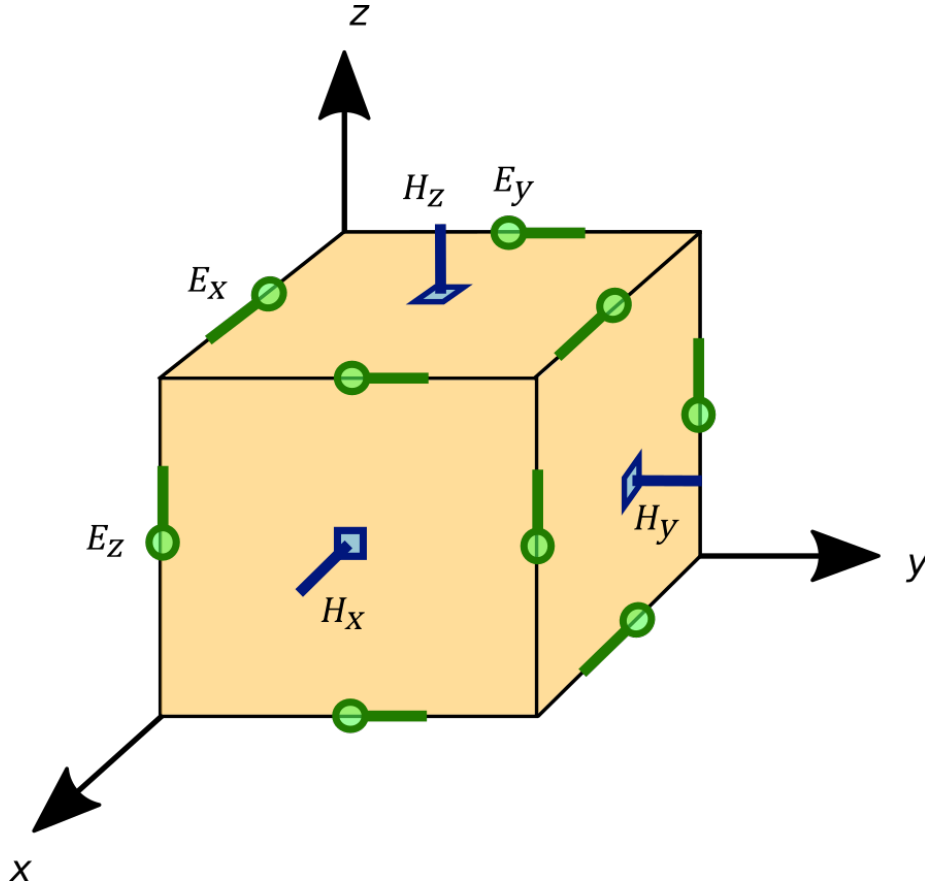


**Figure 3.4:** Arrangement of the electric and magnetic field nodes on the FDTD unit cell, based on Yee algorithm.

Eq. 3.9c, two adjacent pairs of  $E_{x1}$  and  $E_{x2}$ , also  $E_{y1}$  and  $E_{y2}$ , are used for calculating  $\Delta E_x = E_{x2} - E_{x1}$  and  $\Delta E_y = E_{y2} - E_{y1}$ . The future value for  $H_z$  can then be calculated from  $\Delta H_z(t)$ . The rest of field nodes are calculated in the same manner. This includes updating the electric fields which involves two pair of adjacent  $\vec{H}$  components. To visualise this, the Yee cell can be shifted by a half spatial-step in every direction, which leads to the locations of the electric and magnetic fields on the cell being swapped, where the electric field nodes are now at the faces and the magnetic field at the edges of the cell (e.g.  $H_z$  becomes  $E_z$  and  $E_x$  becomes  $H_x$  in Fig. 3.4).

Because the algorithm has to calculate the change in the electromagnetic field as a function of time, the time-step cannot be made too large because of the limitation caused by the speed of light,  $c$ . The time step

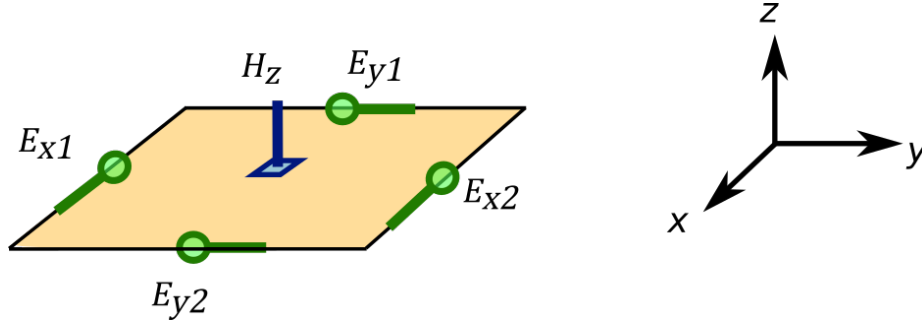


**Figure 3.5:** Closer look at the field nodes on the top face of Yee cell shown in Fig. 3.4.

has to be small enough to account for the electromagnetic field change between neighbouring nodes. The condition is called Courant-Friedrichs-Lewy (CFL) condition, which is given by

$$\Delta t \leq \Delta t_{max} = \frac{1}{c \sqrt{\frac{1}{\Delta x^2} + \frac{1}{\Delta y^2} + \frac{1}{\Delta z^2}}}, \quad (3.10)$$

This condition practically limits the time step  $\Delta t$  that can be used in relation to the mesh size employed for the simulation. The most accurate representation is achieved using the smallest possible mesh size however, in practice, a finer mesh impacts the smallest possible time step and consequently the number of iterations required for the FDTD algorithm to achieve convergence. The increase in the number of data points associated with finer mesh grids increases the amount of computer memory and the processing time required. The simulations presented in this thesis were optimised to provide a fine enough mesh that the essential features of the model could be reproduced while maintaining a reasonable time-step given the computational resources that were available.

In addition to the mesh size, boundary conditions also play a major role in determining the accuracy of the model. Perfectly Matched Layers (PML) are commonly used in FDTD simulations to absorb the outgoing waves at the edges of the simulation, which is a feature of infinite boundary conditions. Several parameters, such as the number of layers, can affect the performance of the simulations and must be examined carefully to avoid numerical artifacts being introduced in the calculation.

### 3.3.2 Components of the FDTD Simulation

By utilising the Yee algorithm discussed Section 3.3.1, the electromagnetic wave propagation can be determined. Figure 3.6 shows an example of a typical set-up of the FDTD simulation which includes one or more objects, generated EM source, boundary conditions at the edges of the simulation region, and detectors to record the EM fields at particular positions. The screenshot was taken from the Lumerical FDTD software [93], which is a commercially available software for electromagnetic simulation based on the FDTD method.

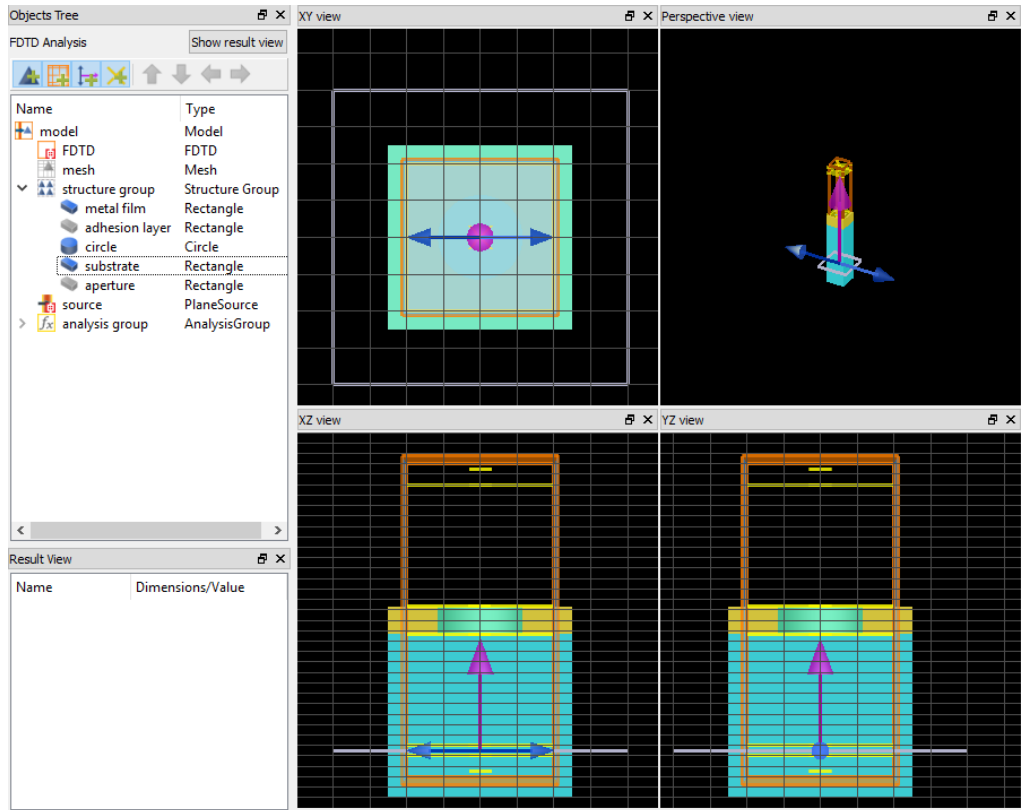


**Figure 3.6:** Overview of the Lumerical FDTD software interface.

In Fig. 3.6, there are several objects shown. There is a metal film (yellow), with a circular aperture in it (bright green), which rests on the top of a glass substrate (light blue). Materials are assigned in all cells where these objects are located. Each cell has a single value of  $\epsilon$  and  $\mu$  which determines what material in that cell. Many naturally-occurring materials are nonmagnetic, and their relative permeability is  $\mu = 1$ . In

this case, the relative permittivity  $\varepsilon$  can be obtained from the refractive index  $n$ , according to

$$\varepsilon = n^2 \quad (3.11)$$

which is valid for most dielectric materials. In contrast, metals are very dispersive and their refractive indices vary greatly over a small range of frequencies or wavelengths. In order to assign metal as the material of a cell, an additional algorithm is needed. In addition to the  $\varepsilon$  and  $\mu$ , the term current density  $\vec{J}_e$  in Eq. 3.6 needs to be calculated to account for the induced electrical current in the metal. The Drude model is one of the methods used to model the metal behaviour in the FDTD simulation. For a more accurate description of metals in the simulation, the Drude model can be modified with extra terms. The Drude-Lorentz model [94] and Drude-critical points model [95] are modified forms of the Drude model, extending the validity of the model to a higher frequency range in the violet region. Every metals have a different set of fit-parameters to satisfy the  $n(\omega)$  in a certain range of frequencies or wavelengths.

The simulation region has a finite size, it cannot be made too large due to computer memory restrictions. Often that the EM waves propagate to infinity after interacting with the object inside the simulation. The absorbing boundary condition (BC) needs to be applied at the simulation boundaries in all directions. This will absorb the outgoing waves so that they do not reflect back into the simulation region. An advance absorbing boundary condition to model the infinite boundaries is called PML. PML can absorb any wave propagating towards the simulation boundaries at any angle with minimal reflection and is very widely used in the FDTD simulation. An alternative to the PML BC is the periodic BC, if the structure is periodic. This only enables a unit cell of periodic structures to be simulated. The mirror BC can also be used if the structure is symmetric, allowing the simulation size to be reduced to half of its original size for each direction it is applied.

In this study, PML boundary conditions were used to simulate the scattered waves propagating to infinity. For monitoring, two point detectors were placed at two different locations near the boundaries opposite to each other and aligned with the incident wave propagation axis. The EM intensity measured by each of these detectors tends to zero as the



simulation progresses. Symmetric BC were also applied to further reduce simulation time since the characterisation samples used here had a varying degrees of symmetry.

The EM source is an important component of the FDTD simulation. The source can be a point source, which generates EM fields from one specific location in the simulation. The source can also be a plane wave, generated from a plane. An alternative EM source is generated by using the TFSF (total-field/ scattered-field) boundaries. With this method, the simulation region is divided into two regions, the total-field region and the scattered-field region. The total-field region is usually an enclosed space situated within the middle of the simulation. The source is only present inside the box, and the boundaries subtract the incident EM field from the total field. This causes the field existing outside of the boundary to be the scattered field from the object inside the total-field region. A focussed beam can be generated using a Gaussian source defined by the parameters of the beam waist size and the focussing angle.

The EM source in the simulation can be monochromatic (composed of a single wavelength) or broadband (composed of multiple wavelengths). Depending on the type of the source, the simulation is terminated according to different criteria. If a monochromatic source is used, the simulation is run until the steady-state condition is achieved, that is, until the magnitudes of the fields inside the simulation are unchanged (within a defined error range). For a broadband source, a pulse of electromagnetic waves composed of continuous frequencies is generated. The simulation terminates when the waves have left the simulation region. The spectra are then determined by using the Fourier transform. For consistency, a monochromatic source can also be simulated using a pulse source, and the Fourier transform is calculated only at the central wavelength of the source spectrum.

The final component is the detector which records the EM fields as a function of time. In the simulation, the algorithm calculates the propagation of the EM waves. Each node stores a new value of the field every time the update equation for that particular node is applied, the old value is overwritten by this new value to preserve the computer memory. The records of the EM fields are only calculated at specific locations, such as

on the planes above and below the metal film to calculate the transmittance and reflectance. Detectors can be placed at several locations, which stores changes in the EM fields during the simulation duration. During post-processing, the fields can be analysed, for example, by applying the Fourier transform to investigate the frequency response of the simulated objects.

### 3.4 Image Deconvolution using the Richardson-Lucy Algorithm

In this study, Richardson-Lucy deconvolution was performed to restore the degraded images produced by the SNOM system. This algorithm performs iterations of deconvolution on the degraded images using the known PSF. PSF describes the spreading of the intensity profile from a point source or object detected by the imaging device. In the case of SNOM, this is heavily influenced by the SNOM probe tip that is used for illuminating the sample, or for detecting the near-field intensity transmitted through the samples. With an accurate PSF, the image quality can potentially be improved by ameliorating the effects of the finite resolution of the imaging system.

The Richardson-Lucy algorithm was derived from Bayes's theorem and was named after William Richardson and Leon Lucy, who independently reported on the algorithm [6, 90]. Bayes's theorem relates the conditional probability of an event to a known prior knowledge of conditions that might be related to the event. In imaging, this correlates the probability of an original image, based on the known PSF that degrades the image, as described below.

Bayes's theorem is given by

$$P(u|v) = \frac{P(v|u)P(u)}{\int P(v|u)P(u)du} \quad (3.12)$$

where  $P(u)$  is the probability of an event  $u$ , and  $P(v|u)$  is the probability of an event  $v$ , provided an event  $u$ . On the other hand,  $P(u|v)$  is the inverse of the conditional probability of an event  $u$ , given  $y$ . In imaging,

$P(u)$  can be interpreted as the object distribution and  $P(v|u)$  as the PSF, centred at  $u$ , and  $P(v)$  as the degraded image. From here, the recursive algorithm is derived to determine the most likely original image, calculated from the degraded image, based on known PSF.

For the image  $f(x, y)$  and PSF  $g(x, y)$ , the  $(i + 1) - th$  iteration of the restored image using the Richardson-Lucy deconvolution is given by

$$f_{i+1}(x, y) = \left\{ \left[ \frac{c(x, y)}{[f_i(x, y) * g(x, y)]} \right] * g(-x, -y) \right\} f_i(x) \quad (3.13)$$

where  $*$  denotes the convolution operation,  $c(x, y)$  is the original degraded image, and  $g(-x, -y)$  is the mirrored PSF (against  $x$ - and  $y$ -axis).

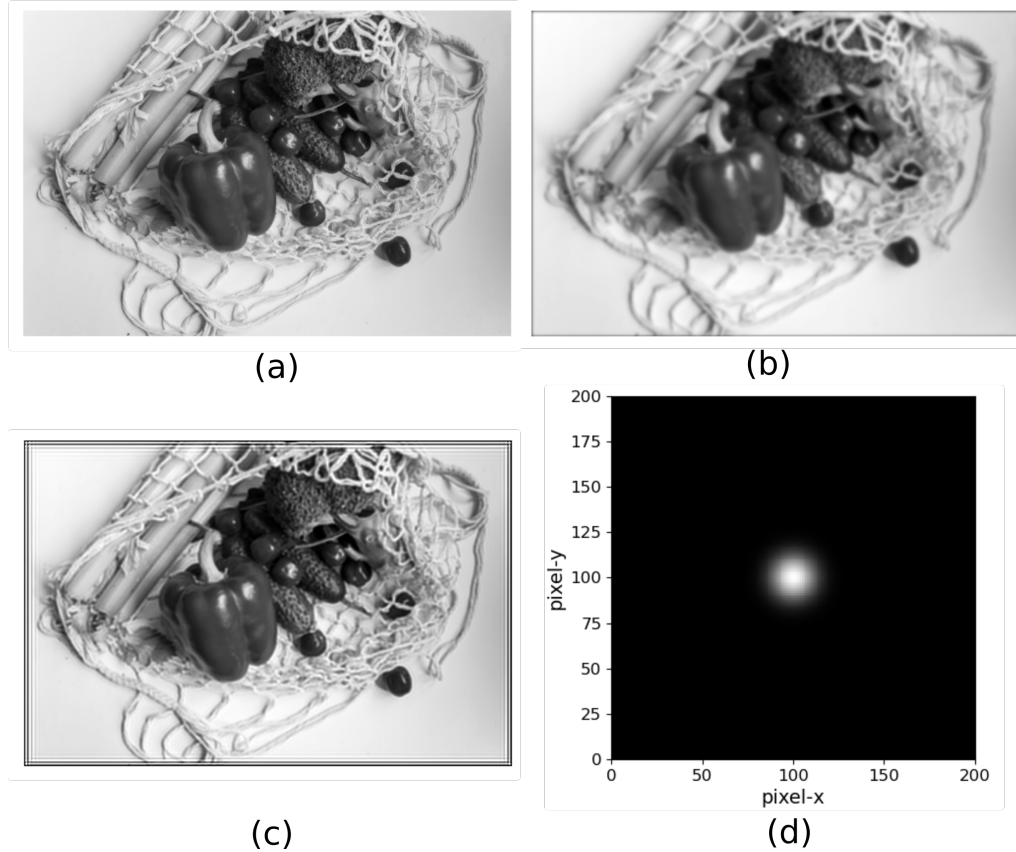


**Figure 3.7:** A demonstration of Richardson-Lucy algorithm to restore blurred image. (a) The original image, (b) the degraded image, (c) the restored image using the Richardson-Lucy algorithm, and (d) the Gaussian PSF used in this demonstration. Figure adapted from Ref. [96].

A demonstration of the Richardson-Lucy deconvolution algorithm is

shown below. An original image shown in Fig. 3.7(a), with the size of  $3000 \times 2000$  pixels, was convolved with a Gaussian PSF with a full-width at half-maximum of  $\text{FWHM} = 20$  pixel. Poisson noise is then applied to the image. The degraded image is shown in Fig. 3.7(b), as the image to be restored via the deconvolution algorithm. After applying the algorithm, the image was restored as shown in Fig. 3.7(c). The image shows that the algorithm was able to reverse the blurring effect due to convolution, resulting in a clearer and sharper image. The PSF used in this demonstration is shown in Fig. 3.7(d).

### 3.5 Chapter Summary

The methods used for the experimental and simulation work presented in this thesis have been discussed. The SNOM equipment was set-up in the collection mode, in which the near-field intensity was detected by the SNOM probe tip with the sample illuminated in the far-field. Averaging of the intensity profiles across one-dimensional structures was performed to improve the signal-to-noise ratio. A fitting function based on the linear combination of Gaussian and Lorentzian functions, called a pseudo-Voigt function, was used to analyse the intensity profiles.

The FDTD method is used as the basis for the simulation models developed and investigated in this study. This method rigorously calculates electromagnetic interactions between the objects in the simulation and the incident light. The method was derived from the fundamental Maxwell's equations, without any approximations or assumptions applied. This approach is suitable for the accurate calculation of the near-field intensity of an object measured by SNOM, and was used to investigate the influence of the SNOM probe tip in the image formation.

Finally, after the simulation models were developed and investigated, the quality resulting SNOM images may be further improved. This can be performed by using a deconvolution algorithm that restores the degraded image due to finite resolution of the imaging system, characterised by the PSF. Accurate knowledge of the PSF of the system can be utilised for the deconvolution process. The Richardson-Lucy algorithm was used in this study in order to carry out PSF deconvolution during

---

image post-processing. It is based on the Bayes's theorem and employs the recursive method to restore the degraded image to its original quality with higher resolution. The method was discussed and an example application for a blurred image was demonstrated.



## Chapter 4

# Simulation Model of the SNOM Imaging System

### 4.1 Introduction

In investigating image formation using SNOM, a suitable method must be selected for calculating the electromagnetic properties of the near-field optics. Kirchhoff diffraction theory is a classical approach for calculating the diffraction pattern of any object [46]. Due to the approximations involved in forming the boundary conditions, however, it is not valid within the near field region [97]. Kirchhoff diffraction theory is also mathematically inconsistent, as the assumed boundary conditions cannot be reproduced [46]. The Rayleigh-Sommerfeld theory of diffraction addresses this issue with more consistent mathematics, but its application is limited to apertures in plane screens [46].

Unfortunately, there is no simple analytical solution to the electromagnetic field problem in the near-field regime. The rigorous solution to the diffraction problem necessitates complex mathematics. A previous study investigated the solutions for light propagation through a circular aperture using vector diffraction theory with nonparaxial approximations [98]. This paper reported analytical solutions which are valid in the near-field regime. Further complexity is introduced when additional objects are involved in the problem.

Numerical methods such as the finite-element method (FEM) [99] and finite-difference time-domain (FDTD) method [33] were constructed based on Maxwell's equations, which are fundamental to electromagnetism. There are no approximations or assumptions involved in the calculation of the electromagnetic fields using these approaches, so they are suitable for use in solving problems in the near-field regime. The limitations of these numerical methods are in the discretization of the simulation and the accuracy of the model in terms of the material responses implemented in the algorithm. Finer resolution of the mesh used in the simulation can increase the accuracy of the simulations, but that also comes with higher requirements for computational resources (i.e. computer processing power and memory) and the time required to finish the calculation.

In this study, calculations of the electromagnetic fields within near-field zones were performed using the FDTD method. A brief summary of this method was provided in the previous chapter (Chapter 3, Section 3.3). This is an appropriate method for solving the electromagnetic problem in the near-field without requiring complex mathematical calculation. The formulation for calculating the electric and magnetic fields is available using the Yee algorithm.

In this chapter, simulation models based on the FDTD method were investigated, with two different types of models. One was the simulation without the SNOM probe tip involved, using a two-dimensional plane detector placed at a near-field distance from the sample to measure the intensity profiles. The other was the simulation model with the probe tip involved in the calculation, which is a more realistic approach. The simulation set-ups for these approaches are discussed, followed by the results produced using these simulation models. The models were investigated using well-characterised samples, consisting of apertures in a metal film in several configurations, a single isolated aperture and a pair of adjacent apertures. The shapes of the apertures being investigated were circular and slit apertures, which are discussed in detail in this chapter.

The simulation models discussed in this chapter are the fundamental components in this study, which focusses on the probe tip influence in the



SNOM imaging. With an appropriate simulation model, the characterisation of the probe tip can be performed and validated against experimental data, which is discussed in the next chapter (Chapter 5). Furthermore, knowledge of the SNOM probe tip was used for determining the PSF of the SNOM system. The PSF is used for deconvolution during post processing of the SNOM images, which is discussed in Chapter 6.

## 4.2 Simulation Model of Subwavelength Structures and SNOM Imaging

Subwavelength structures have been extensively studied in the field of nanophotonics. On the subwavelength scale, nanostructures exhibit specific interactions with incident light. The responses of these nanostructures depend on their shape, dimensions, as well as the materials they are made of. Nanostructures arranged in an array configuration exhibit local electromagnetic interactions between themselves. These interactions produce a modified bulk optical response with respect to the incident light, which is different to that of the original optical materials they are made from [100, 101].

In understanding the behaviour of a subwavelength structures, a careful investigation of their near-field interactions with the incident light needs to be performed. Various numerical approaches and methods are available for analysing these subwavelength structures, such as the FDTD, FEM, surface integral, volume integral, and hybrid methods [102]. The FDTD method is a widely used method for investigating nanostructures due to its robustness and flexibility. Objects of any shape composed of any material can be modelled with a proper set of simulation parameters, material libraries, and appropriate boundary conditions.

The experimental observation of subwavelength structures is restricted by the diffraction limit. As described previously (Chapter 2), SNOM is one of the microscopy methods that allows the observation of near-field signals with very high spatial resolution. The presence of the probe tip at a very close distance to the sample surface, however, induces modifications to the electromagnetic properties of the subwavelength structures

being examined. The extent to which the presence of the probe impacts SNOM image formation is still an open question [5].

In this section, simulation models based on the FDTD method are described to investigate several subwavelength structures including circular and slit apertures. These structures have been widely studied in the literature [103–107] and are suitable as characterisation samples for testing the accuracy of the simulation models.

The simulations were performed using commercially available FDTD software from Lumerical [93]. The software release version used in this study was 2017b and 2020a. The software was running on a desktop computer with Intel Xeon CPU E5-1650 v4 @3.60 Hz (6 cores and 12 threads) and 128 GB of RAM. Depending on the size of the simulation and the mesh resolution, a single simulation typically runs for 5 to 20 minutes. For a set of simulations involving a probe scan on a single line involving 10 to 25 points, this typically takes 1 to 4 hours of running time.

#### 4.2.1 Simulation Model with Two-Dimensional Plane Detectors

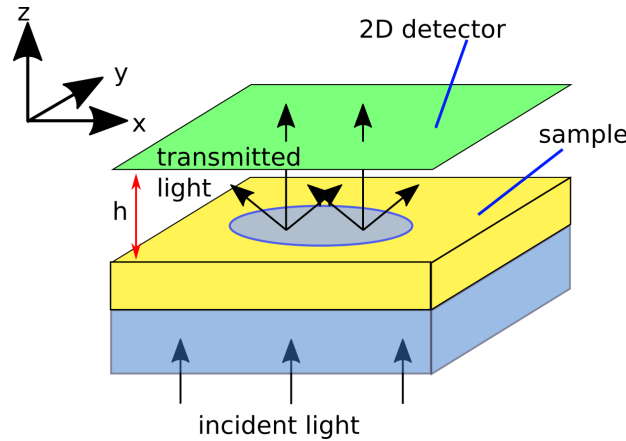


**Figure 4.1:** Schematic of simulation model with a 2D plane detector, without the probe. The detector is placed at a near-field distance  $h$ .

The most common set-up for characterising subwavelength structures is to use a simple plane detector [15, 16, 32]. In the FDTD model, a two-dimensional (2D) plane detector is placed at a very close distance to the

sample surface. In this set-up, the detector records the near-field electromagnetic fields which can then be analysed further. Figure 4.1 shows the simulation model with a plane detector. The detector is placed at a distance  $h$  from the surface of the sample. The light illuminates the sample from the bottom side and the transmitted light through the sample is detected by the 2D plane detector.

In the simulation, the 2D plane detector is a nonphysical object and it only records the electromagnetic fields at a specified plane. It does not interact with the existing electromagnetic fields which are generated by the object, which is in direct contrast to when the near-field signal is measured using an optical probe. The electromagnetic waves propagate through the detector plane as if there is no physical interface or boundary disturbing the waves. The detector records the electromagnetic fields on the plane as a function of time. Signal processing with the Fourier Transform allows the detector to convert the recorded signal into a function of frequency (or wavelength).

#### 4.2.2 Simulation Model with the Probe Tip Included

The second type of simulation model studied here is the one with the probe tip included. It is flexible enough to include any object in the FDTD simulation if the material libraries are available for the objects. For example, the electric permittivities of gold and silver are readily available in the literature [108, 109] and can be implemented in the FDTD method using the standard Drude model [33]. The Drude model is, however, not valid at shorter wavelengths, above a certain frequency limit of the incident light due to the interband transitions of the electrons. Therefore, some modifications to the Drude model may also be applied for more accurate modelling of these materials [94, 95].

For modelling the image formation, the SNOM probe tip can be easily included in the simulation, but its model must be carefully designed. The SNOM probe tip is made from a tapered optical fibre, with a very sharp tip at the end, coated with metal layers. The size of the simulation region is on the order of a few micrometres for objects or nanostructures with the size of a few hundreds of nanometres. A simplified model of the probe

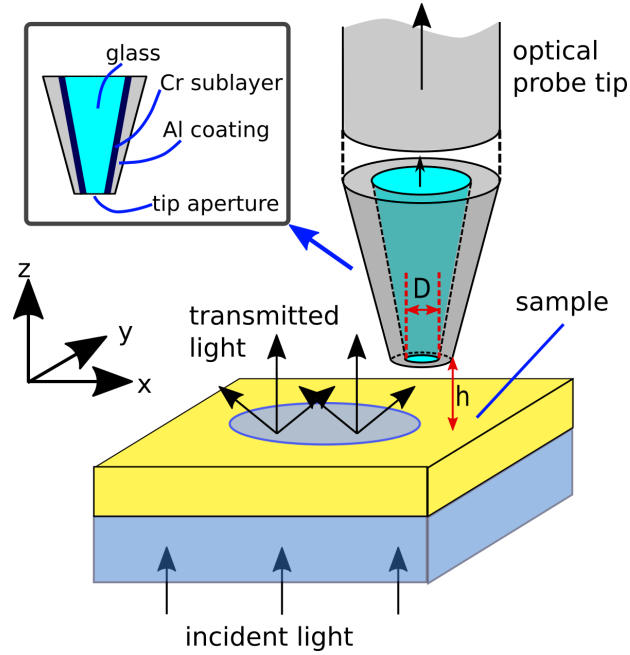


**Figure 4.2:** Schematic of simulation model with the probe tip included. The set up scans the sample at a near-field distance  $h$ , with a tip aperture diameter  $D$ . Inset: lateral section of probe tip, showing the probe materials.

tip was used for the simulation, which only included a few micrometres of the tip, with the probe extended outside of the simulation boundary.

The tip is modelled as concentric truncated cones with a glass core ( $n = 1.50$ ), enclosed in metallic coatings made of Cr and Al layers, as shown in the inset of Fig. 4.2. With this configuration, the cross-section of the tip aperture is circular with a diameter of  $D$ . The tip of the probe is located at the height or distance  $h$  from the sample surface. The speed of the probe movement during a SNOM scan is much less than the speed of light, so in the modelling, the intensity collected by the probe was calculated only at one certain position  $(x, y)$  with respect to the sample, in a single simulation. To model how the SNOM probe tip scans the sample, a systematic repetition of the simulations was performed to collect the signal as a function of position  $(x, y)$ , and this created a set of simulations with the probe placed at different positions. The whole set of simulations contains the image of the sample measured using SNOM.

As seen in Fig. 4.2, the structure was illuminated from the bottom side and the transmitted light was detected by the probe tip located above the

sample surface. In calculating the light detection by the probe, it was assumed that the probe tip behaves like a waveguide with a truncated conic shape. The transmission power is calculated at the tip aperture and it was assumed that all optical signals are transferred through the optical fibre to the PMT for detection.

The time-averaged power  $P$  transmitted into the optical probe was calculated by integrating the Poynting vector over the probe tip aperture area  $A$ , which is given by

$$P = \int_A \text{Re}(\vec{S}) \cdot d\vec{A}, \quad (4.1)$$

where  $\vec{S} = \frac{1}{2}(\vec{E} \times \vec{H}^*)$ , is the complex Poynting vector.

After repetition of the simulations was completed, the transmitted power detected by the probe (and hence the PMT) can be described as  $P(x, y)$  which forms the image of the scanned sample. The intensity  $I(x, y)$  is proportional to the power detected by the probe,

$$I(x, y) = \frac{P(x, y)}{A_{\text{detector}}} \quad (4.2)$$

where  $A_{\text{detector}}$  is the surface area of the detector (PMT). Hence, in arbitrary units, the two terms  $I$  and  $P$  are equivalent. The image is described as the intensity profile detected by the probe tip as a function of the probe tip position. A scan over a finite sample area represents the resulting SNOM scan image.

## 4.3 Simulation without the Probe Tip

### 4.3.1 Transmission Spectra of Periodic Structures

Before creating a simulation model of SNOM imaging, the simulation results from previously published literature were investigated. This to ensure that the model used in this study is correct and accurate. Arrays of circular apertures and slit apertures (or gratings) were investigated for a broadband light source. The transmission spectra of the structures

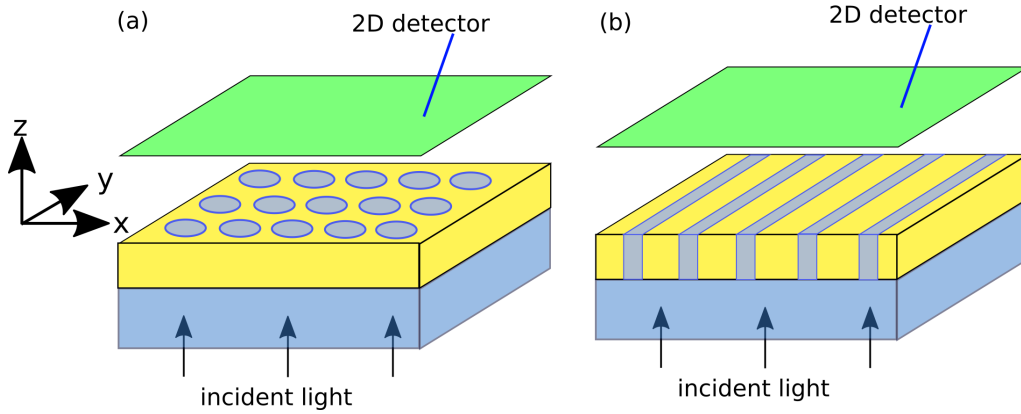


**Figure 4.3:** Schematic of simulations for calculating the transmittance through an array of (a) circular apertures and (b) slit apertures using a 2D plane detector.

were calculated and compared with the experiments. Data were taken from Refs. [110] and [111].

Figure 4.3 shows the schematic of the simulations described in this section. The simulations included either a 2D array of circular apertures or a 1D array of slit apertures. Both simulations were performed and the transmittance through the periodic structures were calculated. Periodic boundary conditions were applied in the direction parallel to the sample, perpendicular to the incident light.

Figures 4.4 and 4.5 show the transmission spectra of an array of circular apertures in various different metal films. A broadband source was used with a wavelength range of 400 nm to 900 nm. The reference spectra were taken from [110], which were also produced using FDTD simulations.

The simulations were tested with different mesh sizes. With a coarse mesh of 10 nm, the features from the spectra were successfully reproduced, although with a slight redshift compared to the spectra from the literature. A finer mesh of 2 nm was then used and the transmittance spectra were able to be reproduced with better accuracy, particularly for gold and aluminium films. The trend was the opposite for the silver film, with the result from the simulation with coarser mesh producing a better fit. The discrepancies potentially due to the different fitting parameters used for the metals and the algorithm implementing them in the simulation, and other fine-tuning details of the simulations. These results

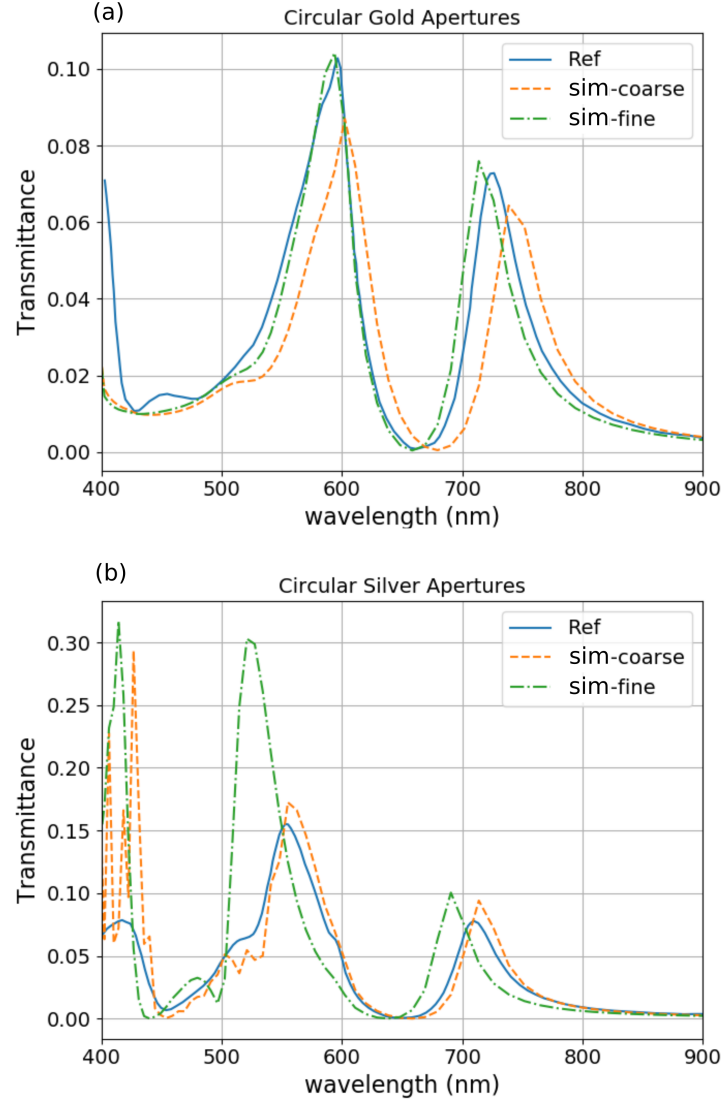


**Figure 4.4:** The transmittance through an array of circular apertures with a periodicity of  $p = 400$  nm and a 250 nm-thick metal film made from (a) gold and (b) silver. The aperture diameter was  $d = p/1.75$ . The reference (Ref) data was taken from [110], with simulated data generated using the simulation (sim), with coarse (10 nm) and fine (2 nm) meshes.

showed that the FDTD model was correct and valid. From here on, the simulation model was modified via the addition of an optical probe and 2D detectors for the analysis of SNOM imaging.

To further verify the simulation, the results using a different method were also used for comparison, shown in Fig. 4.6. The structures were periodic slit apertures with a width of 50 nm and periodicity 600 nm, with

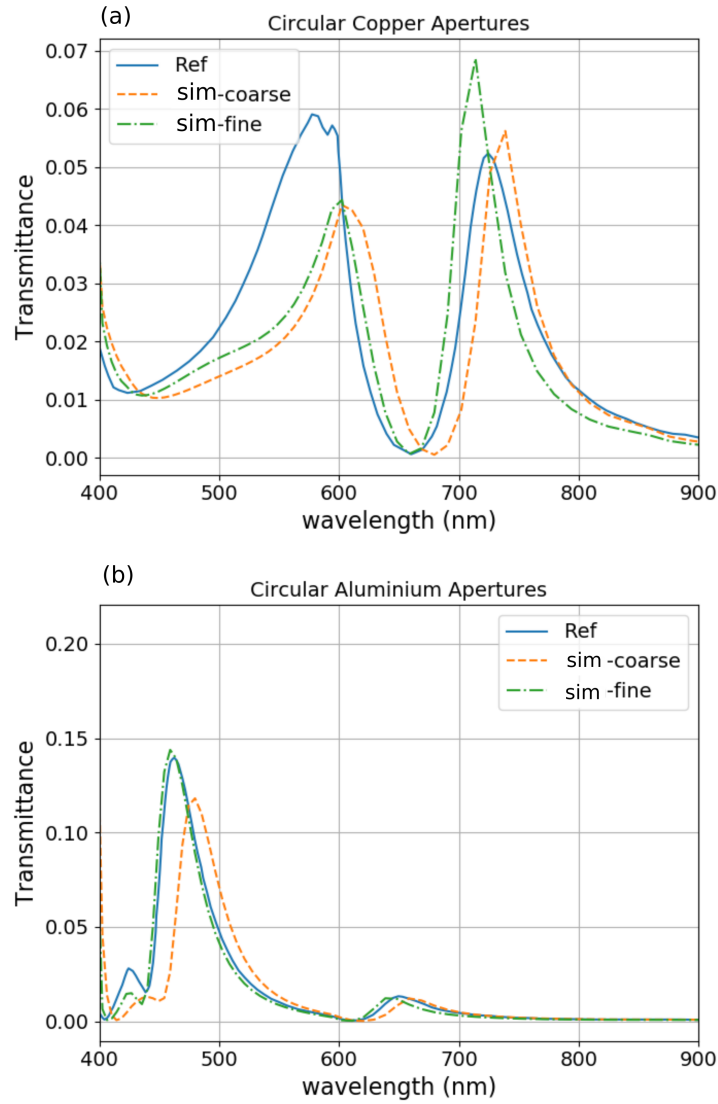


**Figure 4.5:** The transmittance through an array of circular apertures with the same configuration as in Fig. 4.4, but the metal film was made from (a) copper and (b) aluminium [110], showing the reference (Ref) data from the literature and simulated data using the FDTD (sim).

varying metal film thickness. The reference used a rigorous coupled-wave analysis method (RWCA) to calculate the transmittance through the slits [111]. The reproduced transmittance spectra are redshifted when using the coarse mesh. The discrepancies were reduced when the mesh resolution was improved to 2 nm. This is the expected outcome, i.e. that finer mesh gives better accuracy. The optimum value, in terms of mesh resolution, used throughout this study was 5 nm as the minimum mesh



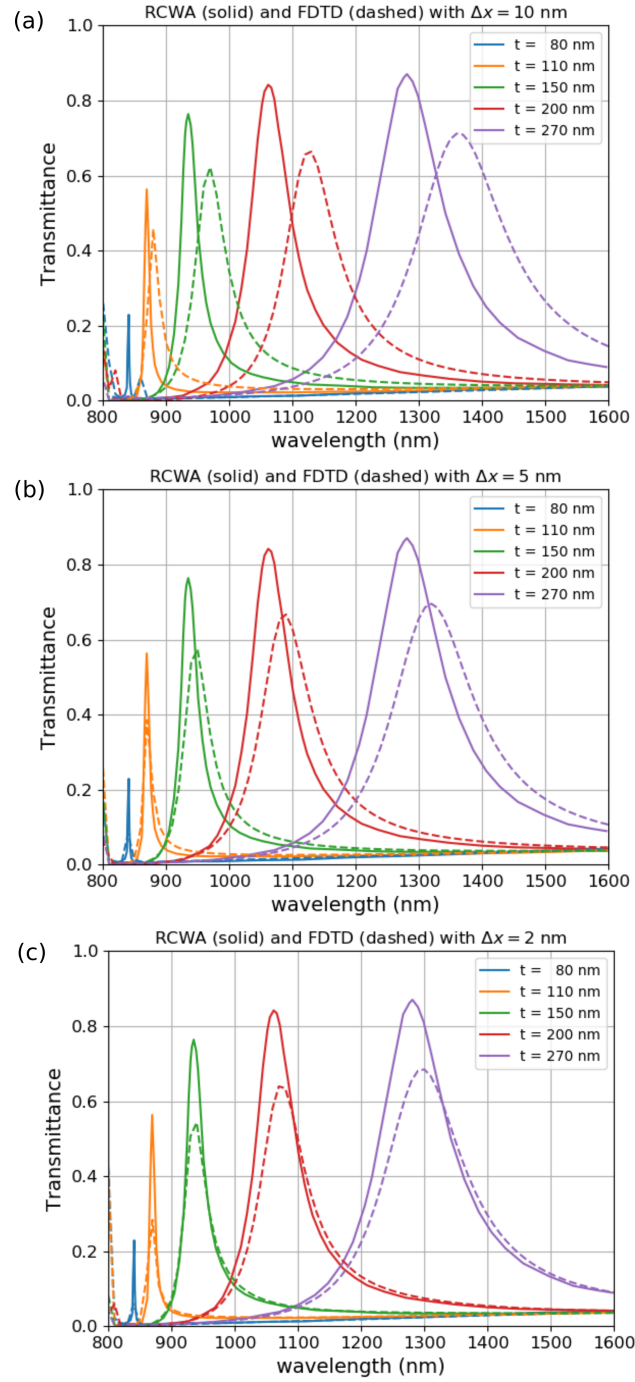


**Figure 4.6:** The transmittance through an array of slit apertures in a metal film with various thickness  $t$  using the RCWA method (solid lines) [111]. Data was reproduced using the FDTD simulations (dashed lines) with (a) coarse mesh of 10 nm, (b) medium mesh of 5 nm, and (c) fine mesh of 2 nm.

size in order to accurately describe the objects involved in the simulation, while also not being too slow or computationally demanding.

### 4.3.2 Near-field Images of Apertures

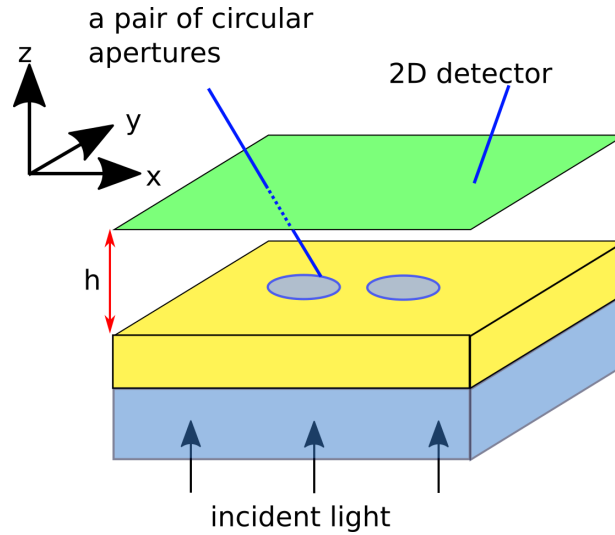


**Figure 4.7:** Schematic of the simulation for calculating the near-field intensity profile of adjacent objects in the form of a pair of circular apertures. The profile was detected using a 2D plane detector, placed at a height  $h$  from the sample, without including the probe tip.

One of the purposes of using SNOM is its ability to produce high spatial resolution images [8, 9]. One way to characterise this is by using SNOM to scan two adjacent objects separated at a very close distance. The resulting image obtained from the scan is then analysed to characterise their visibility and to determine if the objects are resolved. Two subwavelength circular apertures with a subwavelength gap between them were investigated. The simulations used a 2D detector to image the objects at a near-field distance.

Figure 4.7 shows the schematic of the simulations using a 2D plane detector. The simulation was performed without involving the probe tip in the calculation, to measure the intensity profile of two adjacent objects.

Figures 4.8, 4.9, and 4.10 show the near-field intensity profiles of two adjacent circular apertures with different separations. For a very small gap of 50 nm (Fig. 4.8), the simulation predicted that the two apertures

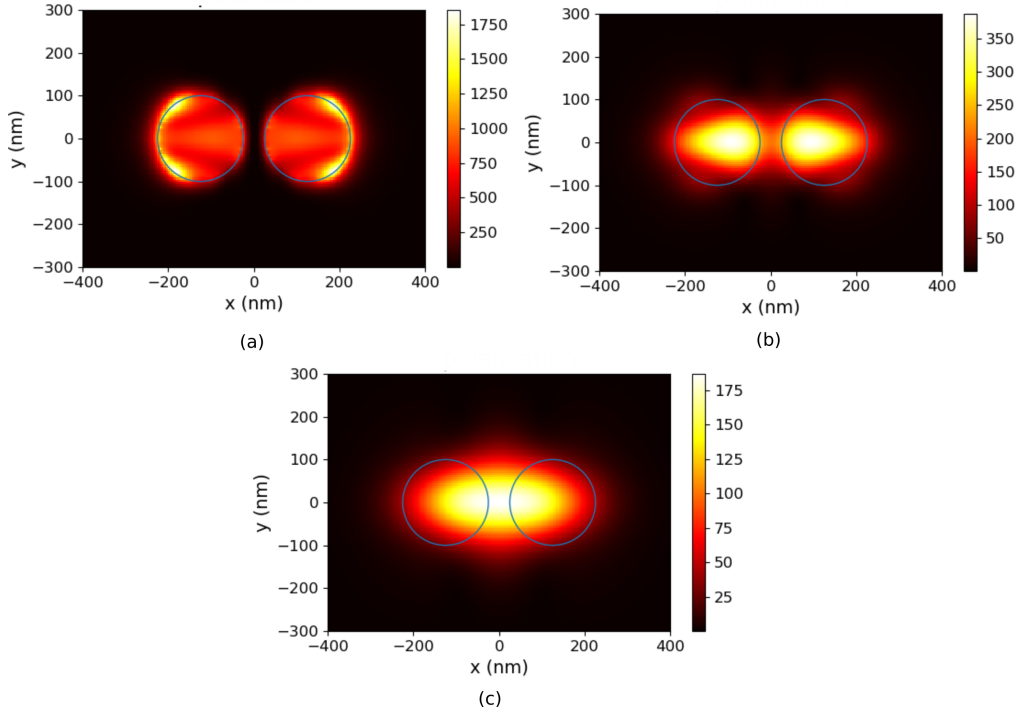
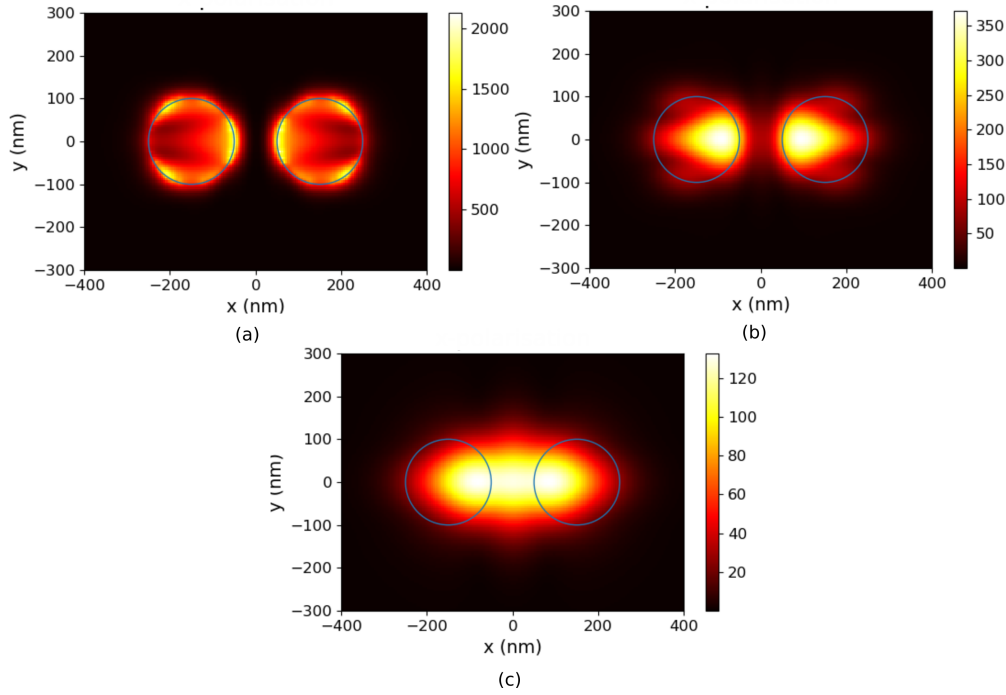


**Figure 4.8:** Intensity profiles of a pair of circular apertures with  $d = 200$  nm and  $s = 50$  nm at a distance of (a) 10 nm, (b) 50 nm, and (c) 100 nm, using simulations incorporating a 2D detector. The locations of the apertures are annotated with blue circles.

will be resolved clearly at  $h = 10$  nm with two circular bright spots observed. At a larger distance,  $h = 50$  nm, the shapes are no longer circular, but can still be clearly resolved. At  $h = 100$  nm, however, the two objects were no longer separable and merged into one peak.

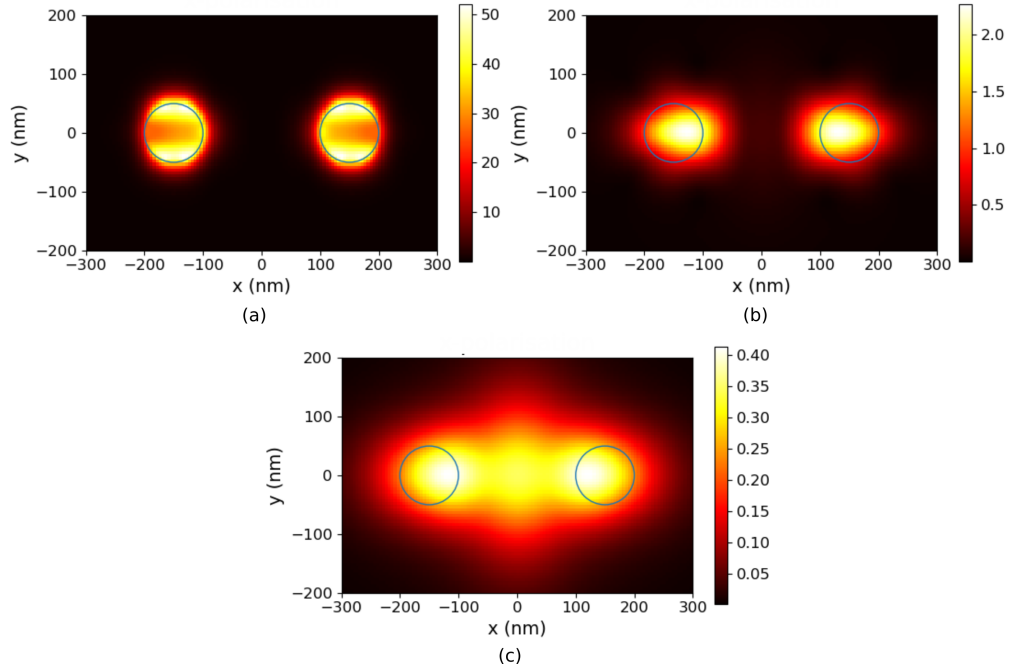
The results for a larger gap of 100 nm are shown in Fig. 4.9 are similar to the gap of 50 nm. At  $h = 10$  nm, the two peaks are clearly resolved. At  $h = 50$  nm, the objects were better resolved compared to those for the 50 nm gap. At  $h = 100$  nm, the two objects were still not resolved despite having a larger gap or separation between them.

Figure 4.10 shows the result for the largest gap  $s = 200$  nm with smaller apertures  $d = 100$  nm. The centre-to-centre distance is the same as that in Fig. 4.9, which is 400 nm. For  $h = 10$  nm and 50 nm there are no issues with resolving the objects. At  $h = 100$  nm, the peaks are blurry but they did not merge into a single intensity peak, although the gap in between them was not clearly defined.



**Figure 4.9:** Intensity profiles of a pair of circular apertures with  $d = 200$  nm and  $s = 100$  nm at a distance of (a) 10 nm, (b) 50 nm, and (c) 100 nm, obtained from the simulations with 2D plane detector. The locations of the apertures are indicated by blue circles.

In conclusion, the simulation model without the probe tip was demonstrated by using a 2D plane detector for recording the near-field intensity profiles of the apertures in a metal film. The simulation model was confirmed to be correct by looking at the transmittance through an array of circular and slit apertures and comparing it with data from the literature. The intensity profiles of adjacent circular apertures were calculated using this simulation model. The intensity profiles were observed to be sensitive to the height or distance of the 2D detector from the sample surface.



**Figure 4.10:** Intensity profiles of a pair of circular apertures with  $d = 100$  nm and  $s = 200$  nm at a distance of (a) 10 nm, (b) 50 nm, and (c) 100 nm, obtained from simulations using a 2D plane detector. The locations of the apertures are indicated by blue circles.

## 4.4 Simulation including the Probe Tip

### 4.4.1 Snapshots of Intensity Profiles

Since the probe tip is a physical object placed at a very close distance to the sample being observed/investigated, its presence can effect the overall intensity distribution of the sample. There will be electromagnetic interactions between the sample and the probe tip which can cause discrepancies compared to the results from the simulation model without the probe tip included. Figure 4.11(a) shows the intensity profile at a height of 50 nm from the sample when the probe is not included in the simulation. The sample was a circular aperture with  $d = 200$  nm. In Fig. 4.11(b), the probe was located right above the aperture. As can be seen from the images, the intensity profile is affected by the presence of the probe. The intensity profile appears more concentrated near the aperture when the probe is present. This shows a strong interaction between

the probe and the object when the probe is scanning over the object or sample.

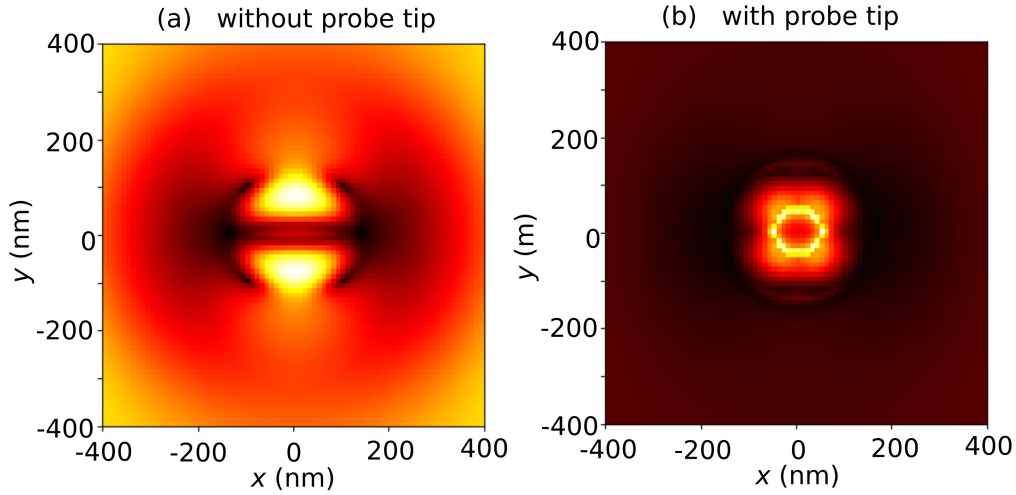


**Figure 4.11:** (a) Intensity profile at  $h = 50$  nm from the sample, generated from the simulation without the probe. (b) Intensity profile at the tip of the probe, at a distance  $h = 50$  nm from the sample, generated from the simulation with the probe.

#### 4.4.2 Absorption by the Nanostructure

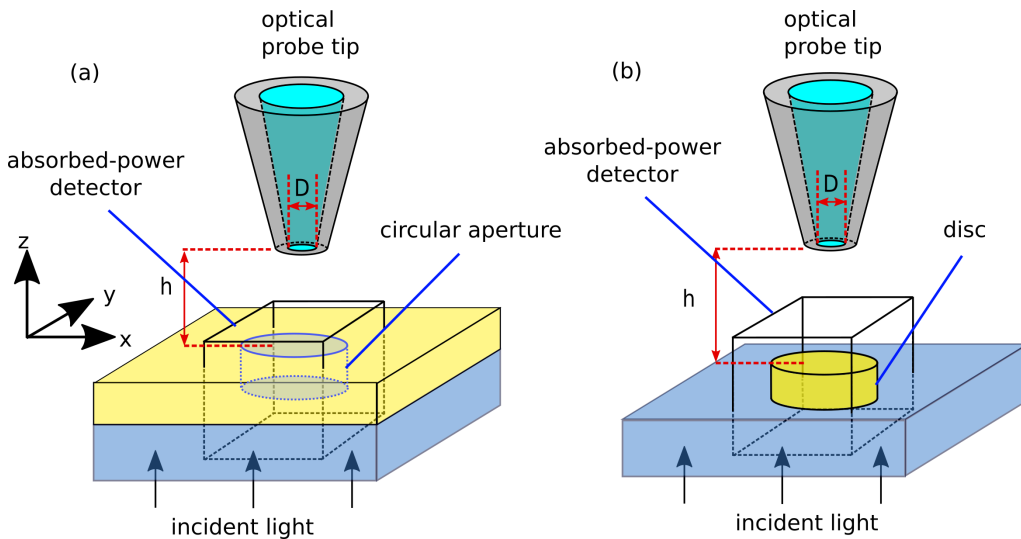


**Figure 4.12:** Schematic illustrating calculations of the absorption using a detector enclosing the object for (a) a circular aperture in a gold film and (b) a disc on a glass substrate.

The probe tip interaction with the object can affect the resulting SNOM image. To investigate this further, the absorption of an object due to the presence of the probe tip was calculated. The test object used for this was a circular aperture in a gold film. The schematic for this simulation is shown in Fig. 4.12(a) for the circular aperture sample. The aperture was illuminated using a plane wave, and was enclosed in a box with all 6 faces being 2D detectors. This set of detectors is used for calculating the absorbed power by the structure, by measuring the amount of power exiting the box. If the net power from all 6 faces is negative, that means the power is going into the box, or in other words, the power is absorbed by the object inside the box.

The absorption of the circular aperture as a function of probe tip height is shown in Fig. 4.13. There are small discrepancies in the absorption due to the presence of the probe tip. In the zoomed-in version of the spectra (Fig. 4.13(b)), the absorption is not a monotonically varying function of height. At a probe tip height of less than 100 nm, the object absorbs less power than when there is no probe present. The absorption increases between  $h = 150$  nm and 200 nm. The simulation condition where there is no probe tip can be viewed as the probe being located at an extremely large distance from the sample, so that absorption will eventually decrease again as the probe tip height increases.

Larger changes in the absorption can be observed with a circular disc used as an object instead of a circular aperture, with the corresponding schematic shown in Fig. 4.12(b). A circular disc with the same diameter as the circular aperture above, was illuminated using the same range of wavelengths. The results are shown in Fig. 4.14. With varying height, the absorption spectra indicate that the absorption is mostly higher compared to when no probe tip is present, with the exception being when  $h = 10$  nm. Focusing on the red part of the spectrum between wavelengths of 600 nm to 700 nm, shown in Fig. 4.14(b), the presence of the probe tip causes the sample to exhibit a higher absorption when the probe tip height is 50 nm or more above the sample. These changes in the absorption by the object confirm that the presence of the probe tip near the sample surface modifies the electromagnetic fields in the near-field.

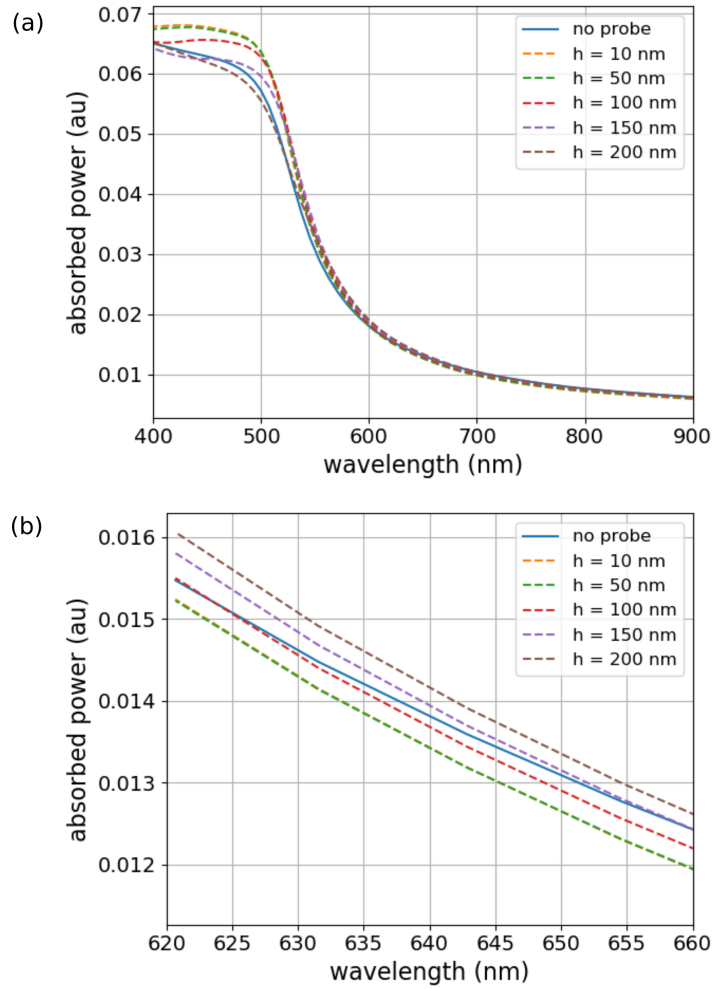


**Figure 4.13:** The absorbed power by a circular aperture with  $d = 200$  nm and film thickness  $200$  nm using a probe tip with  $D = 100$  nm at various tip distances  $h$  from the aperture. (a) The absorption spectra in the wavelength range  $\lambda = 400$  nm to  $\lambda = 900$  nm and (b) zoomed-in version in the range  $\lambda = 620$  nm to  $\lambda = 660$  nm.

#### 4.4.3 Intensity Profiles of a Single Object

Schematics of simulations with the probe tip included for calculating the intensity profiles of a single object are shown in Fig. 4.15. The figure shows two different types of apertures; a single circular aperture and a single-slit aperture being used as test samples. The probe tip moves as a function of position  $(x, y)$  in the simulation, with each position treated as a single simulation. Multiple simulations were performed with different probe positions to obtain the whole scanned image.



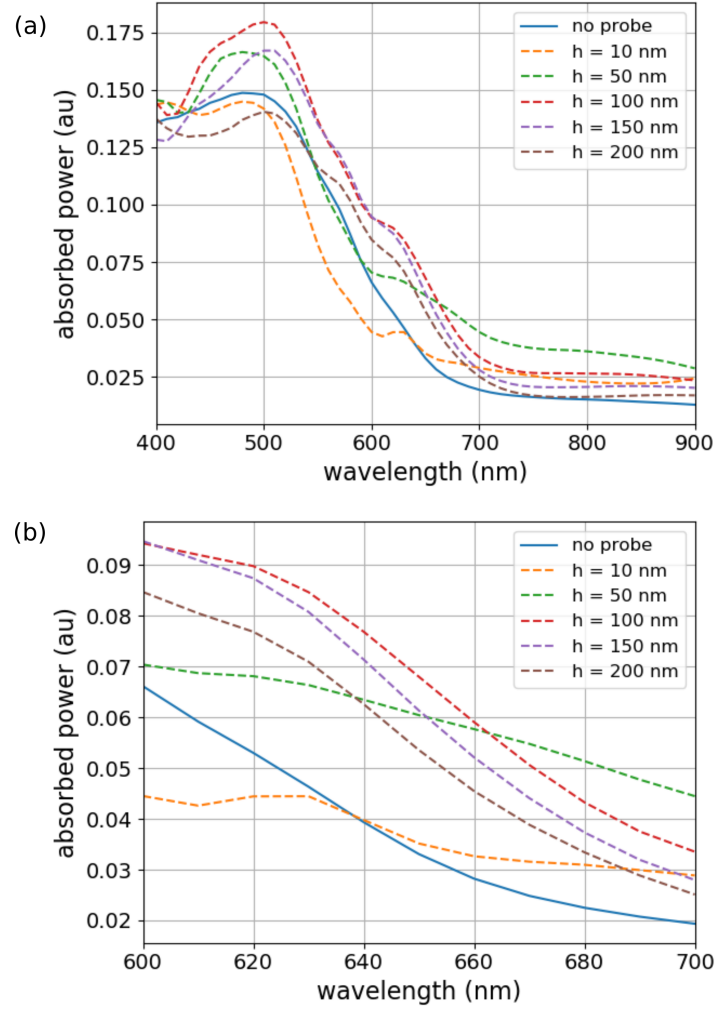


**Figure 4.14:** The absorbed power by the disc with  $d = 200$  nm and thickness 200 nm using a probe tip of size of  $D = 100$  nm located at a distance  $h$  from the top surface of the disc. (a) The absorption spectra in the wavelength range of  $\lambda = 400$  nm to  $\lambda = 900$  nm and (b) zoomed-in version in the range of  $\lambda = 600$  nm to  $\lambda = 700$  nm.

The first sample is a circular aperture as shown in Fig. 4.15(a). A complete image was determined with a full 2D raster scan, but it took a considerable amount of time to finish (8 to 24 hours). First, the demonstration of the simulation with the probe tip was performed on a single line scan through the centre of the circular aperture. Later, full 2D scans of the sample were also performed in addition to the single line scan results. The incident light had a wavelength of 640 nm (which was later used in the experiment) and the polarisation was parallel to the  $x$ -axis. In

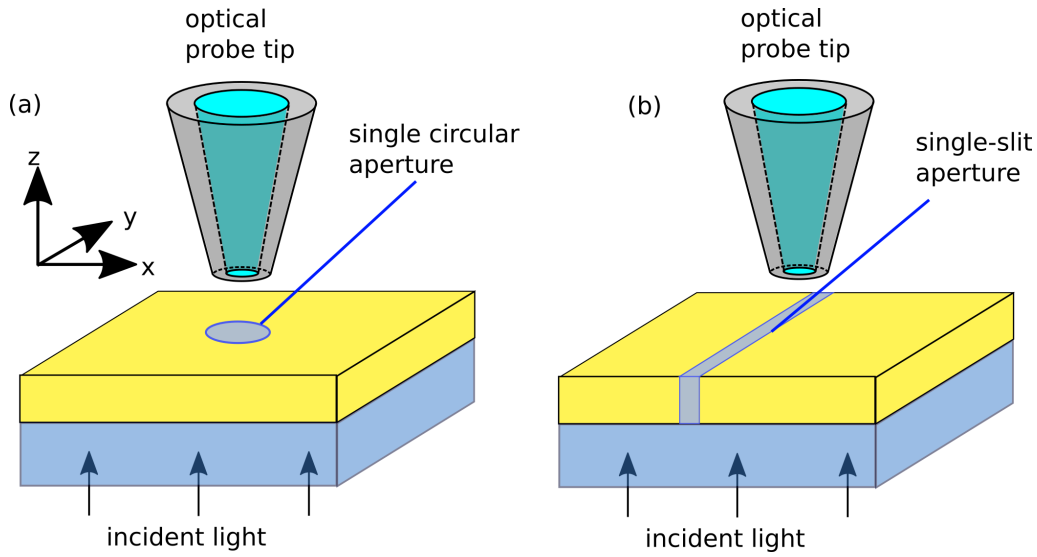
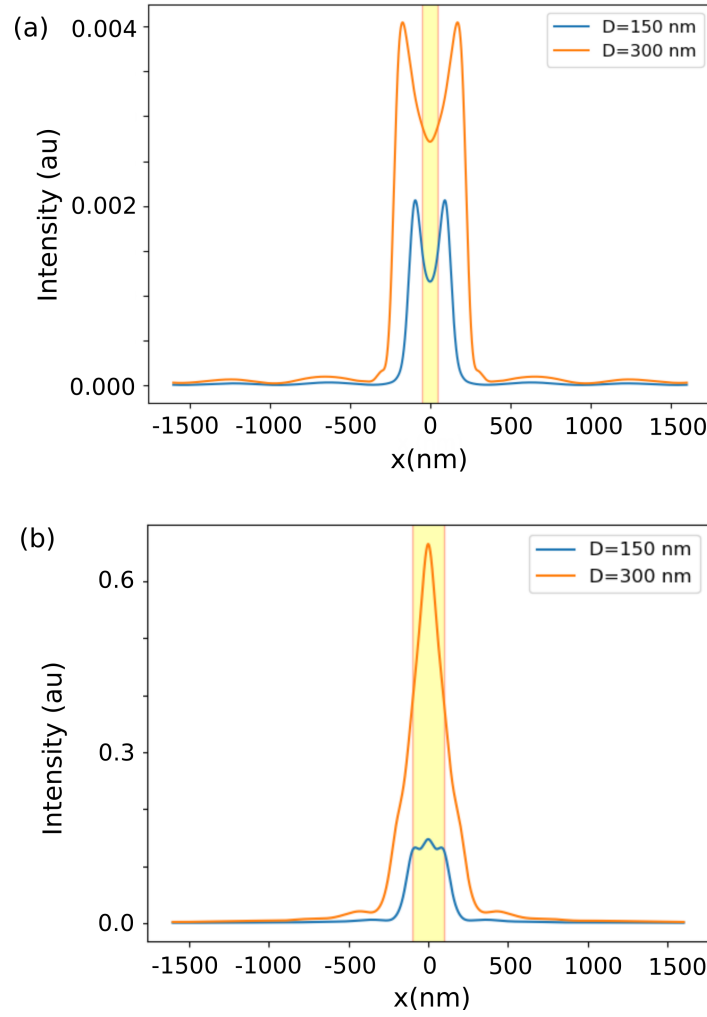


**Figure 4.15:** Schematic of the simulation for calculating the intensity profile of a single structure measured using SNOM, with the probe tip included. The samples are (a) a single circular aperture and (b) a single-slit aperture in a metal film.

the case of a pair of apertures, this polarisation direction was parallel to the line connecting the two centres of the circles.

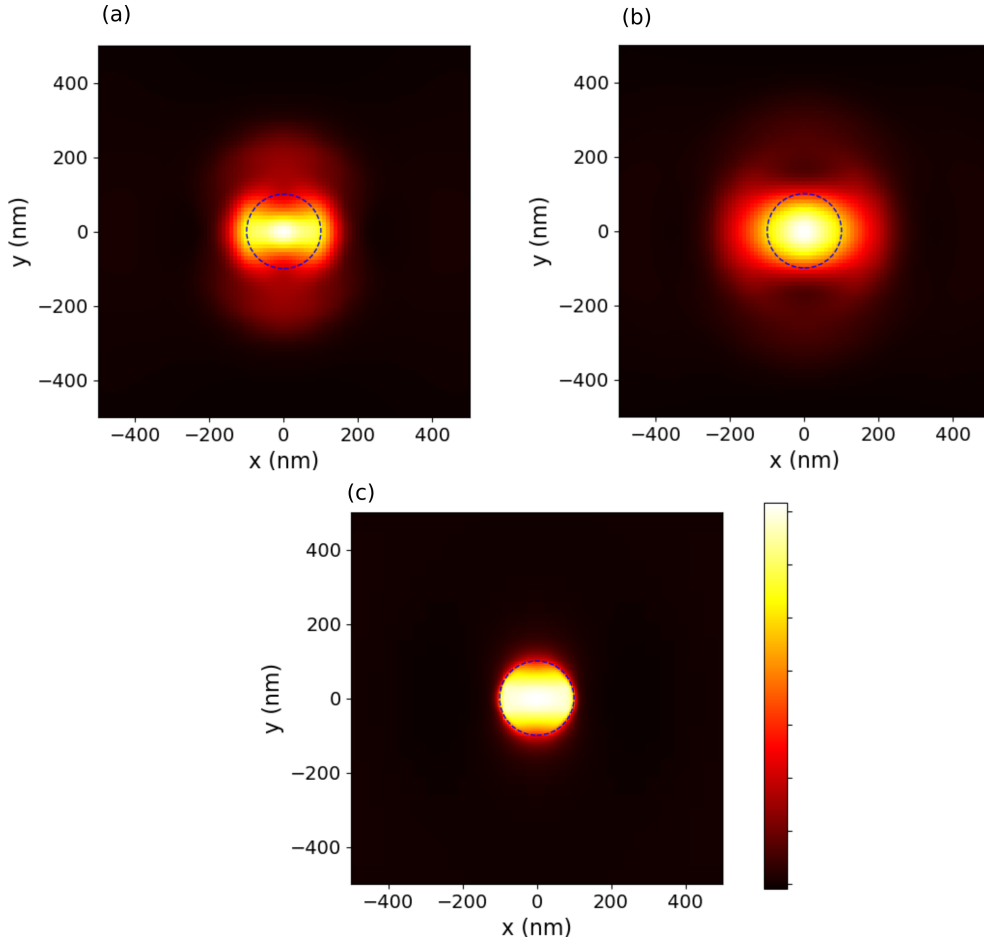
The simulated intensity profile of a single circular aperture along its centre is shown in Fig. 4.16. The intensity profiles were calculated using a probe tip size  $D = 150$  nm and  $D = 300$  nm, at a height  $h = 10$  nm from the surface. The physical location of the aperture is denoted by the yellow rectangle in the figure. An aperture of size  $d = 100$  nm could not be imaged properly. The detected profile was much larger than size of the actual aperture. In contrast, an aperture with  $d = 200$  nm could be imaged properly, showing the peak located inside the expected location (shaded in yellow). We note that the width of the intensity peak also closely matches the actual diameter of the aperture. The smaller probe tip ( $D = 150$  nm) produced a flatter intensity peak compared to the larger probe tip ( $D = 300$  nm) which had a sharper intensity peak and stronger relative magnitude.

Figure 4.17 shows a 2D raster scan of the circular aperture instead of the 1D scan performed on a single line. The images of simulated intensity profiles for a circular aperture using the probe tip are shown in



**Figure 4.16:** Intensity profiles measured using SNOM along the line through the centre of a circular aperture with (a)  $d = 100 \text{ nm}$  and (b)  $d = 200 \text{ nm}$ .

Figs. 4.17(a,b) for  $D = 150 \text{ nm}$  and  $D = 300 \text{ nm}$  respectively. For comparison, another image obtained without the probe tip is shown in Fig. 4.17(c). The physical location of the aperture is indicated by a circle with a dashed blue line. Both simulations performed with different probe parameters could generate images of the apertures with high fidelity, with the peaks appearing at the expected location of the aperture, although with a slightly different shape. The peak has a stronger intensity along the polarisation direction of the incident light, showing the peak elongated in the  $x$ -direction. The peak obtained with  $D = 300 \text{ nm}$  is slightly larger compared to that obtained with a smaller tip,  $D = 150 \text{ nm}$ .



**Figure 4.17:** Simulated intensity profile detected by the probe tip for a single circular aperture with  $d = 200$  nm, using probe parameters  $h = 10$  nm and (a)  $D = 150$  nm and (b)  $D = 300$  nm. (c) Simulated intensity profile using a 2D plane detector at  $h = 10$  nm.

Comparing the results of the simulated intensity profile with and without the probe tip included, the overall peak size obtained using the probe tip is slightly larger than the actual size of the aperture. With a 2D plane detector placed at the same distance as the probe tip from the sample, almost the whole intensity peak is contained at the expected location of the aperture. This is an idealised version of the near-field image when there are no disturbances from the probe tip.

Figure 4.18 shows a scan with  $D = 150$  nm but at a greater distance from the sample,  $h = 50$  nm. An image for comparison obtained from the simulation without the probe tip is also shown with the 2D plane detector located at the same height. The observed behaviours are still

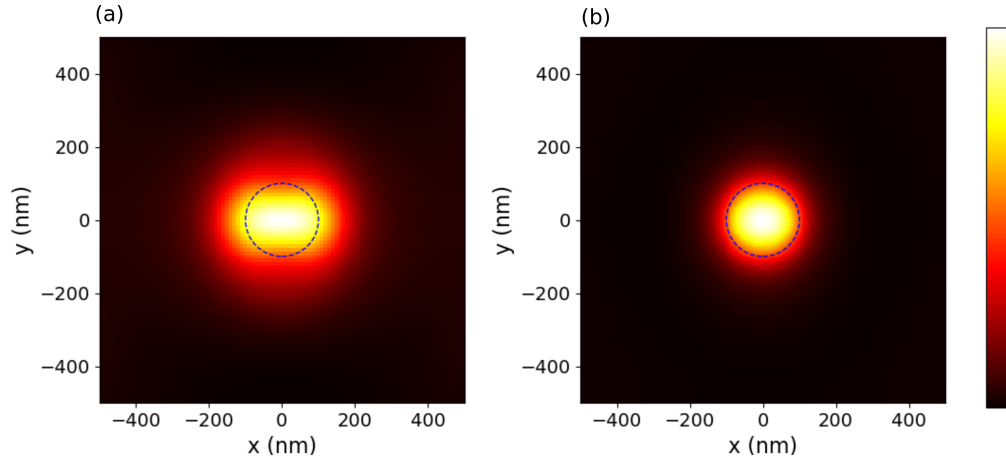


**Figure 4.18:** (a) Simulated intensity profile detected by the probe tip for a single circular aperture with  $d = 200$  nm, using probe parameters  $h = 50$  nm and  $D = 150$  nm. (b) Simulated intensity profile using a 2D plane detector at  $h = 50$  nm.

consistent, with the image obtained using the probe tip appearing more blurry compared to that obtained when using just a 2D plane detector. Comparing this to the image in Fig. 4.17(a), at a closer distance to the sample ( $h = 10$  nm), the change is insignificant, with a similar overall shape of the intensity peak, only with a slightly larger FWHM.

For a simpler calculation, the circular aperture was replaced by a slit aperture. In the ideal case of a very long slit aperture, it only needs to be scanned in the direction parallel to its width. As a result, the scan is reduced to a one-dimensional line, equivalent to a single scan line through the centre of the circular aperture discussed previously. Figure 4.19 shows the simulated intensity profiles across a single-slit aperture with a width of  $w = 200$  nm and  $w = 400$  nm, and a film thickness of 200 nm. The probe scans the aperture with various values of  $h$  and  $D$ . The actual slit location is indicated by the black square. Each of the intensity profiles has one large peak, corresponding to the single slit being investigated. As can be seen from the figure, the simulations produced various shapes of the intensity line profiles depending on the probe parameters being used. The probe tip size  $D$  looks to be the dominant factor in the resulting width of the intensity peak. A small  $D$  leads to a narrower peak, with the width comparable to the actual size of the slit. Both  $D = 150$  nm and  $D = 300$  nm fall into this category, although the peaks show different

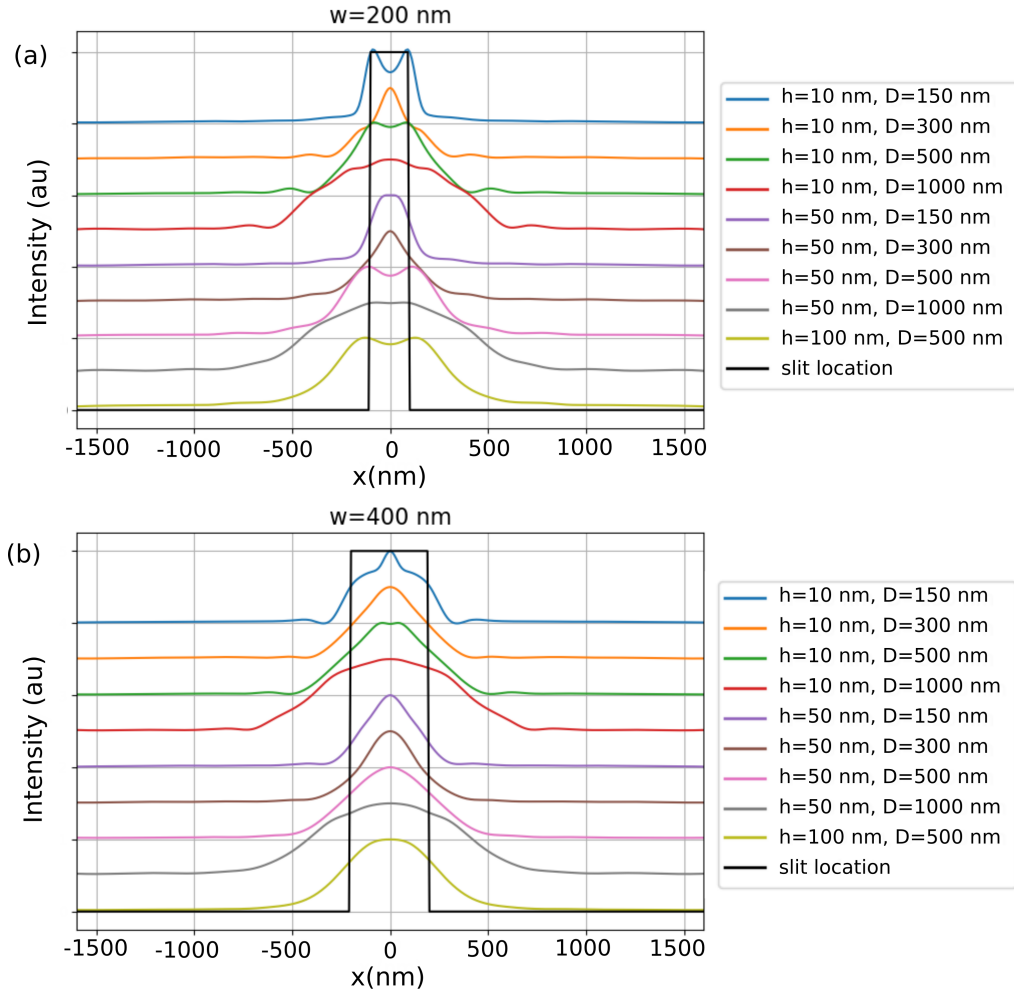


**Figure 4.19:** Simulated intensity profiles across a single-slit aperture with a width of (a)  $w = 200$  nm and (b)  $w = 400$  nm, measured using an optical probe with various  $h$  and  $D$ .

shapes. If the probe tip is too large (e.g.  $D = 500$  nm and  $D = 1000$  nm), the resulting intensity profile will be very wide, considerably larger than the actual slit size itself.

In simulating the scanning process, the probe was moved with inhomogeneous steps. The probe moved with a smaller step near to the object, which in this case is a slit aperture. As the probe moved away from the object, the intensity decreased and the probe moved with a larger step size. To check the accuracy of this approach, a comparison was performed with another simulation using homogeneous steps of the probe movement across the slit.

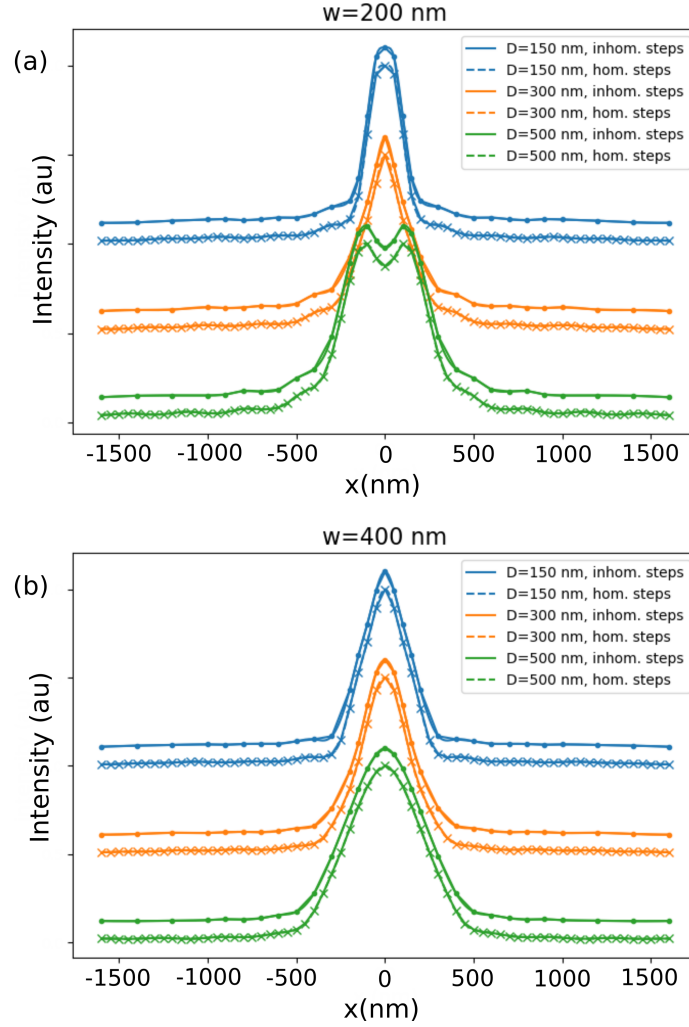


**Figure 4.20:** Simulated intensity profiles calculated with inhomogeneous and homogeneous spacing between the probe measurements for a single-slit aperture with (a)  $w = 200$  nm and (b)  $w = 400$  nm. The data points are indicated by dots (inhomogeneous step) and crosses (homogeneous step). Profiles are shifted upward for clarity.

The results of the probe step comparison are shown in Fig. 4.20. The profiles were moved upward to provide an off-set between the profiles. The data points were marked with dots and cross markers in the profile, with the lines connecting the data points. In calculating the profiles, the data points were interpolated using a cubic function to give a smoother curve. The main result is the data points, which show that the spacings or steps between the probe movements are insensitive to whether the steps are homogeneous or inhomogeneous when far from the object. At the

location of the imaged object, the step has to be smaller to account for a rapid change in intensity and to give a more accurate intensity peak profile. All intensity profiles presented in this study were calculated using inhomogeneous probe spacings to minimise calculation time while preserving accuracy.

#### 4.4.4 Intensity Profiles of Adjacent Objects

In this section, the ability of the SNOM system to resolve two objects located at a very close distance to each other, is investigated. This time, the calculation was performed in the simulation with the probe tip. The simulations investigated two objects separated by a very small gap. Figure 4.21 shows the schematics for the simulation with a pair of circular apertures and a pair of slit apertures (double-slit). The circular aperture has the diameter of  $d = 200$  nm, with the separation between them equal to  $s = 100$  nm and  $s = 200$  nm. The results are shown in Fig. 4.22. The incident light has a polarisation vector parallel to the  $x$ -axis.

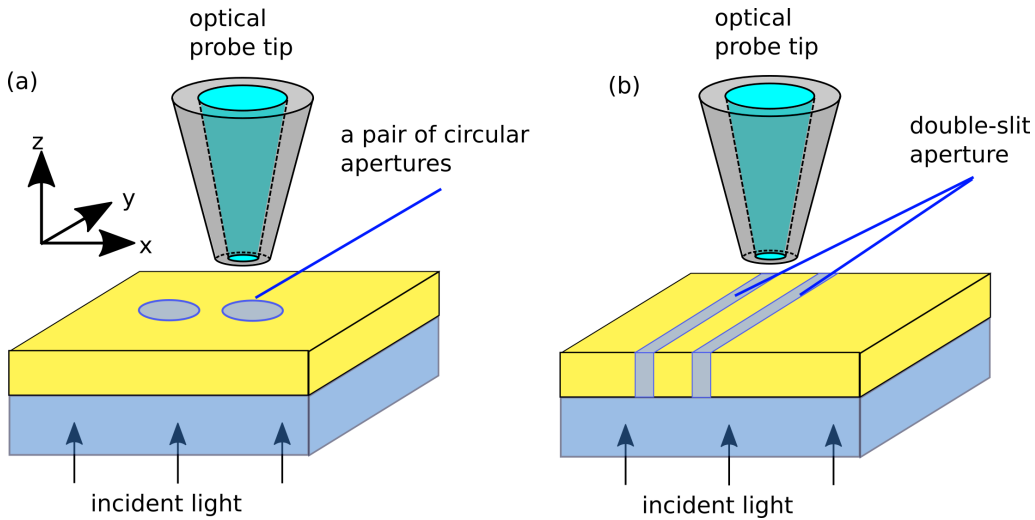


**Figure 4.21:** Schematic of the simulation for calculating the intensity profile of two adjacent structures measured using SNOM, with the probe tip included. The samples are (a) a pair of circular apertures and (b) a double-slit aperture in a metal film.

Both probe tips with  $D = 150$  nm and  $D = 300$  nm struggled to resolve two circular apertures when their separation was 100 nm (Fig.



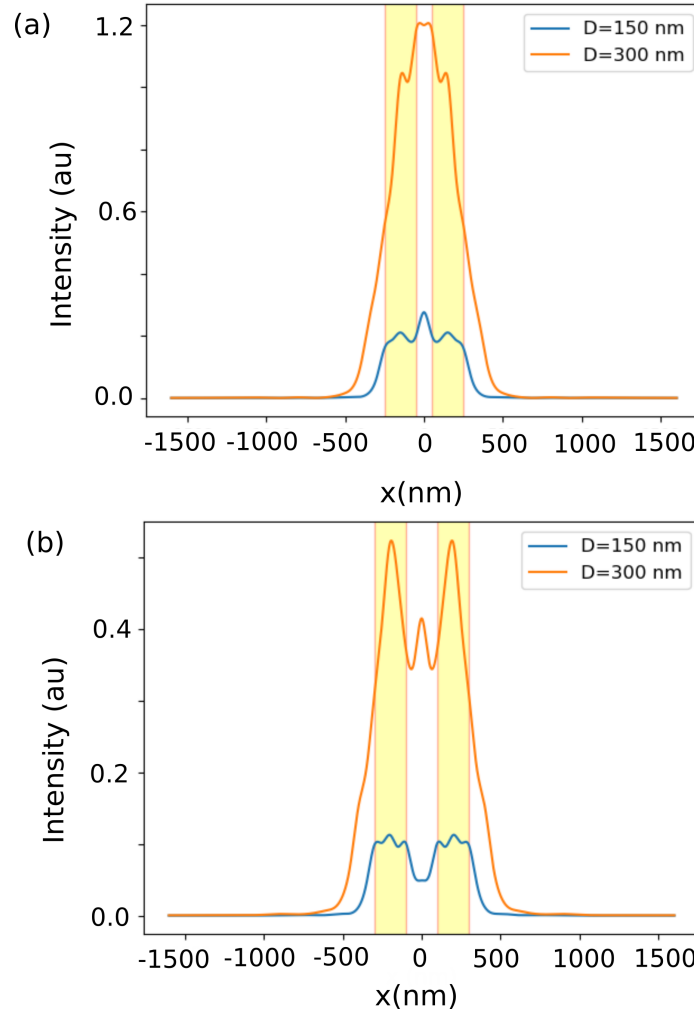


**Figure 4.22:** Intensity profiles measured using SNOM along the line through the centre of a pair of circular apertures with (a)  $d = 200$  nm,  $s = 100$  nm and (b)  $d = 200$  nm,  $s = 200$  nm.

4.22(a)). The peaks from both apertures merged into one large peak, although the ripples in the peak were still indicative of the locations of the apertures. The two apertures were not able to be resolved. When the apertures were separated by a larger gap of 200 nm (Fig. 4.22(b)), the intensity profiles showed that using both probe tips, two apertures could be identified, with two peaks observed in the profiles. The characteristics of the peaks were similar to those found in a single circular aperture. The peaks are flatter for  $D = 150$  nm compared to that detected by a larger probe tip with  $D = 300$  nm.

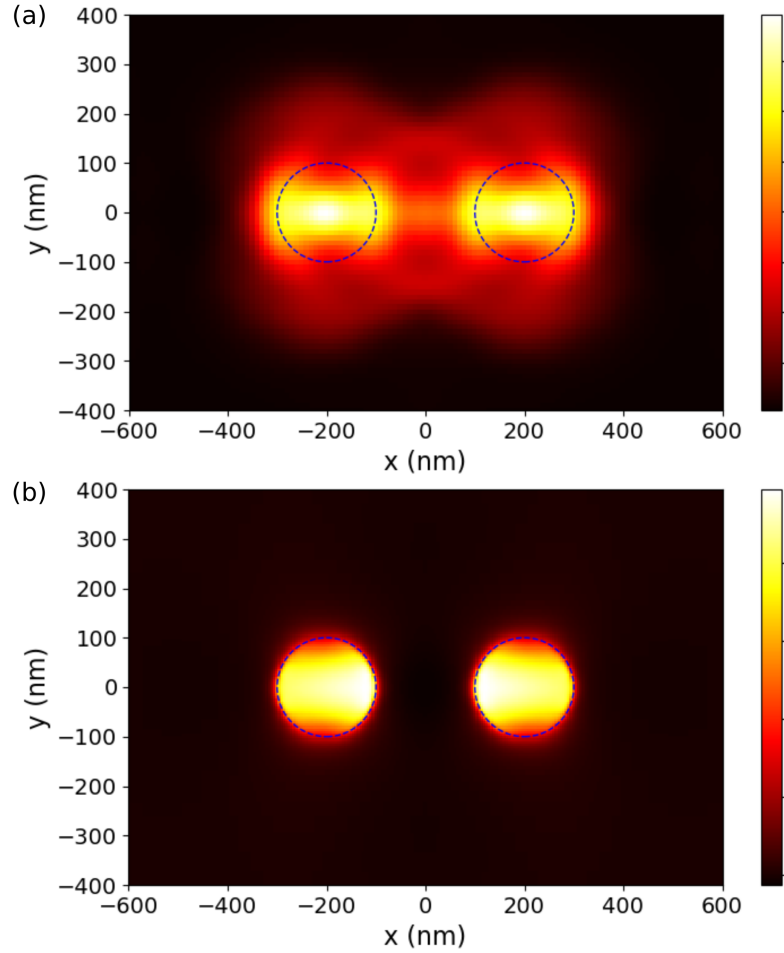


**Figure 4.23:** (a) Simulated intensity profile detected by the SNOM probe tip with  $h = 10$  nm and  $D = 150$  nm for a pair of circular apertures with  $d = 200$  nm and  $s = 200$  nm, and (b) simulated intensity profile detected by a 2D plane detector at  $h = 10$  nm.

Figure 4.23 shows that the resulting intensity profile from the simulation with a full 2D raster scan. It includes both images obtained with and without the probe tip, with two circles indicated by the dashed line showing the physical locations of the two apertures. As expected from the 1D scan through both centres shown in Fig. 4.22, two intensity peaks, corresponding to both circular apertures, can be identified in Fig. 4.23(a). This image was obtained with the SNOM probe tip included in the simulation. The intensity peaks are not circularly symmetric, with higher intensity observed parallel to the incident polarisation.

In contrast, when the intensity profile is detected by a 2D plane detector without including the probe tip, the peaks appear mostly within the physical locations of the circular apertures (Fig. 4.23(b)). This is an ideal intensity profile and does not take into account of the influence of the SNOM probe tip. The apertures are fully resolved with the two circles appearing very clearly with the correct size. However, this model is unrealistic because the the influence of the probe tip was neglected.

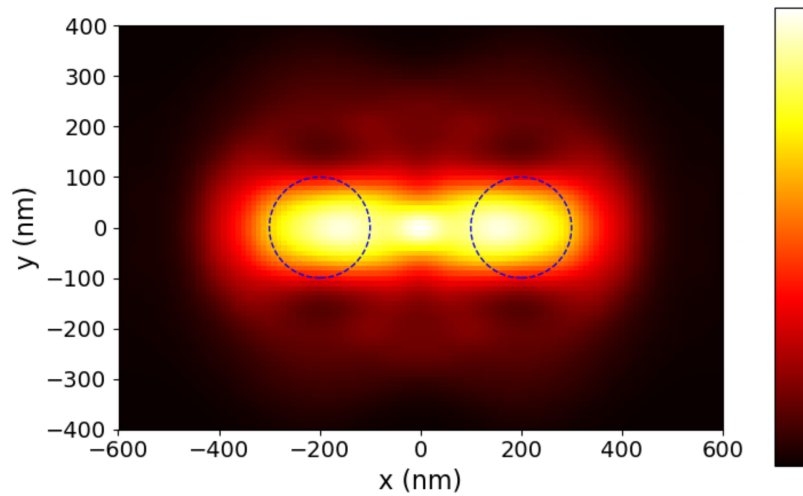


**Figure 4.24:** Simulated intensity profile detected by the SNOM probe tip with  $h = 10$  nm and  $D = 300$  nm for a pair of circular apertures with  $d = 200$  nm and  $s = 200$  nm.

In Fig. 4.24, the same pair of circular apertures were simulated with a larger probe tip,  $D = 300$  nm. Comparing this to the previous result with  $D = 150$  nm, the two peaks are more blurry, with the gap between them still having a relatively high intensity. The two circles can still be identified with peaks present inside the circle locations, but the apertures are not circular. As expected, the probe tip size affects the spatial resolution of the SNOM system, as demonstrated here.

Figure 4.25 shows the images obtained from the simulation with the probe tip for a double-slit aperture. The schematic for the simulation is shown in Fig. 4.21(b). The width of the aperture was 200 nm, with varying separation  $s$  between the two slits. With a probe tip size of  $D = 150$  nm (Fig. 4.25(a)), the probe could not resolve the two slits when the gap was  $s = 100$  nm. For a gap of  $s = 200$  nm, the slits could be

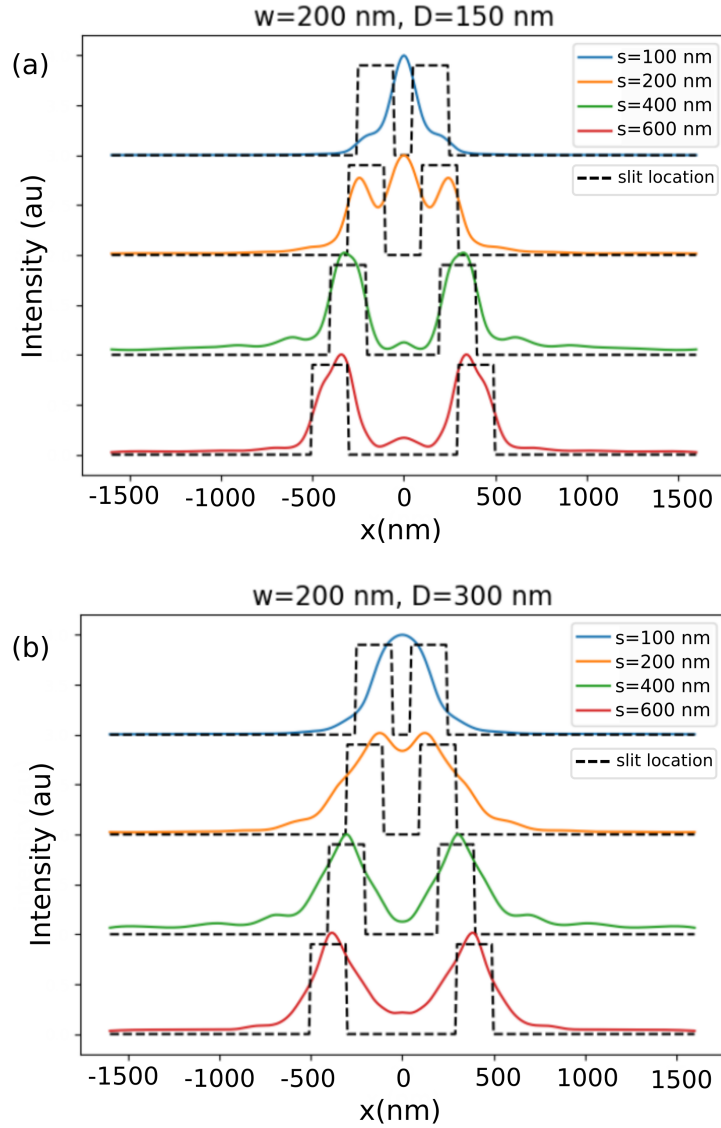


**Figure 4.25:** Simulated intensity profile measured using a probe tip with  $h = 50$  nm, and probe tip size parameters of (a)  $D = 150$  nm and (b)  $D = 300$  nm, across a double-slit aperture with  $w = 200$  nm and various separation gap  $s$ .

identified from the peaks, but the gap also produced an additional peak, giving three peaks in total. The slits were resolved when the gap between them was large enough with  $s = 400$  nm or larger. Figure 4.25(b) shows the same set of double-slit apertures imaged with a larger probe tip, with  $D = 300$  nm. With this probe tip, the additional peak inside the gap was not observed anymore. As with the smaller probe tip, slit separations of 100 nm and 200 nm could not be resolved. However, all gaps with a size

of 200 nm and larger could be identified as two separate intensity peaks, corresponding to two adjacent slits. This showed that the probe tip affects the appearance of adjacent objects in the images obtained using SNOM. Careful investigation of the probe tip parameters must be performed in order to construct a simulation model with high accuracy in terms of the actual experimental conditions.

## 4.5 Chapter Summary

The calculation of near-field optics is typically not simple and involves complex mathematics. Further complexity is introduced when there are several objects within the near-field zone. In addition, the presence of the probe tip near the sample also needs to be considered. Numerical approaches can be used to address this problem. In this study, the FDTD method was used to simulate the electromagnetic fields associated with the near-field optics involved in SNOM imaging.

A model for SNOM image formation was constructed based on simulations using the FDTD method. Using Maxwell's equations, the fundamentals of electromagnetics are covered for any objects involved in the simulation. The characterisation samples for the investigation are apertures in a metal film. The apertures are circular and slit apertures, both in single (isolated object) and double (adjacent objects) configurations.

To study the influence of the probe tip presence in the near-field regime, two simulation models were investigated, one with a nonphysical 2D plane detector (without the probe tip) and another with a probe tip as the near-field detector. Both the 2D plane detector and the probe tip were placed at a very short distance from the samples ( $\leq 100$  nm) in the simulation region.

Different results were generated from these two types of simulation models. In general, when no probe tip was included in the simulation, the resulting intensity peaks corresponding to the apertures have a width which corresponds closely to its actual physical size and location. This is an ideal image in the near-field region, which is equivalent to recording a near-field intensity with a point-sized probe, scanning over the sample.

This model is beneficial in terms of rapid calculation to quickly investigate the near-field properties of a sample, but it is not very realistic. On the other hand, the intensity profile produced from the simulation with the probe tip included showed that the intensity profiles of the apertures are significantly affected by the probe tip. This was investigated by changing the probe parameters,  $h$  and  $D$ , corresponding to the probe tip distance from the sample surface and the diameter of the tip aperture within an aperture probe.

Using the probe tip, it was shown that the simulated images of both circular and slit apertures are blurred compared to the results of simulations with no probe tip. The widths of the intensity peaks are generally still comparable to the actual physical size of the apertures. As expected using a larger probe tip affects the resolution of the SNOM image producing a widened intensity peak from the object, leading to an inaccurate estimation of the size of the object. For adjacent objects separated by a subwavelength distance, the probe tip also influences the ability of the SNOM system to resolve the two objects as two separate intensity peaks. The gap between the objects is less clear when a probe tip with a larger diameter is used.

## Chapter 5

# The Probe Tip Influence in the SNOM Imaging

### 5.1 Introduction

In this chapter, the simulation models discussed in the previous chapter (Chapter 4) were further tested using experimental data obtained from the SNOM scans. Both simulation models, with and without the probe tip, were investigated. Using the simulation models established in the previous chapter, the intensity profiles for several configurations of apertures were investigated and discussed. The intensity profiles obtained from the experiments were used to validate the simulation models by comparing the results from the simulations with an appropriate set of probe tip parameters.

In extracting near-field optical signals from a sample using SNOM, an optical probe scans the sample at a subwavelength distance from the sample surface. Near-field signals are nonpropagating and in the Fourier domain, contain high spatial-frequency components [1]. These components carry information that is otherwise limited due to diffraction. Using an optical probe tip, the bandwidth of the detected spatial-frequency components is increased due to local illumination or detection at a near-field distance.

A simple approach for investigating near-field optics is performed by recording electromagnetic fields at a very short distance from the sample

surface via a 2D detector plane [15, 16, 32]. Using this approach, the electromagnetic field distribution in the near-field can be calculated relatively fast and efficient. This is, however, not a realistic approach to modelling SNOM experiments as it neglects the influence of the probe tip.

A simulation-only study was performed using the FDTD method, to investigate the intensity profile measured using SNOM [41]. The study reported the difference in the intensity profile observed when the probe tip is incorporated in the simulation compared to when the simulation includes only a two-dimensional detector. In another study, the resolution of a scattering-type SNOM was investigated using the metal/ dielectric boundary as a characterisation sample [5]. The intensity gradient at the boundary was investigated and an asymmetry was observed in the intensity profile across the boundary. A simulation was performed with the probe tip included and the asymmetry observed experimentally was able to be reproduced and analysed. An in-depth analysis of the SNOM probe influence was performed by investigating the interference patterns produced from SPPs generated by an arrangement of slit apertures [4]. With the probe tip incorporated in the simulation, the distribution of electromagnetic components measured using SNOM was investigated.

The examples above highlight the important influence of the probe tip in SNOM measurements. Important characteristics of the intensity profiles observed experimentally were able to be analysed when the probe tip influence is considered in the simulation. Therefore, it is important for the simulation model of SNOM imaging to incorporate the presence of the probe tip in the calculation.

Literature suggests that the dimension and geometry of the probe tip impact the spatial resolution of the SNOM device [1, 28, 40]. Ideally, the probe is designed to induce a very strong light localisation by making the tip size incredibly small and as sharp as possible with a small opening cone angle. In practice, making a very small tip is usually difficult due to the challenging fabrication process. In addition, if a probe tip is too small, it transmits or scatters very weak signals that are difficult to separate from the background noise. That tip will also be very prone to breaking when it is moved across the sample due to the force interaction with the sample surface.



In this study, the characterisation samples used in the experiments were slit apertures in a gold film. The transmission through slit apertures has been studied in a number of previous publications, both in the form of singular [112, 113] and arrays of apertures/ gratings [106, 107]. Enhanced transmission was observed in these nanostructures, with surface plasmons playing an important role in this phenomenon. These slit apertures exhibit a more complex behaviour compared to discrete boundaries [5]. Their dimensions, including the width and separation, were varied to show the relative influence of the probe tip on the resulting SNOM images of these samples. The calculation of these, effectively, one-dimensional apertures was also straightforward in the simulation as only the variation along one axis (perpendicular to the slit) needed to be considered. In terms of fabrication, one-dimensional apertures can be made at very high quality with well-defined length scales.

An article [34] was published in the open-access *OSA Continuum* journal based on the results presented in this chapter, with the title of "Investigating the probe-tip influence on imaging using scanning near-field optical microscopy". It focuses on the analysis of the intensity profiles of slit apertures using SNOM and the investigation of the influence of the SNOM probe tip in image formation.

## 5.2 Slit Apertures as Characterisation Sample

### 5.2.1 Single-Slit and Double-Slit Apertures

To investigate the probe tip influence in SNOM imaging, one-dimensional (1D) characterisation samples were used. The samples were slit apertures fabricated in a continuous gold film. The subwavelength feature size of the slits is an important feature that is imaged using SNOM to investigate the influence of the probe tip. Additionally, the intensity profiles from the SNOM images obtained experimentally can be measured for several different lines across the slits. The intensity profiles across the slits was then averaged to improve the signal-to-noise ratio for the measurements [5].

Two types of slit apertures used in this study were single-slit and double-slit apertures. A schematic of the slits is shown in Figure 5.1,

with their size parameters, width  $w$  for the single-slit, and width  $w$  and separation  $s$  (or gap) between the slits for the double-slits.

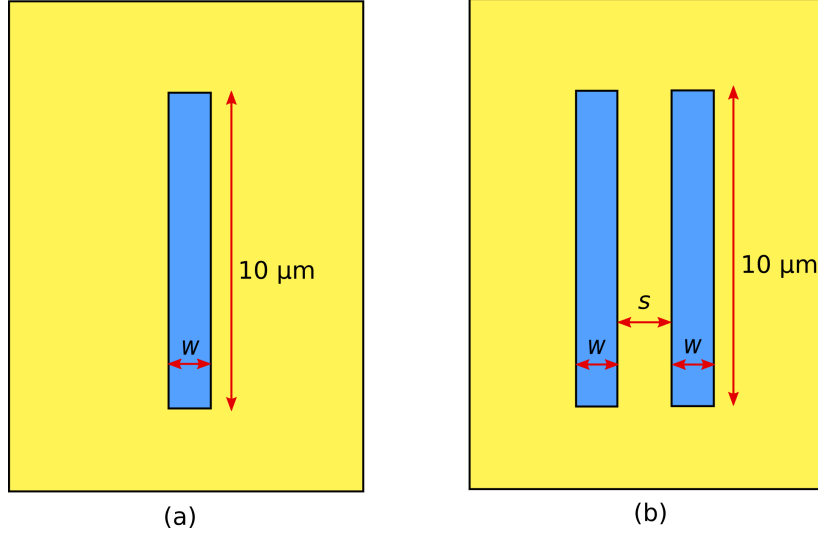


**Figure 5.1:** Schematics of the characterisation samples, (a) single-slit aperture and (b) double-slit aperture.

**Table 5.1:** The slit apertures dimensions (width  $w$  and separation  $s$ ), confirmed using scanning electron microscopy (SEM).

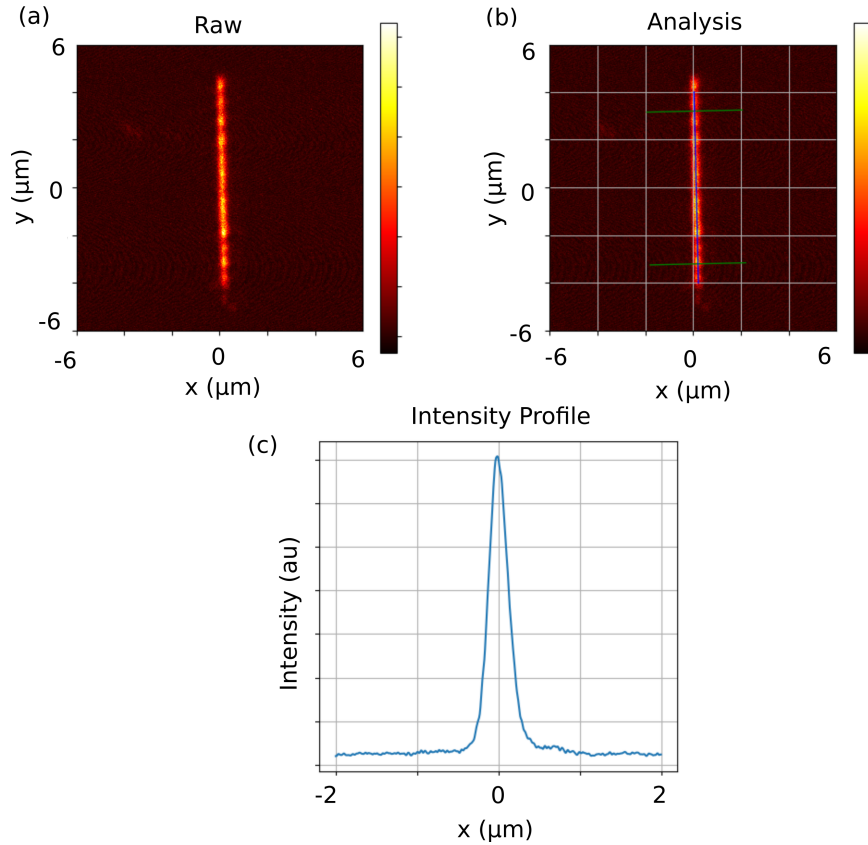
single-slit	double-slit	
$w$ (nm) $\pm 5$ nm	$w$ (nm) $\pm 5$ nm	$s$ (nm) $\pm 5$ nm
150	410	80
180	470	140
410	480	230

The samples were fabricated using the FIB (focussed ion beam) technique. The samples were designed by the author and the fabrication was performed by Dr. Guangyuan Si at the Melbourne Centre for Nanofabrication (MCN). Table 5.1 shows the sizes of the slit apertures, which were measured from the SEM images. Two samples had different thickness of gold film, with single-slit apertures fabricated in 200 nm thick films and double-slit apertures fabricated in 120 nm thick films. The reason for the different thickness was because fabricating a very narrow gap between the slits was much easier in the thinner film, due to limitations on the achievable aspect ratio. The optical transmission through these different

thickness of gold film was found to be negligible. The apertures were separated by at least  $20\text{ }\mu\text{m}$  between them to ensure there is no interference between different slits during the SNOM scans.

### 5.2.2 SNOM Images of Characterisation Sample

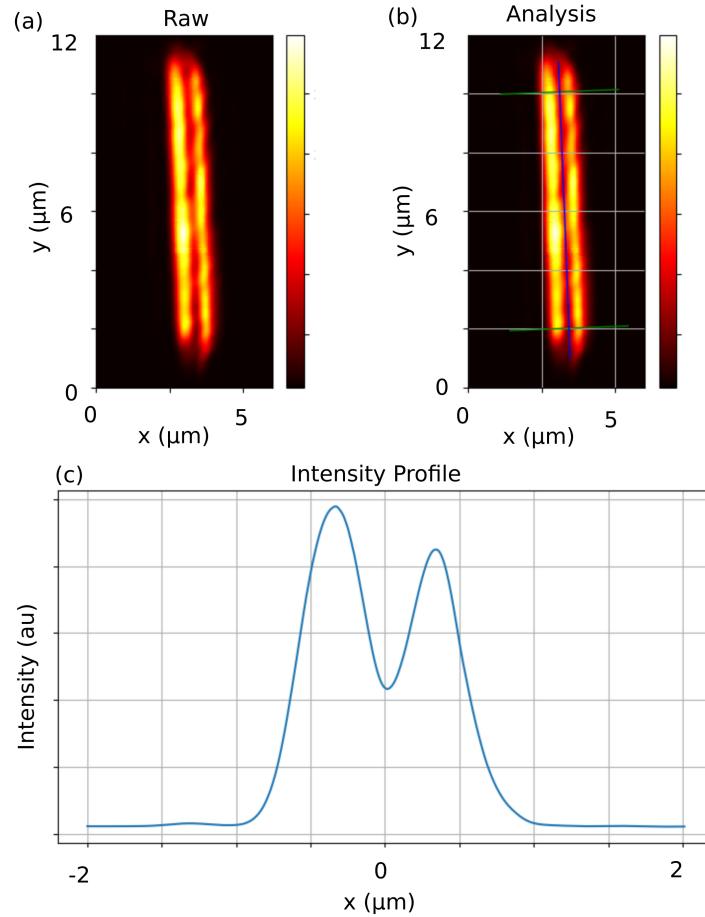
Scans of the apertures were performed using SNOM in collection mode, in which the near-field probe detected the transmitted fields through the sample. Details are provided in Chapter 3, Section 1. The sample was illuminated with a monochromatic light source, with a wavelength of  $640\text{ nm}$ .



**Figure 5.2:** SNOM scan result of a single-slit aperture with  $w = 180\text{ nm}$ . (a) The raw SNOM image, and (b) the same image showing the lines used for the slit profile analysis. (c) The average intensity profile across the slit, resulting from averaging 100 lines between two green lines shown in (b).

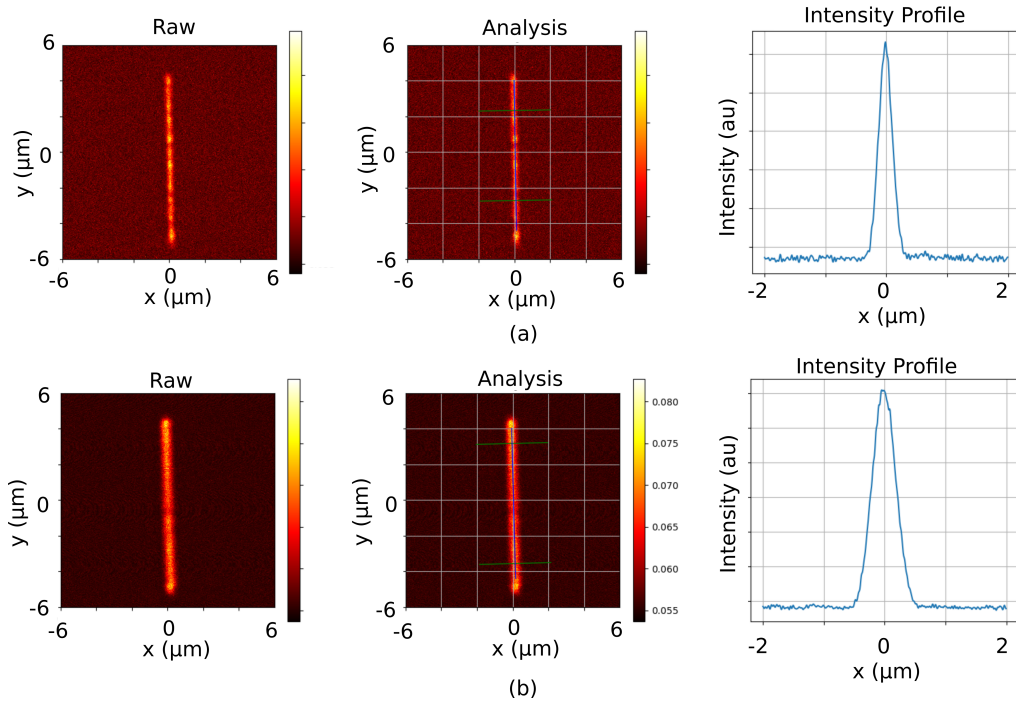
Figure 5.2 shows the results of SNOM imaging of a single-slit aperture with  $w = 180\text{ nm}$ . Figure 5.2(a) is the image from the SNOM scan, and

Fig. 5.2(b) is the same image with annotations indicating the locations where the intensity line profiles have been measured. The values from multiple different lines across the slit were averaged to calculate the intensity profiles across the slit. The blue line was placed in the middle of the slit, along the length of the aperture, and two green lines were drawn perpendicular to the green lines at different positions. The intensity profiles were calculated in the direction perpendicular to the long-axis of the slit by averaging 100 individual line profiles spaced equally between these two green lines (see Chapter 3, Section 3.2.2 for details). The final intensity profile shown in Fig. 5.2(c). The intensity profile is analysed more in depth in Section 5.4.



**Figure 5.3:** SNOM scan result of a double-slit aperture with  $w = 470$  nm and  $s = 140$  nm. (a) The raw SNOM image, and (b) showing the lines used for the slit profile analysis. (c) The average intensity profile across the slit, measured from 100 lines between two green lines shown in (b).

Figure 5.3 shows a SNOM image of a double-slit aperture with the intensity line profile taken across the double-slit. Two slits could be identified by the two peaks observed in the intensity profile. The peaks, however, do not have the same amplitude. These asymmetries were attributed to the imperfection in the fabrication, for example, materials re-deposited at the edges of the slits.



**Figure 5.4:** SNOM scan results of single-slit apertures with (a)  $w = 150$  nm and (b)  $w = 410$  nm and intensity profiles across the slits.

Figure 5.4 shows the SNOM scans of the other two single-slit apertures with different widths. The first image is from a single-slit with  $w = 150$  nm (Fig. 5.4(a)), which is only slightly smaller than the one shown in Fig. 5.2 ( $w = 180$  nm). The width of the peak in the intensity profile is very narrow, similar to that with  $w = 180$  nm. By comparison, the SNOM image for  $w = 410$  nm (Fig. 5.4(b)) appears wider than both  $w = 150$  nm and  $w = 180$  nm, consistent with increasing physical width of the aperture. This is also confirmed by the width of the peak in the intensity profile across the slit.

On the other hand, the SNOM scan results for double-slit apertures with different dimensions are shown in Fig. 5.5, one with larger separation,  $s = 230$  nm, and another smaller separation  $s = 80$  nm. The image from the SNOM scans of the double-slit with  $s = 230$  nm, is not very clean, with various inhomogeneities in the intensity along the length of the slits. A small fraction in the upper part of the image is, however, quite clean. The intensity profile across the slit was taken in this section (between two green lines in the middle figure of Fig. 5.5(a)). The asymmetric amplitudes of the two peaks were also observed here, similar to what were found in a double-slit with  $s = 140$  nm. The other double-slit with  $s = 80$  nm (Fig. 5.5(b)), however, could not be resolved using SNOM. The two peaks merged and presented as one peak in the image. The intensity profile analysis shows that the peak has an asymmetric shape, which is again consistent with the asymmetric amplitudes observed in the other double-slit apertures.

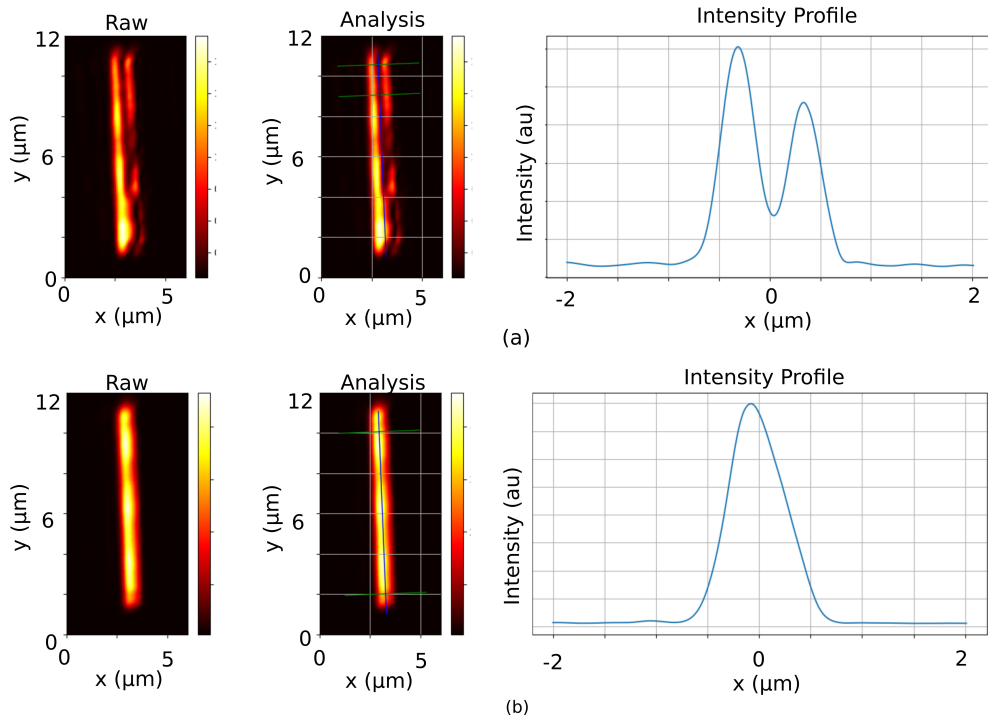


**Figure 5.5:** SNOM scan results of double-slit apertures with (a)  $w = 480$  nm,  $s = 230$  nm, and (b)  $w = 410$  nm,  $s = 80$  nm, and intensity profiles across the slits.

### 5.2.3 Estimating the SNOM Spatial Resolution

The SNOM scan results from single-slit apertures with  $w = 150$  nm and 180 nm were used to estimate the resolution of the SNOM system used here. The spatial resolution were estimated using the line spread function (LSF) method for the one-dimensional structures [5, 80, 81]. The sharpness of the intensity profiles at the edges of the slits determines the spatial resolution, called the edge response function (ERF). To estimate the spatial resolution, the intensity gradient  $dI/dx$  was calculated for both slits. The peaks in the derivative curves correspond to two edges of the single-slit. The absolute values of the curve were taken and the peaks were fitted using an asymmetric pseudo-Voigt function (see Section 3.2.3 in Chapter 3) to estimate their widths based on the FWHM. The results are shown in Fig. 5.6. The average values of the fitting results were used to estimate the spatial resolution of the SNOM system, which was found to be  $178\text{ nm} \pm 14\text{ nm}$ . This experimental estimate provides an approximate guide as to the resolution capability of the SNOM system used in this study.

The method used here was adapted from one which is routinely used on the slit aperture samples, which typically assumes an isolated single edge [5]. In cases where the slit width is comparable to the optical resolution, the results of applying this method could potentially be impacted due to interference between the slit edges. We note, however, that the calculated value is consistent with the experimental observation of the resolvability of the double-slit apertures using SNOM.

## 5.3 Influence of the Probe Tip Parameters on the Intensity Profiles using FDTD Simulations

The experimental SNOM scan results discussed in the previous section were compared with the results from the simulation models using FDTD.

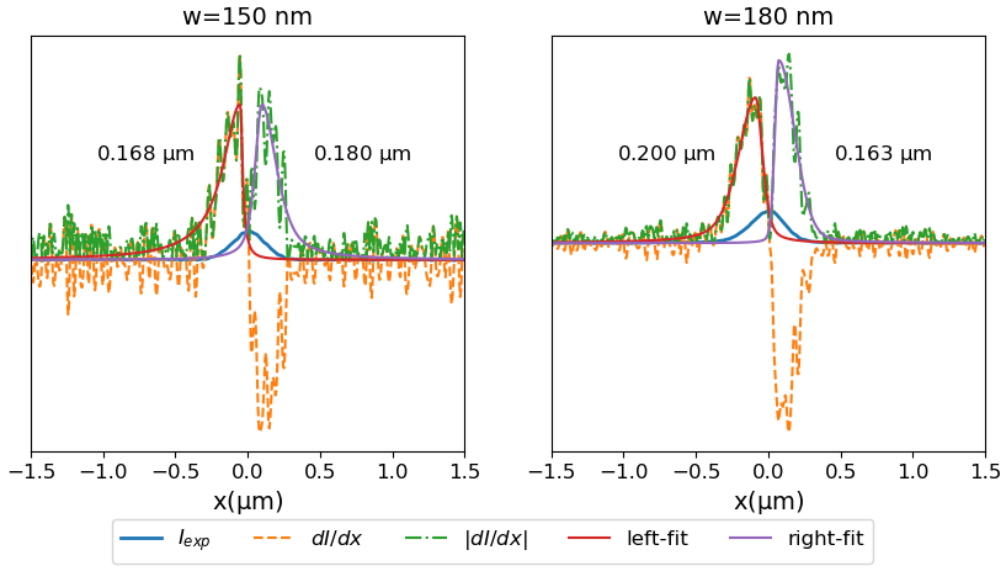


**Figure 5.6:** Estimating the spatial resolution of the SNOM using the derivative of the intensity profiles to determine the FWHM associated with the sharp edges of the slits. The intensity profiles are taken from single-slit apertures of width of  $w = 150$  nm and  $w = 180$  nm.

Two different approaches were used in the simulation models: one without the probe tip, and one with the probe tip included. In the simulations without the probe tip, a 2D detector was placed at a subwavelength distance from the sample surface to record the intensity profile. In the simulations with the probe tip, the probe tip was placed inside the simulation, and the simulations were repeated for various probe positions with respect to the sample, to form an image of the aperture. The reader is referred to Sections 4.2.1 and 4.2.2 for additional details.

Figure 5.7 shows the results of varying the height of the 2D detector in the simulations for single-slit and double-slit apertures. The height  $h$  was varied from 10 nm to 100 nm. The results show large variations in the shape of the intensity profiles with different values of  $h$ . For the smallest height,  $h = 10$  nm, the peaks for both single-slit and double-slit have very sharp edges showing rapid decay at the tails of the intensity peaks. These were accompanied by peak oscillations at the edges of the slits. The oscillations are reduced at larger distances from the sample surface. For the single-slit, at  $h = 50$  nm and  $h = 100$  nm, the peak becomes a smooth curve with gradual decay within the intensity tails. The same behaviour



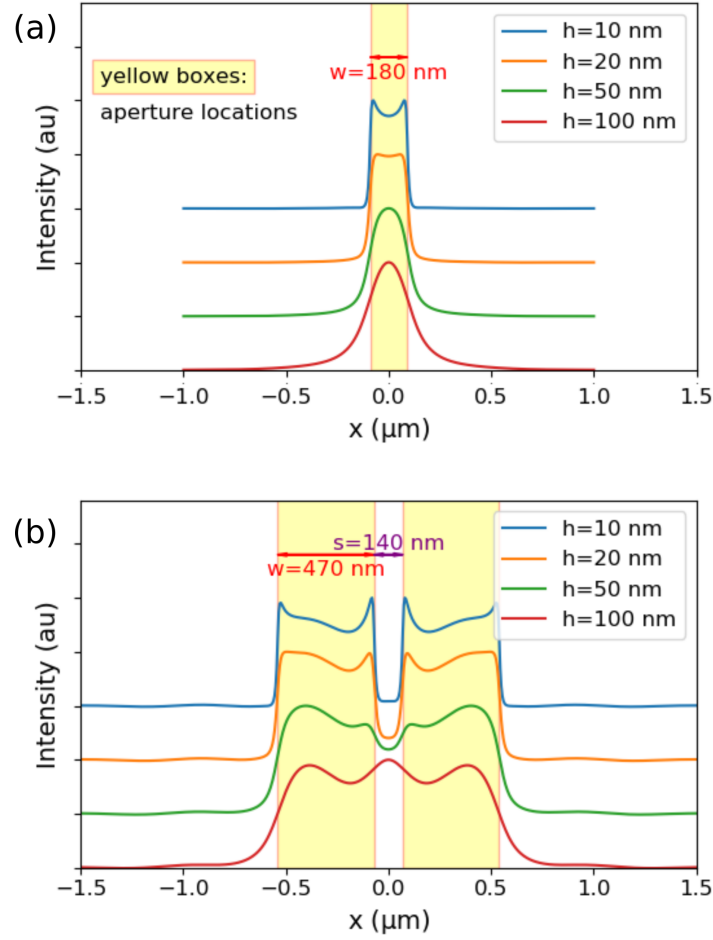


**Figure 5.7:** Intensity profiles across (a) single-slit with  $w = 180$  nm and (b) double-slit with  $w = 470$  nm and  $s = 140$  nm from simulations without the probe, using a near-field 2D detector at height  $h = 10$  nm to 100 nm from the sample. The intensity profiles were normalised to the same amplitudes and displaced vertically for clarity.

was also observed in the double slits, although another peak appeared in the gap between the slits.

The slit apertures being investigated in this study generated surface plasmons at the interfaces between the metal and dielectric. The oscillatory peaks found in the intensity profiles were mainly due to localised surface plasmons (LSPs) generated in the isolated nanostructures, although the overall shape will be the combination of both LSPs and SPPs (surface plasmon polaritons) at the metal film and dielectric interfaces. As can be seen in Figs. 5.2 to 5.5, these oscillatory peaks were not observed in the SNOM scans of the apertures from the experiments.

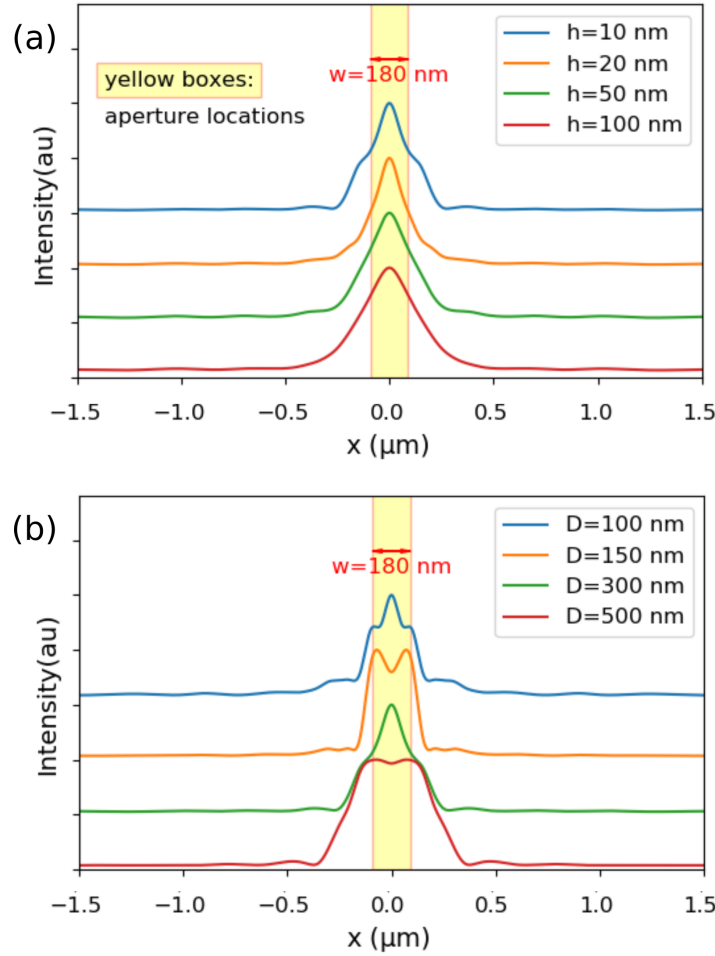


**Figure 5.8:** Intensity profiles across a single-slit aperture with  $w = 180 \text{ nm}$  from simulations with the probe at (a) constant  $D = 300 \text{ nm}$ , different  $h$ , and (b) constant  $h = 10 \text{ nm}$ , different  $D$ . The intensity profiles were normalised to the same amplitudes and displaced vertically for clarity.

A more realistic model for the simulations is when the probe tip is included in the calculation of the generated intensity profiles. Figures 5.8 and 5.9 show the results of simulated intensity profiles when the probe tip was included. The details of the simulation were described in Chapter 4, Section 4.2.2, with the power collected by the probe was calculated by integrating Poynting vector over the area of the tip aperture, assuming the probe tip behaves like a waveguide.

Figure 5.8(a) shows the variation of the height  $h$  of the probe tip from the sample surface, similar to what was varied in the simulations without the probe, over the same range of  $h$ . It is interesting to note that, in this

case, the intensity profile shape did not significantly change with  $h$ . As long as the probe was still within the near-field range, the resulting image was insensitive to change in  $h$ . The effect of changing  $D$  is shown in Fig. 5.8(b). In contrast to varying  $h$ , the resulting intensity profiles showed a significant difference in shape. The sharp edges, similar to those observed in the simulations without the probe, appear at smaller  $D$ . The width of the peak in the intensity profile increases as  $D$  increases.

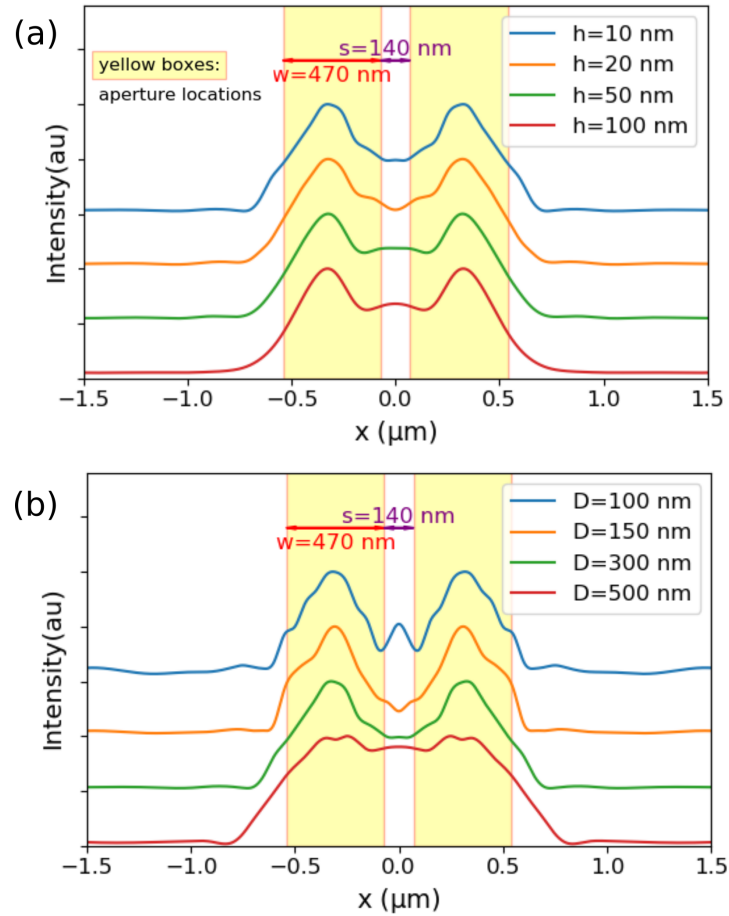


**Figure 5.9:** Intensity profiles across a single-slit aperture with  $w = 180$  nm from simulations with the probe at (a) constant  $D = 300$  nm, different  $h$ , and (b) constant  $h = 10$  nm, different  $D$ . The intensity profiles were normalised to the same amplitudes and displaced vertically for clarity.

The effects of the probe parameters,  $h$  and  $D$ , on the simulated intensity profiles of a double-slit are shown in Fig. 5.9. In Fig. 5.9(a), the same behaviour as in the single-slit was observed, with the shape of the

intensity profiles having only very small variation as a result of changing near-field distance  $h$ . The size of the probe tip has a more significant effect on the resulting intensity profiles. As  $D$  increases, the peaks corresponding to the two adjacent slits appear to be wider, and this results in the double slits not being resolved for  $D = 500$  nm.

It is interesting to note that from the results shown above, as long as the probe tip is kept within the near-field zone, the SNOM scans will produce the same image quality, irrespective of how far the probe tip is from the sample. The size of the probe tip, characterised by the tip aperture size ( $D$ ), is the dominant factor in producing high-quality SNOM images. The effects of the probe tip size are consistent with the reported results that it impacts the resulting image quality, and hence, the spatial resolution of SNOM [40].

## 5.4 Comparison between Experimental and Simulated Results

### 5.4.1 Single-Slit Apertures

In this section, the results from the simulation (without and with the probe) and from the experiments are compared. In the following figures, the intensity profiles from the simulation and experiment are plotted on the same graph. Because of the approaches when measuring data from the simulation and experiment, the amplitudes of the profiles need to be scaled appropriately. In order to do so, the profiles were normalised with respect to the total energy detected, corresponding to the total area under the intensity curve. For each intensity profile, the profile was scaled so that the area under the curve  $I(x)$  is equal to unity, using the integration  $\int I(x)dx$ , with the background (minimum) intensity reduced to 0 beforehand.

Figure 5.10 shows the comparison between the experimental and simulated results for a single-slit, with the physical aperture location indicated by the yellow shaded rectangle. Visually, the SNOM scan result is comparable to the SEM image shown in the inset. The intensity profiles are overlaid on top of each other. Using the simulation with the probe tip

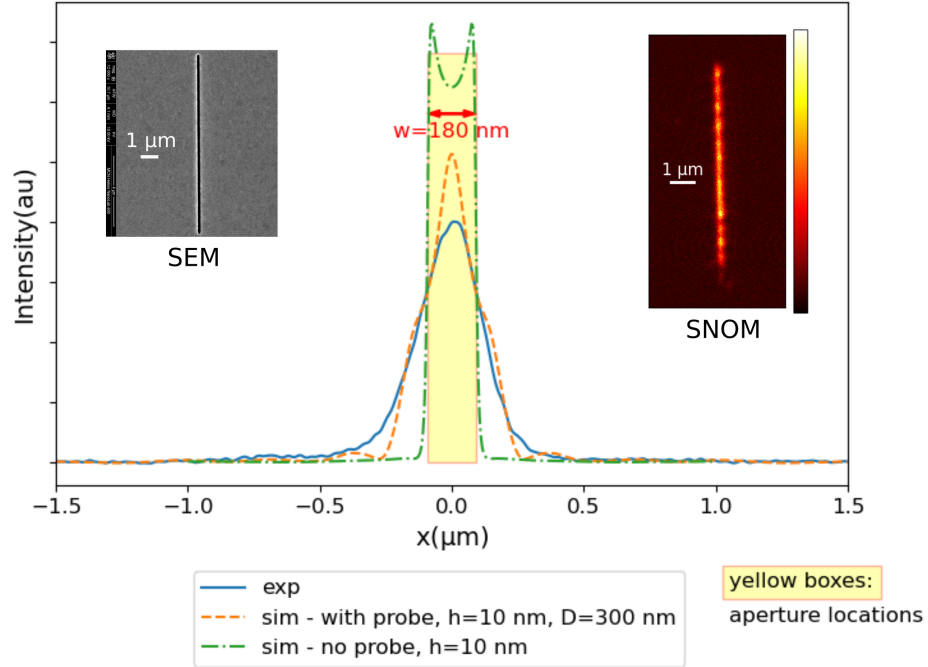


**Figure 5.10:** Example comparison between the experimental (exp) and simulated (sim) intensity profiles for a single-slit with  $w = 180 \text{ nm}$ . The simulated results are shown for both simulations with and without the probe tip. Inset: SEM and SNOM images of the single-slit.

included (dash-dotted green), the intensity profile obtained from the experiment (solid blue) could be reproduced, with an appropriate selection of the probe tip set of probe parameters,  $h = 10 \text{ nm}$  and  $D = 300 \text{ nm}$ . The profile has a relatively smooth peak at the location of the slit. Without the presence of the probe tip, the simulated intensity (dashed orange) was significantly different to what was observed in the experiment. In this case, the simulated intensity instead exhibits a very sharp decay at the edges of the slit. Two sharp intensity maxima were also observed at the edges of the slit, as part of a larger intensity peak.

Results for single-slit apertures with different widths are shown in Fig. 5.11. The characteristics of the intensity profiles were unchanged with variation of the slit width. The simulated intensity profiles were able to reproduce the experimental profile when the probe tip is included in the simulation. Comparing the actual width of the apertures confirmed

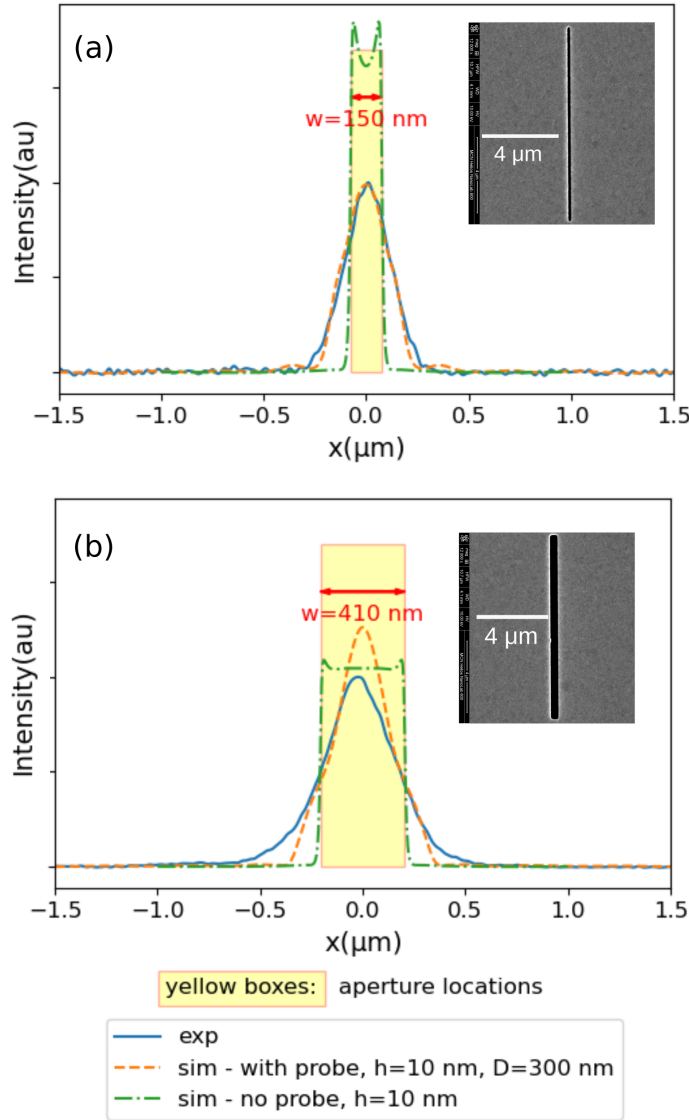


**Figure 5.11:** Comparison between the experimental (exp) and simulated (sim) intensity profiles for single-slits with (a)  $w = 150$  nm and (b)  $w = 410$  nm. The simulated results are shown for both simulations with and without the probe tip. Inset: SEM images of the single-slit.

from the SEM image, the width of the intensity peak (which was later analysed based on the FWHM) also increases for both simulation types when the slit width increases.

According to the specifications from the manufacturer, the SNOM probe tip has an aperture diameter of  $125 \pm 25$  nm. In the calculation

obtained from the simulation, the model used  $D = 300$  nm as tip aperture diameter, larger than the size in the specifications provided by the manufacturer. The model used in the simulation is a simplified model of the probe tip with a truncated cone shape with ideal concentric circular cross-sections of the glass core and its cladding. The difference in the manufacturer SNOM aperture diameter and the one determined from the model is likely due to the inhomogeneities and asperities of the probe tip. In addition, scattered light reaching the PMT, originating from the ideally sharp edges of the slits or the probe itself, could also impact the model fitting [41]. These factors effectively broaden the size of the ideal probe used in the simulation. The parameter  $D$  used here should be viewed as the 'effective' probe tip aperture size. The quality of the fit between the experiment and simulation indicated that these effects were accounted for, to a first-order approximation, by increasing the effective size of the probe used in the model.

**Table 5.2:** Summary of FWHM of the intensity profiles from the experimental (exp) and simulated (sim) results of single-slit apertures.

SEM $w$ (nm)	FWHM (nm)	
	exp	sim
150	265	255
180	275	250
410	400	335

For the quantitative analysis, a summary of the FWHM of the experimental and simulated intensity peaks in the intensity profiles for single-slit apertures is shown in Table 5.2. The value of the FWHM is equivalent to the width of the aperture. Focusing on the results from the SNOM scans, the widest aperture has a very small discrepancy with the size obtained from SEM. This discrepancy increases for smaller apertures. This was expected due to the resolution of the SEM being very high (8 nm) compared to the SNOM system (178 nm). Comparing the values of FWHM from the experiment and simulation, the discrepancies were actually smaller for the small apertures ( $w = 150$  nm and  $w = 180$  nm),

which were within 25-nm difference. The simulation for the widest aperture,  $w = 410$  nm, predicted a FWHM with 65-nm difference. With the largest discrepancy being 16% between the results from the simulation compared to the experimental results, it can be concluded that the simulation model is able to reproduce, with reasonable accuracy, the intensity profiles from the experiments.

### 5.4.2 Double-Slit Apertures

In addition to the width of the slit aperture, the separation between the slits in the double-slit aperture is an important subwavelength feature to be measured using SNOM. Figure 5.12 shows the comparison for a double-slit aperture, with  $w = 470$  nm and  $s = 140$  nm. This double-slit aperture was able to be resolved, with two peaks observed with asymmetric amplitudes, as described in Section 5.2.2.

The SNOM scan result was again visually comparable to the SEM image, although with different apparent widths of the slit, as shown in the inset. The locations of the peaks were confirmed to be inside the expected aperture locations (indicated by the yellow-shaded rectangle). The gap between the slits was visible as a local minimum between the peaks. Intensity profiles obtained from the experiment (exp) were again able to be reproduced by simulation (sim) with the probe tip included. The peaks were reproduced using  $h = 10$  nm and  $D = 300$  nm. The intensity profile obtained from the simulation of the probe tip was not able to replicate the shape of the intensity profile from the experiment. The intensity profile using this approach resulted in a sharp decay in the intensity profile, rather than the smooth peaks found in the experimental profile, similar to the characteristics found in the single-slit apertures.

Two more double-slit apertures with different separation or gap between the slits were investigated. The comparisons for the analysis of their intensity profiles are shown in Fig. 5.13. For a larger separation,  $s = 230$  nm (Fig. 5.13(a)), the local minimum between the peaks had greater visibility compared to  $s = 140$  nm. The intensity profile from the simulation without the probe showed rounded intensity peaks corresponding to two slits, but the rapid decay at the edges of the slits were



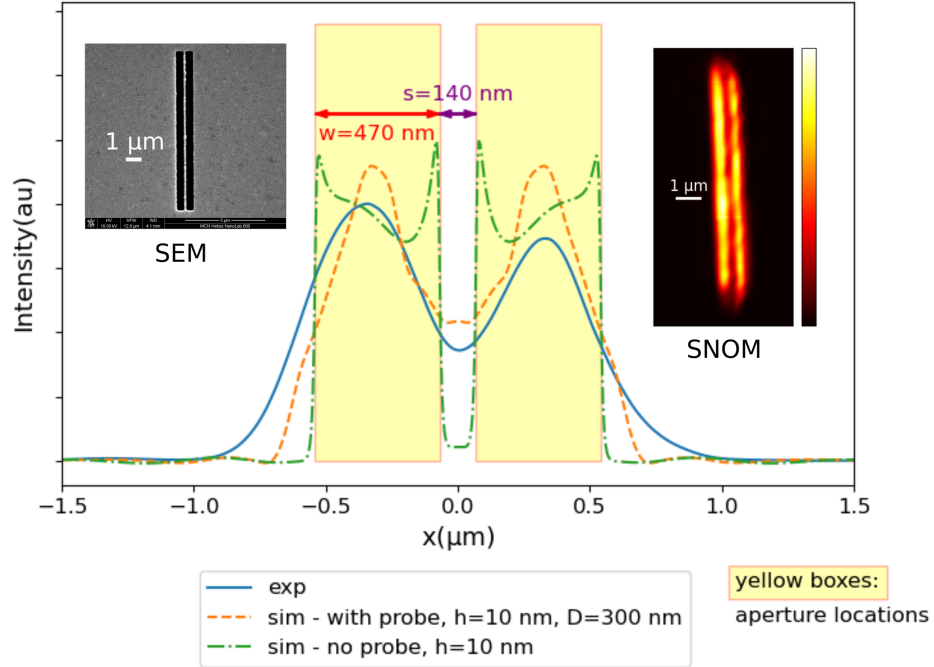


**Figure 5.12:** Example comparison between the experimental (exp) and simulated (sim) intensity profiles for a double-slit with  $w = 470$  nm and  $s = 140$  nm. The simulated results are shown for both simulations with and without the probe tip. Inset: SEM and SNOM images.

still observed. In Fig. 5.13(b), the separation of  $s = 80$  nm was too small to be detected by the SNOM system, which was smaller than the estimated resolution of the SNOM system used here. This was confirmed by the result from the simulation with the probe tip, which showed merged peaks with no distinct visible gap. The results from the simulation without the probe, however, predicted that the gap would have been visible, but this was not observed in the experiment.

A summary of the quantitative values extracted from the intensity profiles for double-slit apertures are presented in Table 5.3, which includes the FWHMs and the peak-to-peak distances. The peak-to-peak distance is equivalent to the centre-to-centre distance obtained from the SEM image. The FWHM discrepancy between the experimental data and simulation was smaller for a wider aperture as the slits could be resolved

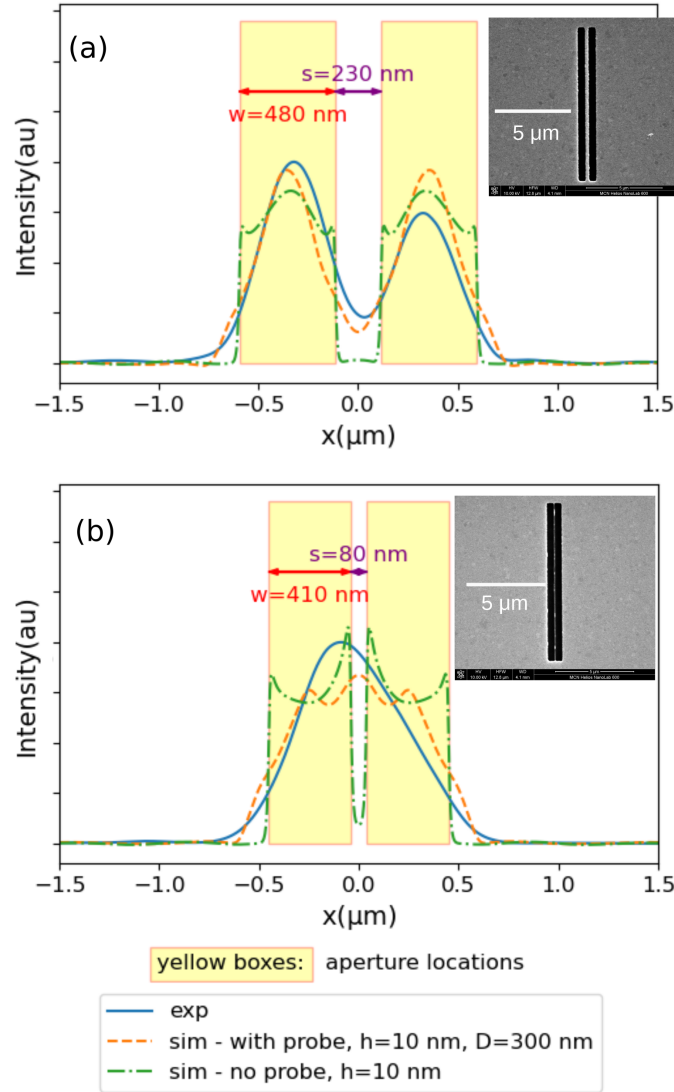


**Figure 5.13:** Comparison between the experimental (exp) and simulated (sim) intensity profiles for double-slits with (a)  $w = 480$  nm and  $s = 230$  nm and (b)  $w = 410$  nm and  $s = 80$  nm. The simulated results are shown for both simulations with and without the probe tip. Inset: SEM images.

better. The peak-to-peak distances predicted by the simulation had similar differences to the peak-to-peak distances observed in the experiment. The simulation underestimated the value by 55 nm for the double-slit with  $s = 140$  nm but overestimated the value by 50 nm for  $s = 230$  nm. No gap was observed for  $s = 80$  nm and it was excluded from the table. The results again show that the simulation model for the double-slit was

able to reproduce the experimental results with reasonable accuracy.

**Table 5.3:** Summary of the differences between experimental and FDTD simulation results for double slit apertures, comparing FWHM, and peak-to-peak distance. Center-to-center distances between the slits obtained from SEM images are included. Note that data for  $s = 80$  nm is omitted as the peaks could not be resolved (see Fig. 5.13(b)).

SEM			FWHM (nm)			peak-to-peak (nm)	
$w$ (nm)	$s$ (nm)	center-to-center (nm)	exp,left	exp,right	sim	exp	sim
470	140	610	495	455	420	685	630
480	230	710	390	375	370	655	705

## 5.5 Predicting the Actual Slit Size from SNOM Images using Iterations

From the analysis of the FWHM, the width of the peak in the intensity profile across the slit is correlated with the actual physical width of the aperture. The size of the probe tip affects how the aperture appears in the image. Suppose that the probe parameters were characterised using another well-characterised sample. With this information, it is possible for the simulation to predict the actual physical dimension of the other samples. For the single-slit aperture, the width of the slit in the simulation was iteratively updated until the best match between the intensity profiles between experimental and simulated data is found.

Figure 5.14 shows the iterative process of finding  $w$  using the simulations for slit width  $w_{SEM}$  confirmed from the SEM images. To quantify the difference between the intensity profiles, the absolute error between data points from the experiment and simulation was calculated. The absolute error is given by

$$e_{abs} = \sum_j |I_{exp}(j) - I_{sim}(j)| \quad (5.1)$$

where  $j$  is the  $j$ -th data point along the  $x$ -axis in the figure.

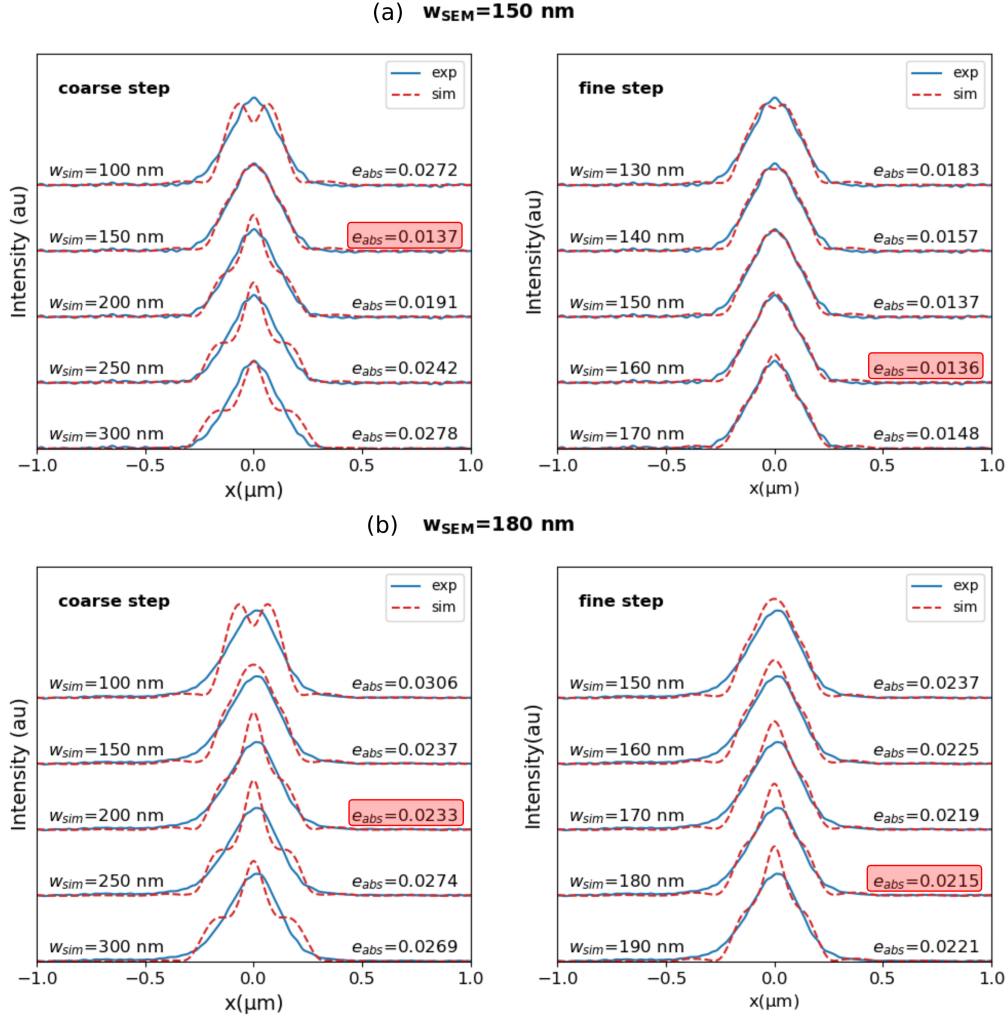


**Figure 5.14:** Estimating the physical dimension of single-slit apertures by finding the best match with the smallest absolute error  $e_{abs}$  between the experimental (exp) and simulated (sim) intensity profiles. The probe parameters used were  $D = 300$  nm and  $h = 10$  nm. The iterations were performed for (a)  $w_{SEM} = 150$  nm and (b) 180 nm as confirmed from SEM images. Minimum error values are highlighted in red-shaded boxes, initially using coarse step of 50 nm (left column), then with finer steps of 10 nm (right column). The profiles are displaced vertically for clarity.

The first iteration for the slit width  $w_{sim}$  in the simulation, was performed using a coarse step of 50 nm to increase  $w_{sim}$  (left column figures). The best match between the simulated and experimental profiles were found to be 150 nm for  $w_{SEM} = 150$  nm and 200 nm for  $w_{SEM} = 180$  nm respectively. The process continued with a finer step of  $w_{sim}$ , in 10 nm

increments. The best match between the experimental and simulated results were found when  $w_{sim} = 160$  nm and  $w_{sim} = 180$  nm for these two apertures, within 10 nm of the confirmed dimension from SEM  $w_{SEM}$ . The accuracy of the predictions demonstrated that the simulation model of SNOM is a valid approach to the realistic modelling of the system. Further investigation of this method is required with greater variation of the slit aperture samples and using different types of samples. The preliminary results presented here however highlight the potential applications of using a simulation model in combination with a well-characterised probe tip.

## 5.6 Effect of Wavelength Variation

In the experiment, only one monochromatic wavelength (640 nm) was used to image the samples. The effect of moving to a shorter source wavelength is shown in Figure 5.15 using simulations. The wavelength of the source was varied from 500 nm to 640 nm for single-slit and double-slit apertures. Both simulation types, with and without the probe, were investigated. The same normalisation process for comparing the intensity profiles were performed using the integration of  $I(x)$  with respect to  $x$ . The amplitude of the profile with  $\lambda = 640$  nm was normalised to 1.00 and the other profiles were scaled accordingly so that the total area under the curve has the same value.

With the variation of wavelength in the range shown, no significant differences in the amplitude and width of the intensity peaks were observed for the simulations with the probe included. One smooth peak for the single-slit and two smooth peaks for the double-slit look as though they may have undergone a very minor variation, however, the overall shape is unchanged. For the simulations without the probe, the shape of the peak is rounder for smaller wavelengths, but the characteristic sharp decay of the intensity is still present.

A summary of the key parameters of the intensity profiles with wavelength variation is presented in Tables 5.4 and 5.5 for the single-slit and double-slit shown in Fig. 5.15. The amplitude variation for the single-slit is within 15% of the value obtained from the profile with  $\lambda = 640$  nm.

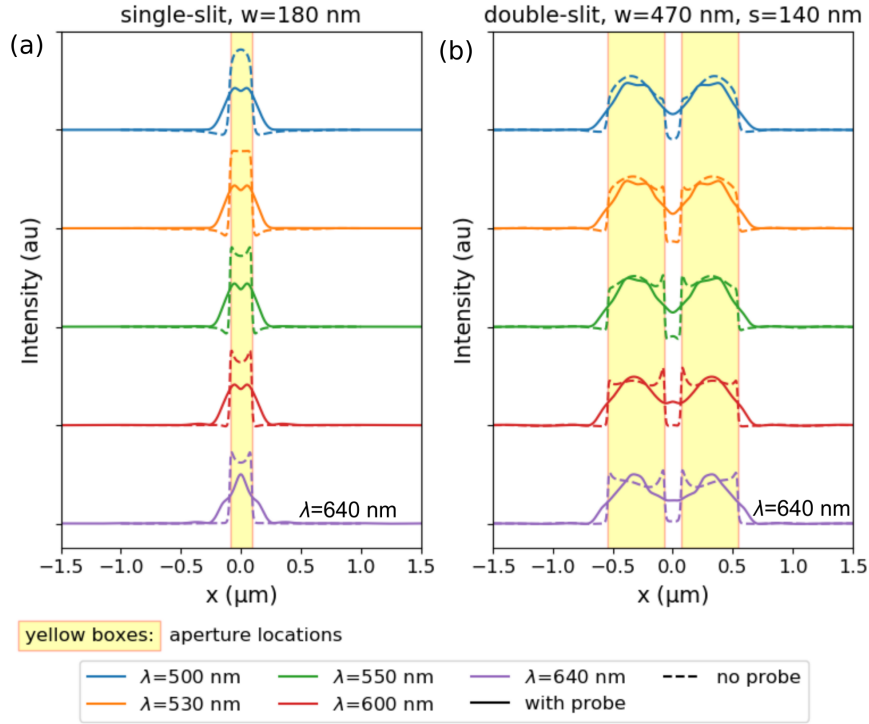


**Figure 5.15:** Simulated intensity profiles across a single-slit aperture with  $w = 180$  nm and double-slit apertures with  $w = 470$  nm and  $s = 140$  nm. The results from five incident wavelengths between 500 nm and 640 nm are shown with the probe-tip included (solid lines) and without the probe-tip included (dashed lines). The yellow shaded areas indicate the physical extent of the slit(s). The profiles were normalised such that the integral over the distance ( $x$ ) (i.e. area under the profile) was the same in each case.

The values of the FWHM follow the same behaviour with no consistent variation as a function of wavelength, with discrepancies within 25 nm.

For the double-slit, the variation of the generated intensity profile as a function of wavelength was also insignificant. The relative intensity amplitude variation is within 10% and the value of FWHM within  $\pm 30$  nm. The peak-to-peak distance in the profiles have a very small variation within 5 nm. Hence, there is no indication of a strong wavelength dependence of the parameters associated with the near-field intensity profile.

In summary, these simulated results show that using an incident source wavelength of 640 nm is valid for wavelengths within the visible range.

**Table 5.4:** Summary of simulated intensity profiles for the single-slit aperture with  $w = 180$  nm for 5 different incident wavelengths. The relative intensity amplitudes were normalised such that the integral over the distance ( $x$ ) (i.e. area under the profile) are the same for all profiles. FWHM is calculated from the pseudo-Voigt fitting.

$\lambda$ (nm)	relative intensity amplitude		FWHM (nm)
	with probe	without probe	
500	0.85	1.63	276
530	0.87	1.57	271
550	0.88	1.61	270
600	0.82	1.51	277
640	1.00	1.45	252

**Table 5.5:** Summary of simulated intensity profiles for the double-slit apertures with  $w = 470$  nm and  $s = 140$  nm, for 5 different incident wavelengths. The relative intensity amplitudes were normalised such that the integral over the distance ( $x$ ) (i.e. area under the profile) are the same for all profiles. FWHM and peak-to-peak distance are calculated from pseudo-Voigt fitting.

$\lambda$ (nm)	relative intensity amplitude		FWHM (nm)	peak-to-peak (nm)
	with probe	without probe		
500	0.95	1.09	406	627
530	0.96	1.05	407	627
550	0.99	1.05	395	628
600	0.98	1.17	418	631
640	1.00	1.08	422	628

## 5.7 Chapter Summary

For validating the simulation models described and discussed in the previous chapter, analysis were performed using experimental data. Experiments were performed using SNOM scans of well-characterised samples. The samples were slit apertures in a gold film, arranged in the configurations of one isolated slit (single-slit) and two adjacent slits (double-slit). As the samples were one-dimensional, the intensity profiles were investigated in the direction perpendicular to the long axis of the slits. Averaged intensity profiles were calculated to reduce noise from the measurements.

The influence of the probe tip on SNOM image formation was characterised using the probe parameters  $h$  and  $D$ , corresponding to the distance between the probe tip and the sample surface, and the size of the tip aperture, respectively. It was found that  $h$  does not significantly affect the intensity profiles measured using characterisation samples, provided that it is still within near-field range ( $\leq 100$  nm). On the other hand, the parameter  $D$  has a strong influence on the intensity profiles being detected by the SNOM system. Another simulation approach, without involving the probe tip, was also investigated and the results found to be sensitive to the distance of the detector from the sample.

Comparing the simulated intensity profiles with those obtained from the experiment, the 'best fit' parameters were found to be  $h = 10$  nm and  $D = 300$  nm. The parameter  $D$  was, however, overestimated compared to the manufacturers' value for the size of the probe tip, which was attributed to the simplified model of the probe tip in the simulation. The simulation results could reproduce the experimental data with reasonable accuracy. A quantitative comparison was performed using fitting based on pseudo-Voigt function to generate the full-width at half-maximum (FWHM) of the intensity peaks. In the case of double-slit, the peak-to-peak distances were also calculated. It was shown that the predicted peak parameters from the simulation are within the estimated uncertainty ranges for those calculated from the experimental data.

On the other hand, the results obtained from the simulations without the probe tips, showed that it does not realistically provide an accurate description of the intensity profiles derived from the experimental data. The characteristic features of the data were rapid intensity decay at the edges of the slit apertures, showing a sharp contrast between the objects and the background. These were, however, not observed in the experiments, with the profiles strongly affected by the presence of the probe tip.

Knowledge of the probe tip was used for predicting the actual slit size of the slit apertures. This showed potential exploiting *a priori* knowledge of the well-characterised probe tip, although further investigation is needed to analyse the performance. The effects of variation in the wavelength were demonstrated using simulation and it was shown that the



results were not significantly affected by small variations of the wavelength between 500 nm and 640 nm.



## Chapter 6

# Restoring SNOM Images using Deconvolution

### 6.1 Introduction

The point spread function (PSF) is one of the inherent characteristics of imaging devices. As the name implies, it measures how wide a point source or a point object spreads in the image detected by the device. In the case of far-field imaging, the wavenumber  $k_0 = \omega/c$ , determines the limit of the optical signal bandwidth that is possible to detect, which is related to the diffraction limit. The numerical aperture (NA) of the lens being used in the imaging equipment is the practical limit of the possible spatial-frequency bandwidth that can be detected by the imaging system.

In the near-field, the bandwidth is ideally unlimited if the probe tip is infinitely small. In practice, this ideal case is impossible to achieve due to the the probe tip having a finite size. A smaller probe tip produces weaker signals and there is a trade-off between the signal-to-noise ratio and the spatial resolution made possible by using the smallest probe tip. There is also the size limitation depending on the fabrication technique used for the probe tip, as well as the type of the probe tip (i.e. aperture-type tip or scattering-type tip). Nevertheless, SNOM probe tip has a major role in influencing the quality and spatial resolution of the images obtained using SNOM.

Deconvolution is one of the techniques for improving image quality due to the inherent blurring characteristics of the imaging equipment, using knowledge of the PSF. When the PSF of the imaging system is accurately known *a priori*, the results from deconvolution can be more accurate and will produce better results. On the other hand, another deconvolution approach called blind deconvolution is available, which is performed without knowing the exact PSF. However, it has been shown that the accuracy is improved when at least the general behaviour of the PSF is known (called semiblind deconvolution) [7].

Image deconvolution is commonly used for deblurring images due to object movement [114, 115], as well as to improve the images in astronomy [42, 83]. Research into the deconvolution in microscopy has been conducted across several different microscopy techniques, including OCT [85], fluorescent microscopy [86], and confocal microscopy [84]. It has previously been suggested that the deconvolution algorithm may also be applicable in the SNOM imaging [87].

The investigation of the simulation model for SNOM with the probe tip included was discussed in Chapter 4, and the validation of the model with the experimental data was provided in Chapter 5. One of the important results was the confirmation that the probe tip size affects the appearance of the object being imaged. This also affects the spatial resolution of SNOM, which can increase with decreasing probe tip size. With the model having been validated using experimental data, the knowledge of the probe tip influence was characterised. In the simulation model, the probe tip was characterised with the probe parameters  $h$  and  $D$ , which are related to the tip distance from the sample and the probe tip aperture size, respectively. The model was further utilised to improve the results of SNOM scans using deconvolution, which is the main topic of discussion in this chapter.

The PSF of the SNOM system was calculated using the simulation model with the probe tip included, with a circular aperture used as the point source model. The PSF was then used in the deconvolution process to improve the quality of the image measured by SNOM. As previously

mentioned, these effects are largely influenced by the probe tip. The deconvolution process effectively removes the probe tip influence, equivalent to reducing the probe tip to a point size (or to a very small size). This is the ideal condition of near-field imaging where the probe tip effectively has a zero size, leading to better spatial resolution and contrast of the images.

In this chapter, an investigation of a model sample as a point source for determining the PSF is discussed. The sample being used was a circular aperture in a metal film. The PSF was determined using simulation, with examples from experimental data included as a demonstration of the principle. The experimental SNOM images of the slit apertures, used as well-characterised samples, were deconvolved using the PSF of the SNOM system. Deconvolution was performed using the Richardson-Lucy algorithm. As discussed in Chapter 3, this method is relatively simple to apply using an iterative approach, while also robust to the presence of noise [6, 90]. An additional SNOM scan image of the Fresnel zone plate obtained experimentally was also investigated with the deconvolution algorithm. All simulated and experimental data presented here were produced using light with a wavelength of  $\lambda = 640$  nm.

## 6.2 Point Spread Function (PSF) of the SNOM System

In order to use the deconvolution algorithm, the PSF of the imaging system is required. The PSF determines the blurring effects due to the finite resolution of the imaging device, effectively 'spreading' the image of a point source or a point object. In one example from the literature with optical coherent tomography (OCT), the PSF of the imaging system was determined using a solid phantom consisting of gold nanoparticles [85]. The nanoparticles acted as a point source for the OCT system to be imaged. Study of the deconvolution on SNOM images [87] involves a simplified version of the PSF, which was modelled as a circle with a radius of 200 nm. This which was then convolved with the image obtained from

atomic force microscopy (AFM). It was demonstrated that the degraded image could be restored using deconvolution.

The required PSF size was determined using an object smaller than the resolution of the system. In our study, the point source was modelled as a small circular aperture in a metal film. The estimated SNOM resolution was 178 nm (see Section 5.2.3) and circular apertures with a diameter of  $d = 80$  nm,  $d = 100$  nm, and  $d = 150$  nm, were used as well-characterised samples. The gold film had a thickness of 120 nm, the same as that of double-slit apertures. The simulation model was used for calculating a 2D scanned image of the circular aperture as a model for a point source, which included the probe tip.

### 6.2.1 Determining PSF using the Simulation Model

The PSF of the SNOM system was calculated via simulation with the probe tip included (refer to Section 4.2.2). As the object was a circular aperture, the 1D approach was no longer valid. With the slit aperture samples, the probe was moved only in the direction perpendicular to the slit long axis. For the circular aperture sample, a two-dimensional image of the aperture was required. A 2D raster scan was performed with the probe being moved across a designated area of the sample.

The comparison between the three apertures with different diameters is shown in Fig. 6.1, for  $x$ -polarised illumination of circular apertures with  $d = 80$  nm,  $d = 100$  nm, and  $d = 150$  nm. The probe tip parameters were  $h = 10$  nm and  $D = 300$  nm. It can be observed that the profiles for  $d = 80$  nm and  $d = 100$  nm are very similar in size and shape. For the smaller diameter, however, the peak maximum has a lower amplitude and the background noise becomes more visible. The profile for  $d = 150$  nm appears slightly different in shape with the peak elongated in the  $x$ -direction, but in general, the overall size is similar to that using smaller diameters.

The results of the intensity profiles when the aperture was illuminated

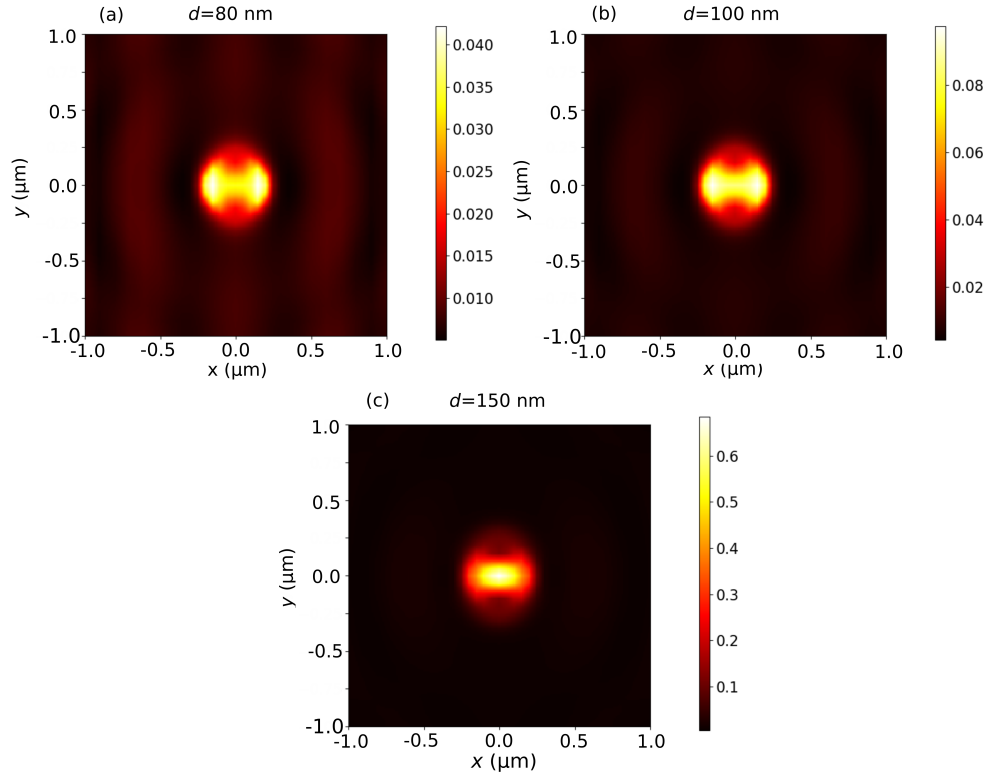


**Figure 6.1:** Simulated intensity profiles of the transmitted light through the circular aperture with diameter (a)  $d=80$  nm, (b)  $d=100$  nm, and (c)  $d=150$  nm, illuminated with  $x$ -polarised beam, detected using a probe tip with  $h = 10$  nm and  $D = 300$  nm.

by unpolarised light are shown in Fig. 6.2, for the same range of diameters. The intensity peaks associated with all apertures have circular symmetry when the light was unpolarised. Again, the resulting profiles obtained from the apertures with  $d = 80$  nm and  $d = 100$  nm are similar. In contrast, the aperture with  $d = 150$  nm produced a more concentrated intensity peak at the centre, with a lower intensity tail at the edges of the peak. The overall sizes of the peaks are similar to each other regardless of the size in this diameter range.

A more significant difference was observed when the probe tip size parameter  $D$  was changed. Figure 6.3 shows the resulting intensity profiles for  $D = 100$  nm and  $D = 500$  nm, in contrast to  $D = 300$  nm used in Fig. 6.1(b). With the same circular aperture size in the sample ( $d = 100$  nm), it can be observed that the size of the peak increases with increasing  $D$ . The diameters of the peaks are approximately 300 nm,

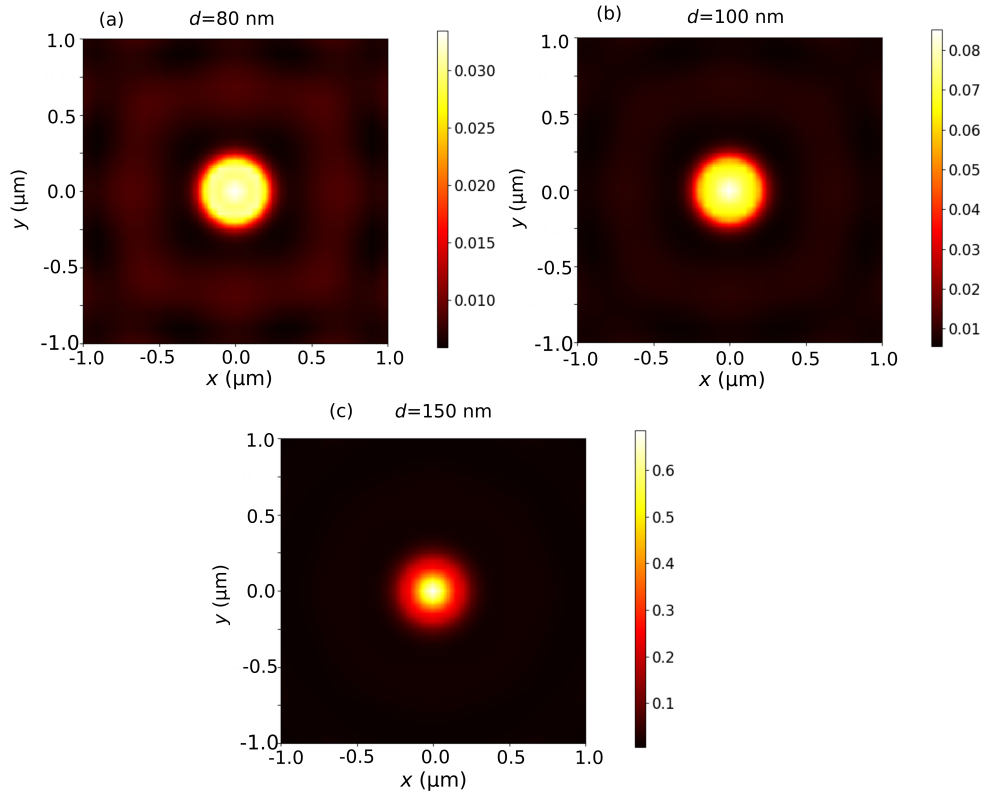


**Figure 6.2:** Simulated intensity profiles of the transmitted light through the circular aperture with diameter (a)  $d = 80$  nm, (b)  $d = 100$  nm, and (c)  $d = 150$  nm, illuminated with unpolarised beam, detected using a probe tip with  $h = 10$  nm and  $D = 300$  nm.

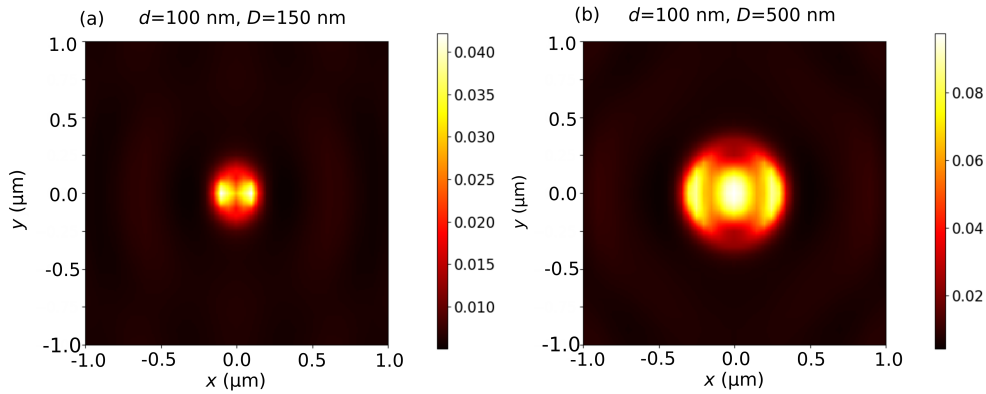


**Figure 6.3:** Simulated intensity profiles of the transmitted light through a circular aperture with diameter  $d = 100$  nm, illuminated with an x-polarised beam, detected using the probe tip with the size of (a)  $D = 150$  nm and (b)  $D = 500$  nm.



500 nm, and 700 nm, for  $D = 150$  nm,  $D = 300$  nm, and  $D = 500$  nm respectively. With  $x$ -polarised illumination, the characteristics of brighter intensity in the  $x$ -direction can be observed in all cases.

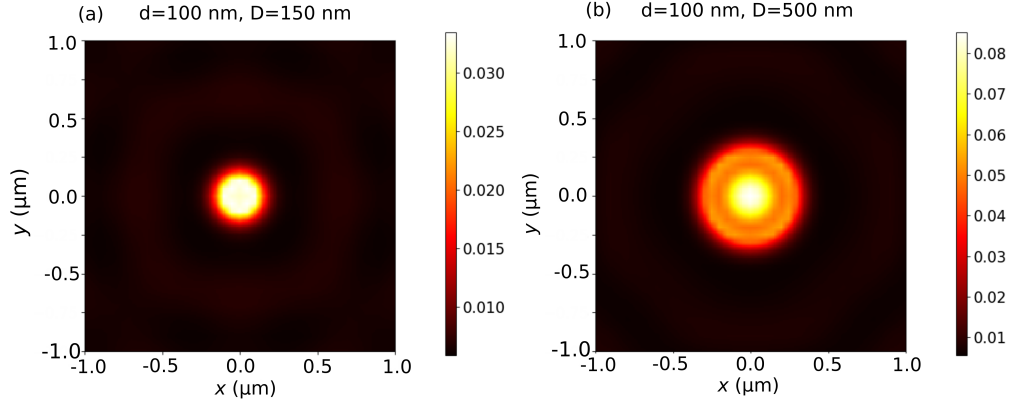


**Figure 6.4:** Simulated intensity profiles of the transmitted light through the circular aperture with diameter  $d = 100$  nm, illuminated with an unpolarised beam, detected using a probe tip with the size of (a)  $D = 150$  nm and (b)  $D = 500$  nm.

Consistent with the results for  $x$ -polarisation, the peaks observed from the transmitted signal through the circular aperture with unpolarised light appeared to increase with increasing probe size,  $D$ . These are shown in Fig. 6.4, with the intensity peaks having rounder shapes compared to those calculated using  $x$ -polarisation. The intensity profiles for smaller diameters,  $d \leq 100$  nm, are more homogeneous compared to the intensity profile associated with larger hole diameter,  $d = 150$  nm.

### 6.2.2 Determining PSF from the Experimental Data

Another set of samples was fabricated, consisting of circular apertures with diameters of  $d = 80$  nm,  $d = 100$  nm, and  $d = 150$  nm in a thin gold film of thickness 120 nm. SEM images of the circular apertures are shown in Fig. 6.5. Fabrication was performed by Dr. Guangyuan Si at MCN, with the sample being designed by the author. These apertures were used as a point object for determining the PSF of the SNOM system experimentally.

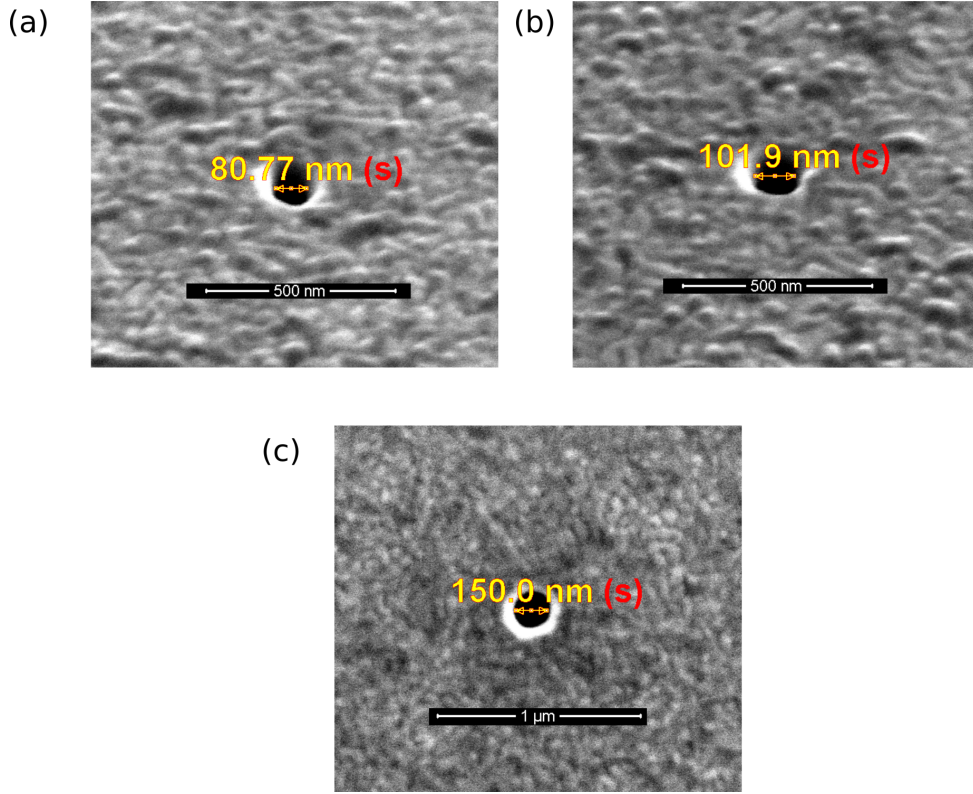


**Figure 6.5:** SEM images of the circular apertures in a metal film with a diameter of (a)  $d = 80$  nm, (b)  $d = 100$  nm, and (c)  $d = 150$  nm.

The circular aperture samples were scanned using SNOM and the scan results are shown in Fig. 6.6. These images were used as the experimental PSF for deconvolving the SNOM images. This experimental method for determining the PSF is equivalent to the simulation model described in the previous section. The circular apertures had different sizes, but the resulting scanned images did not show significant differences in terms of the peak size in the PSF. This is consistent with what was found using the simulation model. The images, however, were scanned with a slightly blunt probe tip, which was confirmed by the inspection under the microscope before SNOM scanning was performed. This effectively made the resulting intensity peaks larger than expected based on the simulation.

Figure 6.7 shows a comparison between the PSF obtained from the simulation and from the experiment. Using the polarisation parallel to the  $x$ -axis, the image predicted from the simulation has brighter intensity

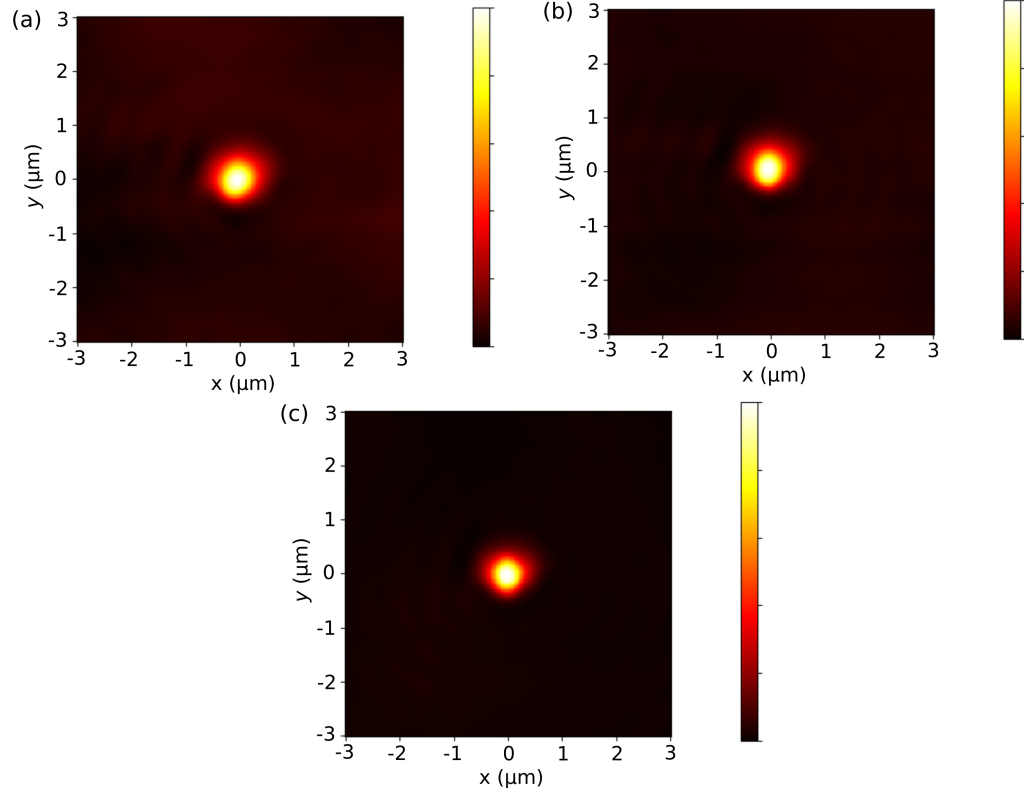


**Figure 6.6:** Experimental data obtained from the SNOM scans of circular apertures in a metal film with a diameter of (a)  $d = 80$  nm, (b)  $d = 100$  nm, and (c)  $d = 150$  nm (the colour range is not to scale).

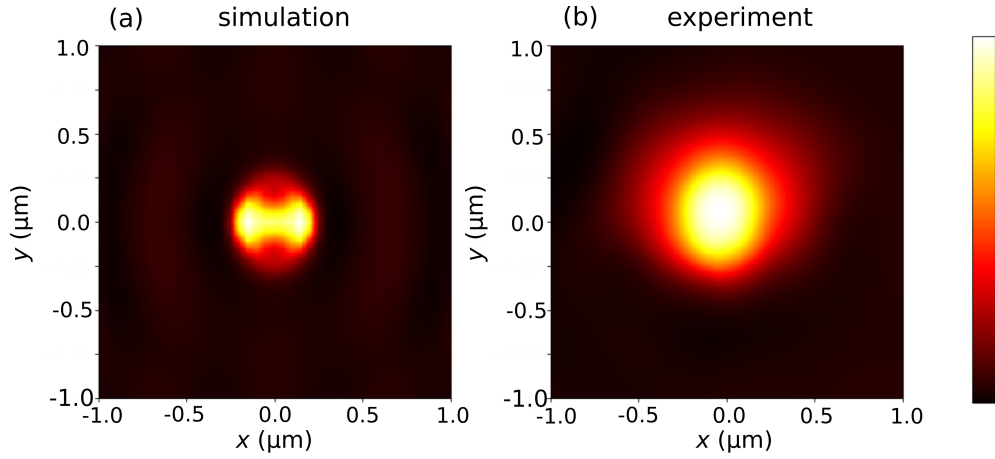


**Figure 6.7:** Comparison between (a) simulated and (b) experimental PSF, using a SNOM scan of a circular aperture with  $d = 100$  nm.

in the  $x$ -direction, whereas the experimental image does not show this symmetry. Although the shape is slightly asymmetric, it is closer to being

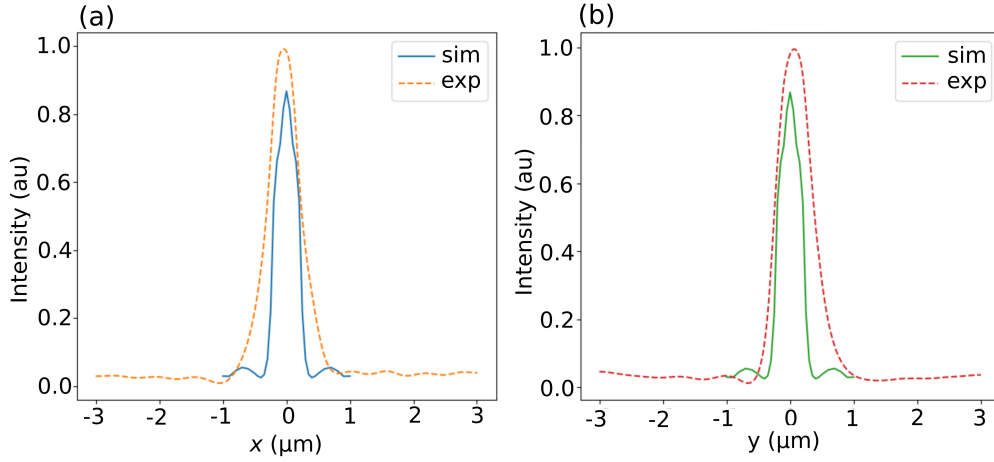


**Figure 6.8:** The (a)  $x$ - and (b)  $y$ -sections of the intensity profiles of simulated (sim) and experimental (exp) PSF shown in Fig. 6.7, along the lines through the centre of the image.

circular in shape. The probe had an imperfection not accounted for in the simulation, and it had overestimated the size of the intensity peak in the image compared to the simulated results, although the diameter of the intensity peaks from both simulation and experiment are still relatively similar in size.

The sections through the  $xy$ -axes of the intensity profiles, through the centre of the simulated and experimental PSF are shown in Fig. 6.8. In Fig. 6.8(a) (through the line  $y = 0$  nm), the peak calculated from the simulation has a slightly smaller size, with sharper edges, compared to the experimental image. The difference between the profiles is larger Fig. 6.8(b) (through the line  $x = 0$  nm), with the experimental peak having a larger width compared to the simulated one. These discrepancies were noted when these were used in the deconvolution process, as discussed in Section 6.5.3 in this chapter.

### 6.3 Denoising SNOM Images

Before the deconvolution algorithm was applied, the noise in the images was reduced using the total variation method by Chambolle [116], with a weighting parameter  $W$  determining the ‘strength’ of the denoising. The denoised image is important for the deconvolution algorithm to produce

a clear deconvolved image [87]. Although the Richardson-Lucy deconvolution algorithm is robust with respect to noise, the results of the deconvolved images are improved when the denoising algorithm was applied before the image is deconvolved.

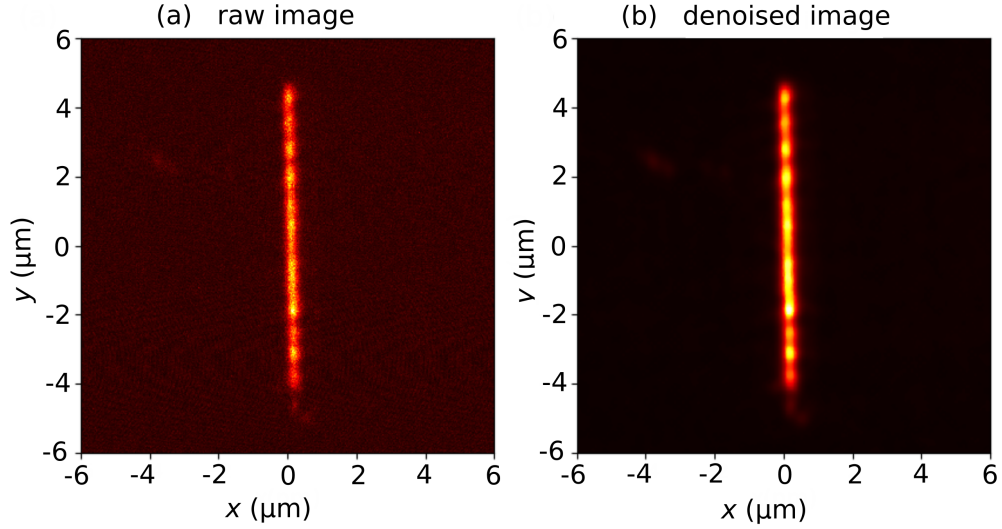


**Figure 6.9:** The images of a single-slit aperture with  $w = 180$  nm, (a) before and (b) after the noise was reduced.

Two examples of comparison between images before and after denoising are given in Fig. 6.9 and 6.10, for single-slits of two different sizes. The ‘grainy’ background noise in the raw image was removed, and a darker background can be observed in the denoised image. Both single-slit images appeared with more contrast between the slit image and the background.

In both cases, the denoising process was performed sparingly and only used to remove the background noise without impacting the sample. The weighting parameter used for denoising was  $W = 0.01$ . Excessive denoising could alter the intensity profile and produce a different image to that observed in the raw image. Hence, it can lead to an inaccurate representation of the object in the image.

An example of overly aggressive denoising is shown in Fig. 6.11, using a weighting parameter of  $W = 0.2$ . In this case, the slit aperture appears larger than was observed in the raw image. The slit in the denoised image has a width  $w = 180$  nm, and the resulting denoised image appears to have a similar width to the single-slit with  $w = 410$  nm. The

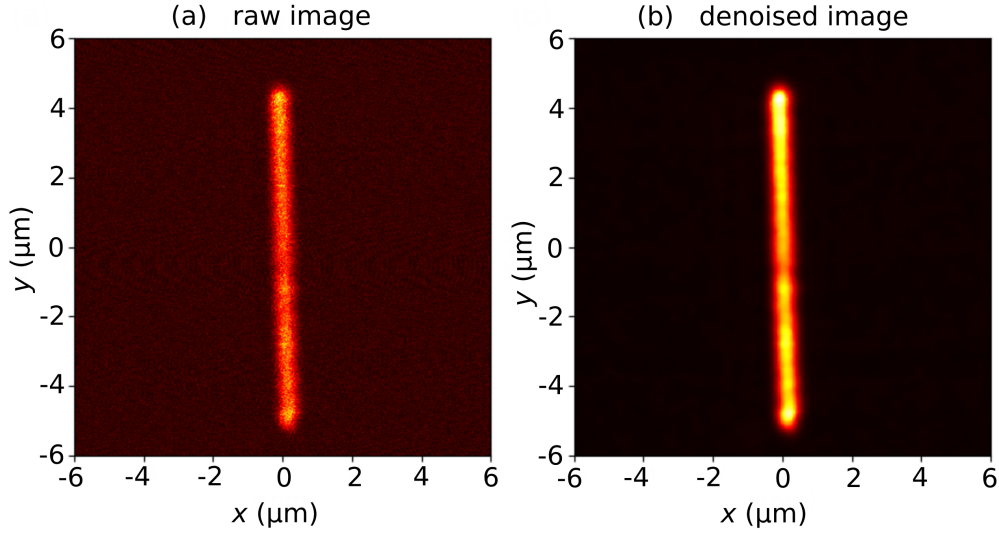


**Figure 6.10:** The images of a single-slit aperture with  $w = 410$  nm, (a) before and (b) after the noise was reduced.

error, which can potentially be produced by the denoising process, can impact the deconvolution process, producing an inaccurate deconvolved image. Hence, it is important to ensure that appropriate noise removal is performed to produce a good quality image.

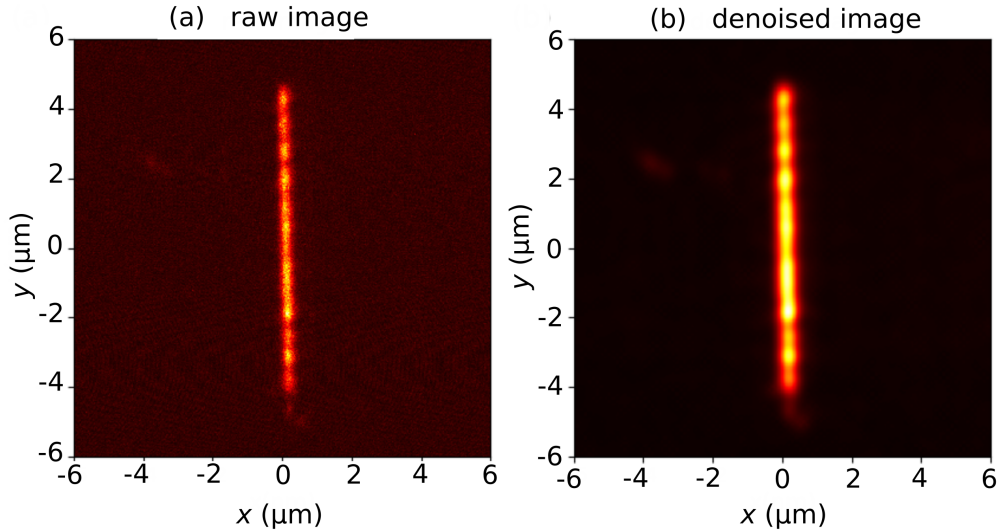


**Figure 6.11:** The images of a single-slit aperture with excessive denoising leads to innacurate image. Images are shown for single-slit with  $w = 180$  nm, (a) before and (b) after denoising.



## 6.4 Convergence Test with Gaussian and Pseudo-Voigt PSF

A simple approximation of the PSF of the system was used to test the convergence of the deconvolution algorithm. It was demonstrated in Chapter 5 that the intensity profiles of slit apertures can be fitted with the pseudo-Voigt function, a linear combination of Gaussian and Lorentzian functions. The PSF had a FWHM of 300 nm, consistent with the probe parameter  $D = 300$  nm demonstrated in the previous chapter. The PSF using this approach is shown in Fig. 6.12.

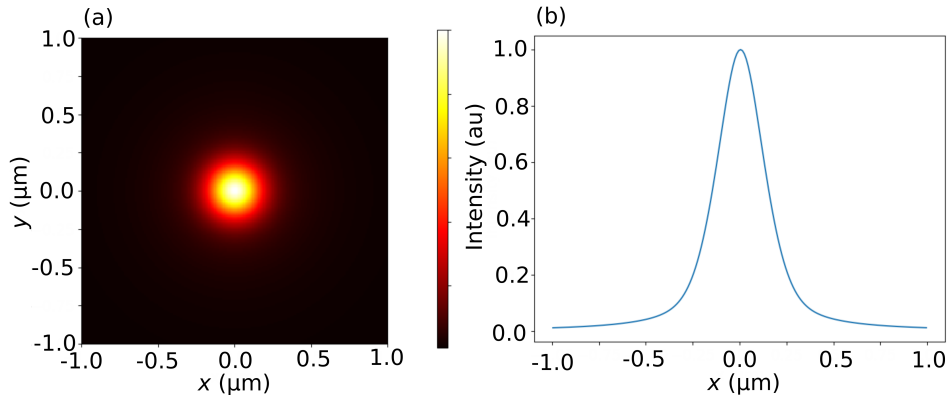


**Figure 6.12:** (a) Approximated PSF using pseudo-Voigt function with FWHM=300 nm and (b) its line profile across the centre.

The Gaussian or pseudo-Voigt function allows for a fast approximation of the PSF of the SNOM system. A larger SNOM probe tip produces a PSF with a wider intensity peak (refer to Section 6.2.1). Changing the FWHM effectively means that the SNOM probe tip has a larger tip size. With a symmetrical round shape, this approximates the simulated PSF obtained using the unpolarised light.

The convergence test with a Gaussian function as the PSF is shown in Fig. 6.13 for a single-slit aperture. The deconvolved images were captured at several different iterations of the algorithm, up to 200 iterations. The original image shown has been denoised with a total variation method. With 20 iterations, the image exhibited more contrast and the apparent width became smaller. The image continued to improve at the 50th iteration, with a narrower apparent width of the aperture, closer to

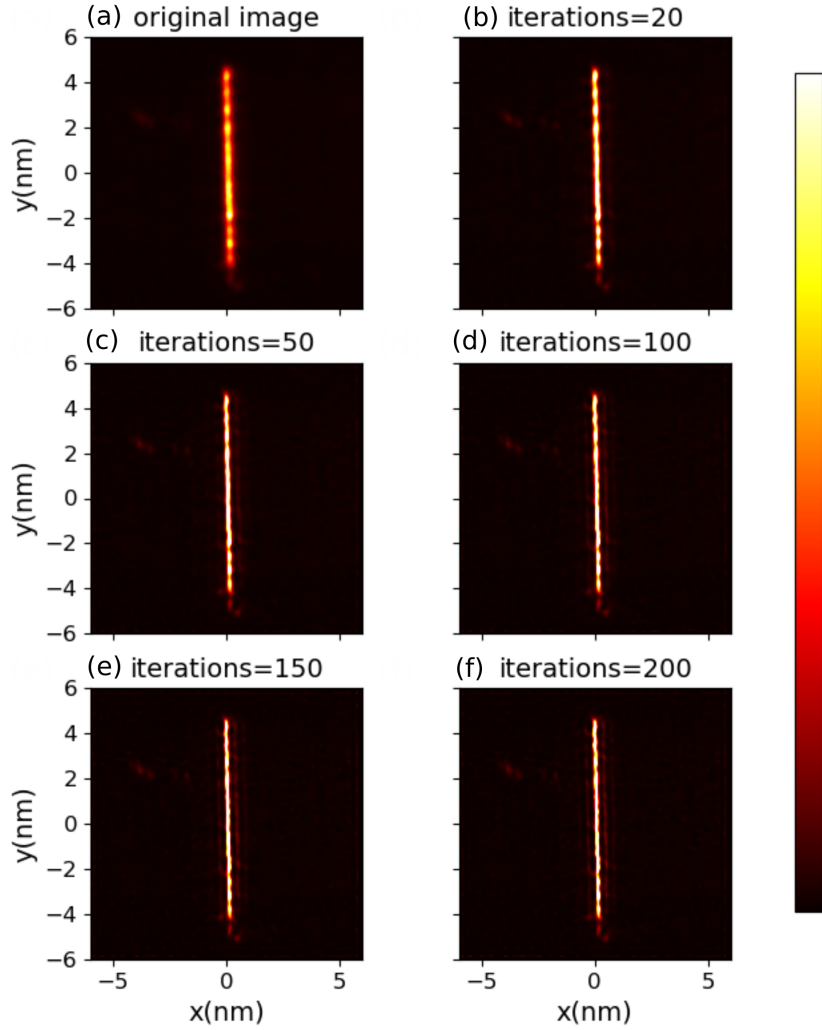


**Figure 6.13:** Deconvolution process of a single-slit aperture with  $w = 180$  nm using a Gaussian PSF with FWHM=300 nm, showing (a) original image before deconvolution, and (b-f) the resulting deconvolved images after 20, 50, 100, 150, and 200 iterations.

the actual width observed. This is discussed further in Section 6.5. At the 100th, 150th, and 200th iterations, the change is barely visible and the results from further iterations all appear very similar. The resulting image at the 100th iteration, however, appears slightly wider than those at the 150th and 200th iteration. It can be concluded that to reach the converged solution of the deconvolved image in this situation, at least 150 iterations are required.

As previously demonstrated in Chapter 5, the pseudo-Voigt function



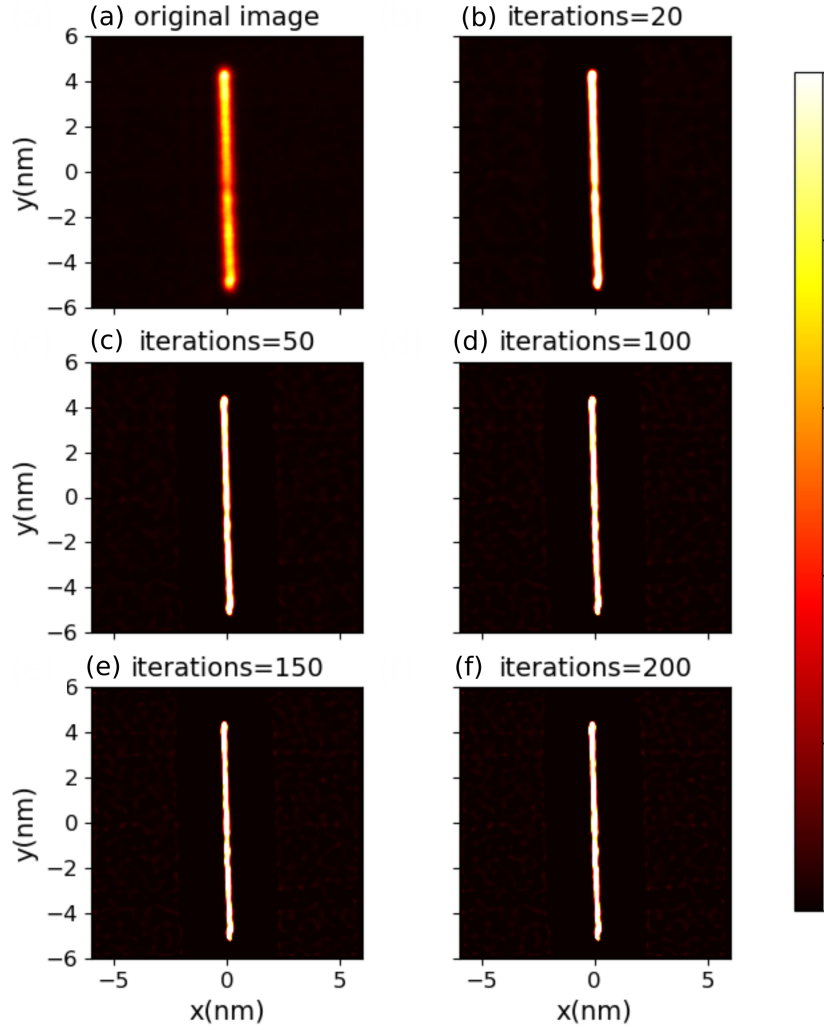


**Figure 6.14:** Deconvolution process of a single-slit aperture with  $w = 180$  nm using a pseudo-Voigt PSF with FWHM=300 nm, showing (a) original image before deconvolution, and (b-f) the resulting deconvolved images after 20, 50, 100, 150, and 200 iterations

provides a reasonable best fit to the intensity profile. The behaviour of the intensity profile of a small circular aperture is expected to be similar. In that case, instead of using Gaussian function like in Fig. 6.13, the PSF was approximated with pseudo-Voigt function and the convergence test on the same slit aperture is shown in Fig. 6.14. The linear combination factor was set at  $\eta = 0.5$ , based on the fitting results of the intensity profile of the slit aperture.

In both cases of PSF with Gaussian and pseudo-Voigt functions, the

deconvolution process converges after the same number of iterations. The deconvolution result using a pseudo-Voigt PSF, however, produced a sharper image compared to the Gaussian PSF. For the model samples studied here, the pseudo-Voigt function provides a better approximation of the PSF.

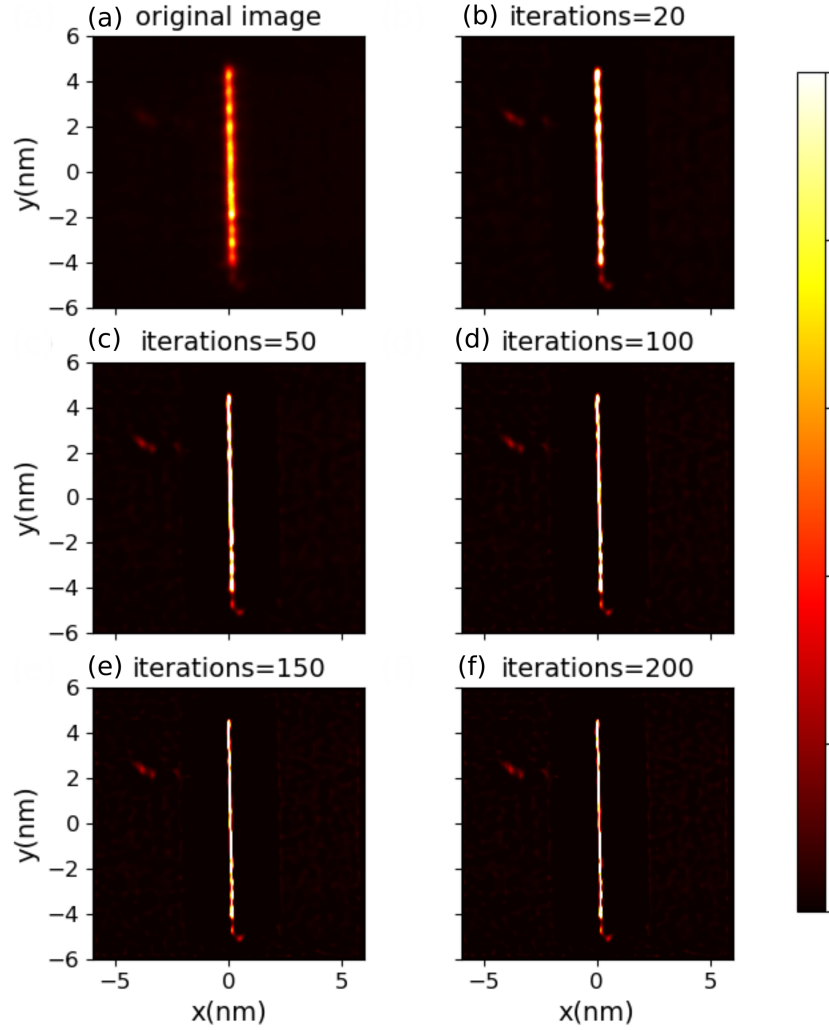


**Figure 6.15:** Deconvolution process for a single-slit aperture with  $w = 410$  nm using a pseudo-Voigt PSF with FWHM=300 nm, showing (a) original image before deconvolution, and (b-f) the resulting deconvolved images after 20, 50, 100, 150, and 200 iterations

Figure 6.15 shows the deconvolution process using the pseudo-Voigt function for a larger slit aperture with a size of 410 nm. Convergence

occurred after fewer iterations and after 50 iterations, the image did not change significantly. The final deconvolved image had excellent contrast.

It can be concluded that a certain number of iterations has to be performed to reach a converged solution for the deconvolved image [117, 118]. Based on the test with a single-slit aperture, the minimum number of iterations is 150. All deconvolution results shown in the following sections were performed with 200 iterations to ensure convergence in all images.

## 6.5 Deconvolution of Slit Apertures Images

The experimental SNOM images of model samples and slit apertures, investigated in Chapter 5 were analysed further using deconvolution. The aim is to demonstrate the ability of the deconvolution algorithm to restore the image to its ideal quality. The images were deconvolved using the Richardson-Lucy algorithm with the PSF determined from pseudo-Voigt approximation, FDTD simulation, and the experiment using a SNOM scan. The improvements in the image quality after deconvolution are discussed.

### 6.5.1 Deconvolution with Gaussian and Pseudo-Voigt PSF

As previously discussed, the PSF with Gaussian and pseudo-Voigt functions provide a fast approximation of the PSF to predict the resulting deconvolved image. A more accurate calculation of the PSF is also discussed in Section 6.5.2, with the images deconvolved using PSF obtained from the simulation. The simulation included the probe tip as a crucial component of the SNOM system.

The original and final images in the deconvolution process in Fig. 6.14 are shown in Fig. 6.16. The deconvolution was performed using a Gaussian PSF with FWHM = 300 nm. The deconvolved image shows a sharper image with better contrast and narrower width. The size of the slit appearing in the deconvolved image is a better representation of the actual slit, observed in the SEM images.

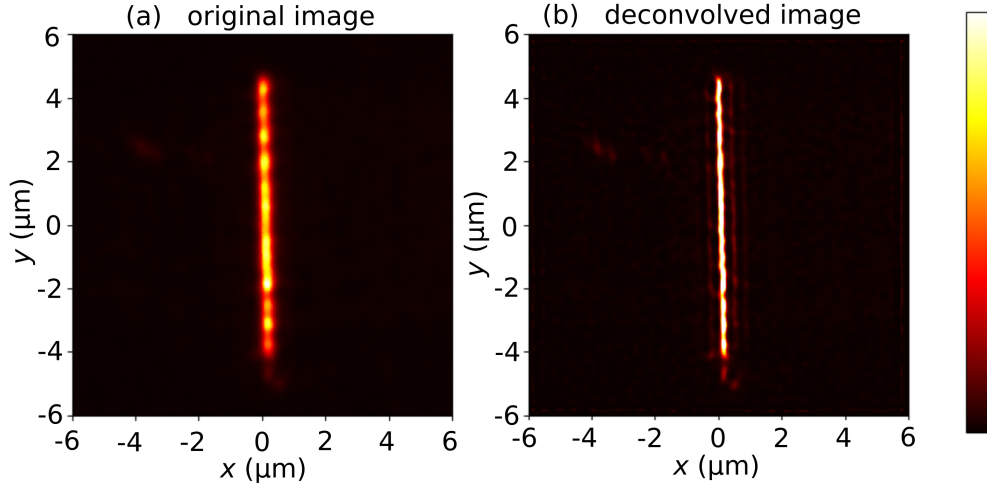


**Figure 6.16:** Deconvolution of the SNOM image of a single-slit aperture with  $w = 180$  nm using Gaussian PSF with FWHM=300 nm, showing (a) original image before deconvolution and (b) deconvolved image.

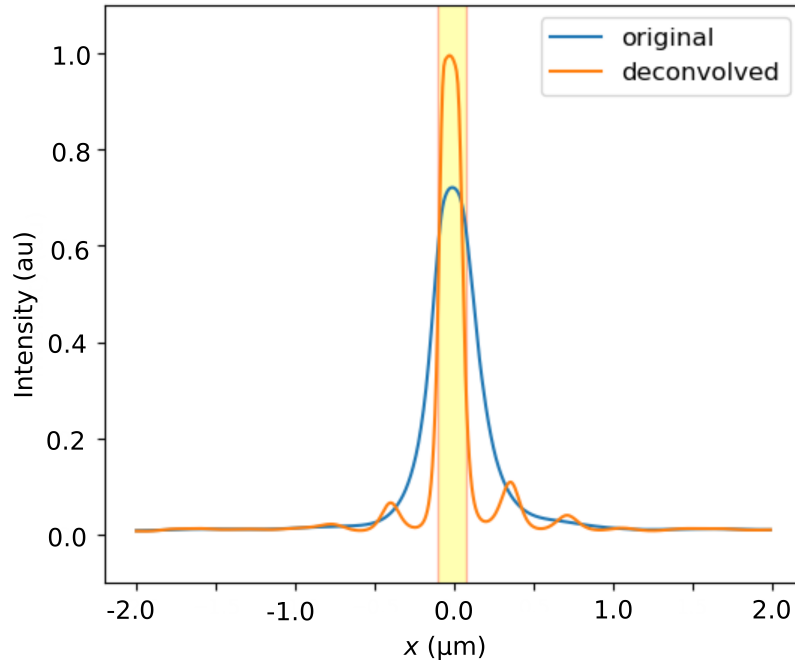


**Figure 6.17:** Intensity profile across the slit from the original and deconvolved images of single-slit aperture with  $w = 180$  nm, using a Gaussian PSF with FWHM=300 nm.

To analyse the shape of the intensity profile, the intensity in the direction perpendicular to the slit was calculated by taking the average values from multiple line scans (refer to Section 3.2.2 in Chapter 3). The 1D

profile for this single-slit aperture is shown in Fig. 6.17. The expected physical location of the slit is indicated by the yellow shaded rectangle. After deconvolution, the width of the slit is closer to the value measured using SEM. The peak, however, after deconvolution appears to exhibit small oscillations near the edges of the aperture, which is an artifact from the deconvolution process known as ringing artifacts [119–121]. These ripples were reduced in the deconvolved images using a simulated and experimental PSF discussed in Sections 6.5.2 and 6.5.3.

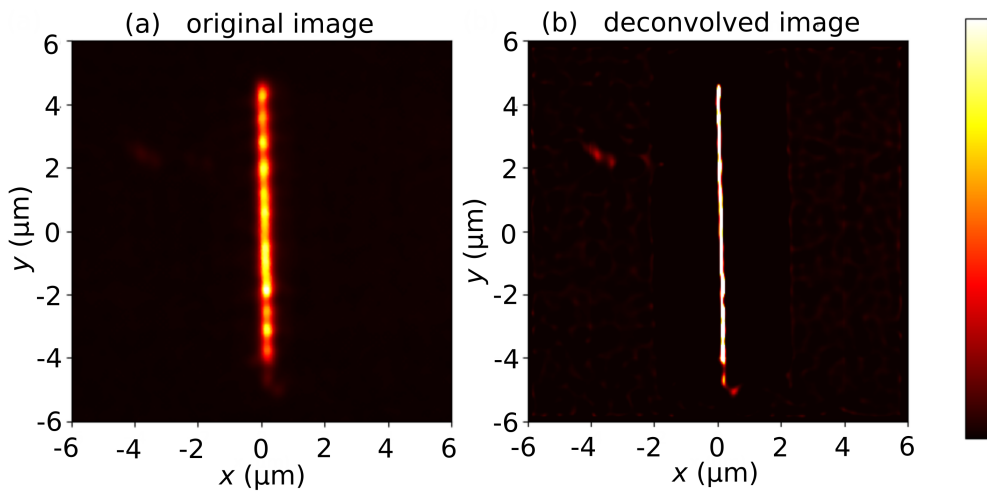


**Figure 6.18:** Deconvolution of the SNOM image of the single-slit aperture with  $w = 180$  nm using the pseudo-Voigt PSF with FWHM=300 nm, showing (a) original image before deconvolution and (b) deconvolved image.

A better representation of the PSF was provided by the pseudo-Voigt function compared to the Gaussian function. This is reflected in the result of the deconvolution using the pseudo-Voigt function as the PSF. The deconvolved image shows similar characteristics to the deconvolved image with the Gaussian function, but it appears with less ringing artifacts and a sharper image.

A closer analysis of the 1D intensity profile across the slit, shown in Fig. 6.19, shows that the full width of the peak appears inside the location of the slit, indicated by the yellow shaded rectangle. The deconvolved image now appears without the ripple of oscillations at the edges of the peak, which were observed when using deconvolution with a Gaussian PSF. It can be concluded that the pseudo-Voigt function is the

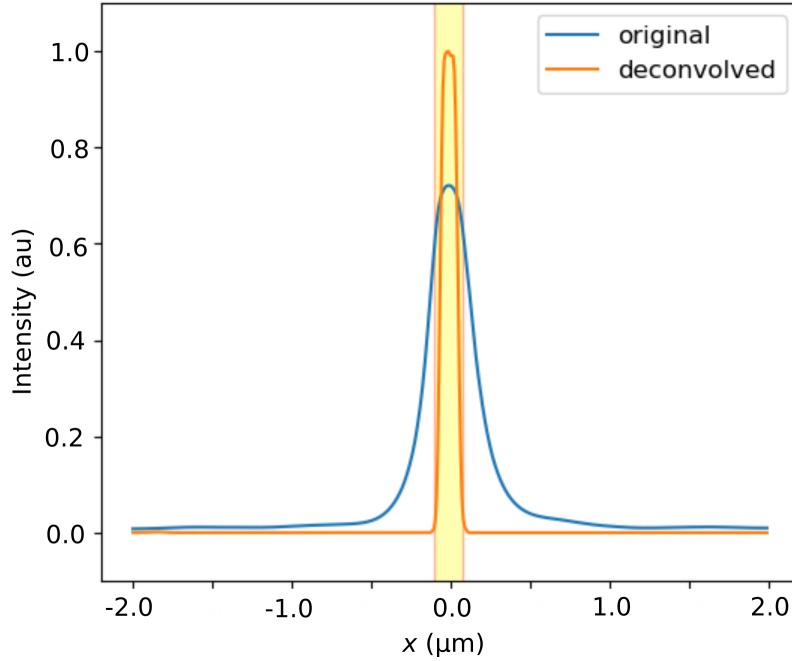


**Figure 6.19:** Intensity profile taken across the slit for the original and deconvolved images of the single-slit aperture with  $w = 180$  nm, using the pseudo-Voigt PSF with FWHM=300 nm.

more appropriate function for approximating the PSF of the SNOM, with the model sample composed of slit apertures.

A further analysis of the PSF was performed with a different width of the pseudo-Voigt function, with FWHM= 150 nm and 500 nm. This is equivalent to deconvolving the image with a different probe tip size. The intensity profiles across the slit with this variation of the PSF are shown in Fig. 6.20. Using a PSF with smaller FWHM led to the deconvolved image producing an aperture with larger width. On the other hand, when the PSF had a large FWHM, the deconvolution made the aperture become smaller, suggesting that the deconvolution aggressively reduced the size of the objects on the image.

These results for the variation of the peak width (FWHM) of the PSF are expected. If the probe tip is very small, the resolution of the image is very high, so that the resulting image is already close to its actual size and shape. Using the PSF with a small width in this case means that it is assumed that the probe tip used for obtaining the image was already extremely sharp and the deconvolution only has a very minor influence

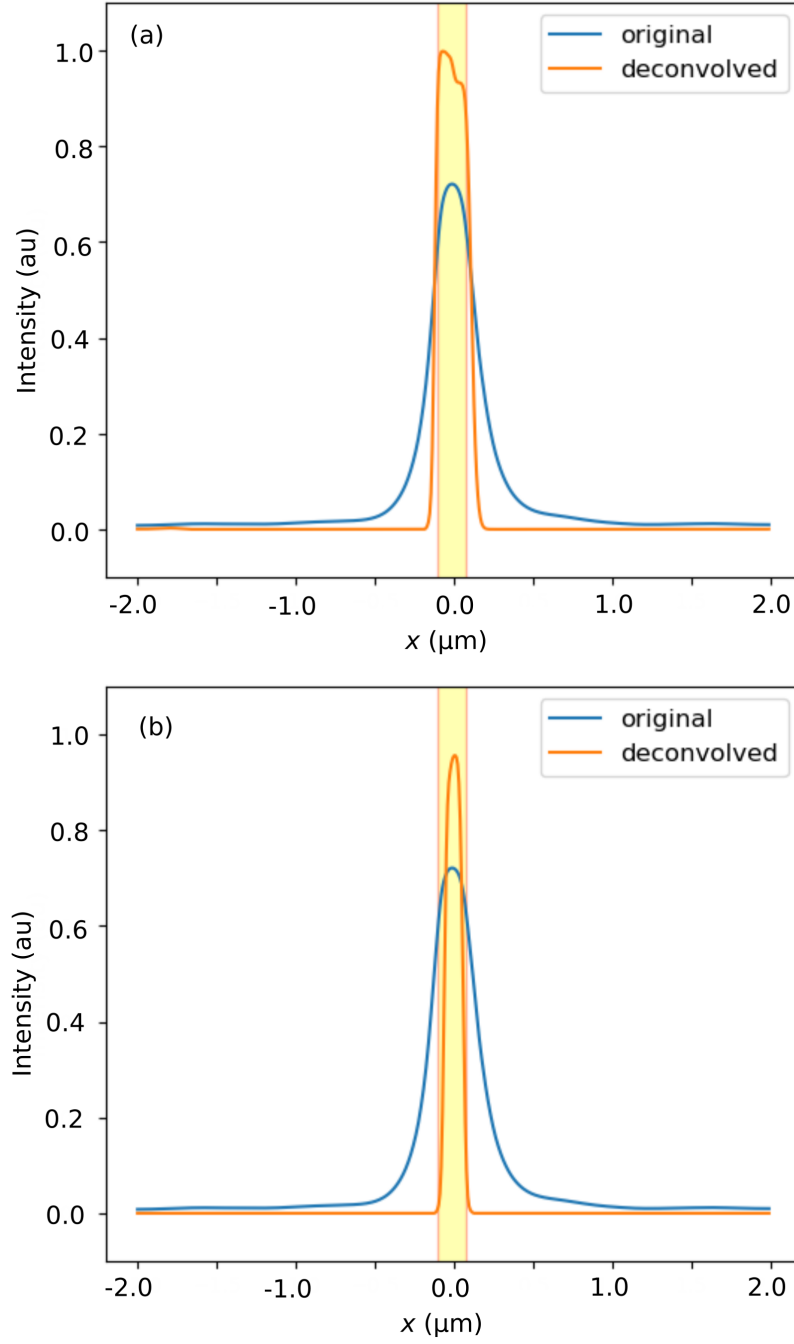


**Figure 6.20:** Intensity profile across the slit for the original and deconvolved images of the single-slit aperture with  $w = 180$  nm, using the pseudo-Voigt PSF with (a) FWHM=150 nm and (b) FWHM=500 nm.

on the intensity profile. In the experiment, the probe tip parameter for this slit was  $D = 300$  nm, confirming it to be the best width of the peak for the PSF being used. On the other hand, a large peak width in the PSF

results in more aggressive deconvolution, reducing the width of the slit in the deconvolved image.

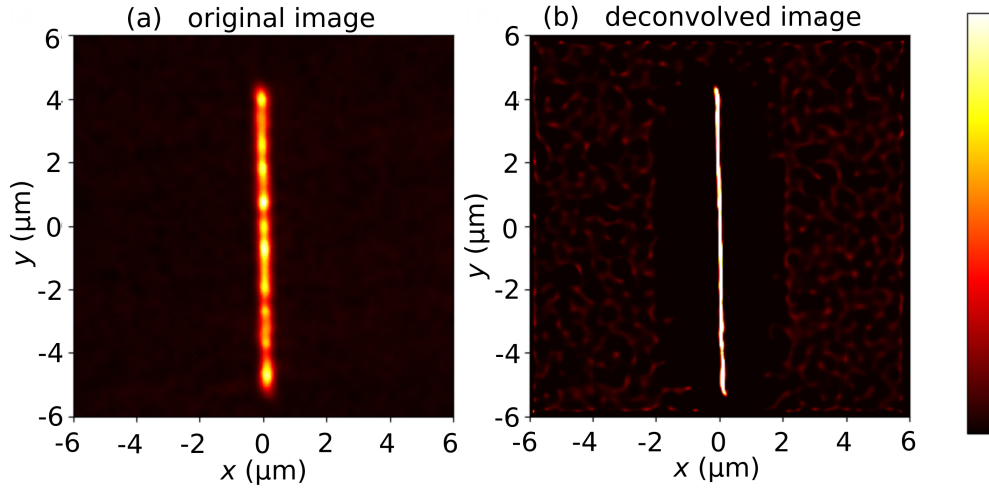


**Figure 6.21:** Deconvolution of the SNOM image of a single-slit aperture with  $w = 150$  nm using the pseudo-Voigt PSF with FWHM=300 nm, showing (a) original image and (b) deconvolved image.

Further testing with the pseudo-Voigt PSF was performed using different aperture sizes. The images of single-slit apertures with a size of  $w = 150$  nm and 410 nm were deconvolved, the results are shown in Fig. 6.21 to 6.24.

In Fig. 6.21, an image of a slightly smaller aperture,  $w = 150$  nm, could be deconvolved using the pseudo-Voigt PSF. The deconvolved image shows a much thinner slit that is closer to the SEM result. The width of the aperture is confirmed in Fig. 6.22, in which the whole intensity peak is located inside the yellow shaded area, where the location of the aperture is expected.

The result of image deconvolution of a single-slit aperture with  $w = 410$  nm is shown in Fig. 6.23, with the intensity line profile shown in Fig. 6.23. It is interesting to see how the algorithm works for a larger size of aperture. We observe that the deconvolved image has excellent contrast. It is clear that the result for  $w = 410$  nm shows an aperture with a larger width. The size can be confirmed from the intensity line profile for this slit. The actual width of the slit is the same as the width of the yellow shaded rectangle in Fig. 6.24. Compared to the smaller apertures, the



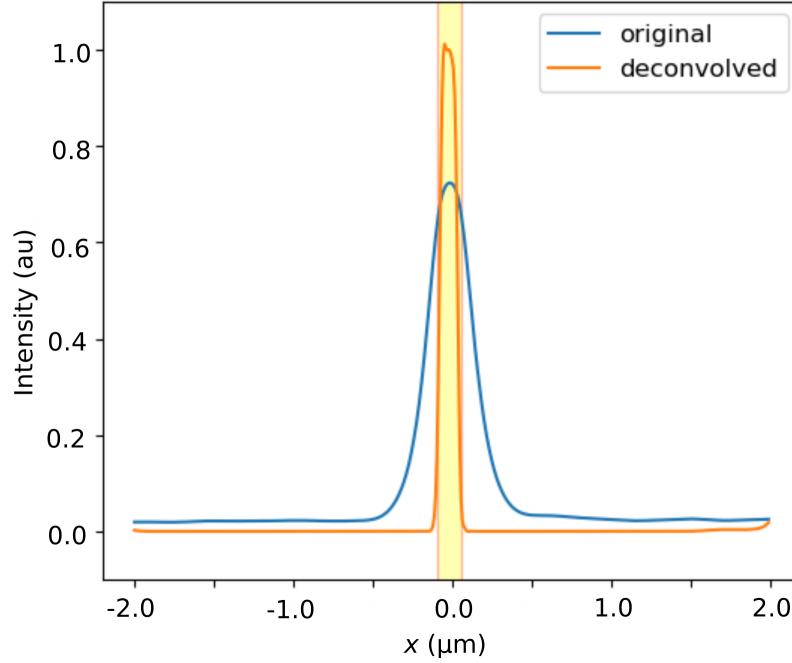


**Figure 6.22:** Intensity profile across the slit using the original and deconvolved images of a single-slit aperture with  $w = 150$  nm, using the pseudo-Voigt PSF with FWHM=300 nm.

whole intensity peak in the deconvolved image lies inside the expected location of the slit. The peak is narrower than the actual slit itself. Nevertheless, the shape of the peak is closer to being a top-hat function than a smooth Gaussian or pseudo-Voigt curve. The discrepancies can be attributed to imperfections of the pseudo-Voigt function to model PSF of the SNOM.

It can be concluded that despite some inaccuracies in the larger-sized aperture, the pseudo-Voigt function is able to approximate the PSF of the SNOM. The width of the peak in the PSF is correlated to the size of the probe tip, which can be altered easily when generating the function. A more accurate approach is using the simulated PSF, which is a more realistic representation of the actual experiment when the image was acquired using SNOM.

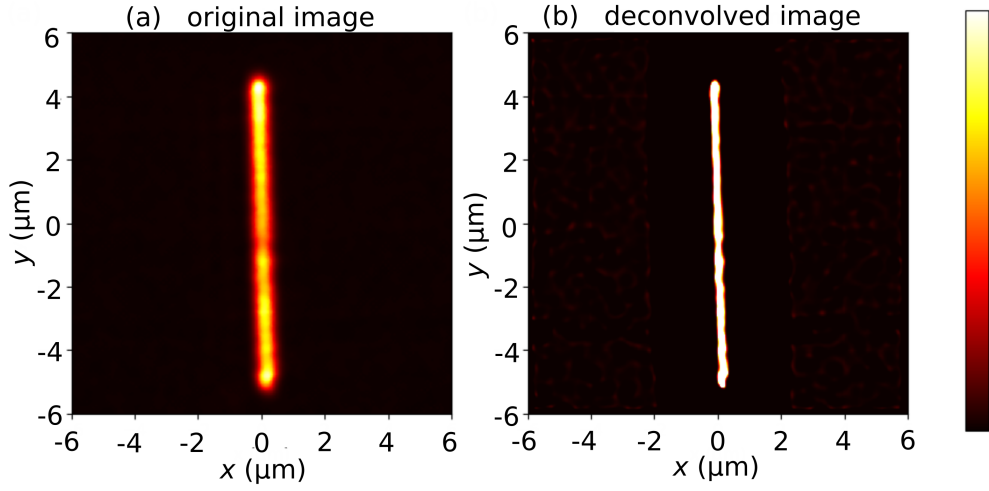


**Figure 6.23:** Deconvolution of the SNOM image of a single-slit aperture with  $w = 410$  nm using the pseudo-Voigt PSF with FWHM=300 nm, showing (a) original image before deconvolution and (b) deconvolved image.

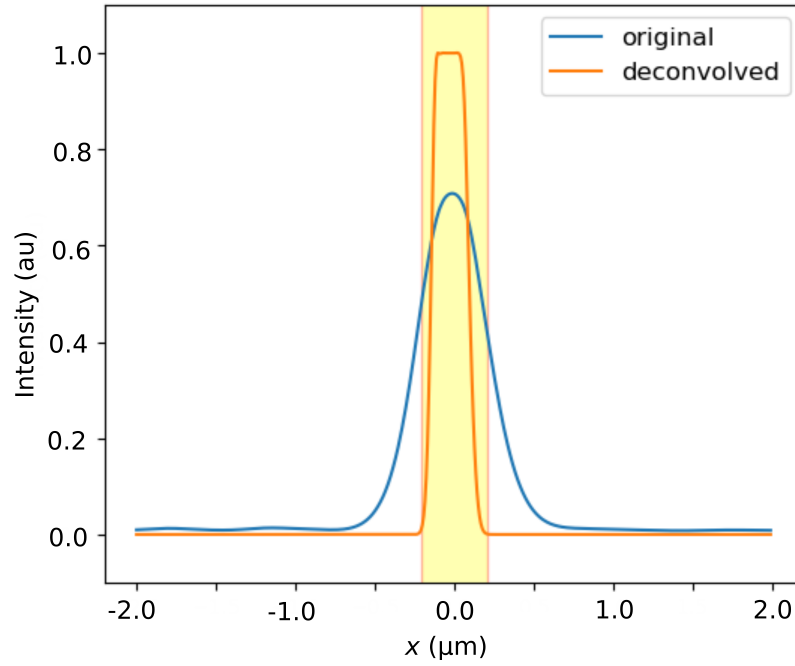


**Figure 6.24:** Intensity profile across the slit for the original and deconvolved images of single-slit aperture with  $w = 410$  nm, using the pseudo-Voigt PSF with FWHM=300 nm.

### 6.5.2 Deconvolution with a Simulated PSF

The simulated PSF was discussed in Section 6.2.1. The simulation uses a more detailed calculation than the approximation using either Gaussian or pseudo-Voigt function. Hence, it is expected that a more accurate representation of the PSF will lead to a better deconvolution result, with a more accurate image representing its true size and shape.

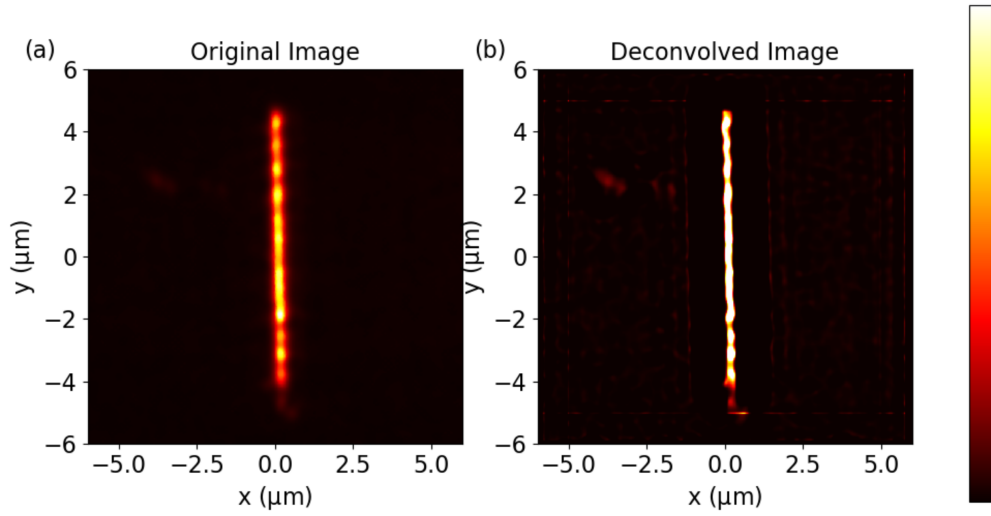


**Figure 6.25:** Deconvolution of the SNOM image for a single-slit aperture with  $w = 180$  nm using a simulated PSF obtained from a circular aperture with  $d = 100$  nm and probe parameters  $h = 10$  nm and  $D = 300$  nm, showing (a) original image before deconvolution and (b) deconvolved image.

The deconvolution of a single-slit aperture image with  $w = 180$  nm using a simulated PSF is shown in Fig. 6.25. The resulting deconvolved image shows a very good contrast with a flatter peak observed in the intensity profile. The deconvolution worked well, producing an image of the aperture with a narrower width, which is closer to its actual width. The performance of this deconvolution is equivalent to that when using the approximate pseudo-Voigt function.

Using a simulated PSF, the slit aperture could be restored to its original width. This was confirmed by looking at the intensity profile across the slit, shown in Fig. 6.26. The width of the intensity peak is within the width of the actual slit indicated by the yellow-shaded rectangle in the

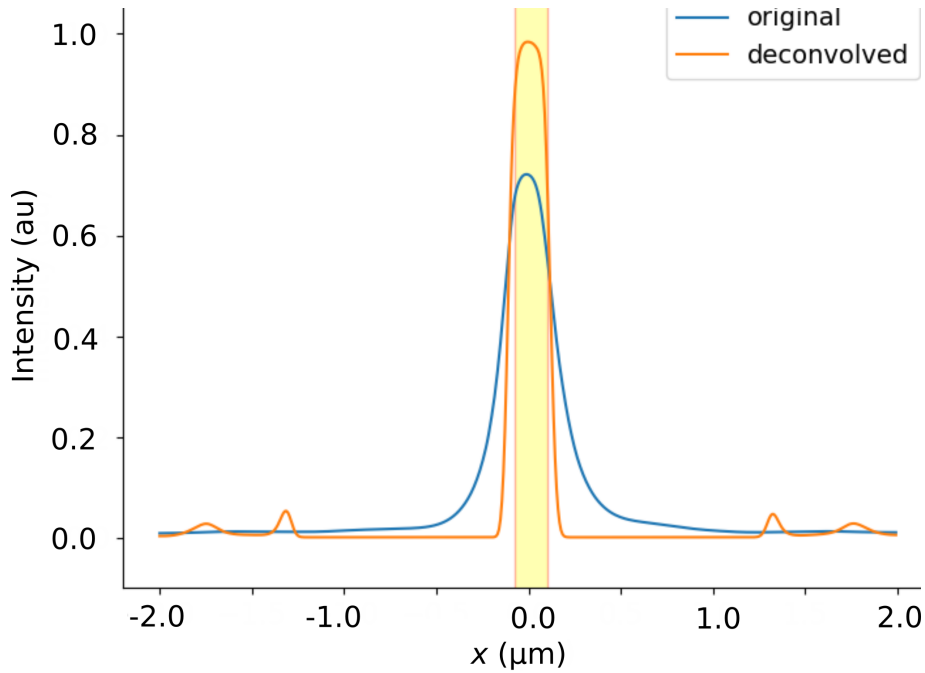


**Figure 6.26:** Intensity profile across the slit for the original and deconvolved images of a single-slit aperture with  $w = 180$  nm, using a simulated PSF obtained from a circular aperture with  $d = 100$  nm and probe parameters  $h = 10$  nm and  $D = 300$  nm.

figure. In the model, the probe tip was set according to the best-fit parameters discussed in Chapter 5, with the probe tip parameters  $h = 10$  nm and  $D = 300$  nm. There are two small peaks found at both sides of the main peak, which are not present in the original image. The deconvolution produces a ringing effect which is a common artifact in the deconvolution process [119, 121], but it is located reasonably far from the object compared to the result using the PSF approximated with the pseudo-Voigt function.

The simulated PSF used on the image of a single-slit aperture with  $w = 180$  nm was also tested using a single-slit with different widths. The results for the deconvolved images are shown for  $w = 150$  nm and 410 nm in Fig. 6.27. Again, the simulated PSF was able to improve the quality of the SNOM images resulting in better contrast and spatial resolution. The width of the slit could be recovered to match the SEM determined width. This time, the slit aperture with the larger width appears to be more accurately reproduced.

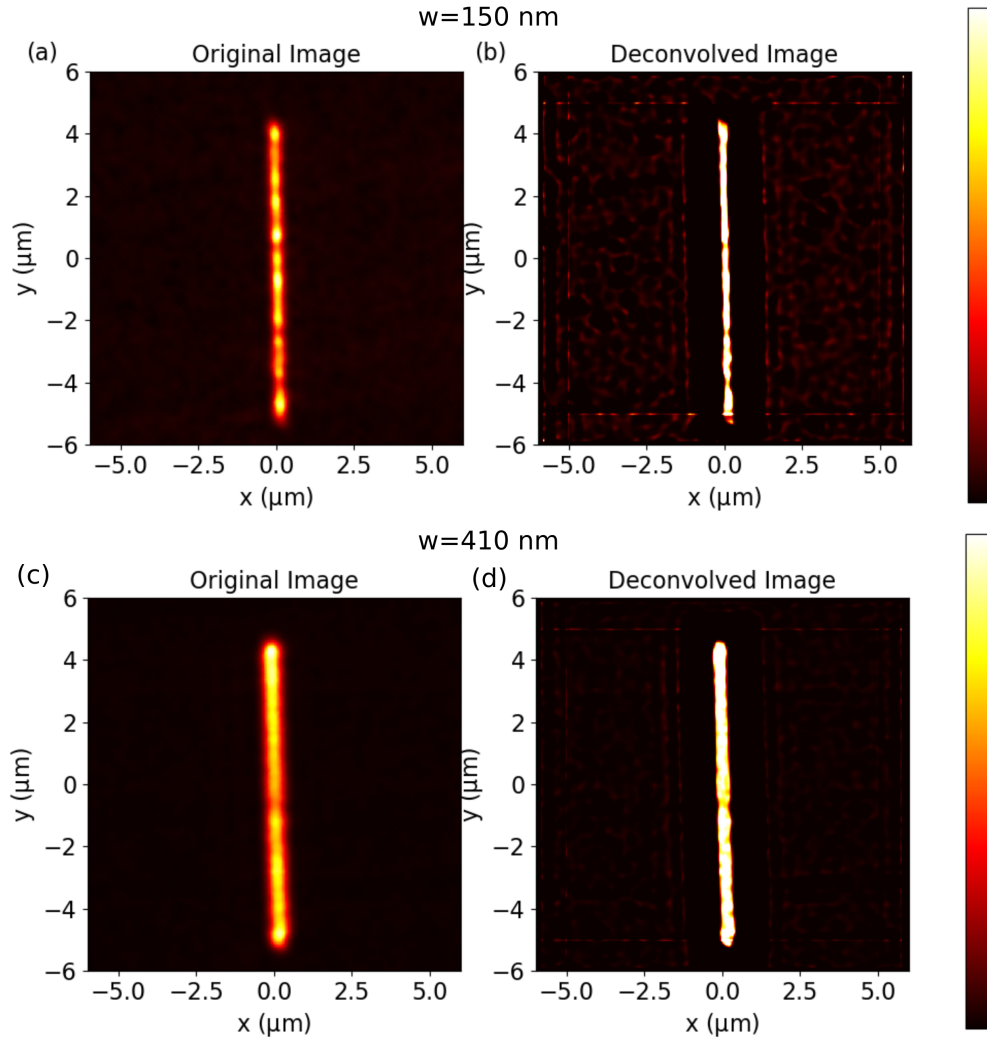


**Figure 6.27:** Deconvolution of the SNOM image for a single-slit aperture with (a-b)  $w = 150$  nm and (c-d)  $w = 410$  nm using a simulated PSF obtained from a circular aperture with  $d = 100$  nm and probe parameters  $h = 10$  nm and  $D = 300$  nm, showing (a,c) original images before deconvolution and (b,d) deconvolved images.

A closer analysis of the intensity profiles is shown in Fig. 6.28. For both  $w = 150$  nm and  $w = 410$  nm, each of the intensity peaks now has the correct width equal to the width of the aperture. The line shape of the intensity profile in  $w = 150$  nm aperture is not too different from the one with  $w = 180$  nm. For  $w = 410$  nm, the accuracy is much better than the approximate PSF via the pseudo-Voigt function. With the pseudo-Voigt PSF, the deconvolved image exhibits a smaller size aperture compared to its actual size. With the simulated PSF, the width is closer to its actual

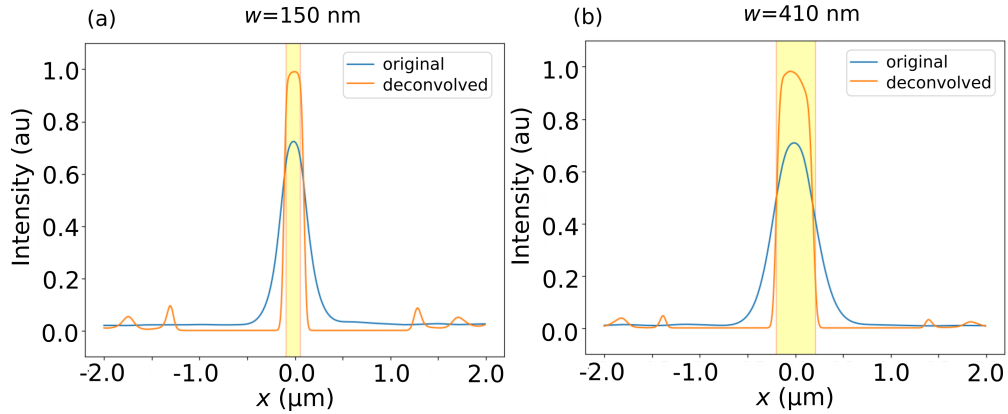


**Figure 6.28:** Intensity profile across the slit for the original and deconvolved images of single-slit apertures with (a)  $w = 150$  nm and (b)  $w = 410$  nm, using a simulated PSF obtained from a circular aperture with  $d = 100$  nm and probe parameters  $h = 10$  nm and  $D = 300$  nm.

width confirmed from SEM images.

One important thing to note is that the deconvolved intensity peak shows a sharp intensity peak decay at the edges of the slit, with the shape closer to a top-hat function. This was observed in the result of the intensity profile from the simulation without the probe tip included (refer to Section 5.4 in Chapter 5). In that simulation, the intensity profile was not affected by the probe tip, because the optical signal was detected only with a 2D plane detector which has no physical presence. The 2D detector records the near-field electromagnetic field transmitted through the aperture. The deconvolution effectively removes the influence of the probe tip in the image formation.

A further investigation of the simulated PSF was performed by deconvolving the image with a PSF obtained from different sizes of circular aperture. The results shown above were calculated using the PSF obtained from the transmitted light through a circular aperture with a size of  $d = 100$  nm. Provided that the aperture is small enough, there should be a negligible difference compared to the deconvolution results. A single-slit aperture was deconvolved using two different PSFs, obtained from the simulations using the circular aperture with  $d = 80$  nm and  $d = 150$  nm. The results are given in Fig. 6.29, with the intensity line profiles given in Fig. 6.30.

Looking at the two results, the deconvolved images appear identical

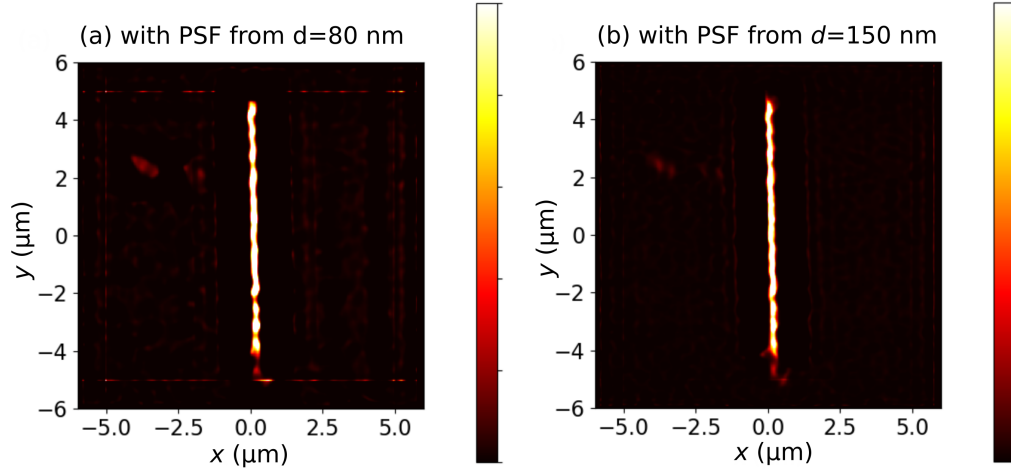


**Figure 6.29:** Deconvolved images of single-slit aperture with  $w = 180$  nm using simulated PSF obtained using a circular aperture with (a)  $d = 80$  nm and (b)  $d = 150$  nm and probe parameters  $h = 10$  nm and  $D = 300$  nm.

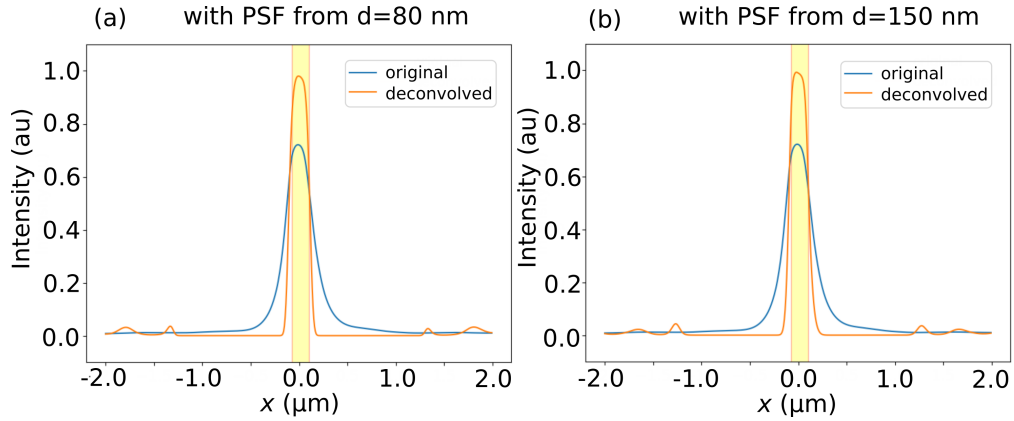


**Figure 6.30:** Intensity profile across the slit for the original and deconvolved images of single-slit aperture with  $w = 180$  nm, using a simulated PSF obtained from a circular aperture with (a)  $d = 80$  nm and (b)  $d = 150$  nm, and probe parameters  $h = 10$  nm and  $D = 300$  nm.

to the variation of  $d$  for obtaining the PSF. Comparing these results with the results in Figs. 6.25 and 6.26, they are consistent with each other. It can be concluded that the apertures with sizes ranging from  $d = 80$  nm to 150 nm are suitable for generating the PSF of the SNOM system studied here.

The effects on the variation of the PSF using different probe tip parameters  $D$  were investigated. The PSFs obtained for different  $D$  were used to

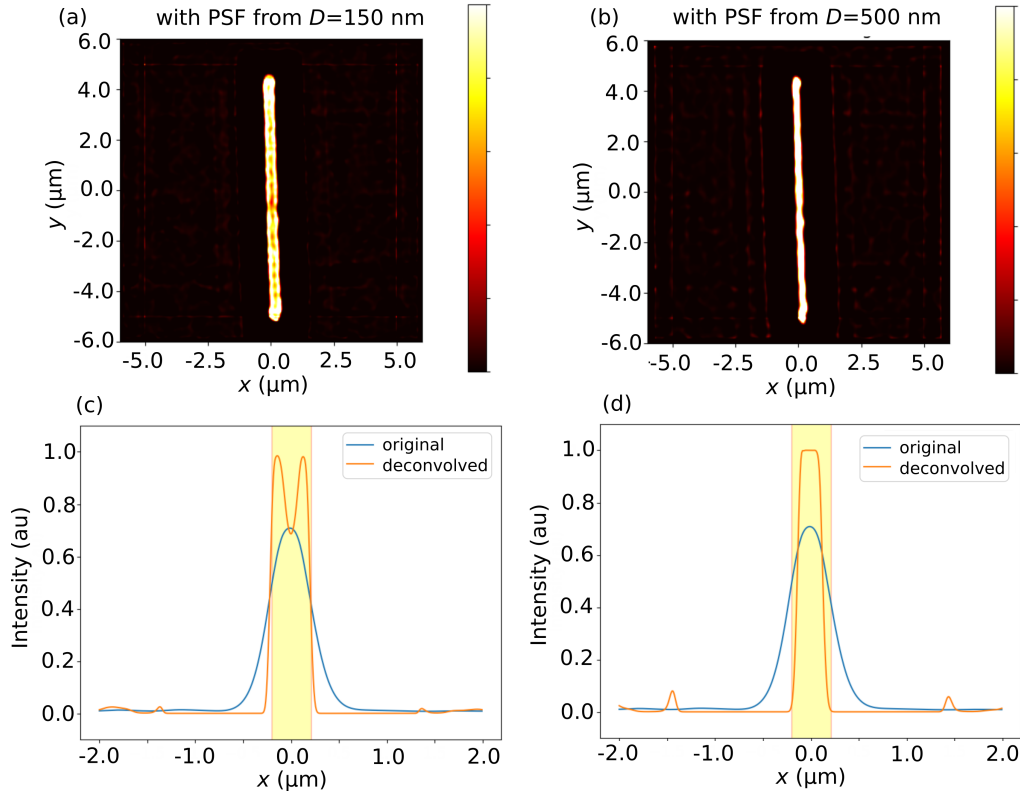


**Figure 6.31:** Deconvolved images of single-slit aperture with  $w = 410$  nm using a simulated PSF obtained from a circular aperture with  $d = 100$  nm, with probe parameters  $h = 10$  nm, and (a)  $D = 150$  nm and (b)  $D = 500$  nm. (c,d) The intensity line profiles across the slit, from the images above, for  $D = 150$  nm and  $D = 500$  nm respectively.

deconvolve an image of a single-slit with  $w = 410$  nm, which is shown in Fig. 6.31. The pseudo-Voigt approximation of the PSF was shown to affect the resulting width of the aperture in the deconvolved image. Here, using the simulated PSF, the results are still consistent, but with better accuracy. If the simulated PSF was obtained from the probe with smaller  $D$ , the image would have had a weak convolution effect. This effectively would lead to a deconvolved image with a wider aperture size. If the probe size is larger, the slit for the resulting deconvolved image will get narrower. This is because the large probe tip has a strong effect on the broadening of the intensity profile of the slit and deconvolution reverses this effect, as if it comes from a slit with a much narrower width.

A closer view on the intensity profile can be seen in Fig. 6.31(c-d), with the two profiles having different shapes and widths. Using a PSF



obtained with  $D = 150$  nm, the deconvolved image shows the oscillating peak with two maxima at the edges. This profile shape was found in the simulation using a plane detector, without the probe tip included (refer to Sections 5.3 and 5.4). On the other hand, the PSF with  $D = 500$  nm shows a rounder peak with a narrow width and an intensity drop at the edges of the slit which is not as sharp as that obtained using a PSF with  $D = 150$  nm.

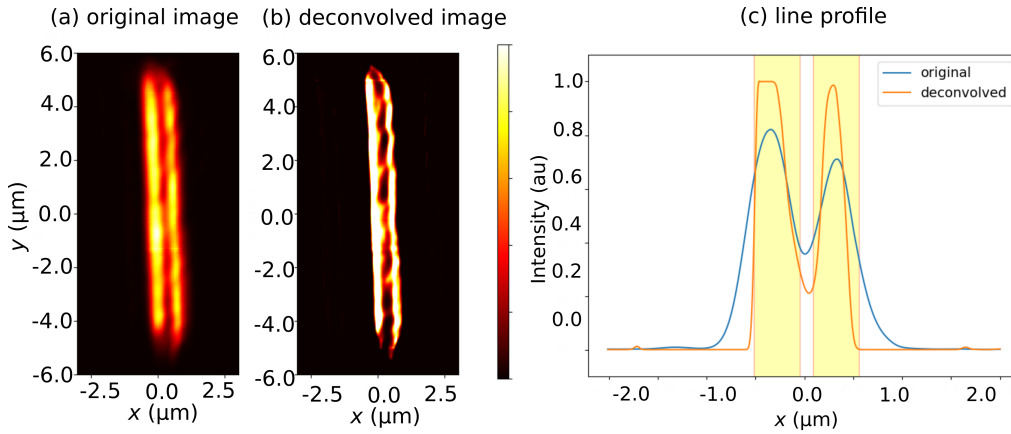


**Figure 6.32:** Deconvolution of a SNOM image of the double slit aperture with  $w = 470$  nm and  $s = 140$  nm, using a PSF obtained with parameters  $d = 100$  nm,  $h = 10$  nm, and  $D = 300$  nm. (a) Original and (b) deconvolved images are shown, the intensity profiles perpendicular to the double-slit shown in (c).

The simulated PSF could be used for deconvolving the single-slit aperture images with high accuracy. The image clarity was increased with sharper edges and accurate width of the slits observed in the deconvolved image. The PSF was then further tested for double-slit apertures. SNOM scan images (before deconvolution) showed that the double-slit with  $s = 140$  nm was able to be resolved. The edges of the slits, however, were not very sharp because the intensity peaks corresponding to the slit apertures decrease gradually at the edges of the slits. This is the same behaviour as that observed in single-slit apertures.

Figure 6.32 shows the deconvolution result of this double-slit aperture. Intensity peaks corresponding to the left and right slits are asymmetric in amplitude. The deconvolved images still exhibit asymmetric behaviour noting that no asymmetry was introduced in the PSF model.

The left slit appears larger than the right slit, with the inhomogeneous (zig-zag) edges of the slits in the gap appearing more prominently. The intensity profile was calculated and the comparison before and after deconvolution is shown in Fig. 6.32(c). Both peaks are inside of the expected location of the apertures, with the left slit having a larger width. This is consistent with the actual size of the left slit. The right slit, however, appears smaller than expected based on the SEM data. As previously discussed in Chapter 5, this asymmetry was attributed to imperfections in the fabrication, which was not included in the simulation model.

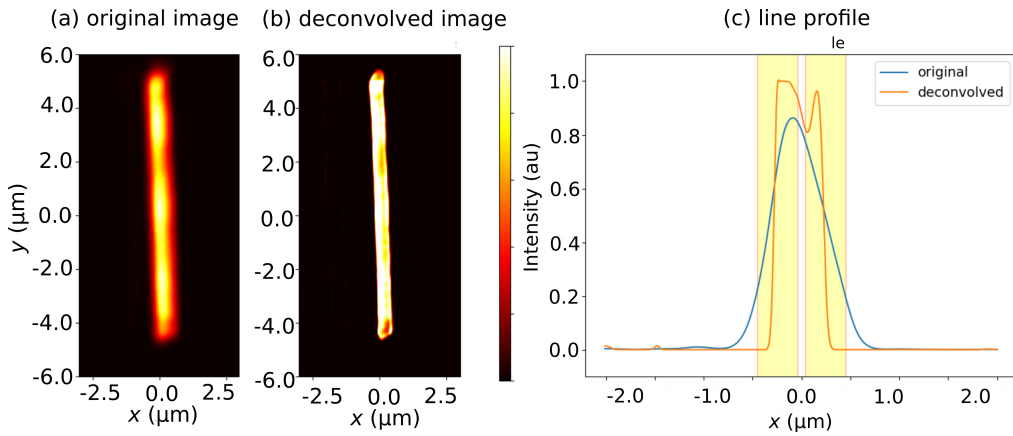


**Figure 6.33:** Deconvolution result for a SNOM image of the double slit aperture with  $w = 410$  nm and  $s = 80$  nm, using a PSF obtained with parameters  $d = 100$  nm,  $h = 10$  nm, and  $D = 300$  nm. (a) Original and (b) deconvolved images are shown, with the intensity profiles perpendicular to the double-slit shown in Fig. (c).

The double-slit with  $s = 80$  nm is an interesting case. Using SNOM, no gap could be observed. The peak shape is, however, asymmetric, which is consistent with the other double-slit apertures. Using the simulated PSF, the image was deconvolved but still no clear gap was observed. Looking closely at the profile perpendicular to the double-slit, the gap was faintly restored. There is no clear indication that the deconvolution has restored the appearance of the gap in between the slits, but it indicates that the algorithm works well in terms of restoring the image. If the gap was slightly larger, for example, if  $s = 100$  nm, the SNOM scan could potentially pick up a faint gap between the slits, which could be enhanced further using the deconvolution algorithm.

### 6.5.3 Deconvolution with Experimental PSF

After testing the deconvolution using the simulated PSF, image deconvolution was then performed using the experimental PSF. The circular apertures were milled in a gold film with the thickness of 120 nm. The circular apertures have diameters of  $d = 80$  nm,  $d = 100$  nm, and  $d = 150$  nm. The SEM images of the circular apertures are shown in Fig. 6.5, in Section 6.2.2. The illumination was set to be linearly polarised in the  $x$ -direction.

The resulting image of the circular aperture was then denoised to reduce the background noise from the experiment. The experiment was performed with a 20 nm step of the probe tip. Both the PSF and image must have the same scale, so that if one of them has a different step size, a 2D interpolation must be performed beforehand to ensure both have the same step size.

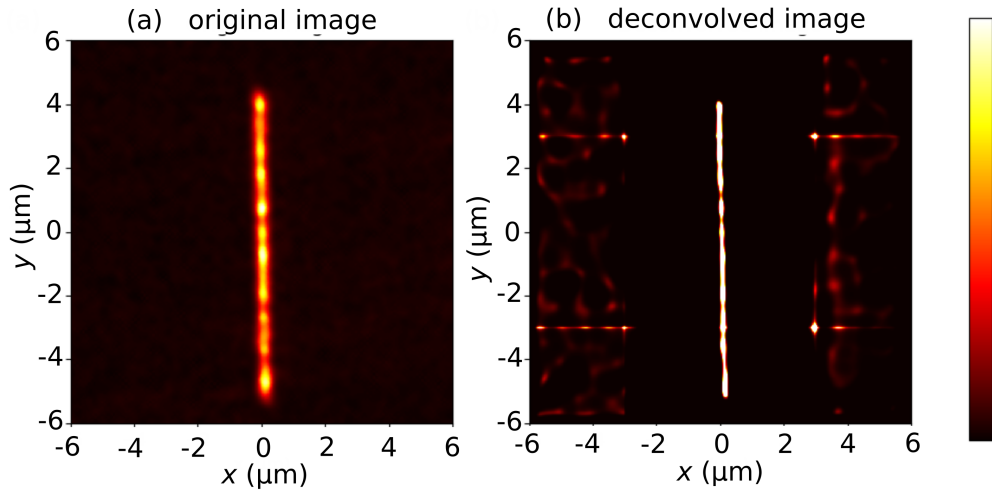


**Figure 6.34:** Deconvolution of the SNOM image of a single-slit aperture with  $w = 150$  nm using the experimental PSF obtained from a circular aperture with  $d = 100$  nm, showing (a) original image before deconvolution and (b) deconvolved image.

Since all of the apertures are very small, the differences between images taken from these apertures were minimal, as discussed in Section 6.2.2. The aperture of diameter  $d = 100$  nm was chosen as the PSF to deconvolve the slit aperture images.

The deconvolution of a single-slit aperture with  $w = 150$  nm was performed using the experimental PSF, the results are shown in Fig. 6.34. There was more noise in the background of the experimental PSF compared to the simulated PSF, and this led to the deconvolved image containing stronger background noise and ringing effects. The slit aperture, however, could be restored. The slit aperture appears very sharp with better contrast and a smaller width. This is consistent with what was found in deconvolution using a simulated PSF.

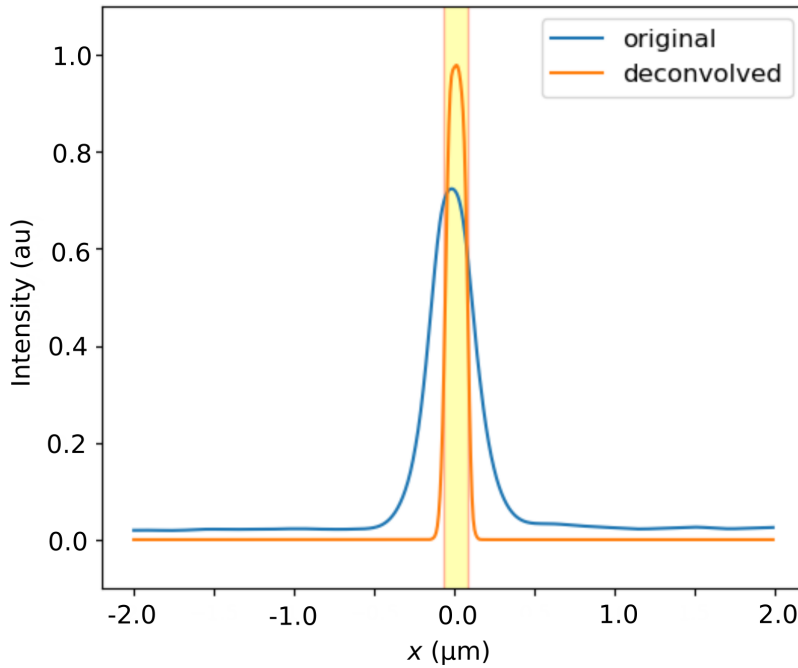


**Figure 6.35:** Intensity profile across the slit for the original and deconvolved images of single-slit aperture with  $w = 150$  nm, using an experimental PSF obtained from a circular aperture with  $d = 100$  nm.

The width of the peak in the intensity profile is confirmed in Fig. 6.35, where the peak is located inside the the expected location of the aperture. The edge is sharper, although the peak maximum is still rounded and not flattened, and there is no indication that the oscillation in the intensity peak was observed in the simulation without the probe tip.

The same PSF obtained from the experiment was applied to deconvolve the slit aperture images with  $w = 180$  nm. The deconvolution results are shown in Fig. 6.36. The deconvolved image has a better SNR compared to the smaller slit with  $w = 150$  nm. We conclude that the

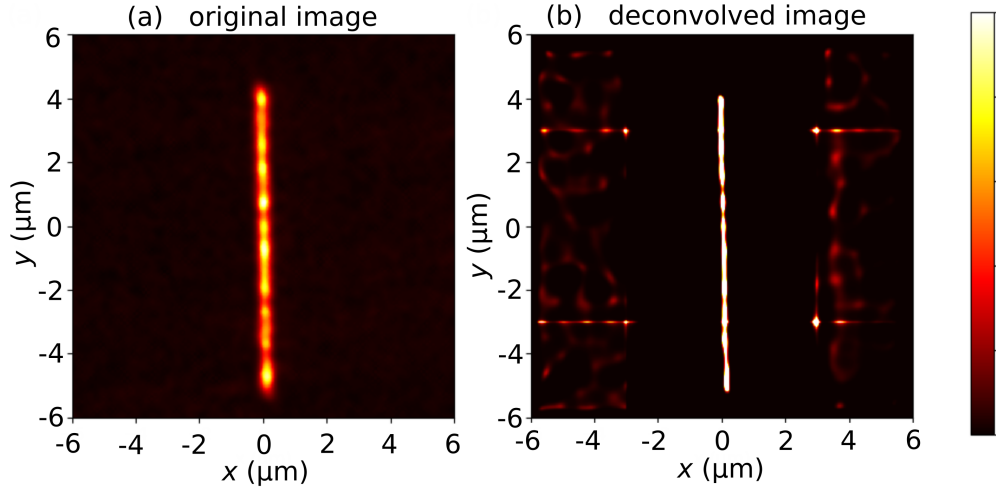


**Figure 6.36:** Deconvolution of the SNOM image of the single-slit aperture with  $w = 150$  nm using the experimental PSF obtained from a circular aperture with  $d = 100$  nm, showing (a) original image before deconvolution and (b) deconvolved image.

deconvolution was successful in improving the quality of the aperture image.

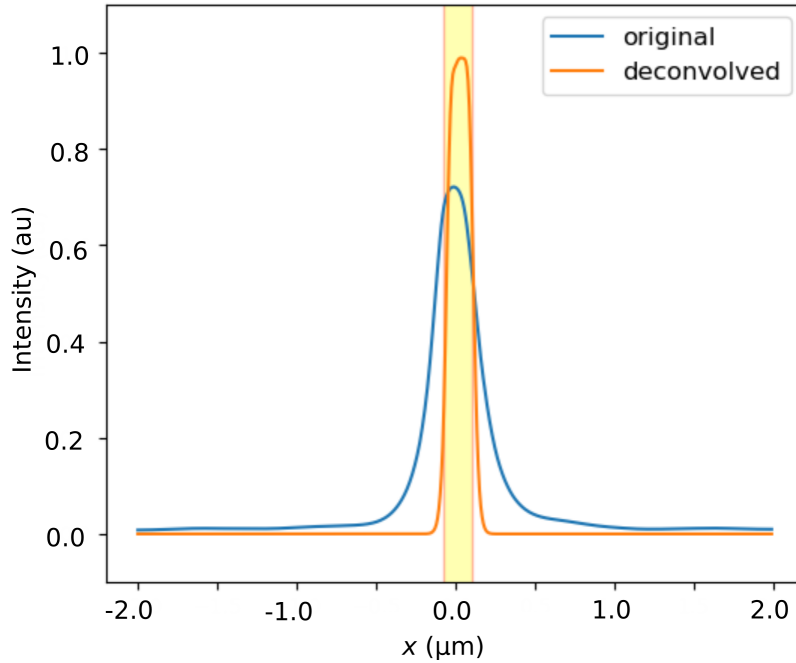


**Figure 6.37:** Intensity profile across the slit for the original and deconvolved images of single-slit aperture with  $w = 150$  nm, using experimental PSF obtained from a circular aperture with  $d = 100$  nm.

The intensity profile for this aperture is shown in Fig. 6.37. This is consistent with the expected width of the slit aperture. It was noted that the experimental PSF overestimates the peak size compared to that obtained from the simulation. The deconvolution results for very small apertures, less than 200 nm in width, suggest that the deconvolution still improves the image quality, with the width of the apertures close to the expected values.

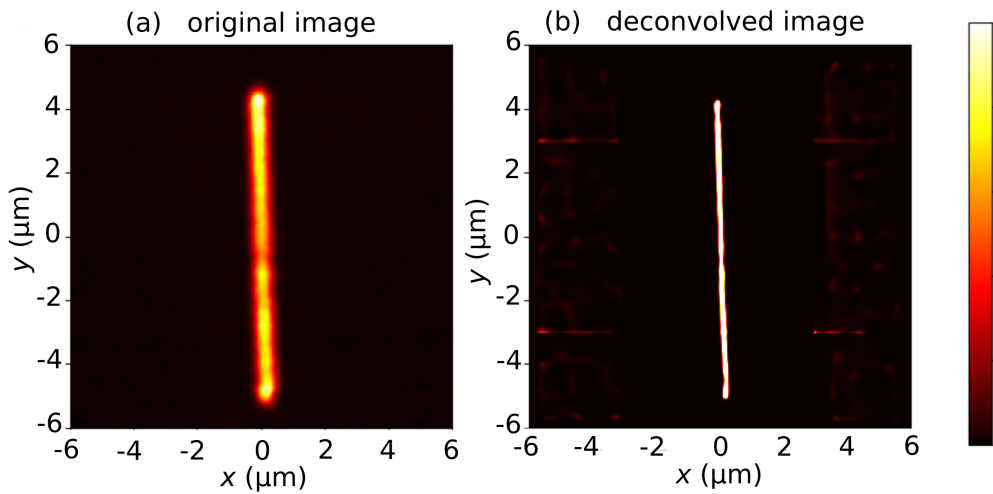


**Figure 6.38:** Deconvolution of the SNOM image for a single-slit aperture with  $w = 410$  nm using an experimental PSF obtained from a circular aperture with  $d = 100$  nm, showing (a) original image before deconvolution and (b) deconvolved image.

The overestimated PSF, however, did not lead to an improvement in the image when used for deconvolving the single-slit aperture with a larger width,  $w = 410$  nm. The result is shown in Fig. 6.38, with the deconvolved image showing a very narrow aperture thinner than the expected width. The deconvolution aggressively reduces the width of the slit to about half of its actual size.

In the case of the double-slit aperture, a similar behaviour was observed with the width of the intensity peaks being smaller than its actual size confirmed via SEM. The width of each slit of the aperture pair is  $w = 470$  nm, comparable to the single-slit with  $w = 410$  nm shown in Fig. 6.38. The deconvolution result of the double-slit aperture using the experimental PSF is shown in Fig. 6.38. The overestimated PSF led to the deconvolved image showing two apertures with very small widths. The

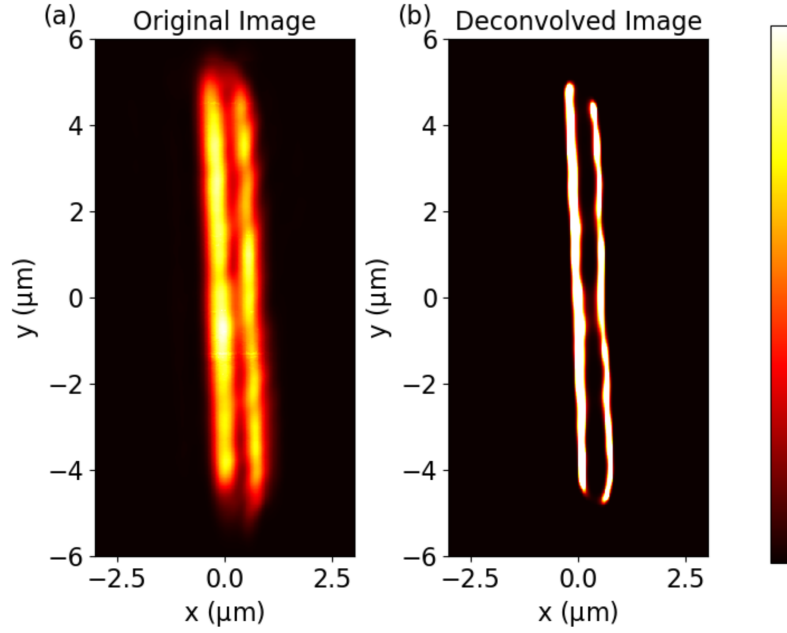


**Figure 6.39:** Deconvolution of the SNOM image of the double-slit aperture with  $w = 470$  nm and  $s = 140$  nm using the experimental PSF obtained from a circular aperture with  $d = 100$  nm, showing (a) original image before deconvolution and (b) deconvolved image.

slits are still asymmetric, with the left slit being slightly larger than the right slit. Although the widths are not accurate, this demonstrates that the small gap between two objects can be enhanced using deconvolution.

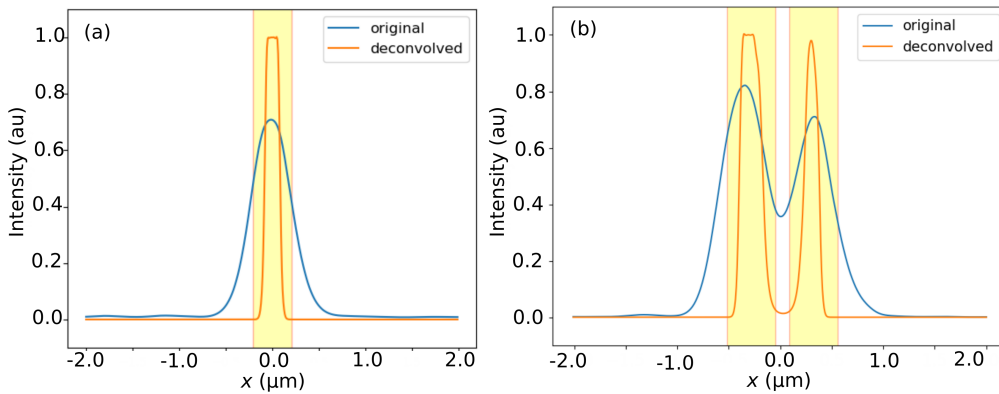


**Figure 6.40:** Intensity profile across the slit using the original and deconvolved images of (a) single-slit aperture with  $w = 410$  nm and (b) double-slit apertures with  $s = 140$  nm shown in Figs. 6.38 and 6.39 respectively, using the experimental PSF obtained from a circular aperture with  $d = 100$  nm.

Intensity profiles across the slits for the images in Figs. 6.38 and 6.39 are shown in Fig. 6.40. The expected location of the aperture within the yellow-shaded rectangle was obtained from the SEM images. The over-estimated PSF produced intensity peaks corresponding to the slits with a width of about half their expected size. A more accurate experimental PSF would have resulted in a higher accuracy, but this calculation demonstrate that the results using the experimental PSF are consistent with those using the simulated PSF.

## 6.6 SNOM Images of Fresnel Zone Plate

The Fresnel zone plate (FZP) is a focusing device with a concentric periodic metallic ring. This device is also used extensively in the x-ray regime. Here, the metal material used for the FZP is Ni and the periodicity is  $1.2\ \mu\text{m}$ . The device was scanned using SNOM with a  $20\ \text{nm}$  step size. The SNOM scan of this device was performed by Dr Arif Siddique, with the deconvolution process performed by the author. The SNOM image is shown in Fig. 6.41(a). The areas with bright intensity are the transparent zones of the FZP, and the dark areas are the absorbing concentric Ni rings. The image was deconvolved using a simulated PSF, the result is shown in Fig. 6.41(b). Due to the structure being resolved clearly

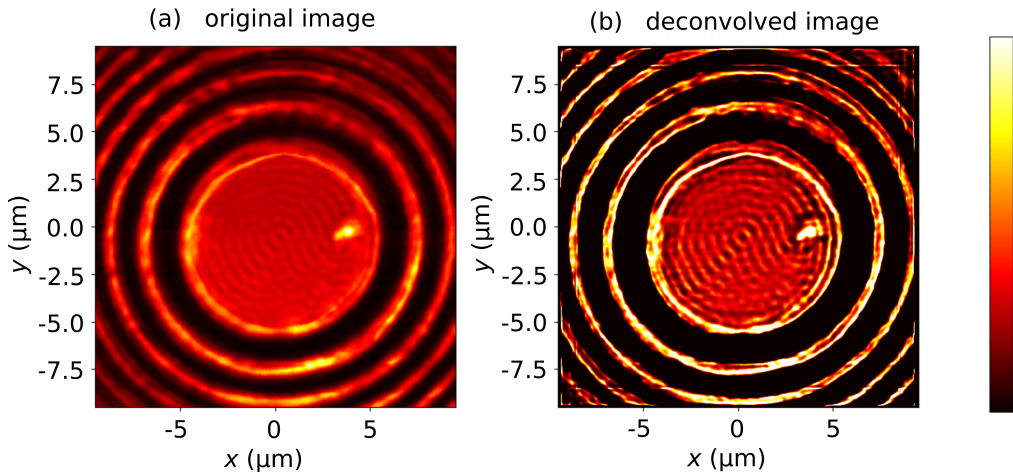


**Figure 6.41:** Deconvolution of the SNOM image of a Fresnel zone plate using experimental simulated PSF obtained from a circular aperture with  $d = 100\ \text{nm}$  and probe parameters  $h = 10\ \text{nm}$  and  $D = 300\ \text{nm}$ , showing (a) original image before deconvolution and (b) deconvolved image.



in the original image, the deconvolved image did not show significant improvement in the apparent resolution. Instead, the resulting image has more well-defined edges of the rings. The overall brightness of the structure has also improved as well as the contrast between the dark and bright areas.

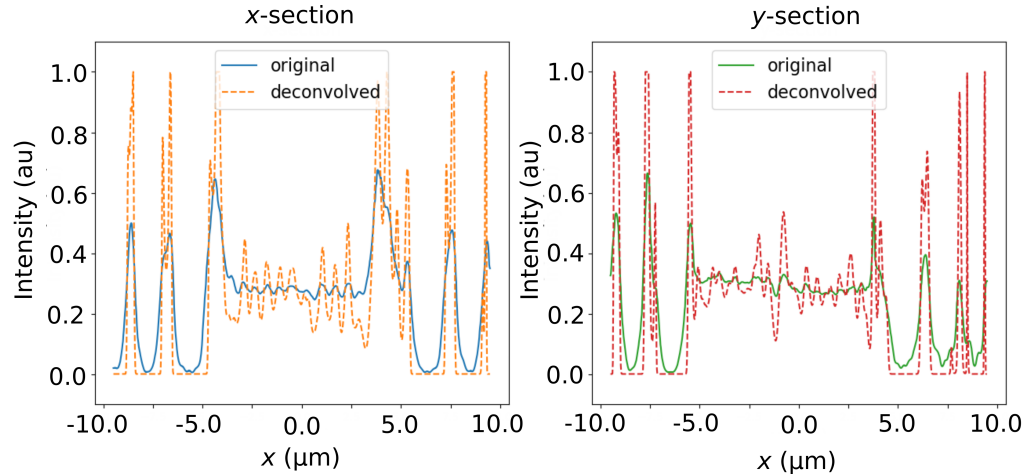


**Figure 6.42:** Intensity line profiles taken across the  $x$ - and  $y$ - sections of the images in Fig. 6.41, for both the original and deconvolved images.

The sections of the intensity profile were taken through the middle of the image, along the  $x$ - and  $y$ -axes. In Fig. 6.42, it can be seen that the edges between the opaque and transparent area become more defined with sharp edges on the intensity peaks. The contrast for the deconvolved image was improved with the peak maximum higher than the original image.

The same zone plate was imaged with a larger scan area and this time with a smaller step size of 10 nm instead of previous 20 nm. The original and deconvolved images are shown in Fig. 6.43. Due to the structure size being much larger than the step size, this does not affect the appearance on the SNOM image. Due to slightly inhomogeneous illumination, the areas near the  $x$ -axis (where  $y = 0$ ) are slightly brighter. The deconvolution result is still consistent with what is found in the image with the smaller scan area, where the maximum of the intensity peaks in the deconvolved image is higher than in the original image.

The shapes of the intensity profiles through the middle of the images are shown in Fig. 6.44. In the  $x$ -section of the image, the intensity of the

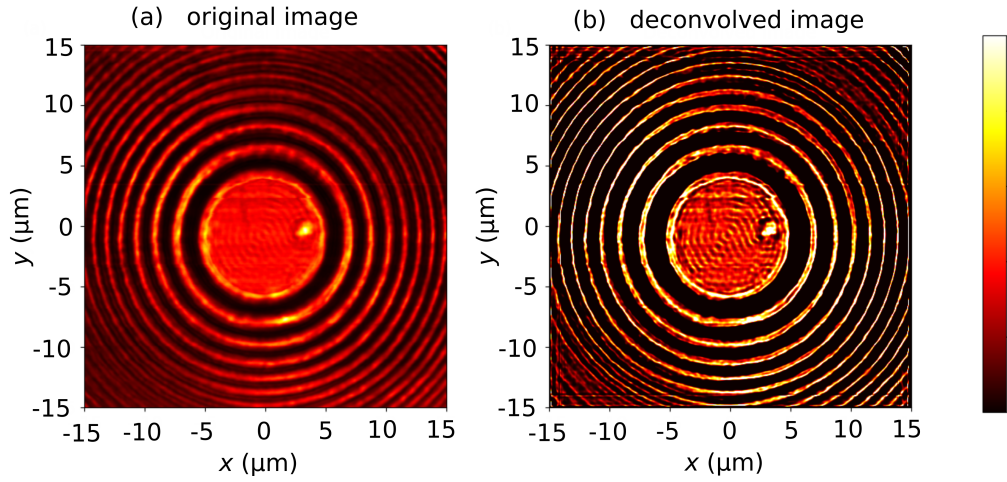


**Figure 6.43:** Deconvolution of the SNOM image of a Fresnel zone plate using a simulated PSF obtained from a circular aperture with  $d = 100$  nm and probe parameters  $h = 10$  nm and  $D = 300$  nm, showing (a) original image before deconvolution and (b) deconvolved image.

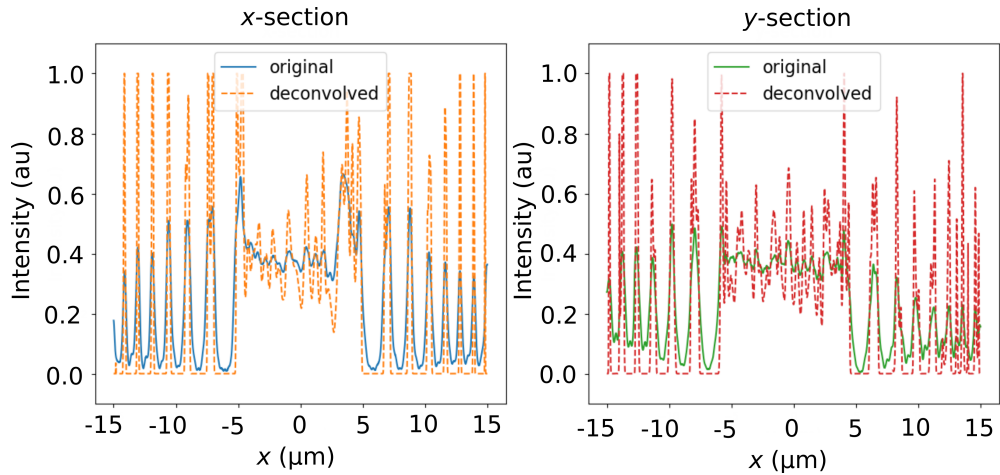


**Figure 6.44:** Intensity line profiles taken across the  $x$ - and  $y$ - sections of the images in Fig. 6.43, for both the original and deconvolved images.

deconvolved image is homogeneous with better contrast, whereas the variation in the maximum of the peak is found in the  $y$ -section. The deconvolution was able to increase the image contrast resulting in more clearly defined structures.

## 6.7 Chapter Summary

The PSF describes how the imaging device leads to blurring or degradation of the recorded images compared to the ideal undisturbed images. In the case of SNOM, the PSF is predominantly affected by the probe tip as the key component of SNOM, detecting the near-field intensity profile of the sample. Knowledge of the probe tip from the simulation model and its validation using experimental data is valuable for determining the accurate PSF of the SNOM system.

Image deconvolution is a post-processing method for improving image quality using knowledge of the PSF. Using the Richardson-Lucy algorithm, SNOM image deconvolution was performed via a recursive algorithm, until convergence was achieved. The PSF obtained from the simulation model and from the experimental data was tested in order to deconvolve the SNOM images.

Deconvolution was performed on SNOM images of the single-slit and double-slit apertures and a Fresnel zone plate. It was shown that the quality of the slit aperture images was improved, with the deconvolved images showing better sharpness and contrast, as well as improved accuracy in terms of matching the SEM images. The image of FZP was shown to have sharper edges after deconvolution.

Knowledge of the probe tip is important to obtain an accurate PSF. An overestimated PSF with a larger width or peak diameter can lead to aggressive reduction of the size of the objects in the deconvolved image. On the other hand, an underestimated PSF will only have a very weak influence on the deconvolved image. The simulation model was shown to have a good accuracy, using the previous knowledge of the probe tip obtained from Chapter 5, where the comparison between the simulation results and experimental data was investigated. The experimental PSF provided here was overestimated but it demonstrated consistent behaviour predicted by the simulation. This showed that the deconvolution algorithm works properly and improvements in the SNOM images were still observed.

The results discussed in this chapter, in principle, show the potential of image deconvolution in the context of SNOM using different types

of PSF. Images generated by a non-ideal probe tip with asymmetry or deficiencies could still be restored if the probe tip condition can be determined accurately and used to characterise the PSF. Image artifacts due to the presence of the probe tip can also potentially be avoided by ameliorating its effect via image deconvolution.

## Chapter 7

# Conclusions and Future Work

### 7.1 Conclusions

In this thesis, the influence of the optical probe tip on SNOM imaging was investigated. An optical probe scanning the sample at a near-field distance from the sample surface is a key element of SNOM. A simulation model of the image formation using SNOM was built based on the FDTD method for a full-wave simulation of electromagnetic wave interactions. The simulation model included the probe tip and was investigated by varying the probe tip parameters (tip aperture size  $D$  and sample-tip distance  $h$ ). It was confirmed that the probe has a significant influence on the images obtained using SNOM, which can significantly alter the intensity profiles measured by the SNOM system.

The simulated results were validated using experimental data for accurate modelling. By using well-characterised samples of slit apertures, the images obtained using SNOM were investigated and were compared to the results from the simulation. By varying the probe tip parameters, the best fit between the simulated and experimental data were found, with  $h = 10$  nm and  $D = 300$  nm. It was also demonstrated that the simulation without the probe tip was not able to reproduce the intensity profiles observed from experiments. Understanding the influence of the probe tip in the SNOM imaging process is crucial for correct interpretation of SNOM data.

Furthermore, knowledge of the probe tip was useful for determining the PSF of the SNOM system via simulation. The PSF was calculated from the simulation using a small circular aperture (diameter  $d \leq 150$  nm) as a model for a point source. The PSF was used in the image post-processing with a deconvolution process based on the Richardson-Lucy algorithm. The image quality of the slit apertures, as well-characterised samples, was improved following the deconvolution process, with sharper edges and better contrast observed. In addition, the deconvolution produced images of the slits with dimensions closer to their actual physical sizes as confirmed with SEM.

In the following sections, the conclusions for each part are discussed in detail.

### 7.1.1 Simulation model of the SNOM Imaging System

Here we provide a summary of Chapter 4 where we used simulation models for the SNOM system based on the FDTD method. The FDTD method iteratively solves Maxwell's equations. With this method, no approximations or assumptions were made, which ensures the validity of the calculation of near-field optics. The only limitation is resolution of the mesh, which needs to balance accuracy versus computational efficiency. In this study, the smallest mesh size used was 5 nm, and the largest mesh size was up to 40 nm, with the latter used at large distances from the sample and probe tip. For the simulations presented in this thesis the optimum mesh resolution was chosen which enabled practical calculation while still preserving a high degree of accuracy.

The simulation models investigated here incorporated the probe tip, with a second model without the probe tip also explored as a control. The probe tip was modelled as an object in the simulation in the shape of a truncated cone, composed of a glass core and metal cladding (Cr and Al). In each set of simulations, the probe was placed at different positions across the sample, in order to mimic an actual SNOM scan. Each set of simulations contains one sample scanned by the probe tip with a specific set of probe parameters. The intensity measured by the probe tip during the scan was calculated in the post-processing stage, after all

simulation runs in the set were completed. A simplified model without the probe tip was generated for the detection of near-field signals using a two-dimensional plane detector placed at a subwavelength distance from the sample surface.

Before analysing the simulation models, the simulation set-up was validated by reproducing results from the published literature. The transmittance spectra of various periodic structures, in the form of arrays of circular apertures and gratings were calculated. Comparing these with the results from the literature provided insight into the choice of the appropriate set of simulation parameters, for example, it enabled us to validate that the mesh resolution was sufficient to accurately reproduce the key features of the SNOM measurement. Based on these parameters, the published transmittance spectra could be accurately reproduced using the model developed for this thesis.

Using two different simulation models (with and without the probe tip), the intensity profiles measured using SNOM were investigated, as discussed in Sections 4.3 to 4.4 in Chapter 4. The model samples used were circular apertures and slit apertures in a metal film, with single (one isolated aperture) and double (two adjacent apertures) configurations. The comparisons between the results for circular apertures from different simulation models, with and without the probe, were presented (Figs. 4.17-4.18 and 4.23-4.24).

In summary, the intensity profiles produced from the simulation with the 2D detector (without the probe tip) had well-defined edges, with a more clearly defined object shape (i.e. circular). These profiles were, however, sensitive to how far the detector was placed from the sample, which showed a gradual change to smoother peaks as the detector was moved further away. In contrast, the results of simulated intensity profiles using the probe tip showed objects with more blurred characteristics, which were heavily affected by the presence of the probe tip. The snapshot of the intensity profiles measured at the probe tip location showed that the probe tip has a strong influence on the electromagnetic field distribution near the sample (Fig. 4.11). Using a single circular aperture and a disc as a test sample, it was shown that the absorption of the object could also be affected by the presence of the probe tip near the sample

(Figs. 4.13 and 4.14).

The probe tip parameters,  $h$  and  $D$ , were varied in order to investigate their effects on the intensity profile measured by SNOM. Parameters  $h$  and  $D$  correspond to the height of the probe tip from the sample surface and the size of the probe tip aperture in an aperture-type probe. These are the 'effective' size parameters of the probe, not the actual physical size. Due to the idealistic nature of the probe tip compared to the actual probe, the probe parameters in the modelling are the effective size of the probe tip. The probe tip model featured a simplified symmetric probe tip with a truncated conic symmetry. The model did not take account for the asymmetry, smooth/ sharp edges, and asperities of the probe tip. This, as a result, meant that the values of the probe tip parameters were overestimated than their real physical size. The resulting intensity profiles measured using different probe parameters were investigated using single-slit and double-slit aperture samples (Figs. 4.19 and 4.25). The best image was obtained when the probe tip was placed as close as possible to the sample, with the tip aperture as small as possible. In the range investigated, the best results were obtained with  $h = 10$  nm and  $D = 150$  nm, with the intensity profiles observed to broaden as the parameter  $D$  increases.

### 7.1.2 Probe Tip Influence in the SNOM Imaging (using Experimental Data)

In this section, a summary of Chapter 5 is presented. The simulation models were verified with experimental data using SNOM scans. Single-slit and double-slit apertures in a gold film with various sizes were fabricated using FIB milling. The widths of the slit apertures were in the subwavelength size range, less than 500 nm. These well-characterised samples were imaged using SNOM in the experiments. The illumination was performed with a laser of incident wavelength 640 nm, with the SNOM system set in collection mode, as described in Chapter 3, Section 3.2.1. The intensity profiles from the resulting experimental images were analysed and compared to those obtained from the simulation.



As a reference, the actual sizes of the slit apertures were measured using SEM images. The spatial resolution of the SEM was much better than that of SNOM, but the samples could still be clearly observed. The single-slit aperture with of width 150 nm could be detected with clear edges (Figs. 5.2 and 5.4). In the case of double slit apertures, the gap in between the slits could be observed, although an asymmetry appeared in the peaks in the intensity profiles, between the right and left slits (Figs. 5.3 and 5.5). This was attributed to imperfection in the fabrication that was not visible in the SEM images. A gap as small as 140 nm could to be observed using SNOM.

The simulation model of the image formation using SNOM was analysed using experimental data using an appropriate set of probe parameters, with  $h = 10$  nm and  $D = 300$  nm. In order to create an accurate model of the SNOM, the probe tip has to be included in the calculation (Figs. 5.10 to 5.13). The simulation including the probe tip could reproduce the intensity profiles measured from the SNOM scans. The smooth intensity decay at the edges of the slit aperture could be modelled accurately. In contrast, when the simulation model without the probe tip was used, it produced a different characteristic intensity profile which was not consistent with the experimental data. Using this model, the slit apertures appeared with sharp edges, which were the ideal shape of the intensity profiles when the probe tip has effectively zero dimension and is not realistic. Further quantitative analysis was performed by comparing the FWHM of the intensity profiles obtained from the simulation and experiment. In the case of double-slit apertures, the peak-to-peak distance was also presented, with the value equivalent to the centre-to-centre distance between the slits. These are summarised in Tables 5.2 and 5.2. The discrepancies between the values obtained from the simulation and experiment are within 70 nm for both types of slit apertures.

Using the method based on the line spread function of the intensity profile of one-dimensional samples, the estimated spatial resolution of the SNOM used in this study was calculated (Fig. 5.6). The spatial resolution of the SNOM was estimated to be  $178 \text{ nm} \pm 14 \text{ nm}$ . The effect of changing the wavelength was investigated using simulation only, for

wavelengths ranging between 500 nm and 640 nm (Fig. 5.15). The results did not show significant differences compared to those obtained with  $\lambda = 640$  nm, with the relative amplitude variation within 10% difference and FWHM within  $\pm 30$  nm. That implies that a small variation of the wavelength does not affect the results of the study presented here.

### 7.1.3 Restoring SNOM Images using Deconvolution

The simulation model developed here was further utilised for improving the results of the SNOM scans. In Chapter 6, the SNOM images were deconvolved to restore the image quality by effectively removing the effect of the probe tip. An image obtained by an imaging device can be described via the convolution of the original image and the PSF of the device with some additional noise. In the case of SNOM, this PSF is highly affected by the probe tip. A deconvolution algorithm could restore the degraded image to its original quality. The Richardson-Lucy algorithm was used in this study due to its robustness to noise [6, 90].

The simulation model developed here was utilised to determine the PSF of the SNOM system. To calculate the PSF, a point source was modelled as a circular aperture in a metal film, illuminated from the far-field. The intensity profile emerging from this aperture was measured in the simulation, with the characterised probe tip included. The circular aperture samples had diameters ranging from 80 nm to 150 nm in a 120 nm-thick gold film, of which were all investigated. It was found that the results obtained with  $d = 80$  nm and  $d = 100$  nm closely matched the actual data and either one was a suitable parameter which could be used. With the characterised probe tip ( $h = 10$  nm,  $D = 300$  nm), an accurate PSF can be determined from the simulation, and the circular aperture of  $d = 100$  nm was chosen as the point source model.

Following deconvolution, the PSF determined from the model was used to restore the slit aperture images, resulting in sharper edges and accurate widths of the slit apertures (Figs. 6.25 to 6.33). In these cases, the intensity peaks appeared inside the expected physical location of the apertures. The resulting images were similar to those produced by the simulation without the probe tip as discussed in Chapter 5. This means

that the influence of the probe tip was effectively removed from the images. This model has the potential to be applied to a wider range of SNOM images with appropriate modelling of the probe tip. This could address the imaging artifacts appearing in SNOM due to deficiency or imperfection of the probe tip.

The original images of the slit apertures before deconvolution had a width slightly larger than their actual width as confirmed via SEM. By using the deconvolution algorithm, the slit apertures were able to be recovered with a smaller width, closer to its actual physical size. The edges also appeared sharper with higher image contrast. The concept was also demonstrated using the PSF determined from experimental data, with the PSF obtained from the measurements of the circular aperture samples using SNOM (Figs. 6.34 to 6.40). The results were consistent with those calculated using the PSF from the simulation model. The narrowing effects of the intensity peaks after deconvolution were observed, although with a reduced width in some samples (e.g. single-slit with  $w = 410$  nm in Fig. 6.38). This was due to the fact that the PSF obtained from the experimental data was larger than expected, which could be due (for example) to wear-and-tear of the probe tip. The deconvolution algorithm was also tested on the SNOM image of a Fresnel zone plate, showing consistently sharper edges and better contrast (Figs. 6.41 to 6.44).

## 7.2 Future Work

The simulation model used in this study was shown to provide a more realistic interpretation of SNOM images. With accurate modelling, it is possible to investigate further the influence of the SNOM probe tip on the imaging. Given more time, several potential research topics could be explored as part of future work, as described in the following sections.

### **7.2.1 Modelling a deficient probe tip and its imperfections**

Due to its dominant influence, the probe tip affects the quality of the images obtained using SNOM, particularly in terms of the spatial resolution and image contrast. A damaged or deficient tip may reduce the image quality obtained using SNOM. There are some artifacts associated with a deficient tip that could lead to the misinterpretation of data [2, 3]. With accurate SNOM modelling, the influence of the damaged or deficient probe can be investigated further.

Combining this simulation investigation with experimental data for validating the model and the parameters involved in the calculation, a complete investigation of the effects of the deficient probe can be performed. The information and knowledge of the probe tip condition could provide accurate data interpretation and to avoid artifacts arising from the deficiency in the probe tip. This includes modelling with an asymmetric probe tip or a blunt probe tip, which can be caused by an incorrect or inappropriate feedback force between the sample and the probe tip during the probe landing process or the scanning process.

In addition to modelling the deficient probe tip, additional parameters of the probe tip may also be added. For example, the taper angle of the probe tip can be changed and different coating materials of the probe tip and its thickness can be investigated. These would make the modelling to be more realistic. The ideal shape of the truncated cone may also be modified to match the actual physical shape, which is not actually flat at the bottom, but instead has a more rounded curved shape. This will further improve the accuracy of the probe-tip model.

### **7.2.2 Modifications of the SNOM probe tip or the sample surface**

Given more time, changes in the probe tip of SNOM can be investigated further. In particular, modifications of the probe tip could be performed to improve the optical response of the probe tip. Modification of the probe tip is an active research area for other microscopy techniques such

as in AFM (atomic force microscopy) and STM (scanning tunneling microscopy) [35–38]. Similar approach to the probe tip modifications can also be extended to SNOM imaging [22, 29, 39]. With a properly designed tip, the probe could improve the quality of the image being produced, either by field enhancement, field localisation, or modified sensitivity. A modified probe tip could potentially make the probe tip more sensitive to a certain type of sample or a specific domain within the sample. This could provide a better contrast in the images of the specific sample being observed. Some literature suggested that attaching a nanoparticle to the probe tip could enhance the light localisation at the location of the tip, and subsequently increase the spatial resolution [13, 122]. The shape and dimension of the nanoparticle affects the resulting localisation, and with a careful design, this could further improve the resolution and contrast of the SNOM images.

A preliminary study was performed as part of the work carried out during this thesis to explore the possibilities of probe tip modification. The probe tip can be modified by applying coating materials to the probe tip, which also modifies the force interaction between the probe tip and the samples. Candidate materials were polyethylenimine (PEI) [123, 124] and self-assembled monolayers (SAM) [125, 126]. This is a very interesting subject as it can alter the probe tip interaction with specific samples due to different sensitivity to e.g. charge or hydrophilic/ hydrophobic properties of the samples.

The modification is not limited to the probe tip, but could also be applied to the sample instead of the probe tip. The environment of the sample could affect the force interaction between the probe tip and the sample. Unstable force interaction can lead to inaccurate results of the imaging due to the probe not being at the designated distance from the sample. By applying a layer that alters either the attractive or the repulsive forces between the sample and the probe tip, the resulting image obtained using SNOM could be modified and possibly improved.

Another possible future direction is to introduce more varieties of the sample using our fully characterised SNOM. A wider range of samples

would provide a deeper understanding of the accuracy of our simulations and approach to PSF deconvolution. Our well-characterised samples were composed of metals and other nanofabricated materials, however, biological samples present a range of challenges which we have not yet explored. Careful attention to probe tip effects need to be considered for these other types of samples. As the probe tip is made from hard materials, modifications to the scanning environment conditions may be needed when biological samples are involved [22].

### 7.2.3 Improving deconvolution method for SNOM image post-processing

Image deconvolution offers a further enhancement to the imaging results. The PSF of the SNOM system was determined using the simulation model which involves the probe tip. A further exploration on the analysis of the PSF can be carried out via additional testing using experimental data from different point sources. Each probe tip can have a unique PSF, as the fabrication may produce slight variations in terms of the physical shape of the probe tip as well as its dimension. With a greater variety of test samples and different approaches to model the point source, the PSF can be investigated in more detail. For example, a point source may be replaced with a single particle instead of a single circular aperture. The initial tests to determine the PSF were obtained using a circular aperture of a very small diameter ( $\leq 80$  nm) to deconvolve images from larger apertures ( $\geq 150$  nm). The test samples can also be replaced by an array of apertures, nanostructures, gratings, or other nanostructured devices with well-known characteristics for further fine-tuning the probe parameters.

With additional characterisation details regarding the probe tip, the accuracy of the modeling could be improved, bringing it closer to the actual experimental condition. More realistic and accurate PSF will improve the results of the deconvolution, producing higher quality images. Furthermore, the study performed for this thesis used only one deconvolution algorithm, which was Richardson-Lucy algorithm. There are other deconvolution algorithms which could be used as part of further investigation, such as the Wiener deconvolution [127] and blind deconvolution

algorithms [7, 128].





## Bibliography

- [1] Lukas Novotny and Bert Hecht. *Principles of nano-optics*. Cambridge university press, 2012.
- [2] Gerd Kaupp, Andreas Herrmann, and Michael Haak. “Artifacts in scanning near-field optical microscopy (SNOM) due to deficient tips”. In: *Journal of Physical Organic Chemistry* 12.11 (1999), pp. 797–807.
- [3] B Hecht et al. “Facts and artifacts in near-field optical microscopy”. In: *Journal of Applied Physics* 81.6 (1997), pp. 2492–2498.
- [4] Petr Dvořák et al. “Imaging of near-field interference patterns by aperture-type SNOM–influence of illumination wavelength and polarization state”. In: *Optics express* 25.14 (2017), pp. 16560–16573.
- [5] Stefan Mastel et al. “Understanding the image contrast of material boundaries in IR nanoscopy reaching 5 nm spatial resolution”. In: *ACS Photonics* 5.8 (2018), pp. 3372–3378.
- [6] William Hadley Richardson. “Bayesian-based iterative method of image restoration”. In: *JoSA* 62.1 (1972), pp. 55–59.
- [7] DA Fish et al. “Blind deconvolution by means of the Richardson–Lucy algorithm”. In: *JOSA A* 12.1 (1995), pp. 58–65.
- [8] Bert Hecht et al. “Scanning near-field optical microscopy with aperture probes: Fundamentals and applications”. In: *The Journal of Chemical Physics* 112.18 (2000), pp. 7761–7774.
- [9] Robert C Dunn. “Near-field scanning optical microscopy”. In: *Chemical Reviews* 99.10 (1999), pp. 2891–2928.
- [10] E Abbe. “E. Abbe, Arch. Mikrosk. Anat. 9, 413 (1873).” In: *Arch. Mikrosk. Anat.* 9 (1873), p. 413.

- [11] Joseph Goodman. *Introduction to Fourier optics*. McGraw-hill, 2008.
- [12] E. Hecht. *Optics*. Pearson education. Addison-Wesley, 2002. ISBN: 9780321188786. URL: <https://books.google.com.au/books?id=T3ofAQAAMAAJ>.
- [13] John T Krug, Erik J Sánchez, and X Sunney Xie. "Design of near-field optical probes with optimal field enhancement by finite difference time domain electromagnetic simulation". In: *The Journal of chemical physics* 116.24 (2002), pp. 10895–10901.
- [14] Aleksandr A Kuchmizhak et al. "Optical apertureless fiber microprobe for surface laser modification of metal films with sub-100 nm resolution". In: *Optics Communications* 308 (2013), pp. 125–129.
- [15] Eric X Jin and Xianfan Xu. "Finite-difference time-domain studies on optical transmission through planar nano-apertures in a metal film". In: *Japanese Journal of Applied Physics* 43.1R (2004), p. 407.
- [16] J Abed et al. "Investigation of broadband surface plasmon resonance of dewetted Au structures on TiO<sub>2</sub> by aperture-probe SNOM and FDTD simulations". In: *Plasmonics* 14.1 (2019), pp. 205–218.
- [17] Bernhard J Bohn et al. "Near-field imaging of phased array metasurfaces". In: *Nano Letters* 15.6 (2015), pp. 3851–3858.
- [18] M Schnell et al. "Controlling the near-field oscillations of loaded plasmonic nanoantennas". In: *Nature Photonics* 3.5 (2009), p. 287.
- [19] Heinrich G Frey, Jan Paskarheit, and Dario Anselmetti. "Tip-enhanced single molecule fluorescence near-field microscopy in aqueous environment". In: *Applied Physics Letters* 94.24 (2009), p. 241116.
- [20] Vahid Sandoghdar and Jürgen Mlynek. "Prospects of apertureless SNOM with active probes". In: *Journal of optics A: Pure and applied optics* 1.4 (1999), p. 523.
- [21] W Trabesinger et al. "Single-molecule near-field optical energy transfer microscopy with dielectric tips". In: *Journal of microscopy* 209.3 (2003), pp. 249–253.

- [22] Annette F Raigoza, Jason W Dugger, and Lauren J Webb. "Recent advances and current challenges in scanning probe microscopy of biomolecular surfaces and interfaces". In: *ACS applied materials & interfaces* 5.19 (2013), pp. 9249–9261.
- [23] Katarzyna Bulat et al. "Live endothelial cells imaged by Scanning Near-field Optical Microscopy (SNOM): capabilities and challenges". In: *Journal of biophotonics* 10.6-7 (2017), pp. 928–938.
- [24] Marina Zweyer et al. "SNOM on cell thin sections: observation of Jurkat and MDAMB453 cells". In: *Journal of microscopy* 229.3 (2008), pp. 440–446.
- [25] Anna Rygula et al. "Raman, AFM and SNOM high resolution imaging of carotene crystals in a model carrot cell system". In: *Spectrochimica Acta Part A: Molecular and Biomolecular Spectroscopy* 197 (2018), pp. 47–55.
- [26] Weihua Zhang, Zheyu Fang, and Xing Zhu. "Near-field Raman spectroscopy with aperture tips". In: *Chemical reviews* 117.7 (2017), pp. 5095–5109.
- [27] JJ Wang et al. "Apertureless near-field Raman spectroscopy". In: *Journal of microscopy* 210.3 (2003), pp. 330–333.
- [28] L Novotny, DW Pohl, and B Hecht. "Scanning near-field optical probe with ultrasmall spot size". In: *Optics letters* 20.9 (1995), pp. 970–972.
- [29] TJ Antosiewicz and T Szoplik. "Corrugated SNOM probe with enhanced energy throughput". In: *Opto-Electronics Review* 16.4 (2008), pp. 451–457.
- [30] Lars Neumann et al. "Extraordinary optical transmission brightens near-field fiber probe". In: *Nano letters* 11.2 (2011), pp. 355–360.
- [31] Jasmin Smajic and Christian Hafner. "Numerical analysis of a SNOM tip based on a partially cladded optical fiber". In: *Optics express* 19.23 (2011), pp. 23140–23152.

- [32] AV Goncharenko, Hung-Chih Chang, and Juen-Kai Wang. "Electric near-field enhancing properties of a finite-size metal conical nano-tip". In: *ultramicroscopy* 107.2-3 (2007), pp. 151–157.
- [33] Allen Taflove and Susan C Hagness. *Computational electrodynamics: the finite-difference time-domain method*. Artech house, 2005.
- [34] Panji Achmari et al. "Investigating the probe-tip influence on imaging using scanning near-field optical microscopy". In: *OSA Continuum* 4.4 (2021), pp. 1143–1154.
- [35] Régis Barattin and Normand Voyer. "Chemical modifications of AFM tips for the study of molecular recognition events". In: *Chemical communications* 13 (2008), pp. 1513–1532.
- [36] Cedric Volcke et al. "Plasma functionalization of AFM tips for measurement of chemical interactions". In: *Journal of colloid and interface science* 348.2 (2010), pp. 322–328.
- [37] Valeria Giliberti et al. "Functionalization of scanning probe tips with epitaxial semiconductor layers". In: *Small Methods* 1.3 (2017), p. 1600033.
- [38] BG Konoplev et al. "Probe modification for scanning-probe microscopy by the focused ion beam method". In: *Russian Microelectronics* 41.1 (2012), pp. 41–50.
- [39] Eugene G Bortchagovsky, Ulrich C Fischer, and Thomas Schmid. "Possibilities of functionalized probes in optical near-field microscopy". In: *Physica Scripta* 2014.T162 (2014), p. 014005.
- [40] Lukas Novotny, Dieter W Pohl, and Bert Hecht. "Light confinement in scanning near-field optical microscopy". In: *Ultramicroscopy* 61.1-4 (1995), pp. 1–9.
- [41] Hiromitsu Furukawa and Satoshi Kawata. "Analysis of image formation in a near-field scanning optical microscope: effects of multiple scattering". In: *Optics communications* 132.1-2 (1996), pp. 170–178.
- [42] Mario Bertero et al. "Image deblurring with Poisson data: from cells to galaxies". In: *Inverse Problems* 25.12 (2009), p. 123006.

- [43] A Cricenti et al. "Scanning probe microscopy in material science and biology". In: *Journal of Physics D: Applied Physics* 44.46 (2011), p. 464008.
- [44] PG Gucciardi et al. "Versatile scanning near-field optical microscope for material science applications". In: *Review of scientific instruments* 68.8 (1997), pp. 3088–3092.
- [45] Giovanni Longo et al. "An inverted/scanning near-field optical microscope for applications in materials science and biology". In: *physica status solidi (b)* 247.8 (2010), pp. 2051–2055.
- [46] Max Born and Emil Wolf. *Principles of optics: electromagnetic theory of propagation, interference and diffraction of light*. Elsevier, 2013.
- [47] Paul Bazylewski, Sabastine Ezugwu, and Giovanni Fanchini. "A review of three-dimensional scanning near-field optical microscopy (3D-SNOM) and its applications in nanoscale light management". In: *Applied Sciences* 7.10 (2017), p. 973.
- [48] Fritz Keilmann and Rainer Hillenbrand. "Near-field microscopy by elastic light scattering from a tip". In: *Philosophical Transactions of the Royal Society of London. Series A: Mathematical, Physical and Engineering Sciences* 362.1817 (2004), pp. 787–805.
- [49] EdwardH Synge. "A suggested method for extending microscopic resolution into the ultra-microscopic region". In: *The London, Edinburgh, and Dublin Philosophical Magazine and Journal of Science* 6.35 (1928), pp. 356–362.
- [50] Dieter W Pohl, W Denk, and M Lanz. "Optical stethoscopy: Image recording with resolution  $\lambda/20$ ". In: *Applied Physics Letters* 44.7 (1984), pp. 651–653.
- [51] Urs Dürig, Dieter W Pohl, and F Rohner. "Near-field optical-scanning microscopy". In: *Journal of Applied Physics* 59.10 (1986), pp. 3318–3327.
- [52] E Betzig, M Isaacson, and A Lewis. "Collection mode near-field scanning optical microscopy". In: *Applied Physics Letters* 51.25 (1987), pp. 2088–2090.

- [53] AMAA Lewis et al. "Development of a 500 Å spatial resolution light microscope: I. light is efficiently transmitted through  $\lambda/16$  diameter apertures". In: *Ultramicroscopy* 13.3 (1984), pp. 227–231.
- [54] A Harootunian et al. "Super-resolution fluorescence near-field scanning optical microscopy". In: *Applied Physics Letters* 49.11 (1986), pp. 674–676.
- [55] Eric Betzig and Robert J Chichester. "Single molecules observed by near-field scanning optical microscopy". In: *Science* 262.5138 (1993), pp. 1422–1425.
- [56] MF Garcia-Parajo et al. "Near-field optical and shear-force microscopy of single fluorophores and DNA molecules". In: *Ultramicroscopy* 71.1-4 (1998), pp. 311–319.
- [57] X Sunney Xie and Robert C Dunn. "Probing single molecule dynamics". In: *Science* 265.5170 (1994), pp. 361–364.
- [58] W Patrick Ambrose et al. "Alterations of single molecule fluorescence lifetimes in near-field optical microscopy". In: *Science* 265.5170 (1994), pp. 364–367.
- [59] MA Bopp et al. "Direct imaging single molecule diffusion in a solid polymer host". In: *Chemical Physics Letters* 263.6 (1996), pp. 721–726.
- [60] AGT Ruiter et al. "Single molecule rotational and translational diffusion observed by near-field scanning optical microscopy". In: *The Journal of Physical Chemistry A* 101.40 (1997), pp. 7318–7323.
- [61] JW Blatchford et al. "Photoluminescence in pyridine-based polymers: Role of aggregates". In: *Physical Review B* 54.13 (1996), p. 9180.
- [62] JA DeAro et al. "Mesoscale optical properties of conjugated polymers probed by near-field scanning optical microscopy". In: *Chemical Physics Letters* 277.5-6 (1997), pp. 532–538.
- [63] Patrick J Moyer, Karsten Walzer, and Michael Hietschold. "Modification of the optical properties of liquid crystals using near-field scanning optical microscopy". In: *Applied Physics Letters* 67.15 (1995), pp. 2129–2131.

- [64] Erwen Mei and Daniel A Higgins. "Near-field scanning optical microscopy studies of electric-field-induced molecular reorientation dynamics". In: *The Journal of Physical Chemistry A* 102.39 (1998), pp. 7558–7563.
- [65] Satoshi Kawata, Yasushi Inouye, and Prabhat Verma. "Plasmonics for near-field nano-imaging and superlensing". In: *Nature photonics* 3.7 (2009), p. 388.
- [66] M Schnell et al. "Real-space mapping of the chiral near-field distributions in spiral antennas and planar metasurfaces". In: *Nano letters* 16.1 (2015), pp. 663–670.
- [67] ERJPD L Betzig et al. "Near-field fluorescence imaging of cytoskeletal actin". In: *Bioimaging* 1.3 (1993), pp. 129–135.
- [68] AV Ankudinov et al. "Investigation of the light field of a semiconductor diode laser". In: *Optics Express* 22.21 (2014), pp. 26438–26448.
- [69] Chien-Chih Lai et al. "Near-field spectroscopy of broadband emissions from  $\gamma$ -Al<sub>2</sub>O<sub>3</sub> nanocrystals in Cr-doped double-clad fibers". In: ().
- [70] Yinlan Ruan et al. "Light confinement within nanoholes in nanostructured optical fibers". In: *Optics Express* 18.25 (2010), pp. 26018–26026.
- [71] B Hecht et al. "Influence of detection conditions on near-field optical imaging". In: *Journal of applied physics* 84.11 (1998), pp. 5873–5882.
- [72] TJ Yang, Guillaume A Lessard, and Stephen R Quake. "An apertureless near-field microscope for fluorescence imaging". In: *Applied Physics Letters* 76.3 (2000), pp. 378–380.
- [73] FYHK Zenhausern, Y Martin, and HK Wickramasinghe. "Scanning interferometric apertureless microscopy: optical imaging at 10 angstrom resolution". In: *Science* 269.5227 (1995), pp. 1083–1085.
- [74] Daniel Courjon. "Scanning tunneling optical microscopy". In: *Scanning Tunneling Microscopy and Related Methods*. Springer, 1990, pp. 497–505.

- [75] Robin Christian Reddick et al. "Photon scanning tunneling microscopy". In: *Review of scientific instruments* 61.12 (1990), pp. 3669–3677.
- [76] Ch Adelman et al. "Experiments on the depolarization near-field scanning optical microscope". In: *Applied physics letters* 74.2 (1999), pp. 179–181.
- [77] N Hosaka and Toshiharu Saiki. "Near-field fluorescence imaging of single molecules with a resolution in the range of 10 nm". In: *Journal of microscopy* 202.2 (2001), pp. 362–364.
- [78] Roarke Horstmeyer et al. "Standardizing the resolution claims for coherent microscopy". In: *Nature Photonics* 10.2 (2016), pp. 68–71.
- [79] Ernst Abbe. "Beiträge zur Theorie des Mikroskops und der mikroskopischen Wahrnehmung". In: *Archiv für mikroskopische Anatomie* 9.1 (1873), pp. 413–468.
- [80] Charles Sumner Williams and Orville A Becklund. *Introduction to the optical transfer function*. Vol. 112. SPIE Press, 2002.
- [81] Warren J Smith. *Modern optical engineering: the design of optical systems*. McGraw-Hill Education, 2008.
- [82] Gordon Wetzstein. *Lecture notes in Computational Imaging and Display: Image Deconvolution*. [https://stanford.edu/class/ee367/reading/lecture6\\_notes.pdf](https://stanford.edu/class/ee367/reading/lecture6_notes.pdf). 2018.
- [83] Jean-Luc Starck, E Pantin, and F Murtagh. "Deconvolution in astronomy: A review". In: *Publications of the Astronomical Society of the Pacific* 114.800 (2002), p. 1051.
- [84] Nicolas Dey et al. "A deconvolution method for confocal microscopy with total variation regularization". In: *2004 2nd IEEE International Symposium on Biomedical Imaging: Nano to Macro (IEEE Cat No. 04EX821)*. IEEE. 2004, pp. 1223–1226.
- [85] SA Hojjatoleslami, MRN Avanaki, and A Gh Podoleanu. "Image quality improvement in optical coherence tomography using Lucy–Richardson deconvolution algorithm". In: *Applied optics* 52.23 (2013), pp. 5663–5670.



- [86] Jason R Swedlow. "Quantitative fluorescence microscopy and image deconvolution". In: *Methods in cell biology* 81 (2007), pp. 447–465.
- [87] F Kiendl and G Güntherodt. "Computational methods to produce enhanced images out of given SNOM raw data". In: *Ultramicroscopy* 102.4 (2005), pp. 299–310.
- [88] Dennis M Sullivan. *Electromagnetic simulation using the FDTD method*. John Wiley & Sons, 2013.
- [89] John B. Schneider. *Understanding the Finite-Difference Time-Domain Method*. <https://eecs.wsu.edu/~schneidj/ufdtd/>. 2010.
- [90] Leon B Lucy. "An iterative technique for the rectification of observed distributions". In: *The astronomical journal* 79 (1974), p. 745.
- [91] Ardavan Farjadpour et al. "Improving accuracy by subpixel smoothing in the finite-difference time domain". In: *Optics letters* 31.20 (2006), pp. 2972–2974.
- [92] Alexei Deinega and Ilya Valuev. "Subpixel smoothing for conductive and dispersive media in the finite-difference time-domain method". In: *Optics letters* 32.23 (2007), pp. 3429–3431.
- [93] *Nanophotonic FDTD simulation software - LUMERICAL FDTD*. URL: <https://www.lumerical.com/products/fdtd/>.
- [94] Jun Shibayama et al. "Simple trapezoidal recursive convolution technique for the frequency-dependent FDTD analysis of a Drude–Lorentz model". In: *IEEE Photonics Technology Letters* 21.2 (2008), pp. 100–102.
- [95] Alexandre Vial and Thierry Laroche. "Description of dispersion properties of metals by means of the critical points model and application to the study of resonant structures using the FDTD method". In: *Journal of Physics D: Applied Physics* 40.22 (2007), p. 7152.
- [96] Polina Tankilevitch. *Photo of Red Pepper Beside Pickles*. [Online; accessed 9 July 2021]. Mar. 2020. URL: <https://www.pexels.com/photo/photo-of-red-pepper-beside-pickles-3872406/>.

- [97] M Totzeck. "Validity of the scalar Kirchhoff and Rayleigh–Sommerfeld diffraction theories in the near field of small phase objects". In: *JOSA A* 8.1 (1991), pp. 27–32.
- [98] Shekhar Guha and Glen D Gillen. "Description of light propagation through a circular aperture using nonparaxial vector diffraction theory". In: *Optics Express* 13.5 (2005), pp. 1424–1447.
- [99] Jian-Ming Jin. *The finite element method in electromagnetics*. John Wiley & Sons, 2015.
- [100] Fengnian Xia et al. "Two-dimensional material nanophotonics". In: *Nature Photonics* 8.12 (2014), pp. 899–907.
- [101] A Femius Koenderink, Andrea Alu, and Albert Polman. "Nanophotonics: Shrinking light-based technology". In: *Science* 348.6234 (2015), pp. 516–521.
- [102] Benjamin Gallinet, Jérémy Butet, and Olivier JF Martin. "Numerical methods for nanophotonics: standard problems and future challenges". In: *Laser & Photonics Reviews* 9.6 (2015), pp. 577–603.
- [103] Thomas W Ebbesen et al. "Extraordinary optical transmission through sub-wavelength hole arrays". In: *Nature* 391.6668 (1998), p. 667.
- [104] Che-Wei Chang, AK Sarychev, and VM Shalaev. "Light diffraction by a subwavelength circular aperture". In: *Laser Physics Letters* 2.7 (2005), p. 351.
- [105] Francisco J Garcia-Vidal et al. "Light passing through subwavelength apertures". In: *Reviews of Modern Physics* 82.1 (2010), p. 729.
- [106] Yong Xie et al. "Transmission of light through slit apertures in metallic films". In: *Optics express* 12.25 (2004), pp. 6106–6121.
- [107] Y Pang, C Genet, and TW Ebbesen. "Optical transmission through subwavelength slit apertures in metallic films". In: *Optics Communications* 280.1 (2007), pp. 10–15.
- [108] Peter B Johnson and R-W Christy. "Optical constants of the noble metals". In: *Physical Review B* 6.12 (1972), p. 4370.
- [109] Shaista Babar and JH Weaver. "Optical constants of Cu, Ag, and Au revisited". In: *Applied Optics* 54.3 (2015), pp. 477–481.

- [110] Sergio G Rodrigo, FJ García-Vidal, and L Martín-Moreno. "Influence of material properties on extraordinary optical transmission through hole arrays". In: *Physical Review B* 77.7 (2008), p. 075401.
- [111] Yongkang Gao, Qiaoqiang Gan, and Filbert J Bartoli. "Spatially selective plasmonic sensing using metallic nanoslit arrays". In: *IEEE Journal of Selected Topics in Quantum Electronics* 20.3 (2013), pp. 96–101.
- [112] Fuzi Yang and J. R. Sambles. "Resonant Transmission of Microwaves through a Narrow Metallic Slit". In: *Phys. Rev. Lett.* 89 (6 July 2002), p. 063901. DOI: 10.1103/PhysRevLett.89.063901. URL: <https://link.aps.org/doi/10.1103/PhysRevLett.89.063901>.
- [113] B. Sturman, E. Podivilov, and M. Gorkunov. "Transmission and diffraction properties of a narrow slit in a perfect metal". In: *Phys. Rev. B* 82 (11 Sept. 2010), p. 115419. DOI: 10.1103/PhysRevB.82.115419. URL: <https://link.aps.org/doi/10.1103/PhysRevB.82.115419>.
- [114] Sunghyun Cho and Seungyong Lee. "Fast motion deblurring". In: *ACM SIGGRAPH Asia 2009 papers*. 2009, pp. 1–8.
- [115] Li Xu and Jiaya Jia. "Two-phase kernel estimation for robust motion deblurring". In: *European conference on computer vision*. Springer. 2010, pp. 157–170.
- [116] Antonin Chambolle. "An algorithm for total variation minimization and applications". In: *Journal of Mathematical imaging and vision* 20.1 (2004), pp. 89–97.
- [117] Stanley J Reeves. "Generalized cross-validation as a stopping rule for the Richardson-Lucy algorithm". In: *International Journal of Imaging Systems and Technology* 6.4 (1995), pp. 387–391.
- [118] Sudhakar Prasad. "Statistical-information-based performance criteria for Richardson–Lucy image deblurring". In: *JOSA A* 19.7 (2002), pp. 1286–1296.

- [119] Yu-Wing Tai, Ping Tan, and Michael S Brown. "Richardson-lucy deblurring for scenes under a projective motion path". In: *IEEE Transactions on Pattern Analysis and Machine Intelligence* 33.8 (2010), pp. 1603–1618.
- [120] Wende Dong et al. "A piecewise local regularized Richardson–Lucy algorithm for remote sensing image deconvolution". In: *Optics & Laser Technology* 43.5 (2011), pp. 926–933.
- [121] Wang Yongpan et al. "An improved Richardson–Lucy algorithm based on local prior". In: *Optics & Laser Technology* 42.5 (2010), pp. 845–849.
- [122] Omar Sqalli et al. "Improved tip performance for scanning near-field optical microscopy by the attachment of a single gold nanoparticle". In: *Applied Physics Letters* 76.15 (2000), pp. 2134–2136.
- [123] Fei Jia et al. "Carbon nanotube/gold nanoparticles/polyethylenimine-functionalized ionic liquid thin film composites for glucose biosensing". In: *Biosensors and Bioelectronics* 24.4 (2008), pp. 945–950.
- [124] Zeineb Ben Aziza et al. "Enhancement of humidity sensitivity of graphene through functionalization with polyethylenimine". In: *Applied Physics Letters* 107.13 (2015), p. 134102.
- [125] Daniel K Schwartz. "Mechanisms and kinetics of self-assembled monolayer formation". In: *Annual review of physical chemistry* 52.1 (2001), pp. 107–137.
- [126] E Ruckenstein and ZF Li. "Surface modification and functionalization through the self-assembled monolayer and graft polymerization". In: *Advances in Colloid and Interface Science* 113.1 (2005), pp. 43–63.
- [127] Fang Lin and Chuanhong Jin. "An improved Wiener deconvolution filter for high-resolution electron microscopy images". In: *Micron* 50 (2013), pp. 1–6.
- [128] Anat Levin et al. "Understanding and evaluating blind deconvolution algorithms". In: *2009 IEEE Conference on Computer Vision and Pattern Recognition*. IEEE. 2009, pp. 1964–1971.